45èmes Journées des Actinides

Průhonice, 15th – 19th April 2015

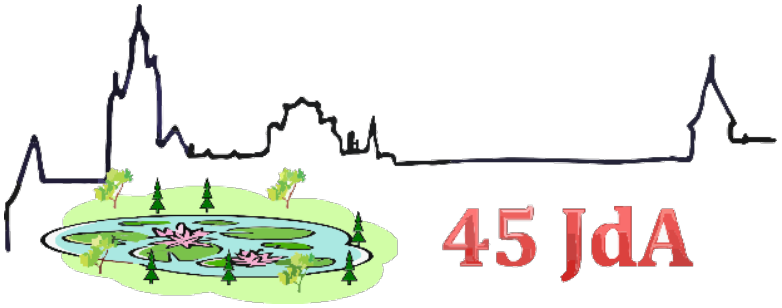

Program & Abstracts

Dear actinide friends,

Welcome to the 45èmes Journées des Actinides (45JdA), which is held in Průhonice, a little town in the outskirts of Golden Prague, and is organized by the *Prague group.* The decision about organization of 45JdA has been made at the meeting of the International Advisory Committee during the 44èmes Journées des Actinides in Ein-Gedi, Dead Sea, Israel.

The great tradition of Journées des Actinides (JdA) was organized by the excellent French scientist and actinide enthusiast Jean Marc Fournier in 1970. Soon an annual periodicity of JdA was established and JdA visited numerous beautiful spots in Europe. Members of the *Prague group* attended first the JdA in Eibsee near Ga-Pa in 1986 and since then we became one of regular participating actinide teams.

Right after the Velvet revolution pushed Czechoslovakia back to civilized part of Europe, we enjoyed confidence given to us by actinide community and organized the 20ièmes Journées des Actinides in Prague in 1990. Some of you may still remember the tower building of the Forum hotel and panorama of the Prague castle. The 33èmes Journées des Actinides took place 13 years later also in Prague, in the Crystal hotel close to the airport. This year we have the pleasure and honor to take care of 45JdA. We relocated to a green area, providing fresh air and peaceful environment for both scheduled and informal activities.

The *Prague group* is part of the *Department of Condensed Matter Physics* of the *Faculty of Mathematics and Physics* at the *Charles University in Prague* – one of the oldest European universities (founded in 1348 by the Roman Emperor Charles IV who was also the King of Bohemia as Charles I). The Faculty of Mathematics and Physics is one of the prominent research institutions in the Czech Republic and the Department of Condensed Matter Physics belongs to the most productive units of the Faculty.

The 45èmes Journées des Actinides will be attended by more than 100 participants from Europe, Asia and America, which we feel as a success. It could not be organized without substantial technical and financial support from our mother department and great effort of the members of the Local Organizing Committee, other members and students of the Department. Good number of young researchers can attend 45JdA owing to generous grants from *TALISMAN*, http://www.talisman-project.eu/ and *The Enlargement and Integration program of the European Commission* (https://ec.europa.eu/jrc/en/working-with-us/enlargement-and-integration/activities).

We thank to all who contributed to make the 45èmes Journées des Actinides a successful event.

On behalf of the *Prague group*

Vladimír Sechovský

Program - 45èmes Journées des Actinides 2015

Wednesday - 15.4.2015

17:00 - 22:00 Registration - Floret Congress Center Průhonic
19:00 - 22:00 **WELCOME PARTY - Floret Congress Center Průhonice**

Thursday - 16.4.2015

8.00-13.00 Registration - Floret Congress Center Průhonic
8.40-8.50 WELCOME ADDRESS

8.50-10.50 ***Section: Electronic properties - experiment I*** **(Chair - Vladimír Sechovský)**

o-01	Fabrice Wilhelm	High Field XMCD studies in UCoGe Ferromagnetic Superconductor
o-02	Michal Vališka	Polarized neutron diffraction and X-ray magnetic circular dichroism study of Ru doped UCoGe
o-03	Krzysztof Domieracki	Superconductivity in a non-centrosymmetric compound ThCoSi
o-04	Petr Opletal	Quantum criticality of an itinerant 5*f*-electron ferromagnet: Ru doped UCoAl
o-05	Alexander Andreev	Stabilization of ferromagnetism in UCoAl by Os doping
o-06	Yoshichika Onuki	Fermi surface properties in actinide compounds

10:50-11:20 *COFFEE BREAK*

11.20-12.40 ***Section: Chemistry and fuels*** **(Chair - Moris Eisen)**

o-07	Peter C. Burns	Properties of Nanoscale Uranyl Cage Clusters in Aqueous Solution
o-08	Yulia Konevnik	Neptunium Behavior in Gneiss Rock Massive Environment
o-09	Michał Dutkiewicz	Heterobimetallic Transuranium Compound via Reductive Functionalization of the Uranyl Dication
o-10	KeunHong Lim	Exchange current density and transfer coefficient of La, Ce, and U in LiCl-KCl eutectic salt

12.40-13.40 *LUNCH*

13.40-15.20 ***Section: Electronic properties - experiment II*** **(Chair - Roberto Caciuffo)**

o-11	Andrei Rogalev	Magnetism of Actinides Studied with Polarized X-rays
o-12	Nicola Magnani	Magnetic polarization of the americium J = 0 ground state in $AmFe_2$
o-13	Gerard Lander	Revisiting the neutron experiments on $AmFe_2$ after 40 years
o-14	Fuminori Honda	Electronic properties and pressure study on $U_2T_3X_5$ (T: Rh, Ir, X: Si, Ge) compounds
o-15	Hiroshi Amitsuka	New Magnetoelectric Effects in a Noncollinear Antiferromagnetic Metal UNi_4B

15:20-15:50 *COFFEE BREAK*

15.50-17.10 ***Section: Electronic properties and new compounds*** **(Chair - Fuminori Honda)**

o-16	Itzhak Halevy	Structural and magnetic properties investigation of Np_2Co_{17} under pressure
o-17	Amir Hen	Site-selective magnetic order of Neptunium in Np_2Ni_{17}
o-18	Attila Bartha	Single crystal study of layered $UnRhIn_{3n+2}$ materials: case of the novel U_2RhIn_8 compound
o-19	Adam Pikul	Crystal structure and physical properties of Np_2PdIn_8 and Pu_2PdIn_8

17.20-18.00 ***Networks and new facilities***

18.00-19.00 ***Posters and refreshment***

(See the list of posters at the end of the program)

Friday - 17.4.2015

8.30-10.30 ***Section: Chemistry*** **(Chair - Peter Burns)**

o-20	Moris Eisen	Actinide Mediated Catalytic Activation of Heterocumulenes
o-21	Olaf Walter	First structural characterization of triscyclopentadienylactinide(iii) derivatives (An: U, Np, Pu)
o-22	Daniel Fröhlich	Complexation of trivalent actinides with acetate studied by TRLFS and EXAFS spectroscopy
o-23	Leila Costelle	Radiolysis driven dissolution of UO_2 using synchrotron radiation
o-24	Igor Izosimov	Applications of Laser Spectroscopy for Actinide Detection in Solutions
o-25	Jakub Višňák	Complexation of uranyl with sulphate and selenate in aqueous solution: experimental data and quantum chemical modelling

10:30-11:00 *COFFEE BREAK*

11.00-12.20 ***Section: Electronic properties - experiment III*** **(Chair - Hiroshi Amitsuka)**

o-26	Nicholas Butch	Magnetic and lattice excitations in hidden order compound URu_2Si_2
o-27	Helen Walker	RXES experiments to explore the $5f$ ground state in URu_2Si_2
o-28	Tatsuya Yanagisawa	Elastic Response of URu_2Si_2 under Pulsed Magnetic Field
o-29	Yoshinori Haga	$5f$-contributions to Fermi surfaces in (U,Th)Ru_2Si_2

12.20-13.20 *LUNCH*

13.20-15.00 ***Section: New compounds I*** **(Chair - Olivier Tougait)**

o-30	Margarida Henriques	Structural and electronic properties of $U_3Fe_4Ge_4$ under pressure
o-31	Moussa Chantal	Study of isothermal sections of ternary systems U-T-Al (T=Ti, Zr)
o-32	Silvie Maskova	The onset of magnetism in UNi(Zn,Al) system
o-33	Daniel Gnida	Quantum interference phenomena due to disorder in the U_2TSi_3 compounds with AlB_2 type structure
o-34	António Pereira Gonçalves	Structure and magnetism of UMB_4 (M = V, Cr, Mo, W) uranium borides

15:00-15:30 *COFFEE BREAK*

15.30-17.10 ***Section: New compounds II*** **(Chair - Mathieu Pasturel)**

o-35	Marian Reiffers	Physical properties of an $UFe_{1-x}Sb_2$ single crystal
o-36	Moussa Chantal	Experimental investigation on the ternary U-Al-Ge system and study of the ternary intermetallic phase $U_3Al_{2-x}Ge_{3+x}$ ($-0.3 \leq x \leq 1.3$)
o-37	Nicolas Brisset	Formation and structural properties of novel ternary intermetallics U_3TGe_5 with T= transition metal of columns 4, 5 and 6.
o-38	Grzegorz Chajewski	Physical properties of U_3TGe_5 (T = V, Cr, Mo) and $U_3Al_{2-x}Ge_{3+x}$ ($-0.3 < x < 1.5$) compounds
o-39	Naoyuki Miura	Local-Fermi-Liquid Behavior in Dilute Uranium Alloys $Th_{1-x}U_xBe_{13}$ ($x \leq 0.11$)

17.20-18.00 ***Networks and new facilities***

o-nnf	Jorge Gavilano	Neutron scattering facilities at PSI and ILL. Case of Study: Novel superconducting and magnetic phases in $CeCoIn_5$ and $Nd_{0.05}Ce_{0.95}CoIn_5$

18.00-19.00 ***Posters and refreshment***

(See the list of posters at the end of the program)

Saturday - 18.4.2015

8.30-10.30 ***Section: U alloys, films and hydrides*** **(Chair - David Geeson)**

o-40	Leduc Jennifer	Nanostructured Bilayered Uranium Oxide- Iron Oxide Thin Films for Solar Hydrogen Production
o-41	Evgeniya Tereshina	Exchange bias effect in CaF_2-based UO_2/Fe_3O_4 thin films
o-42	N.-T.H. Kim-Ngan	gamma-U phase stabilized by combined T doping (T=Mo, Nb, Pt, Pd, Zr) and ultra-fast cooling
o-43	Peng Shi	In situ XPS study of the evolution of chemical nature on U-Ti alloy surface during vacuum annealing
o-44	Ruiwen Li	Hydride Growth Kinetics of U-Nb Alloy — the Role of Strain Energy
o-45	Mykhaylo Paukov	Structure and magnetic properties of doped UH_3 -based hydrides

10:30-11:00 *COFFEE BREAK*

11.00-12.20 ***Section: Theory & Computations I*** **(Chair - Gertrud Zwicknagl)**

o-46	Paul Bagus	Covalent and Ionic Bonding In Heavy Metal Oxides
~~**o-47**~~	~~Jozef Spalek~~	~~Classical and quantum criticalities in the itinerant ferromagnet UGe_2: A microscopic interpretation~~
o-48	Ilja Turek	Ab initio theory of magnetic properties of pure and Zr-doped alpha-UH_3
o-49	Gan Li	Adsorption of O_2, CO, CO_2 and H_2O on α-U (001) surface: A density-functional theory study

12.20-13.20 *LUNCH*

13:20 - 22:00 **Kutná Hora Tour + Dinner in Kutná Hora (restaurant Dačický)**

Sunday - 19.4.2015

8.30-10.30 ***Section: Theory & Computations II*** **(Chair - Paul Bagus)**

o-50	Gertrud Zwicknagl	Heat death of heavy quasiparticles
o-51	Anton Filanovich	Thermal expansion and phonon anharmonicity of alpha-plutonium
o-52	Bouchet Johann	Calculating vibrational properties of actinides with quantum molecular dynamics
o-53	Jindřich Kolorenč	Electronic Structure and Core-Level Spectroscopy of Light Actinide Dioxides
o-54	Bingyun Ao	Search for Hyperstoichiometric Plutonium Oxides from Electronic Structure Calculations
o-55	Karel Carva	Distinct ultrafast dynamics of itinerant and localized magnetic moments in gadolinium

10:30-11:00 *COFFEE BREAK*

11.00-12.20 ***Section: New compounds III*** **(Chair - Antonio P. Goncalves)**

o-56	Asaf Uziel	Relative stability of possible Th$T_2$$Al_{20}$ structures (where T = 3d transition metal)
o-57	Przemyslaw Swatek	Interplay between electronic and magnetic degrees of freedom in U$T_2$$Zn_{20}$ (T = Fe, Ru, Os, Co, Rh, Ir)
o-58	Michał J. Winiarski	Synthesis and physical properties of $A_{0.8}V_2Al_{20}$ (A = Th, Np, Pu) ternary actinide aluminides
o-59	Jacques Lechelle	$PuCrO_3$ compound: synthesis, structural and thermodynamic studies

12.20-13.20 *LUNCH*

13.20-14.40 ***Section: Fuels, materials science I*** **(Chair - Itzhak Halevy)**

o-60	Tzvi Templeman	A New Approach for the Incorporation of Dilute Self-Irradiating Defects in Thin Films
o-61	Jason Jeffries	Martensitic Phase Transformation Inhibition in Pu-1.9 at.% Ga
o-62	Sue Ennaceur	A thermal analytical study of the phase stability of unalloyed and alloyed plutonium.
o-63	Mohamed Naji	Characterization of minor actinide doped uranium oxide fuels: Raman spectroscopy approach

14:40-15:10 *COFFEE BREAK*

15.10-16.10 ***Section: Fuels, materials science II*** **(Chair - Ladislav Havela)**

o-64	Desgranges Lionel	Charge distribution in doped uranium dioxide
o-65	Tomoo Yamamura	Hydrothermal Synthesis of Actinide Dioxide at Low Temperature and Their Physicochemical Studies
o-66	Emily Moore	Thermochemisty of reactor materials: actinide oxides and fission compounds

16.10-16.30 CONFERENCE CLOSING

No.	*List of Posters (all posted throughout JdA)*	**(Chair - Jiří Prchal)**
p-01	Aleksandr Povzner	Magnetic properties and superconductivity of americium metal under pressure
p-02	Leonid Sandratskii	Correlated oscillations of the magnetic anisotropy energy and orbital moment anisotropy in thin films: the role of quantum well states
p-03	Przemyslaw Swatek	Electronic properties of UT_2Al_{20} (T = d-electron element) compounds
p-04	Chihiro Tabata	Crystal Growth and Low-Temperature Magnetic Properties of UAu_2Si_2
p-05	Klára Uhlířová	Single crystal growth and magnetic properties of $U_3Co_4Ge_7$ and $U_3Co_2Ge_7$
p-06	Khrystyna Miliyanchuk	AlB_2-type related crystal structure of $UNiZnH_{2.3}$
p-07	Jan Prokleška	Thermal expansion and magnetostriction in UNiGa
p-08	Alexandre Kolomiets	Magnetic properties of $U_2(Fe,Ni)_2Sn$ intermetallics and their hydrides
p-09	Alexander V. Andreev	Synthesis, structural and physical properties of a novel intermetallic compound $U_3Fe_2Ge_7$
p-10	Anna Maria Adamska	A new thin-film approach to making nuclear fuel research accessible
p-11	Itzhak Orion	Method for Low Atomic Number Sub-Micronic Film Production for keV Electron Scattering Measurements
p-12	Michael Shandalov	Small Volume Chemical Bath Deposition of Thorium-Alloyed and Thorium-Doped PbS Films
p-13	Rajitha Ravithas	Volatile and Air-Stable Uranium (IV) Precursors for Application in Gas Phase Deposition Processes
p-14	Zuzana Molcanova	Magnetic and thermal properties of $CeNi_{1-x}Co_xGe_2$
p-15	Antonios Banos	Statistical analysis of UH3 initiation sites using Electron Backscatter Diffraction (EBSD)
p-16	Shimon Zalkind	In Situ X-ray diffraction measurements of U-0.1w%Cr oxidation
p-17	António Pereira Gonçalves	On the $U_3Fe_2C_5$ uranium-iron carbide
p-18	Stefano Corradetti	Synthesis and thermal characterization of uranium carbide materials for ISOL targets
p-19	Mathieu Pasturel	Neutron diffraction investigation of the eutectoid decomposition of γ-U(Mo) powder produced by magnesiothermic reduction
~~p-20~~	~~Dmitry Maltsev~~	~~Thermodynamic properties of U in Ga-Sn eutectic alloy~~
p-21	Vijay Varsani	The Use of Finite-Element Modelling to Increase the Average Cooling Rate for the Plutonium Casting Furnace
p-22	Haris Paraskevoulakos	Assessment of the behaviour of metallic uranium during encapsulated product evolution
p-23	Yulia Konevnik	Temperature and time depend changes in speciation of radionuclides sorbed on crystalline rock samples
p-24	Itzhak Halevy	Cleanup Procedures for Contaminated Areas
p-25	Itzhak Halevy	Study of cleanup procedures for contaminated area: Evaluation of Rubidium as a surrogate to Cesium
p-26	Itzhak Halevy	Optimization of aerial survey of radiation in outdoor and indoor environments
p-27	Olaf Walter	Tetrakiscyclopentadienyl-actinide(IV)-complexes (Cp_4An): structures and reactivity against Broensted acidic compounds
p-28	Vladimir Sladkov	About protonated uranyl oxalate species. Affinity capillary electrophoresis data.
p-29	Cybelle Soares	CO_2 mitigation and production of methanol over bimetallic copper-lanthanides/actinides oxides catalysts
p-30	Michał Dutkiewicz	Neptunium(IV) Coordination Chemistry and Spontaneous Reduction in a Flexible Small-cavity Macrocycle

High Field XMCD studies in UCoGe Ferromagnetic Superconductor

F. Wilhelm[1], M. Taupin[2], J.-P. Brison[2], D. Aoki[2], J.-P. Sanchez[2], A. Rogalev[1]

[1] *European Synchrotron Radiation Facility (E.S.R.F.), 71 avenue des Martyrs, 38043 Grenoble, France, e-mail: wilhelm@esrf.eu*
[2] *Univ. Grenoble-Alpes, CEA/ INAC-SPSMS, 17 rue des Martyrs, 38054 Grenoble, France*

True coexistence of a homogeneous ferromagnetic state with superconductivity at ambient pressure has been found up to now only in two, strongly correlated, uranium based systems: URhGe and UCoGe. In both systems, the Curie temperature (T_C = 9K and 2.8K respectively) is higher than the superconducting temperature (T_S = 0.25K and 0.5K respectively), and the anticipated ordered moment on the uranium is substantially reduced, compared to the free ion U^{3+} or U^{4+} values: 0.4μ_B in URhGe, 0.07μ_B in UCoGe. They are both orthorhombic, with an Ising-like anisotropy of the magnetization, **c** being the easy axis, **a** the hard axis and **b** intermediate. A striking point is the large upper critical field H_{c2} exceeding the Pauli paramagnetic limit, and reaching record values of H_{c2}/T_S [1]. Moreover, when the field is applied very precisely along the **b**-axis, a field re-entrant superconducting phase, with T_S higher than in zero field, appears in URhGe, whereas an unusual S-shaped H_{c2} curve is observed in UCoGe. These phenomena seem to be closely related to the ferromagnetic instabilities, as T_C is reduced under magnetic field and collapses at the enhanced superconducting phase. This suggests a new pairing mechanism, intimately related to the magnetism of the systems.

We have performed a thorough high field XMCD study of magnetic properties on well-characterized high quality single crystal of UCoGe [2]. First we have concentrated on XMCD measurements at the $M_{4,5}$ edges of Uranium and at the K-edge of Co at 2.1 K and 17 Tesla applied along the **c** axis. A sizeable XMCD signal observed at the Uranium M-edges unambiguously confirms that U 5*f* states are carrying a magnetic moment. Using magneto-optical sum rules we deduce that magnetism of U is dominated by orbital component of ~0.70μ_B at 17 Tesla. The spin component is aligned antiparallel to the orbital one and equals to ~-0.30μ_B at 17 Tesla. The total magnetic moment of Uranium 5*f* states is 0.40μ_B which has to be compared with the total magnetization of 0.44μ_B at 17 Tesla. This observation seems to indicate that Co atoms do not carry a sizeable magnetic moment in UCoGe. This result is confirmed by a rather weak XMCD signal at the Co K-edge. Moreover, its field dependence is following exactly the U magnetization. The results of high field XMCD are nicely confirmed by the measurements performed at 1 Tesla field. The total U 5*f* magnetization is about 0.075μ_B whereas the total magnetization of the crystal along the **c** axis is equal to 0.09μ_B. The ratio of the orbital-to-spin moment is about -2.31±0.03 in both high and low field cases. Secondly, we tried to record XMCD spectra at the Uranium $M_{4,5}$-edges along the **b**-axis of the crystal. The magnetic moment on Uranium induced by 17 Tesla field, is again dominated by the orbital component of 0.165μ_B whereas the spin moment amounts to -0.08μ_B. The total 5*f* Uranium moment is only 0.085μ_B which is again of 0.035μ_B smaller than the total magnetization value. Surprisingly, the orbital-to-spin moment along the **b** axis equals to -2.06 which is very much different from the value along the **c** axis. This is the first time that a difference in magnetic anisotropy in actinide compounds manifests itself through huge changes in μ_L/μ_S ratio.

References

[1] D. Aoki, T.D. Matsuda, V. Taufour, E. Hassinger, G. Knebel, J. Flouquet, *J. Phys. Soc. Japan* **78,** 113709 (2009).
[2] M. Taupin, J.-P. Brison, D. Aoki, J.-P. Sanchez, F. Wilhelm, A. Rogalev, submitted (2015).

Polarized neutron diffraction and X-ray magnetic circular dichroism study of Ru doped UCoGe

Michal Vališka[1], Jiří Pospíšil[1,2], Anne Stunault[3], Yukiharu Takeda[4], Beatrice Gillon[5], Yoshinori Haga[2], Karel Prokeš[6], Gwilherm Nénert[3], Tetsuo Okane[4], Hiroshi Yamagami[4,7], Laurent Chapon[3], Arsène Goukassov[5], Allain Cousson[5], Etsuji Yamamoto[2]

[1]*Charles University in Prague, Faculty of Mathematics and Physics, Department of Condensed Matter Physics, Ke Karlovu 5, 121 16 Prague 2, Czech Republic*
e-mail: michal.valiska@gmail.com
[2]*Advanced Science Research Center, Japan Atomic Energy Agency, Tokai, Ibaraki, 319-1195, Japan*
[3]*Institut Laue Langevin, 71 Avenue des Martyrs, CS 20156, F-38042 Grenoble Cedex 9, France*
[4]*Condensed Matter Science Division, Quantum Beam Science Directorate, Japan Atomic Energy Agency, 1-1-1 Kouto, Sayo-cho, Sayo-gun, Hyogo 679-5148, Japan*
[5]*Laboratoire Léon Brillouin, UMR12 CEA-CNRS, Bât 563 CEA Saclay, 91191 Gif sur Yvette Cedex, France*
[6]*Helmholtz-Zentrum Berlin für Materialien und Energie, Hahn-Meitner Platz 1, D-14109 Berlin, Germany*
[7]*Department of Physics, Kyoto Sangyo University, Motoyama, Kamigamo, Kita-Ku, Kyoto 603-8555, Japan*

We report on microscopic study of the ferromagnetism in the Ru doped ferromagnetic superconductor UCoGe. Single crystals with composition $UCo_{0.97}Ru_{0.03}Ge$ and $UCo_{0.88}Ru_{0.12}Ge$ were prepared. Both were investigated by polarized neutron diffraction (PND) at and the latter one also by the XMCD method. $UCo_{0.97}Ru_{0.03}Ge$ and $UCo_{0.88}Ru_{0.12}Ge$ order ferromagnetically below the T_C=6 K and 8.5 K, respectively, i.e. higher than at T_C=3 K for UCoGe. The increase of T_C is accompanied by enhancement of the spontaneous moment to μ_S=0.11 μ_B/f.u. and μ_S=0.21 μB/f.u., respectively. The analysis of the PND results assigns the ferromagnetism enhancement mainly to the growth of the orbital part of the U 5*f* moment. In contrast to the published results of PND study of the parent UCoGe, we found parallel orientation of the U and Co moments in both cases. Evolution of magnetic characteristics with Ru concentration is discussed within a scenario considering the varying 5*f*-*d* hybridization as the key mechanism.

Superconductivity in a non-centrosymmetric compound ThCoSi

Krzysztof Domieracki and Dariusz Kaczorowski

Institute of Low Temperature and Structure Research, Polish Academy of Sciences,
P.O. Box 1410, 50-950 Wrocław, Poland
e-mail: K.Domieracki@int.pan.wroc.pl

The silicide ThCoSi crystallizes with a tetragonal crystal structure of the LaPtSi-type that lacks an inversion center. Its physical properties have been studied by means of magnetization, electrical resistivity and heat capacity measurements, performed down to 0.35 K in magnetic fields up to 5 T. The compound was found to exhibit bulk superconductivity below T_c = 3.05 K, characterized by the upper critical field close to the Pauli-Clogston limit. The absence of inversion center implies lifting the spin degeneracy of conduction bands due to the Rashba-type anti-symmetric spin-orbit coupling. This may lead to mixed singlet-triplet parity of the superconducting state with line nodes in the energy gap and helical vortex phases. However, at odds with such prospects, the key superconducting parameters of ThCoSi indicate that this compound is likely a moderately-coupled type II BCS-like superconductor, as nearly all the hitherto studied weakly-correlated non-centrosymmetric materials.

o-04

Quantum criticality of an itinerant 5f-electron ferromagnet: Ru doped UCoAl

Petr OPLETAL[1], Jan PROKLEŠKA[1], Vladimír SECHOVSKÝ[1]

[1] *Charles University in Prague, Faculty of Mathematics and Physics, Department of Condensed Matter Physics, Ke Karlovu 5, 121 16 Prague 2, The Czech Republic*

UCoAl is an itinerant 5f-electron paramagnet appearing on the verge of ferromagnetism. It crystallizes in the hexagonal ZrNiAl-type structure and exhibits strong magnetocrystalline anisotropy with easy axis along the c-axis. At low temperatures it undergoes first-order metamagnetic phase transition (FOMPT) to ferromagnetic state with the critical magnetic field B_c ~ 0.7 T applied along the c-axis and the critical temperature T_0 = 11 K where FOMPT changes to crossover behavior. B_c (T_0) increases (decreases) with applying hydrostatic pressure (Fig. 1) [1, 2]. FOMPT disappears at quantum critical point at p = 1.5 GPa and B = 7 T [2]. This is in agreement with the generic H,p,T phase diagram for itinerant quantum ferromagnets proposed in [3] and shown in Fig. 2. From this phase diagram and pressure experiments on UCoAl, the true ferromagnetic phase would appear in negative pressures $p \leq -0.2$ GPa [2], which cannot be put into practice.

The unusual physics of UCoAl has been attracting researchers for many years. Frequent studies dealt with substituting Co by other d-elements. Depending on d-metal dopant and its amount, ground ferromagnetic or paramagnetic state, where FOMPT completely disappears is realized. It has been shown in [4] that as little as 1% of Ru substituted for Co leads to ferromagnetism with T_C = 17 K. By lowering nominal Ru content we move closer to the UCoAl ground state.

We have grown single crystals of $UCo_{1-x}Ru_xAl$ for x = 0.0025, 0.005 and 0.01 and investigated the corresponding H,p,T magnetic phase diagram by magnetic, electrical resistivity, Hall Effect and thermal expansion measurements. $UCo_{0.9975}Ru_{0.0025}Al$ exhibits paramagnetic ground state and FOMPT with critical magnetic field B_c ~ 0.55 T. In $UCo_{0.995}Ru_{0.005}Al$ ground ferromagnetic state and FOMPT is observed. $UCo_{0.99}Ru_{0.01}Al$ exhibits same ground ferromagnetic state as in previous research. Evolution of magnetism in UCoAl and our single crystals within the generic H,p,T phase diagram of itinerant quantum ferromagnets will be discussed.

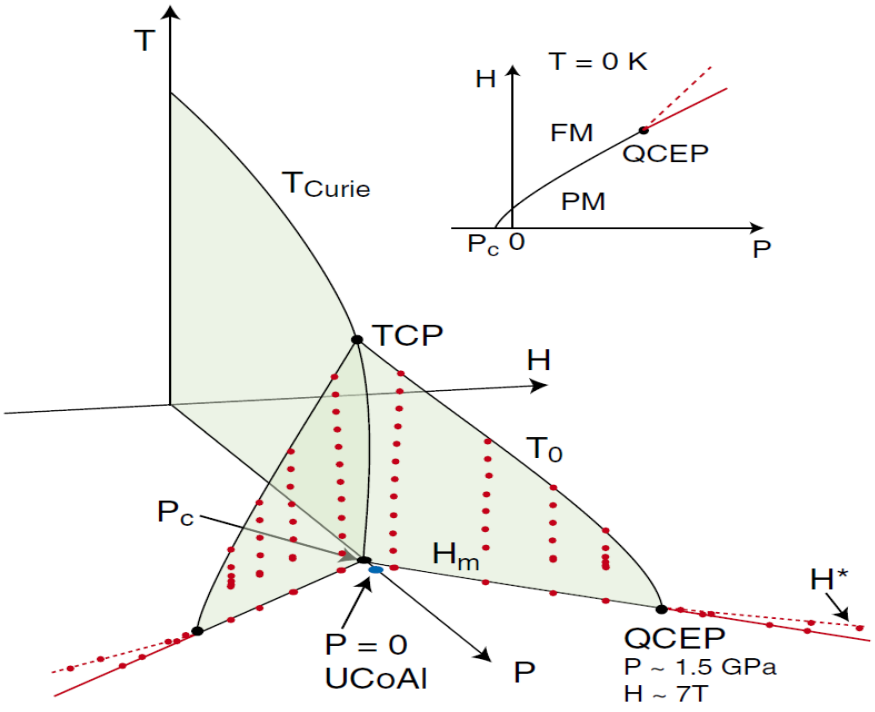

Fig. 1: Magnetic (H, p, T) phase diagram of UCoAl by [2].

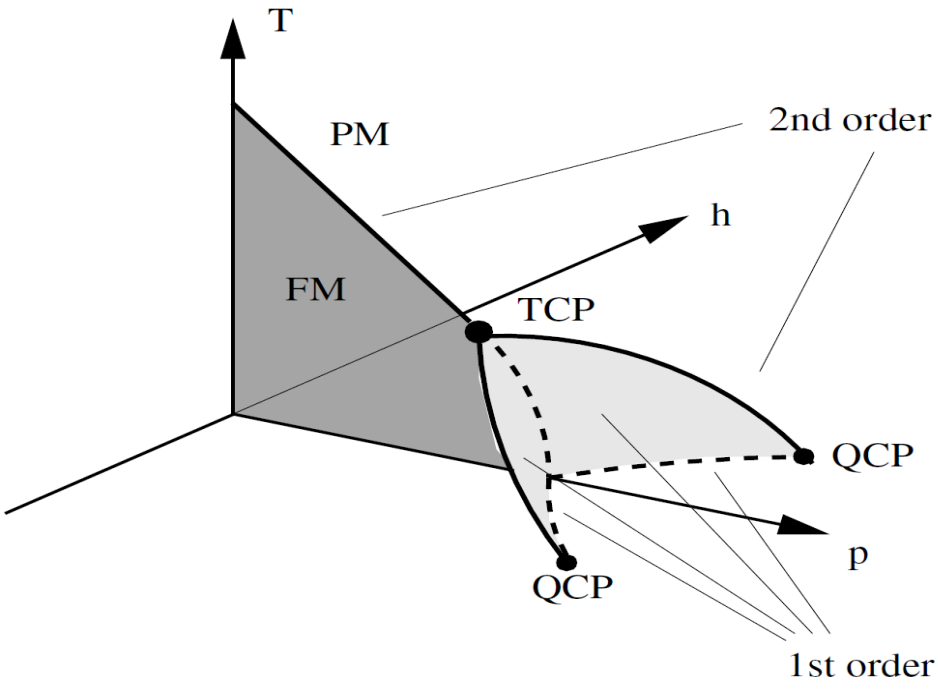

Fig. 2: Schematic (H, p, T) phase diagram of itinerant quantum ferromagnet by [3].

References

1. Mushnikov, N.V., et al., *Magnetic properties of the 5f itinerant electron metamagnet UCoAl under high pressure.* Physical Review B, 1999. **59**(10): p. 6877-6885.
2. Aoki, D., et al., *Ferromagnetic Quantum Critical Endpoint in UCoAl.* J. Phys. Soc. Jpn., 2011. **80**(9).
3. Belitz, D., T.R. Kirkpatrick, and J. Rollbühler, *Tricritical Behavior in Itinerant Quantum Ferromagnets.* Physical Review Letters, 2005. **94**(24): p. 247205.
4. Andreev, A.V., et al., *Ferromagnetism in the UCo1-xRuxAl quasiternary intermetallics.* Philosophical Magazine B-Physics of Condensed Matter Statistical Mechanics Electronic Optical and Magnetic Properties, 1997. **75**(6): p. 827-844.

Stabilization of ferromagnetism in UCoAl by Os doping

Alexander V. Andreev[1], Kenji Shirasaki[2], Josef Šebek[1],
Denis I. Gorbunov[1,3], Stanislav Daniš[4], Tomoo Yamamura[2]

[1] *Institute of Physics, Academy of Sciences, Na Slovance 2, 182 21 Prague, Czech Republic*
E-mail: andreev@fzu.cz
[2] *Institute for Materials Research, Tohoku University, Katahira 2-1-1, Sendai, 980-8577, Japan*
[3] *Dresden High Magnetic Field Laboratory (HLD), Helmholtz-Zentrum*
Dresden-Rossendorf, D-01314 Dresden, Germany
[4] *Department of Condensed Matter Physics, Charles University,*
Ke Karlovu 5, 121 16 Prague, Czech Republic

UCoAl (hexagonal crystal structure of the ZrNiAl type) exhibits in field 0.7 T applied along the *c* axis a metamagnetic transition to the forced ferromagnetic state [1]. It was found that the ground state of UCoAl is paramagnetic [2], so the compound is an itinerant metamagnet with a uniquely low transition field. A magnetic moment at the transition is induced practically exclusively on U [3], but the state of the 5*f* electrons depends very drastically on the interaction with ligands, especially with *d*-metals. When Co is substituted by *T* = Fe, Ru, Rh and Ir in the $UCo_{1-x}T_xAl$ systems, the critical field H_{cr} of the transition rapidly decreases and already few % doping stabilizes spontaneous ferromagnetism [4,5]. Opposite, for *T* = Ni, Pd and Pt, H_{cr} increases and paramagnetism is stabilized [4,6]. Now we completed a study of the influence of a late *d*-metal on the magnetism of UCoAl by testing *T* = Os.

In the case of *T* = Pt, solid solutions form in the whole range of Pt concentrations. In the system with Os, similarly to solid solutions with Ir, the homogeneity range is limited to $x = 0.2$ with a small lattice expansion in the basal plane. Moreover, UOsAl does not form the ZrNiAl-type structure but rather hexagonal Laves phase of the $MgZn_2$ type. A magnetization study of single crystals with x = 0.02, 0.05, 0.10 shows that they are ferromagnets with the easy magnetization axis *c* (Fig. 1). The spontaneous magnetic moment M_s increases from 0.40 μ_B per formula unit (since other atoms are non-magnetic, it corresponds to the magnetic moment per uranium atom, M_U) at $x = 0.02$ to 0.53 μ_B at $x = 0.10$, which is almost twice larger than the magnetic moment induced at the metamagnetic transition in UCoAl.

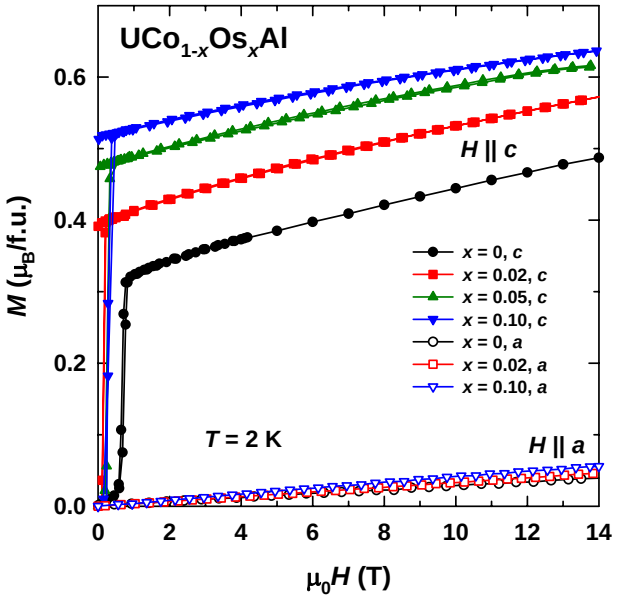

Fig. 1. Magnetization curves of the $UCo_{1-x}Os_xAl$ single crystals with along the *c* axis (filled symbols) and the *a* axis (empty symbols) at 2 K.

Immediately after the stabilization of the ferromagnetism (x = 0.02), the *c*–axis curve demonstrates very high susceptibility above the field where domain-wall movement is completed. It goes parallel to that of meta-magnetic UCoAl showing that the ferro-magnetism is still very weak. The stabilization of the ferromagnetism with increasing x leads to a decrease of this susceptibility, nevertheless, it is still very high at $x = 0.10$.

All the compounds exhibit huge magnetic anisotropy characteristic for UCoAl. Extrapolation of the *a*-axis magnetization curves to crossing with $M = M_s$ gives anisotropy field H_a as 120-130 T. But this method does not take into account that the easy-axis magnetization is not saturated in the maximum applied field and grows even faster that the hard-axis one. So, the real H_a as a field of crossing of the easy- and

hard-axis curves is considerably larger that these already huge values.

Figure 2 shows the low-field part of magnetization curves along the *c* axis. The hysteresis loops show typical behavior for intrinsic coercivity of narrow domain walls characteristic for rare-earth and uranium compounds with very large magnetic anisotropy: low initial susceptibility, rectangular hysteresis loop and typical difference in the temperature dependence of the magnetization of zero-field-cooled and field-cooled samples (Fig. 3). Nevertheless, the coercive field H_c reaches only moderate values, 0.25 T for $x = 0.10$.

Similarly to M_s, the Curie temperature T_C increases with x (Fig. 3) and reaches 48 K for $x = 0.10$. Thus, Os stabilizes ferromagnetism in UCoAl considerably stronger than Rh and Ir and slightly stronger than Fe and Ru.

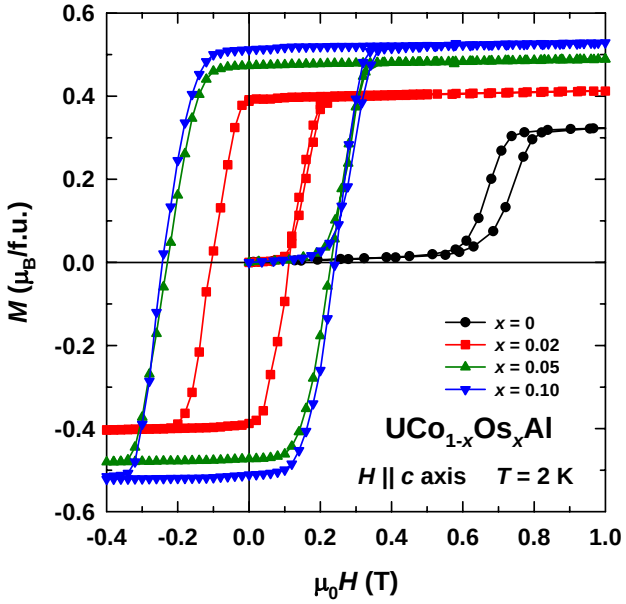

Fig. 2. Hysteresis loops of the $UCo_{1-x}Os_xAl$ single crystals at 2 K. Hysteresis of the metamagnetic transition in UCoAl is also shown.

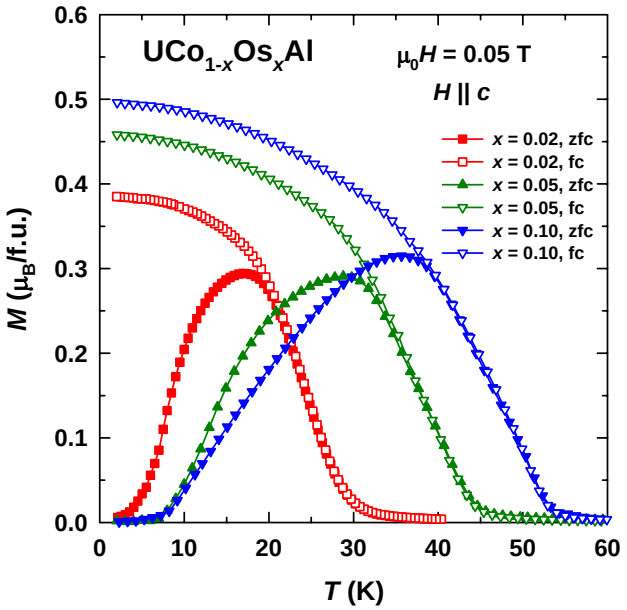

Fig. 3. Temperature dependence of the magnetization in field of 0.05 T applied along the *c* axis. The curves were obtained on the zero-field-cooled and field-cooled samples.

Acknowledgements

The work was supported by the Program of Czech Research Infrastructures (project no. LM2011025).

References

[1] A.V. Andreev et al., Sov. Phys. Solid State 27 (1985) 1145.
[2] V. Sechovsky et al., Physica B 142 (1986) 283.
[3] P. Javorsky et al., Phys. Rev. B 63 (2001) Art. No. 064423.
[4] A.V. Andreev at al., J. Alloys Comp. 224 (1995) 117.
[5] A.V. Andreev et al., J. Alloys Comp. 284 (1999) 77.
[6] A.V. Andreev et al., J. Alloys Comp. 265 (1998) 38.

o-06

Fermi surface properties in actinide compounds

Yoshichika Ōnuki[1]

[1] *Faculty of Science, University of the Ryukyus, Nishihara, Okinawa, 903-0213, Japan, e-mail: onuki@phys.u-ryukyu.ac.jp*

We present the Fermi surface, magnetic and superconducting properties in $NpGe_3$, UPt_3, $NpPd_5Al_2$, and $PuIn_3$, together with their related compounds [1]. Fascinating anisotoropic superconductivity, magnetism, and heavy fermions are observed in these compounds. These are summarized as follows:

1) The 5*f*-itinerant band model is well applicable to the topology of the Fermi surface in an enhanced Pauli paramagnet $NpGe_3$. Note that the cyclotron masses determined from the dHvA experiments are larger than the corresponding band masses because the many-body Kondo effect is not included in the conventional energy band calculations. Furthermore note that the band mass depends on the 5*f*-content in the Fermi surface, which is reflected in the cyclotron mass.
2) The 5*f*-itinerant band model is also applicable to the topology of the Fermi surface in a heavy-fermion superconductor UPt_3. The detected cyclotron masses are extremely large, reaching 110 m_0. UPt_3 possesses three superconducting phases in the magnetic field-temperature phase, named A, B, and C phases. From the precise field-angle-resolved thermal conductivity measurements, the pairing symmetry of UPt_3 is found to belong to an E_{1u} representation in the *f*-wave category.
3) A heavy-fermion superconductor $NpPd_5Al_2$ is found to reside in the vicinity of the quantum critical point, similar to a quasi-two dimensional heavy fermion superconductor $CeCoIn_5$ with the d_{x2-y2}-type symmetry. Therefore, the heavy-fermion superconductivity is realized in the non-Fermi liquid state.
4) The dHvA experiments were also carried out for an antiferromagnet $PuIn_3$ with T_N = 14 K, as well as Np and U compounds mentioned above. The dHvA branch with the cyclotron mass $m_c^* \cong 5\ m_0$ is detected in a narrow field-angle region centered at H || <111>, which is most likely due to a small antiferromagnetic Brillouin zone.
5) A Fermi surface split into two Fermi surfaces if the crystal structure does not possess inversion symmetry. We clarified split Fermi surface properties in Rashba-type $CeIrSi_3$ and $LaIrSi_3$, chiral structure VSi_2, $NbSi_2$, and $TaSi_2$, and PdBiSe, but no uranium compounds. A possible candidate is UIr under pressure. This is our perspective dHvA work.

The present studies are collaborated with R. Settai, N. Kimura, Y. Haga, E. Yamamoto, N. Tateiwa, T. C. Kobayashi, Y. Machida, K. Izawa, F. Honda, D. Aoki, H. Harima, and H.

Yamagami.

References

[1] Y. Ōnuki, R. Settai, Y. Haga, Y. Machida, K. Izawa, F. Honda, and D. Aoki, C. R. Physique 1**5**, 616-629 (2014).

Properties of Nanoscale Uranyl Cage Clusters in Aqueous Solution

Peter C. Burns[1]

[1] *University of Notre Dame, 301 Stinson-Remick Hall, Notre Dame IN 46556, USA, e-mail: pburns@nd.edu*

A decade ago we first reported the spontaneous self-assembly of uranyl peroxide polyhedra into nanoscale cage clusters in aqueous solution.[1] Whereas the initial report was for three novel clusters, our continued efforts have expanded this family to include more than 100 distinct clusters, with more than half of these now reported in the literature.[2] These clusters contain as many as 124 uranyl ions that are bridged through combinations of peroxide, hydroxyl, pyrophosphate, oxalate, etc.

Recently, we have focused considerable efforts on detailed studies of the behavior of two uranyl peroxide clusters, U60 and U24Py, in aqueous solution using a combination of dynamic and static light scattering, small angle X-ray scattering, electrospray ionization mass spectrometry, cryogenic transmission electron microscopy, atomic force microscopy, Raman spectroscopy, nuclear magnetic resonance spectroscopy, and computational simulations. Taken together, these approaches have provided an unprecedented understanding of the behavior of such clusters in solution. These clusters are highly stable in water, where they can persist for many months. They are stable under increased temperature and pressure, and they exhibit aggregation behavior into "blackberry" structures upon aging or when salts are added to solution. Their measured aqueous solubilities are remarkable high, which suggests several potential applications in the nuclear fuel cycle.

References

[1] P.C. Burns, K.A. Kubatko, G. Sigmon, B.J. Fryer, J.E. Gagnon, M.R. Antonio and L. Soderholm, L. *Angew. Chem. Int. Ed.* **44**, 2135 (2005).
[2] J. Qiu and P.C. Burns, P. C. *Chem. Rev.* **113**, 1097 (2013) **2013**.

Neptunium Behavior in Gneiss Rock Massive Environment

Yulia Konevnik, Elena Zakharova

[1] *IPHE RAS, Leninskiy prospect 31, Moscow, Russia 119071*
e-mail: leonenko@gmail.com

Isolation of radioactive wastes, especially of high level wastes (HLW) containing long-lived radionuclides, is a major challenge that may determine the fate of atomic energy. The current approach is to incorporate HLW in an inert matrix for entombment in a deep geological repository designed with multiple levels of safety systems that are both engineered (matrix, container etc.) and geological (rock massive) barriers. An area in gneissic rock near Krasnoyarsk has been chosen as one of the probable sites for a deep geological repository [1].
Neptunium, which has a long half-life, is one of the most mobile of the actinides in the environment, where it can be present in different oxidation states. Since the most probable oxidation state of neptunium at the beginning of repository operation is (V), the initial form of neptunium in all experiments was NpO_2^+. Np(V) sorption from ground water by gneiss and dolerite collected from that site were evaluated in oxic and anoxic environments at temperatures of 20 ºC and 90 ºC. The speciation of sorbed neptunium and its time and temperature dependent changes were studied using a modified Tessier's procedure of sequential extraction. The distribution of sorbed neptunium was studied by autoradiography. Single mineral grains with high concentrations of sorbed neptunium were detected, and the neptunium oxidation state was studied by XPS.

References

[1] Anderson E.B., Belov S.V., Kamnev E.V., Kolesnikov I. Yu., Lobanov N.F., MorozovV.N., Tatarinov V.N. Underground isolation of radioactive wastes. // M. «Gornaya kniga», 2011.

Heterobimetallic Transuranium Compound *via* Reductive Functionalization of the Uranyl Dication

Michał S. Dutkiewicz[1,2], Olaf Walter[1], Markus Zegke[2], Christos Apostolidis[1], Nicola Magnani[1], Jean-Christophe Griveau[1], Eric Colineau[1], Roberto G. M. Caciuffo[1]*, Polly L. Arnold[2]*

[1] *EC-JRC Institute of Transuranium Elements, Postfach 2340, D-76125 Karlsruhe, Germany*
e-mail: michael.dutkiewicz@gmail.com
[2] *The University of Edinburgh, School of Chemistry, West Mains Road, Edinburgh, EH9 JJ, UK*

The rigorously axial and inert d^0f^0 uranyl ion $[UO_2]^{2+}$ is the most abundant motif in the uranium chemistry, being relevant to environmental speciation and nuclear waste remediation. Along with its congeneric neptunyl and plutonyl cations, the singly reduced d^0f^1 uranyl cation $[UO_2]^{+}$ retains the linear, strongly covalent dioxo core but displays enhanced oxo-groups basicity [1]. The latter often associates CCI clustering and disproportionation reactions of U^V species, although the greater oxo-group reactivity remains unknown and its reactions to form new covalent bonds are rare.

In 2004 Arnold and co-workers have reported the syntheses of monouranyl Schiff-base calixpyrrole pacman complexes, $[UO_2(S)(H_2L)]$ (Fig. 1, S = tetrahydrofuran (thf), pyridine (py)) in the deprotonation reaction of H_4L with uranyl silylamide $[(UO_2)(thf)_2\{N(SiMe_3)_2\}_2]$ [2]. The resulting vacancy in N_4-donor compartment has latter accessed diverse heterobimetallic complexes of transition and rare earth metals through further substitution of the remaining two pyrrolic protons and coordination by the uranyl *endo*-oxo moiety [3,4].

Here we report on the synthesis, structure and magnetic properties of the first heterobimetallic U^V-oxo-neptunium compound through an *exo*-oxo activation of the monouranyl Pacman-shaped $[(UO_2)(thf)(H_2L)]$ complex with tris(cyclopentadienyl)neptunium(III), $[^{237}Np(Cp)_3]$ (Fig. 1, right reaction path).

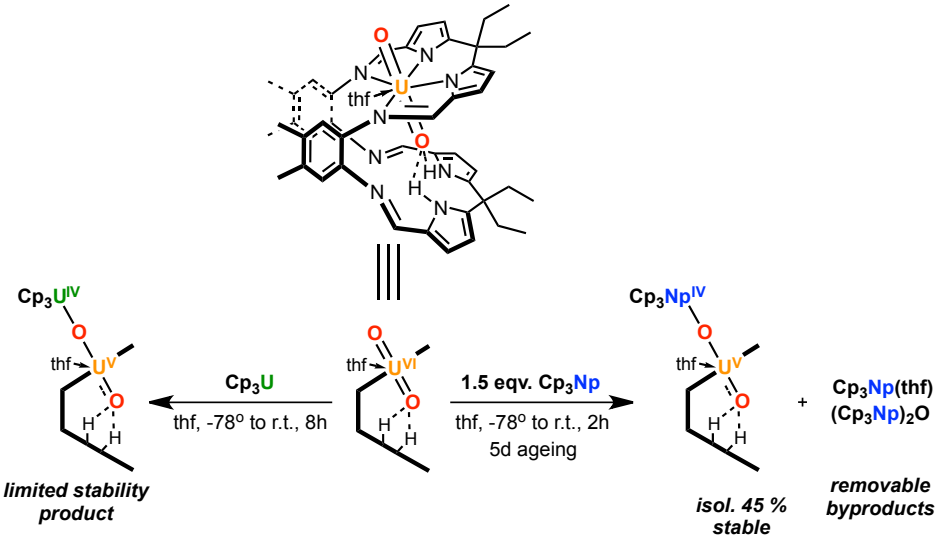

Fig. 1. $[UO_2(thf)(H_2L)]$ complex and its reactivity studies with $(Cp)_3An$ (An = U, Np) reagents.

The observed inability of the Np^{III} ion to exploit the empty N_4-pocket of the ligand can be ascribed to sterical constrains of the three $[Cp]^-$ groups and a spontaneous single electron reduction of the uranyl dication stabilized by *endo*-oxo hydrogen bonding. Interestingly, we remarked greater thermal stability of the resulting $[(Cp)_3Np\{(UO_2)(thf)(H_2L)\}]$ complex over its uranium analogue (Fig. 1, left reaction path). Also, this is paralleled with the possible partial disproportionation of both complexes upon their dissolution in d_8-tetrahydrofuran to form parent $[(Cp)_3An(thf)]$, (An = U, Np) and $[UO_2(thf)(H_2L)]$ compounds, in both cases tracked with ^1H NMR spectra. Despite a local axial symmetry of the uranyl-neptunium moiety (Np1-O1-U1 170.5(1)°), the DC and AC

magnetometry studies of the heterobimetallic complex at various fields and temperatures (0.5–7 T, 2–300 K) showed no visible magnetic communication between Np^{III} ($5f^3$, $J = 9/2$) and U^{V} ($5f^1$, $J = 5/2$) Kramers ions.

We have found the presented structural studies triggered a new discussion about previously not observed actinide ions cross-reactions, and became relevant to aggregation phenomena of the actinide oxide clusters.

References

[1] Arnold, P. L., Love, J. B. & Patel, D. Pentavalent Uranyl Complexes. *Coord. Chem. Rev.* **253**, 1973-1978 (2009).

[2] Arnold, P. L., Blake, A. J., Wilson C. & Love J. B. Uranyl complexation by a schiff-base, polypyrrolic macrocycle. *Inorg. Chem.* **43**, 8206-8208 (2004).

[3] Arnold, P. L., *et al.*, Single-electron uranyl reduction by a rare-earth cation. *Angew. Chem. Int. Ed.* **50**, 887–890 (2011).

[4] Arnold, P. L., Patel, D., Blake, A. J., Wilson, C. & Love J. B. Selective oxo functionalization of the uranyl ion with 3d metal cations. *J. Am. Chem. Soc.* **128**, 9610–9611 (2006).

Exchange current density and transfer coefficient of La, Ce, and U in LiCl-KCl eutectic salt

KeunHong Lim, Seung Park, Jong-Il Yun

KAIST, Yuseong-gu, Daejeon, South Korea, e-mail: neo_jedi@kaist.ac.kr

The pyrochemical process is an electrochemical separation process which has been under development for recycling used nuclear fuel. For the simulation of the pyrochemical process, various electrochemical properties such as exchange current density and transfer coefficient are needed. However, in most simulation studies, assumed data of exchange current density and transfer coefficient of metal chlorides have been used due to the lack of experimental data. In the present work, the exchange current density and the transfer coefficient for La, Ce, and U were investigated in LiCl-KCl molten eutectic at 500 ^{o}C.

All the experiments were carried out in an inert Ar atmosphere glove box (Ar 99.999 % purity). The electrochemical cell consists of three electrodes. Tungsten rods (Φ =1.5 mm) were used as a working electrode and a counter electrode, and a silver wire (Φ =1.0 mm) was used as a reference electrode. The temperature of the sample containing target element with eutectic salt was controlled by the furnace equipped at the lower part of the glove box within uncertainty of ±1 ^{o}C. The concentrations of $LaCl_3$, $CeCl_3$, and UCl_3 in LiCl-KCl eutectic salt were measured by using ICP-AES.

To obtain the equilibrium potentials of the system, a cyclic voltammetry was employed. Several cycles of cyclic voltammogram were measured, and the peak potentials for both oxidation and reduction reactions agreed consistently with those in literature [1]. The equilibrium potentials of $LaCl_3$, $CeCl_3$, and UCl_3 in LiCl-KCl eutectic salt were determined as -2.05 ± 0.01 V, -1.98 ± 0.02 V, and -1.39 ± 0.01 V, respectively. Around each equilibrium potentials, the exchange current densities of La, Ce, and U were investigated by using the Tafel plot and the linear polarization technique. As shown in Fig. 1, the exchange current densities of La, Ce, and U were determined to be 7.77 ± 0.35 mA/cm^2, 17.61 ± 0.20 mA/cm^2, and 18.75 ± 0.42 mA/cm^2, respectively. The transfer coefficients of each element were found to 0.69 ± 0.02 for La, 0.55 ± 0.01 for Ce, and 0.68 ± 0.03 for U with the Tafel slope, whereas in most simulation works the transfer coefficient has been assumed as 0.5 due to the lack of proper electrochemical data.

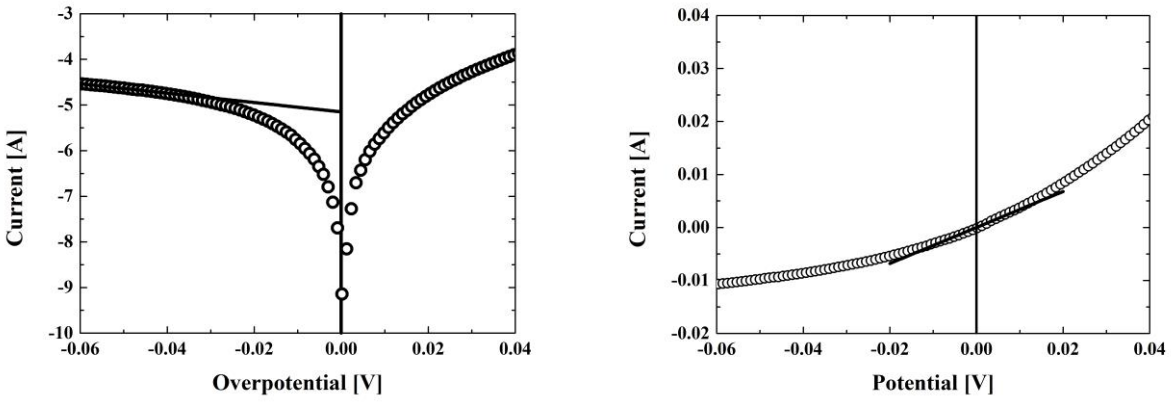

Fig.1. The Tafel plot and the linear polarization of 1 wt.% U in LiCl-KCl molten salt at 500 ^{o}C

Additionally, the exchange current density of each element of interest in the present work was obtained as a function of temperature and concentration. By Arrhenius' law, the logarithmic value of the reaction rate constant and the exchange current density showed the linear relationship with inversed temperature. As anticipated, the exchange current densities were directly proportional to the concentration. The temperature and concentration dependency of exchange current density were employed in comparison with other literature's data which matched well with our data [2,3].

Based on exchange current densities and transfer coefficients of La, Ce, and U, we computed the current density as a function of applied overpotential for the case of assumed data in most simulation papers and data from the present work, as demonstrated in Fig. 2.

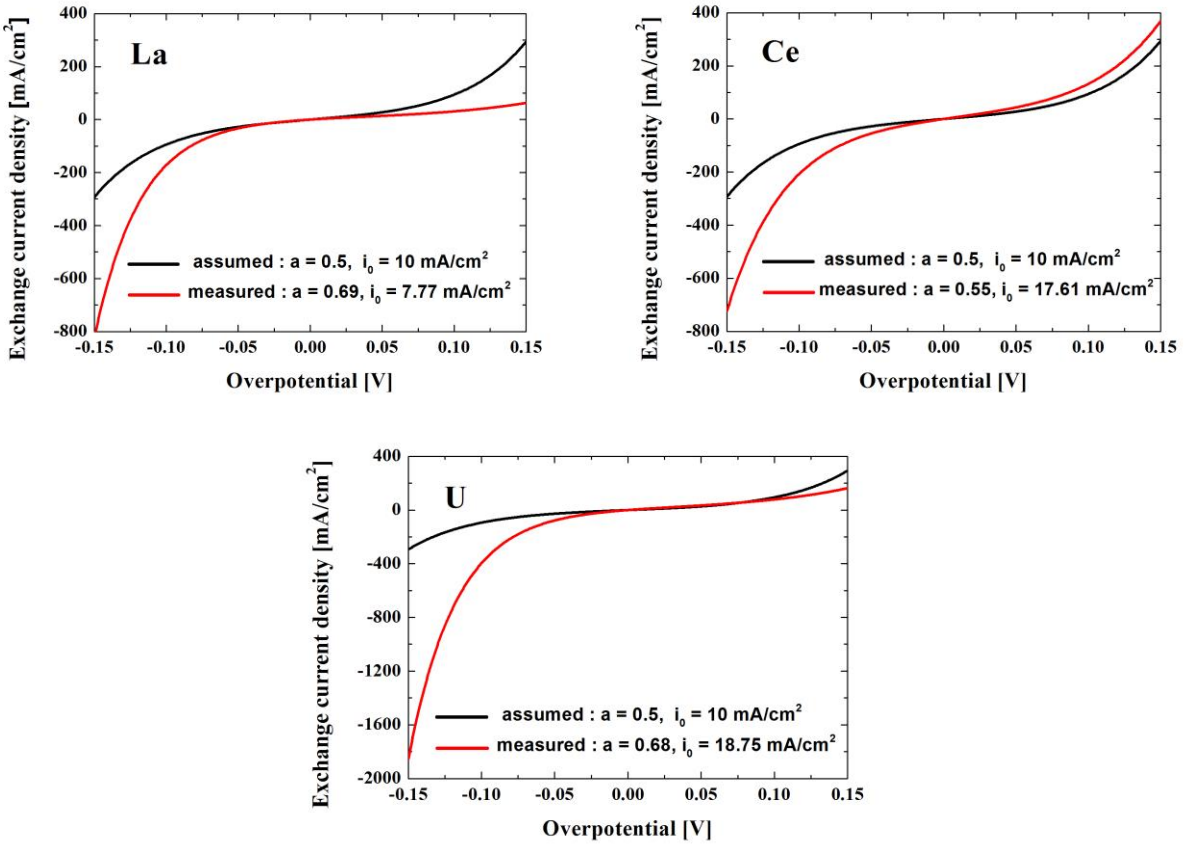

Fig. 2. The simulated current density as a function of overpotential using assumed and measured exchange current density and transfer coefficient of La, Ce, and U.

References

[1] K. Sridharan, "Thermal properties of LiCl-KCl molten salt for nuclear waste separation", Final report, NEUP (2012)
[2] I. Choi, B.E. Serrano, S.X. Li, S. Herrmann, S. Phongikarron, "Determination of exchange current density of U3+/U couple in LiCl-KCl eutectic mixture", Proceedings of Global 2009, Paris, France (2009)
[3] K.C. Marsden, B. Pesic, "Evaluation of the electrochemical behavior of $CeCl_3$ in molten LiCl-KCl eutectic utilizing metallic Ce as an anode", J. Electrochem. Soc. **158**, F111 (2011)

Magnetism of Actinides Studied with Polarized X-rays

Andrei Rogalev and Fabrice Wilhelm

European Synchrotron Radiation Facility (E.S.R.F.), 71 avenue des Martyrs, 38043 Grenoble, France, e-mail: rogalev@esrf.fr

Actinides compounds, which are straddling the magnetic properties of rare-earths and transition metals, have been the subject of increasing interest due to their very different properties, such as Pauli paramagnets, localized and itinerant ferromagnets, and heavy fermion superconductors. The key parameter responsible for the large variety of magnetic properties is obviously the degree of localization of the 5f states which are indeed involved in both the chemical bonding and the magnetism. To unravel the details of the electronic structure and magnetic properties of these 5f states, polarization dependent X-ray spectroscopy and scattering at the $M_{4,5}$ edges appear as the most suitable experimental tools. At the third generation synchrotron radiation facilities, small x-ray beam with flexible polarization sized down to few microns can be routinely achieved. This technique is thus perfectly suited for studying minute samples (a few micrograms) of transuranium materials. Moreover, X-ray spectroscopy based techniques provide quantitative magnetic information with element-specificity as well as sensitivity to valence-state and lattice symmetry. In this talk, we will present an introduction to polarization dependent x-ray spectroscopy and scattering as well recent advances in use of polarized x-rays to study local magnetic properties and electronic structure of actinides compounds.

Magnetic polarization of the americium $J = 0$ ground state in $AmFe_2$

N. Magnani,[1] R. Caciuffo,[1] F. Wilhelm,[2] E. Colineau,[1] R. Eloirdi,[1]
J.-C. Griveau,[1] J. Rusz,[3] P. M. Oppeneer,[3] A. Rogalev,[2] G. H. Lander[1]

[1] *European Commission, Joint Research Centre (JRC), Institute for Transuranium Elements (ITU), Actinide Research Unit, Postfach 2340, D-76125 Karlsruhe, Germany, e-mail: Nicola.Magnani@ec.europa.eu*
[2] *European Synchrotron Radiation Facility (ESRF), B.P.220, F-38043 Grenoble, France*
[3] *Department of Physics and Astronomy, Uppsala University, Box 516, S-75120 Uppsala, Sweden*

Ordered magnetism is a result of spin polarization of the electrons, but there are two elements in the periodic table in which the intrinsic magnetic moment is zero despite the electrons being spin-polarized: europium and americium. For the free Eu^{3+} and Am^{3+} ions the *f*-electron count is six, the spin and orbital moments have the same magnitude and opposite direction, and the resulting $J = 0$ ground state is non-magnetic. Nevertheless, since a large spin polarization is present, the application of a magnetic field can induce a moment by mixing with excited states. Europium, however, has a tendency towards the magnetic f^7 (divalent) configuration [1] and loses its magnetism only under high pressure [2]. Americium, in contrast, exhibits a stable trivalent oxidation state and, like most of its compounds, shows temperature independent susceptibility and no ordered magnetism.

One can expect that long-range order of the moments induced in the virtually nonmagnetic sublattice [3] will be evident when these ions are embedded in a strong ferromagnetic matrix, because of the large molecular field created by the exchange interaction. Using the technique of x-ray magnetic circular dichroism, we show that this is the case in $AmFe_2$. Our result not only confirms the previous indication on the total Am moment from neutron diffraction experiments, but by probing the orbital and the effective spin moment separately, it allows us to attribute the resultant induced moment (antiparallel to the Fe one) to significantly localized 5*f* electrons, a situation very different to the isostructural UFe_2.

The intrinsic relation $\langle S_z \rangle = -\langle L_z \rangle$ resulting from the uniaxial symmetry of the Hamiltonian offered us a unique opportunity to determine directly from the XMCD spectra the expectation value of the magnetic dipole operator $\langle T_z \rangle$, an elusive quantity associated with the spin-dependent asphericity of the electronic cloud which is experimentally accessible only in a limited number of cases and normally requires a combination of several techniques. By assessing the progression of the ratio $3\langle T_z \rangle/\langle S_z \rangle$ across the actinide series [4], we infer that this quantity is well described within a single-ion, intermediate coupling theory for all light actinides, in a way which is largely independent of their electronic (de)localization.

References

[1] B. J. Ruck et al., Phys. Rev. B 83, 174404 (2011).
[2] M. Debessai et al., Phys. Rev. Lett. 102, 197002 (2009).
[3] M. D. Johannes and W. E. Pickett, Phys. Rev. B 72, 195116 (2005).
[4] F. Wilhelm et al., Phys. Rev. B 88, 024424 (2013).

Revisiting the neutron experiments on $AmFe_2$ after 40 years

G. H. Lander[1]

[1] *European Commission, JRC, Institute for Transuranium Elements, Karlsruhe, Germany and Institut Laue Langevin, Grenoble France*

In the previous talk Nicola Magnani has presented XMCD results on Am in the compound $AmFe_2$. He has explained how the condition that $\langle J_z \rangle = 0$ constrains $\langle L_z \rangle = - \langle S_z \rangle$ for all components mixed into the ground state of the Am^{3+} ion in the strong molecular field of the Fe moments in the Laves phase compound $AmFe_2$. The result is that although $\langle J_z \rangle = 0$, the quantity $\langle J^2 \rangle$, which is related to the observed moment, becomes different from zero. This can be seen another way by realising that the orbital moment $\mu_L = - \langle L_z \rangle$ and the spin moment $\mu_S = - 2 \langle S_z \rangle$ and the total moment $\mu_{tot} = \mu_L + \mu_S = + \langle L_z \rangle$. Moreover, this *implies* that the net moment (μ_{tot}) is directed *opposite* to the strong molecular field of the Fe atoms. We have therefore the unusual situation that the strong molecular field (estimated at 180 T in the previous talk) will induce a small moment on the Am site that is opposed to the direction of the molecular field – a counterintuitive situation! (As the molecular field increases further the approximations made by neglecting higher-order effects breakdown, and, at infinite field, the moment at the Am site would be parallel to the molecular field.)

In the 1970s at Argonne National Laboratory the author was involved with some of the early neutron experiments trying to determine the spin and orbital contributions to the actinide moments. An early example of this is given in [1], which discussed Np Laves-phase compounds. Only polycrystalline samples were available, but they were well characterised and of high quality. The measurements used polarised neutrons with an applied field of 6 T to reduce depolarisation effects, and the results are in excellent agreement with later work on single crystals with neutrons [2 – 4] and more recent XMCD experiments [5].

During the course of these measurements a sample of 0.87 g was made of $AmFe_2$. The neutron experiments showed that at the (220) reflection, which has contributions only from the Am sublattice, the flipping ratio (see Ref. [1]) was R = 0.67(4). Since this is significantly < 1, it implies that the total moment at the Am site is directed *opposite* to the applied magnetic field.

To determine the actual magnetic moment requires knowing the magnetic form factor, which was unknown, but an approximation was made by using $\langle j_0 \rangle$ for the Am^{3+} from the relativistic calculations by Desclaux and Freeman. The result was a moment $\mu_{tot} = - 0.4(1)\ \mu_B$. The *sign* of the moment was not understood. However, an overview paper of the work on the actinide Laves phases was presented at the Amsterdam ICM in 1976 [6]. No further paper was written on the $AmFe_2$ results until it was included, with only a brief discussion, in another overview paper [4]. The explanations advanced for the negative sign were incorrect.

This talk will explain how those measurements were made and the dilemma (now resolved!) that they caused in our efforts at that time to understand spin and orbital moments in the actinides. The neutron results, 40 years after they were taken, are crucial to verify the theory advanced in the previous talk.

References

[1] A. T. Aldred *et al.,* Phys. Rev. B 11, 530 (1975)
[2] M. Wulff *et al.,* Phys. Rev. B **37**, 5577 (1988)
[3] M. Wulff *et al.*, Phys. Rev. B **39**, 4719 (1989); B. Lebech *et al.* J. Phys. Cond. Matt. **1**, 10229 (1989)
[4] G. H. Lander *et al.,* Phys. Rev. B **43**, 13672 (1991) and references therein
[5] F. Wilhelm *et al.,* Phys. Rev. B **88**, 024424 (2013)
[6[G. H. Lander *et al.,* Physica B **86-88**, 152 (1977)

Electronic properties and pressure study on $U_2T_3X_5$ (T: Rh, Ir, X: Si, Ge) compounds

Fuminori Honda[1], DeXin Li[1], Yoshiya Homma[1], Yoshinori Haga[2], Dai Aoki[1,3]

[1] *Institute for Materials Research, Tohoku University, Narita-cho 2145-2, Oarai, 311-1313, Ibaraki, Japan*
e-mail: honda@imr.tohoku.sc.jp
[2] *Advanced Science Research Center, Japan Atomic Energy Agency, Shirakata Shirane 2-4, Tokai, 319-1195, Ibaraki, Japan*
[3] *INAC/SPSMS, CEA-Grenoble, 38054, Grenoble, France*

1. *Introduction*

The wide variety of electronic properties in *f*-electron compounds provides ample opportunity for systematic studies from both the fundamental interest and application points of view. This variety is a consequence of the many different kinds of interactions between *f*-electrons and hybridizations with surrounded ligands *d*- and/or *p*-electrons. Furthermore, the *f* electrons play an important role in the heavy-fermion character, magnetic and multipolar ordering, and unconventional superconductivity in the vicinity of quantum critical points. For a systematic understanding of the nature of *f* electrons, it is very important to study families of compounds with the same crystal structure composed of a series of 4*f* rare earth and 5*f* actinide elements having different *f* electron numbers and character, and with ligand elements having a variety of *s*, *p*, and *d* electrons hybridized with the *f* electrons.

The $A_2T_3X_5$ family of *f*-electron compounds (A: rare-earth and actinide elements, T: transition metals, and X: Si or Ge) is a well-known system, which has quite a few members based on rare earth [1,2] and actinide elements (Th, U, Np, Pu) [3-4]. There are three crystal structure types in $A_2T_3X_5$, which are $U_2Co_3Si_5$–type orthorhombic structure (space group: Ibam), $Lu_2Co_3Si_5$–type monoclinic structure (space group: C2/c), and $Lu_2Fe_3Si_5$–type tetragonal structure (space group: P4/mnc). Among them, $U_2Co_3Si_5$ type and $Lu_2Fe_3Si_5$ type structures are quite similar to each other. It should be noted that $U_2Co_3Si_5$–type structure forms a zig-zag chain of U atom along *c*-axis. In rare-earth compounds, for example, antiferromagnetic compound $Ce_2Ni_3Ge_5$ shows heavy-fermion superconductivity under high pressure [5]. In the actinide $A_2T_3X_5$ compounds, many of them orders magnetically at low temperature. One of the most studied compounds among $U_2T_3X_5$ is $U_2Rh_3Si_5$. $U_2Rh_3Si_5$, which crystallizes in the $Lu_2Fe_3Si_5$ type monoclinic structure, is an antiferromagnet with a Neel temperature of 25.5 K [6]. This compound shows a first order magnetic phase transition at T_N accompanied by a discontinuous negative volume magnetostriction [7].

In order to investigate electronic properties in $U_2T_3X_5$, we have surveyed new $U_2T_3X_5$ compounds, and investigate electronic properties under high pressure.

2. *Experimental Procedure*

We have tried to make new $U_2T_3X_5$ compounds such as $U_2Ir_3Si_5$ and $U_2Rh_3Ge_5$ by arc-melting. Obtained poly crystals are confirmed as a single phase by x-ray powder diffraction. We have grown single crystal of $U_2Ir_3Si_5$ by the Czochralski pulling method as shown in Fig. 1(a). We obtained a beautiful Laue pattern, as shown in Fig. 1(b). X-ray powder diffraction on the crashed single crystal of $U_2Ir_3Si_5$ is shown in Fig. 1(c). Obtained data are well explained by the calculated result based on $U_2Co_3Si_5$-type orthorhombic structure with lattice parameters of a = 9.953Å, b = 11.328 Å, and c = 5.881 Å. $U_2Rh_3Ge_5$ also crystallizes with $U_2Co_3Si_5$ type structure with lattice parameters of a = 10.052 Å, b = 11.789 Å, and c = 6.009 Å. Magnetization and magnetic susceptibility are measured by a SQUID magnetometer. Specific heat was measured by physical property measurement system (Quantum design Ltd.). Electrical resistivity is measured by a standard four-probe method. High pressure experiments were done by an opposed anvil type pressure cell (Bridgman method).

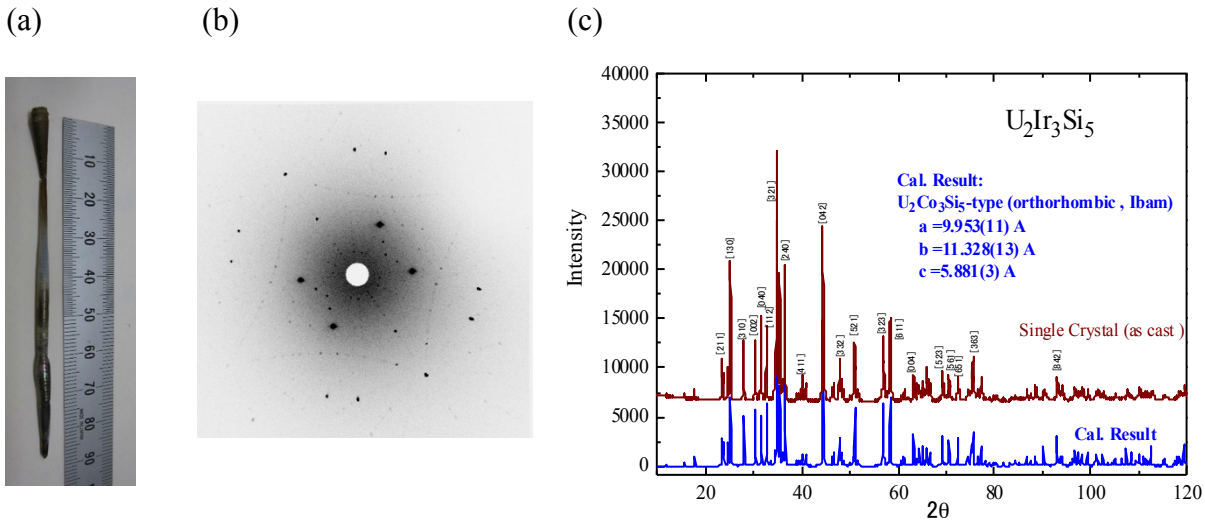

Fig. 1 (a) single crystal of $U_2Ir_3Si_5$, (b) Laue photograph of $U_2Ir_3Si_5$ from (001) plane, and (c) powder diffraction pattern of $U_2Ir_3Si_5$ together with the simulated result of $U_2Co_3Si_5$ type of structure.

3. *Experimental Results and Discussion*

3.1 new compounds $U_2Ir_3Si_5$ and $U_2Rh_3Ge_5$

Fig. 2(a) shows the temperature dependence of the magnetic susceptibility of $U_2Ir_3Si_5$. The magnetic susceptibility follows the Curie–Weiss law at high temperatures. The magnetic susceptibility for $H \parallel a$- and b-axis in the inset of Fig. 2(a) decreases steeply below 36.5 K (= T_N), indicating the antiferromagnetic ordering, and shows another magnetic transition at T_{N2} = 26 K, which might be due to the change of magnetic structure, such as $CeRh_2Si_2$ [8]. While the susceptibility for $H \parallel c$-axis is almost constant below T_N. It is concluded that the antiferromagnetic magnetic easy-axis corresponds to the a-axis, while the c-axes is a hard axis.

The temperature dependence of the electrical resistivity for the current J along three principal directions in $U_2Ir_3Si_5$ is shown in Fig. 2(b). Interestingly, electrical resistivity shows semiconducting like temperature dependence and indicates drastic increase below T_N. Additional anomalies at T_{N2} are also found in all directions. Electrical resistivity in $U_2Rh_3Si_5$ is metallic and shows drastic decrease below T_N [6]. This huge difference in the electrical resistivity between those two related compounds is unclear but may imply important hints for the dominant interactions in these compounds.

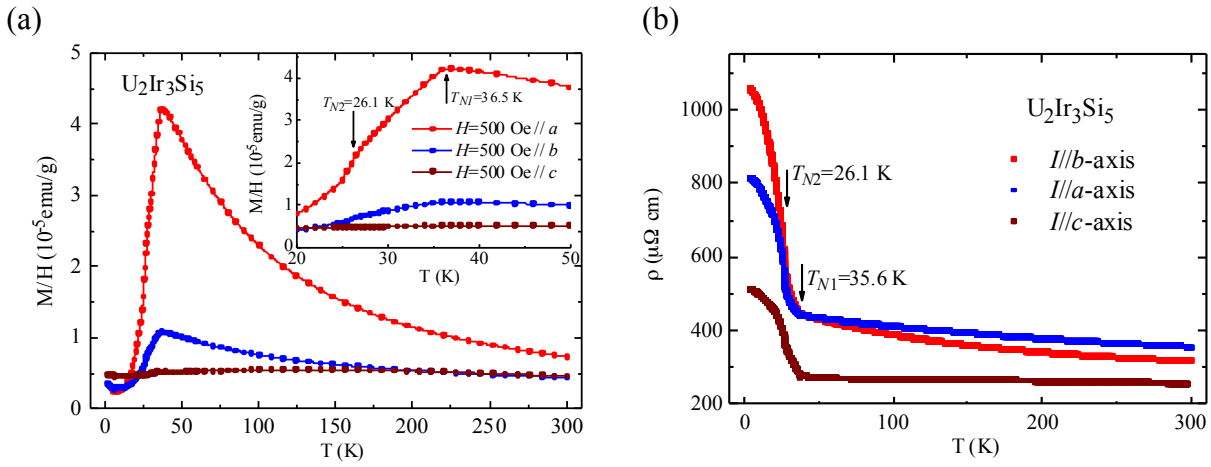

Fig. 2 Temperature dependence of (a) the magnetic susceptibility and (b) the electrical resistivity in $U_2Ir_3Si_5$ along the principal directions. Inset in (a) shows the magnified plot around T_N.

Temperature dependence of the magnetic susceptibility and the electrical resistivity in $U_2Rh_3Ge_5$ polycrystal are shown in Fig. 3(a) and (b), respectively. As is seen here, $U_2Rh_3Ge_5$ is an antiferromagnet with a Néel temperature of T_N = 42 K. No further transition below T_N is found down to 2 K. Electrical resistivity increases with decreasing temperature and shows sudden decrease below T_N, which is similar to the resistivity behavior in the related compound $U_2Rh_3Si_5$. The transition at T_N is confirmed to be a second order phase transition from the specific heat measurement, not shown here. Other bulk properties and comparison to the related compounds will be reported.

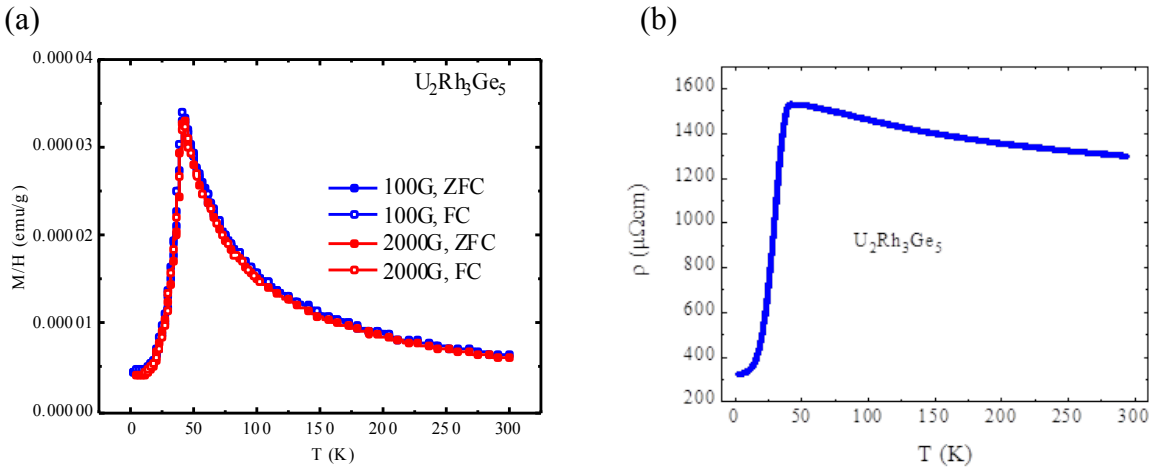

Fig. 3 Temperature dependence of (a) the magnetic susceptibility and (b) the electrical resistivity in $U_2Rh_3Ge_5$ polycrystal.

3.2 Pressure effect on $U_2Rh_3Si_5$

$U_2Rh_3Si_5$ indicates the first order antiferromagnetic transition at 25.5 K, implying the existence of the strong spin-lattice coupling. It is reported that lattice volume expands accompanied by antiferromagnetic ordering. It is also reported that the crystal structure of $U_2Rh_3Si_5$ does not change through the transition [9]. This means that $U_2Rh_3Si_5$ only deforms with different ratios of the lattice parameters. When the magnetism is suppressed by external pressure, not only magnetic but also lattice instability can be expected to occur, which might be a new type of quantum criticality. In order to investigate the effect of pressure on this compound, we measured electrical resistivity under high pressure.

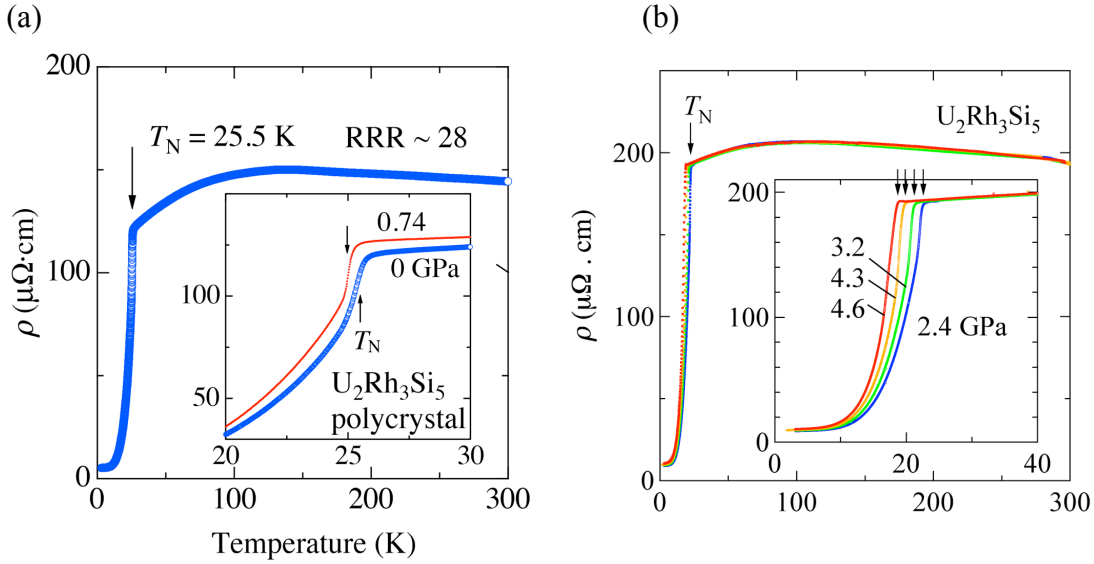

Fig. 4 Temperature dependence of electrical resistivity of $U_2Rh_3Si_5$ under high pressure.

Figure 4 shows the temperature dependence of the electrical resistivity of $U_2Rh_3Si_5$ polycrystal under high pressure. Resistivity shows broad peak around 100 K and decreases suddenly at T_N, reflecting the first order antiferromagnetic transition. T_N decreases monotonically with pressure, as expected from the negative volume magnetostriction at T_N. A small hump in the resistivity is found around T_N at 4.6 GPa, as shown in Fig. 4(b), which can be connected to the "super-zone" gap formation. Figure 5(a) shows the low temperature resistivity with respect to T^2 (K^2). At low temperature resistivity obeys $\rho = \rho_0 + AT^2$ below T_{FL}. T_{FL} decreases but A-value increases with increasing pressure. Pressure dependence of T_N and A-value are plotted in Fig. 5(b). Initial slope of dT_N/dp is nearly -1 K/GPa. Decrease of T_N and increase of A suggests that the system approaches to quantum criticality under high pressure. We need pressure more than 10 GPa to suppress magnetism completely. Further experiment using diamond anvil cell is in progress.

According to the thermal expansion [7] and specific heat measurement [6], volume change (ΔV) and latent heat (ΔS) at T_N is estimated as ΔV = -2.45 x 10^8 (nm^3/mol) and ΔS = 2.44 (J/(mol•K)). For the first order phase transition, pressure dependence of the transition temperature is estimated by the Clausius-Clapeyron relation, $(dT/dp) \sim \Delta V/\Delta S \sim$ -1 K/GPa, which is in a good agreement with our experimental result.

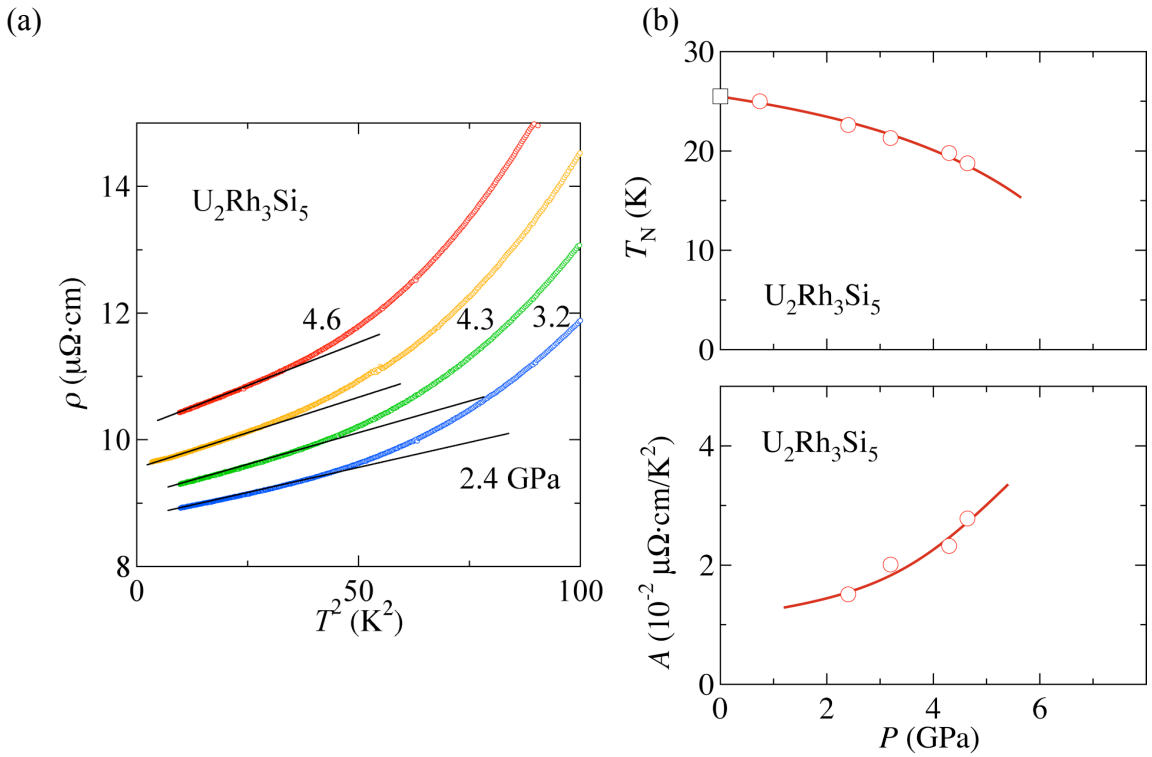

Fig. 5 (a) Low temperature resistivity with respect to T^2 under high pressure and pressure dependence of T_N and A-term in the electrical resistivity in $U_2Rh_3Si_5$.

4. *Summary*

We succeeded in growing new $U_2T_3X_5$ compounds, which are $U_2Ir_3Si_5$ and $U_2Rh_3Ge_5$. Both compounds crystallize with $U_2Co_3Si_5$-type of orthorhombic structure. Below T_N = 36.5 K, $U_2Ir_3Si_5$ shows magnetic order-order transition at 26 K. Electrical resistivity in $U_2Ir_3Si_5$ shows semi-conducting-like behavior. We have also studied electronic properties of $U_2Rh_3Si_5$ under high pressure up to 4.6 GPa. T_N decreases with increasing pressure at a rate of -1 K/GPa in $U_2Rh_3Si_5$.

Acknowledgement

We are very grateful to Prof. Y. Onuki for helpful discussions. This research was carried out (in part) at the International Research Center for Nuclear Materials Science, Institute for Materials Research, Tohoku University. This work was also supported by KAKENHI, REIMEI, and ICC-IMR.

References

[1] G. Venturini *et al*., *Mat. Res. Bull.* **21**, 33 (1986).
[2] C. Mazumdar *et al*., *J. Appl. Phys.* **81**, 5781 (1997).
[3] V. Sechovsky and L. Havela: *Magnetism in ternary intermetallic compounds of uranium,* in: Handbook on Magnetic Materials, ed. K.H.J. Buschow, **11** 1 (1998) (Amsterdam, North Holland).
[4] J.-C. Griveau *et al*., *J. Alloys Compd.* **576**, 409 (2013) and references therein.
[5] M. Nakashima *et al*., *J. Phys.: Condens. Matter* **17** 4539 (2005).
[6] B. Becker *et al*., *Phys. Rev. Lett.* **78**, 1347 (1997) and references therein.
[7] T. Takeuchi *et al*., *J. Phys. Soc. Jpn.* **68**, 1086 (1999).
[8] B. H. Grier *et al*., Phys. Rev. B **29**, 2664 (1984).
[9] R. Feyerherm *et al*., *Phys. Rev. B* **56** 13693 (1997).

New Magnetoelectric Effects in a Noncollinear Antiferromagnetic Metal UNi_4B

Hiroshi Amitsuka[1], Hiraku Saito[1], Chihiro Tabata[1], Naoyuki Miura[1], Kenta Uenishi[1], Hiroyuki Hidaka[1] and Tatsuya Yanagisawa[1]

[1] *Graduate School of Science, Hokkaido University, N10W8 Kita-ku, Sapporo 080-0810, Japan*
e-mail: amiami@phys.sci.hokudai.ac.jp

A uniform alignment of spin vortices on a layered honeycomb lattice can be described as a ferroic order of a microscopic toroidal moment ***t***, which is defined as the sum of vector products of electric- and magnetic-dipole moments over proper magnetic sites in a magnetic unit cell. Recently, S. Hayami, H. Kusunose, and Y. Motome theoretically predicted that exotic magenetoelectric (ME) effects can be generated if such a ferroic toroidal order occurs in a *metallic* compound [1, 2]. For example, an electric current ***J*** flowing along the layers under the toroidal order may induce uniform magnetization in the direction of a vector product as $\Delta \boldsymbol{M} \propto \boldsymbol{t} \times \boldsymbol{J}$. The ***J*** flowing perpendicular to the layers may also enhance or depress the toroidal moment, which is parallel to ***J***. A quasi-hexagonal compound UNi_4B is a plausible candidate for testing the reality of this theory. This compound shows an antiferromagnetic order below $T_N \sim 20$ K with two thirds of uranium 5f moments on a triangle lattice forming a vertex-like magnetic structure [3], which is comparable to the toroidal order given in the theory (Fig. 2). We have performed dc magnetization measurements on a UNi_4B single-crystalline sample using a SQUID magnetometer, MPMS, with electric currents applied along and perpendicular to the hexagonal layer. We observed that in both the current directions spontaneous magnteization $\Delta \boldsymbol{M}$ develops perpendicular to the currents below T_N. In addition, the direction of $\Delta \boldsymbol{M}$ is altered by reversing the current-flow direction in each geometry. We conclude from our experimental results and analyses that the theoretical prediction given by Hayami *et al*. has now been essentially confirmed by experiments, and a new ME phenomenon of current-induced magnetization in a metallic system has been identified, for the first time.

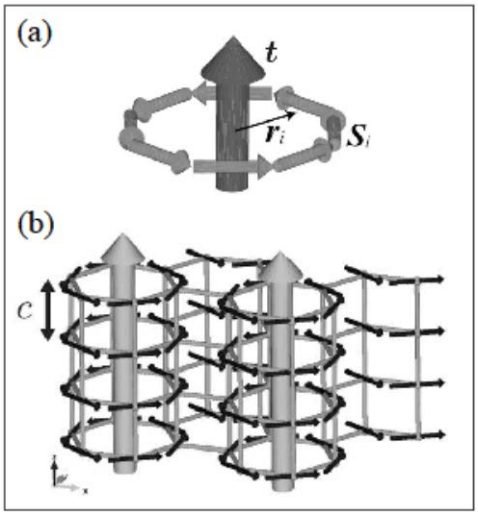

Fig. 1. Schematic views of (a) a microscopic toroidal moment and (b) ferroic order of toroidal moments on a layered honeycomb lattice from Ref. [1].

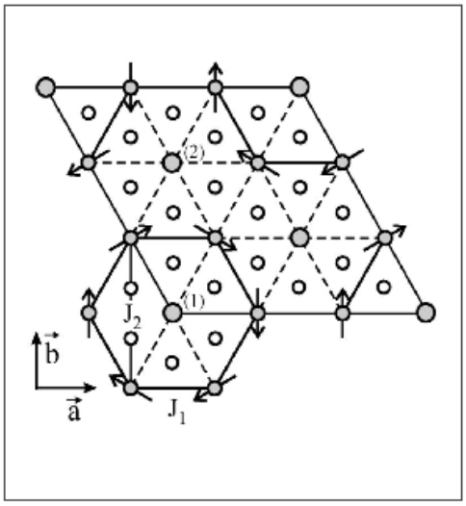

Fig. 1. Magnetic structure of UNi_4B in *a*-*b* plane [3]. U atoms at sites (1) and (2) remain paramagnetic below T_N down to ~ 0.3 K. Open circles denote Ni or B atoms.

References

[1] S. Hayami, H. Kusunose, and Y. Motome, *Phys. Rev. B* **90**, 024432 (2014).
[2] S. Hayami, H. Kusunose, and Y. Motome, arXiv:1409.3657, Condensed Matter.
[3] S. Mentink *et al*., *Phys. Rev. Lett.* **73**, 1031 (1994).

Structural, electronic, and magnetic characteristics of Np_2Co_{17} under ambient and High Pressure

I. Halevy[1,2], A. Hen[2,3], S. Heathman[3], I. Orion[2], E. Colineau[3], R. Eloirdi[3], J.-C. Griveau[3], P. Gaczynski[3], F. Wilhelm[4], A. Rogalev[4], J.-P. Sanchez[5], N. Magnani[3,6], A. B. Shick[3,7], P. M. Oppeneer[8] and R. Caciuffo[3]

[1]Physics Department, Nuclear Research Center Negev, P.O. Box 9001, IL84190 Beer-Sheva, Israel
[2]Nuclear Engineering Department, Ben Gurion University, IL84105 Beer-Sheva, Israel
[3]European Commission, Joint Research Centre, Institute for Transuranium Elements, Postfach 2340, DE-76125 Karlsruhe, Germany
[4]European Synchrotron Radiation Facility (ESRF), Boîte Postale 220, FR-38043 Grenoble, France
[5]SPSMS, UMR-E CEA/UJF-Grenoble 1, INAC, FR-38054 Grenoble, France
[6]Lawrence Berkeley National Laboratory, Chemical Sciences Division, 1 Cyclotron Road, Berkeley, California 94720, USA
[7]Institute of Physics, Academy of Sciences of the Czech Republic, Na Slovance 2, CZ-182 21 Prague, Czech Republic
[8]Department of Physics and Astronomy Uppsala University, Box 516, S-751 20 Uppsala, Sweden

A previously unknown neptunium-transition-metal binary compound Np_2Co_{17} has been synthesized and characterized by means of powder x-ray diffraction, ^{237}Np Mossbauer spectroscopy, SQUID magnetometry, and x-ray magnetic circular dichroism (XMCD). The compound crystallizes in a Th_2Ni_{17}-type hexagonal structure with room-temperature lattice parameters a = 8.3107(1) Å and c = 8.1058(1) Å (FIG 1.).

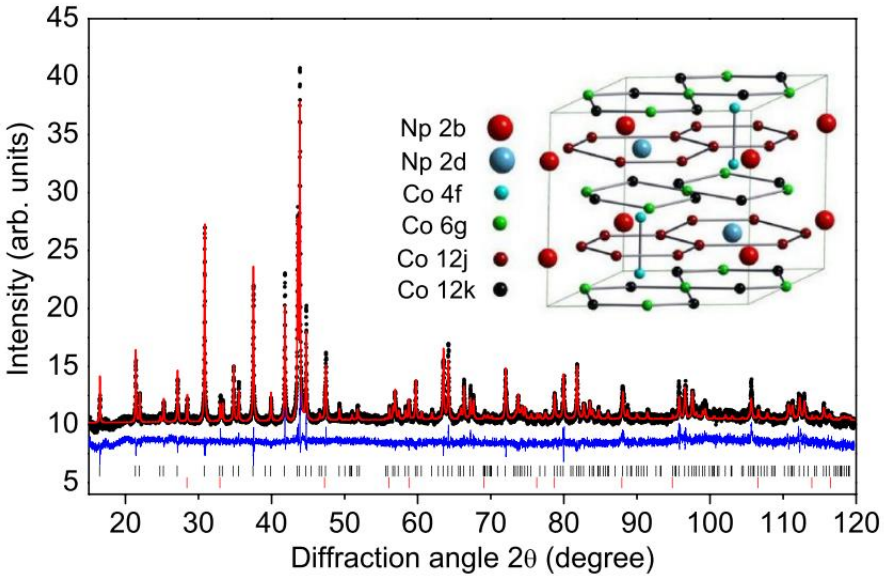

FIG. 1. (Color online) Observed (dots) and calculated (red line) x-ray diffraction pattern recorded at room temperature and ambient pressure for Np_2Co_{17}. The lower trace (blue line) is the difference profile. The intensity distribution is plotted as a function of the full

diffraction angle 2θ (Cu Kα1 radiation). Vertical ticks indicate calculated angular positions of the Bragg peaks for (upper row, black) the Np_2Co_{17} phase and (lower row, red) for an impurity phase (NpO_2, ~3% in weight). The inset shows the crystal structure of Np_2Co_{17}, corresponding to the ABAC stacking sequence characteristic of the ordered Th_2Ni_{17}-type structure.

Refined structural parameters for Np_2Co_{17} at room temperature are shown in TABLE I.

TABLE I. Refined structural parameters for Np_2Co_{17} at room temperature. The parameters refer to the hexagonal axes [space group $P6_3/mmc$, $a = 8.3107(1)$ Å, and $c = 8.1058(1)$ Å]. An isotropic Debye-Waller factor $B_{DW} = 0.5$ Å^2 and full occupation were assumed for all sites.

Atom	Site	Symmetry	x	y	z
Np_1	$2b$	$\bar{6}m2$	0	0	1/4
Np_2	$2d$	$\bar{6}m2$	1/3	2/3	3/4
Co_1	$4f$	$3m$	1/3	2/3	0.1048(5)
Co_2	$6g$	$2/m$	1/2	0	0
Co_3	$12j$	m	0.3241(5)	0.9547(3)	1/4
Co_4	$12k$	m	0.1663(3)	0.3326(6)	0.9775(3)

Magnetization curves indicate the occurrence of ferromagnetic order below $T_C > 350$ K, as it shown in FIG 2.

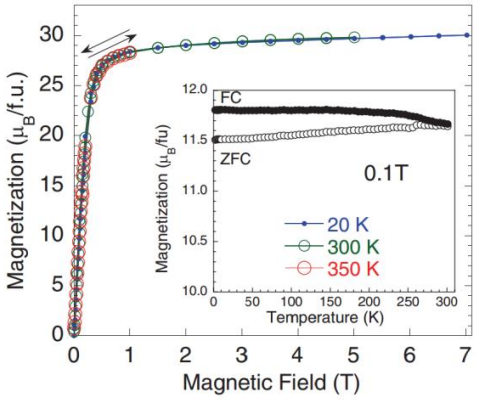

FIG. 2. (Color online) Magnetic-field dependence of the Np_2Co_{17} magnetization measured on a polycrystalline sample at different temperatures from 20 to 350 K. The inset shows the temperature dependence of the magnetization measured up to 300 K in a field $\mu_0H = 0.1$ T under field-cooled (FC) and zero-field-cooled (ZFC) conditions.

Mössbauer spectra suggest a Np^{3+} oxidation state and give an ordered moment of $\mu_{Np} = 1.57(4)\ \mu_B$ and $\mu_{Np} = 1.63(4)\ \mu_B$ for the Np atoms located, respectively, at the 2b and 2d crystallographic positions of the $P6_3/mmc$ space group.

Estimated parameters for the ^{237}Np Mössbauer spectra of Np_2Co_{17} at 4.2 K are given in TABLE II.

TABLE II. Estimated parameters for the ^{237}Np Mössbauer spectra of Np_2Co_{17} at 4.2 K. δ_{IS} is the isomer shift with respect to $NpAl_2$, B_{hf} is the hyperfine field, μ_{Np} is the ordered Np magnetic

Site	Intensity (%)	δ_{IS} (mm/s)	B_{hf} (T)	μ_{Np} (μ_B)	e^2qQ (mm/s)	W (mm/s)
$a(2d)$	50	−13.7(2)	351(1)	1.63(4)	−12.2(3)	2.9(1)
$b(2b)$	50	−15.4(2)	338(1)	1.57(4)	−4.5(3)	2.9(1)

moment, e^2qQ is the quadrupolar coupling constant, and W is the full width at half maximum of individual spectral lines.

The ^{237}Np Mössbauer spectrum of Np_2Co_{17} taken at 4.2 K in the ferromagnetic state is shown in FIG 3.

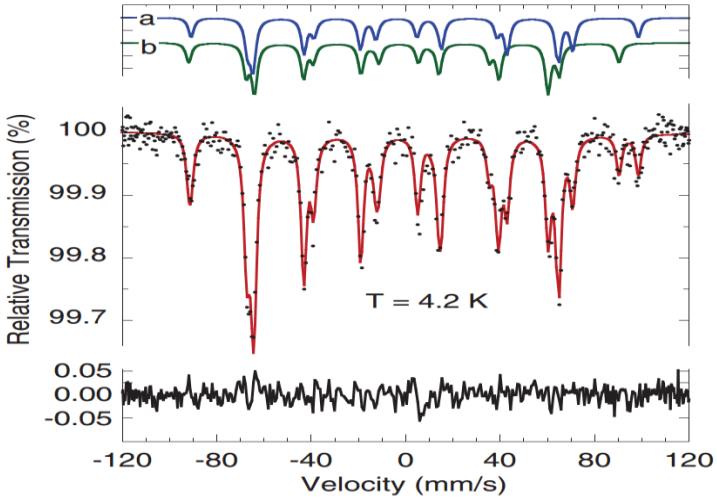

FIG. 3. (Color online) ^{237}Np Mössbauer spectrum of Np_2Co_{17} taken at 4.2 K in the ferromagnetic state. The solid red line represents the best fit to the data (dots) as given by the superposition of component spectra associated with the two inequivalent Np positions. The individual spectra, vertically shifted with respect to the base line, are shown as blue (a) and green (b) lines at the top of the figure. The lower trace (black line) is the difference profile. The fit slightly improves by adding the contribution from the NpO_2 impurity, giving a single broad absorption line at 7.7 mm/s where the difference profile shows a small dip.

Combining these values with a sum-rule analysis of the XMCD spectra , FIG 4,measured at the neptunium $M_{4,5}$ absorption edges, one obtains the spin and orbital contributions to the site-averaged Np moment [$\mu_S = -1.88(9)\ \mu_B$, $\mu_L = 3.48(9)\ \mu_B$]. The ratio between the expectation value of the magnetic-dipole moment and the spin magnetic moment (m_{md}/μ_S = +1.36) is positive as predicted for localized 5f electrons and lies between the values calculated in intermediate-coupling (IC) and jj approximations.

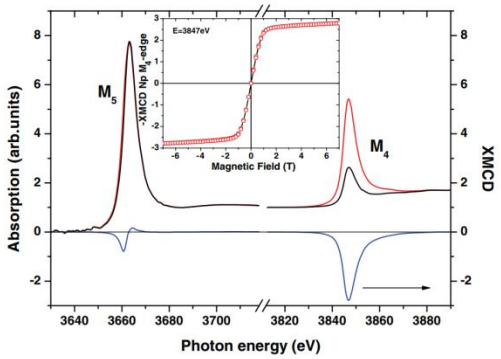

FIG. 4. (Color online) X-ray-absorption spectra $\mu^{+,-}$ measured at 50 K at the $M_{4,5}$ Np absorption edges in Np_2Co_{17}; data have been measured with the photon helicity parallel (red

line) and antiparallel (black line) to a 7-T magnetic field applied along the beam direction. The XMCD signal (blue line, lower trace) is given by $\mu^+ - \mu^-$. The inset shows the field dependence of the XMCD signal at the M_4 edge.

The expectation value of the angular part of the spin-orbit-interaction operator is in excellent agreement with the IC estimate. The ordered moment averaged over the four inequivalent Co sites, as obtained from the saturation value of the magnetization, is μ_{Co} 1.6 μ_B. The experimental results are discussed against the predictions of first-principles electronic-structure calculations based on the spin-polarized local-spin-density approximation plus the Hubbard interaction.

The structural behavior of Np_2Co_{17} is investigated by means of high-pressure diamond-anvil compression measurements and is compared with that of the isostructural compounds Lu_2Co_{17} and Lu_2Ni_{17}. The Th_2Ni_{17}-type hexagonal crystal structure is preserved with no measurable discontinuous volume collapses up to the highest achieved pressure, p = 43 GPa. For Np_2Co_{17}. FIG. 5.

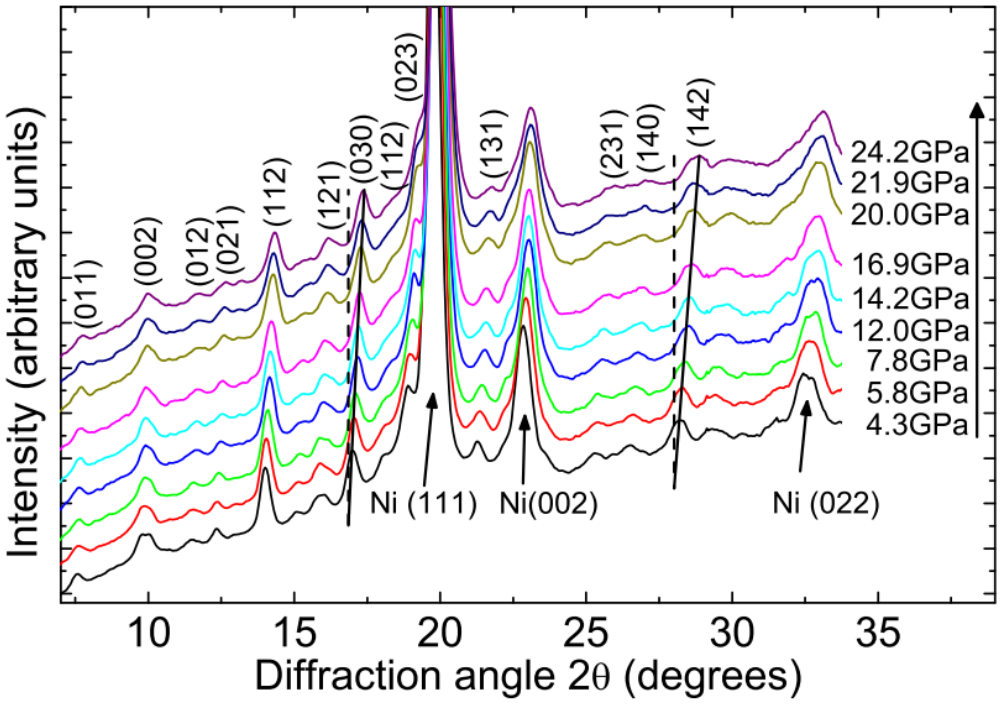

FIG. 5. (Color online) Diffraction patterns of Np_2Co_{17} for selected pressures at room temperature, obtained by integrating Debye-Scherrer rings recorded with the area detector. Patterns are offset vertically for clarity. No splitting of Bragg peaks or extra reflections appear with increasing pressure. The values of the lattice parameters decrease continuously, as indicated by the tilted straight lines. Nickel Bragg peaks from the inconel gasket are indicated by arrows. Full data set have been collected up to 43 GPa.

The Np_2Co_{17} High-Pressure data fits to the Birch-Murnaghan and Vinet equations of state give values of the isothermal bulk modulus and its pressure derivative of B_0 = 286 GPa and B_0 = 3, revealing that this Np compound is a highly incompressible solid with stiffness comparable to that of superhard covalently bonded materials.

$$p(V) = 3B_0 \frac{1 - f_V}{f_V^2} \exp\left[\frac{3}{2}(B_0' - 1)(1 - f_V)\right],$$

For example, Diffraction pattern obtained for Np_2Co_{17} inside a membrane-type diamond anvil cell and submitted to a pressure of 4.3 GPa, is given in FIG 6.

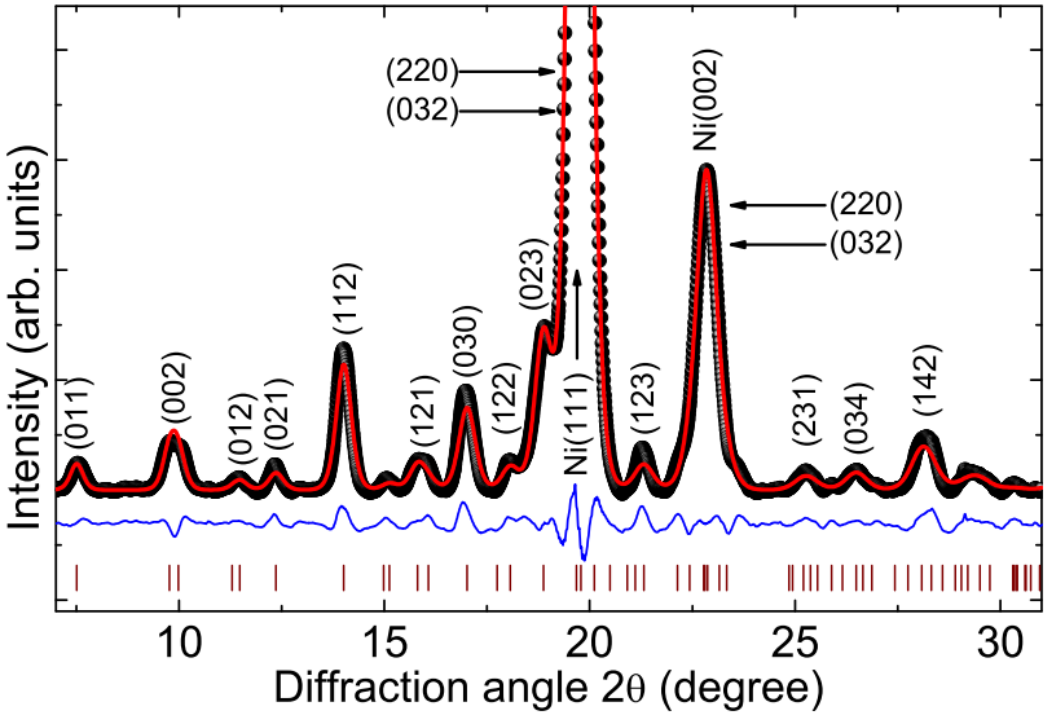

FIG. 6. (Color online) Diffraction pattern obtained for Np_2Co_{17} inside a membrane-type diamond anvil cell and submitted to a pressure of 4.3 GPa using silicone oil as pressure transmitting medium. Black circles represent experimental data, the solid red line is the refined Le Bail profile, vertical lines are reflection tick marks, and the lower blue line represents the difference profile. Nickel Bragg peaks are due to the inconel gasket.

For the Lu_2T_{17} (T = Co, Ni) compounds, the measured bulk modulus changes from B_0 = 137 GPa for T = Co to B_0 = 257 GPa for T = Ni, FIG.7.

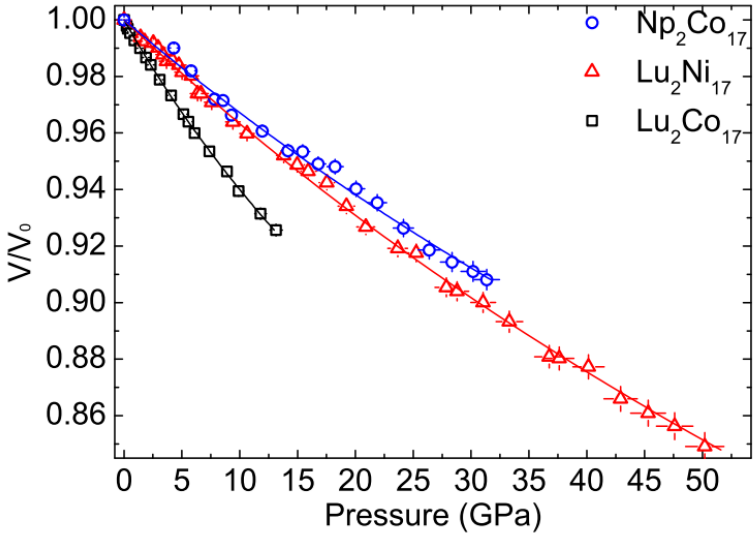

FIG. 7. (Color online) Experimental isothermal equation of state for Np_2Co_{17}, Lu_2Co_{17}, and Lu_2Ni_{17}. The normalized unit cell volume, $V(p)/V_0$, is plotted as a function of applied pressure. The solid lines through experimental data are fit to the third-order Birch-Murnaghan equation of state. Error bars are derived from refinement.

The isothermal equation of state for the studied compounds are in excellent agreement with the results of ab initio fully relativistic, full-potential local spin-density functional calculations. Theoretical estimates of the bulk modulus are given also for Np_2Ni_{17}, for which B_0 is predicted to assume values intermediate between those measured for Lu_2Ni_{17} and Np_2Co_{17}. FIG 8.

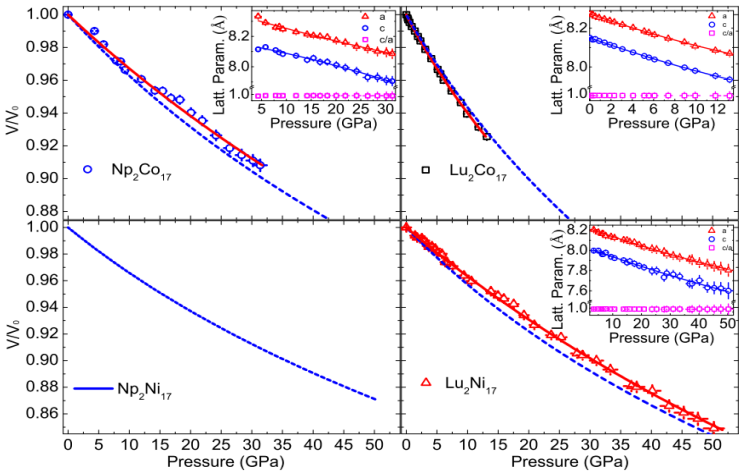

FIG. 8. (Color online) Comparison between experimental (symbols) and ab initio calculated compression curves of Np_2Co_{17}, Lu_2Co_{17}, and Lu_2Ni_{17}. The calculated equation of state (EOS) is shown also for Np_2Ni_{17}, for which experimental data are not available. Solid lines are fit to the Birch-Murnaghan EOS. The calculated curves are shown as blue dashed lines. Insets show the measured pressure variation of the lattice parameters a and c, and of their ratio c/a, demonstrating isotropic compression conditions.

1. I. Halevy, A. Hen, I. Orion, E. Colineau, R. Eloirdi, J.-C. Griveau, P. Gaczynsky, F. Wilhem, A. Rogalev, J.-P. Sanchez, M. R. Winterrose, N. Magnani and R. Caciuffo
Structural, electronic and magnetic characteristics of Np_2Co_{17}.
Physical Review B 85, 014434 (2012)

2. Structural investigation of Np2Co17 and analogue compounds under pressure
Ax. Hen, S. Heathman, R. Eloirdi, J.-C. Griveau, P. M. Oppeneer, S. Elgazzar, I. Halevy, I. Orion, and R. Caciuffo
Physical Review B 90, 054107 (2014)

Site-selective magnetic order of Neptunium in Np_2Ni_{17}

A. Hen,[1,2] E. Colineau,[1] R. Eloirdi,[1] J.-C. Griveau,[1] N. Magnani,[1] J.-P. Sanchez,[5]
I. Halevy,[2,3,4] I. Orion,[2] and R. Caciuffo[1]

[1]*European Commission, Joint Research Centre (JRC), Institute for Transuranium Elements (ITU), Postfach 2340, D-76125 Karlsruhe, Germany e-mail: amir.hen@mail.huji.ac.il*
[2]*Nuclear Engineering Department, Ben Gurion University, IL84105 Beer-Sheva, Israel*
[3]*Physics Department, Nuclear Research Center Negev, P.O. Box 9001, IL84190 Beer-Sheva, Israel*
[4]*California Institute of Technology, W. M. Keck Laboratory 138-78, Pasadena, California 91125, USA*
[5]*SPSMS, UMR-E CEA/UJF-Grenoble 1, INAC, FR-38054 Grenoble, France*

We report the results of a study carried out on a neptunium-transition-metal binary compound Np_2Ni_{17}, synthesized and characterized by means of Powder X-Ray Diffraction, Superconducting-Quantum-Interference-Device magnetometry (SQUID), ^{237}Np Mössbauer spectroscopy (Fig. 1) and specific heat measurements.

Discovered at 1997 [1] during a study of the Neptunium – Nickel binary system, Np_2Ni_{17} is related to the recently reported $NpNi_5$ [2] and is the nickel analogue of the previously reported Np_2Co_{17} [3]. First physical properties of Np_2Ni_{17} were reported at 2011 [4], the current report is of a study made on a sample of improved quality, which was obtained by heat treating the casted sample at 1150 K during 1 week, resulting with a better crystallinity and clearer physical behaviour.

Np_2Ni_{17} crystallizes in the Th_2Ni_{17} hexagonal structure ($P6_3/mmc$ space group no. 194 with room temperature lattice parameters a = 8.28215(7) Å and c = 8.04029(8) Å), containing two non-equivalent Np sites. However unlike its analogue (and parent) compound, Np_2Ni_{17} exhibits an antiferromagnetic order below $T_N \sim 17.5$ K with a complex low temperature magnetization curve. Mössbauer spectra in the ordered state show two ordered Np sites, one with a large ordered moment ($\mu_{Np} \sim 2.25\ \mu_B$),the other with a small one ($\mu_{Np} \sim 0.2\ \mu_B$). Specific heat measurements confirm the onset of an antiferromagnetic order while revealing a complex low temperature behaviour, with both electronic and hyperfine Schottky anomalies present.

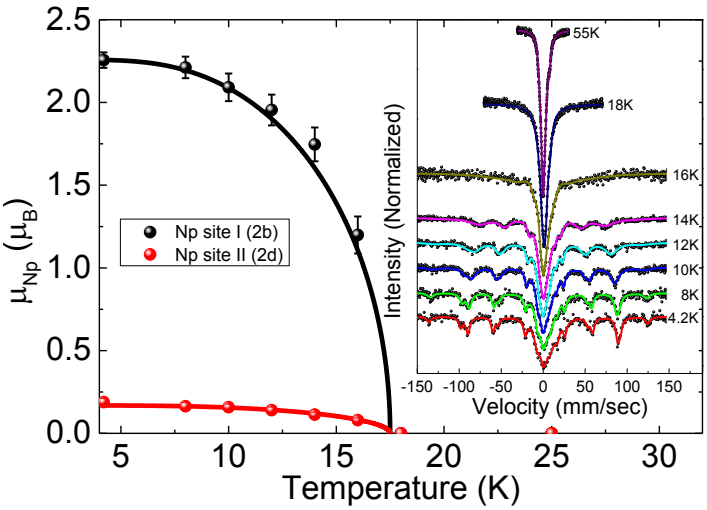

Fig. 1. Temperature dependence of the ordered moment for the two non-equivalent crystallographic Np sites – solid lines are fitted Brillouin curves for J=1/2. Inset – Mössbauer spectra and fits at various temperatures.

References

[1] M. Akabori *et al* J. of Nucl. Mater. **247**,240 (1997)
[2] A. Hen *et al* Phys. Rev. B **90**, 054408 (2014).
[3] I. Halevy *et al* Phys. Rev. B **85**, 014434 (2012).
[4] A. Hen *et al* 41èmes Journées des Actinides, Stará Lesná, Slovakia

Single crystal study of layered U_nRhIn_{3n+2} materials: case of the novel U_2RhIn_8 compound

A.Bartha[1], M. Kratochvílová[1], M. Dušek[2], M. Diviš[1], J. Custers[1] and V. Sechovský[1]

[1] *Department of Condensed Matter Physics, Charles University, Ke Karlovu 5, 121 16 Praha 2, Czech Republic, e-mail of presenting author: bartha@mag.mff.cuni.cz*
[2] *Department of Structure Analysis, Institute of Physics ASCR, Cukrovarnická 10, 162 00 Praha 6, Czech Republic*

We report on the single crystal properties of the novel U_2RhIn_8 compound studied in the context of parent $URhIn_5$ and UIn_3 systems. The compounds were prepared by In self-flux method. U_2RhIn_8 adopts the Ho_2CoGa_8-type structure with lattice parameters a = 4.6056(6) Å and c = 11.9911(15) Å. The behavior of U_2RhIn_8 strongly resembles that of related $URhIn_5$ and UIn_3 with respect to magnetization (see Figure 2), specific heat (see Figure 1) and resistivity (see Figure 3) except for magnetocrystalline anisotropy developing with lowering dimensionality in the series UIn_3 vs. U_2RhIn_8 and $URhIn_5$. U_2RhIn_8 orders antiferromagnetically below T_N = 117 K and exhibits slightly enhanced Sommerfeld coefficient γ = 47 mJ.mol^{-1}.K^{-2}. Magnetic field leaves the value of Néel temperature for both $URhIn_5$ and U_2RhIn_8 unaffected up to 9 T (see Figure 1). On the other hand, T_N increases with applying hydrostatic pressure up to 3.2 GPa. Results of thermal expansion measurement will be discussed in the framework of Ehrenfest relations. The character of uranium 5f electron states of U_2RhIn_8 was studied by first principles calculations based on the density functional theory combined with Hubbard model. The overall phase diagram of U_2RhIn_8 is discussed in the context of magnetism in related UTX_5 and UX_3 (T = transition metal, X = In, Ga) compounds.

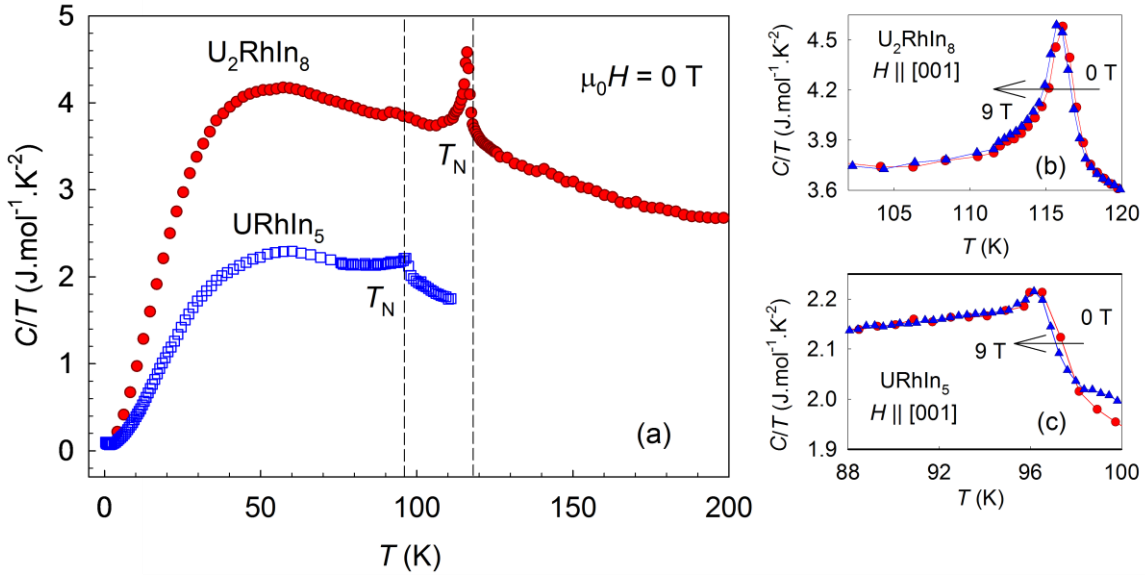

Figure 1: Temperature dependence of the specific heat divided by temperature (a). The transition into the magnetically ordered state at T_N = 117 K (T_N = 98 K) for U_2RhIn_8 ($URhIn_5$) is marked by vertical dashed lines. Comparison of C/T for U_2RhIn_8 (b) and $URhIn_5$ (c) in zero and 9 T magnetic field, respectively, applied along the [001] axis.

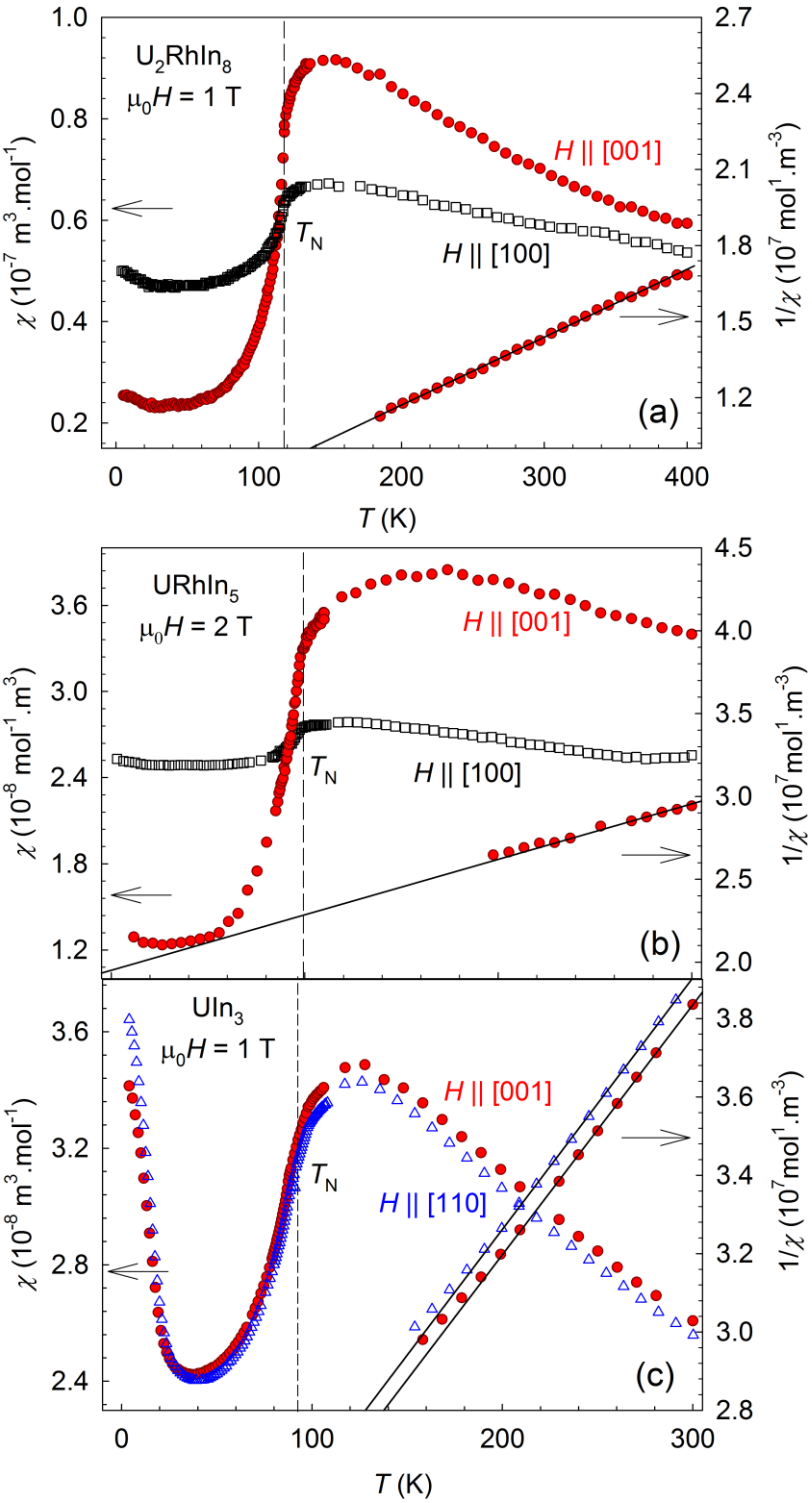

Figure 2: Temperature dependence of $\chi(T)$ and 1/ $\chi(T)$ and Curie-Weiss fit of (a) U_2RhIn_8, (b) $URhIn_5$ and (c) UIn_3 for magnetic field along the [100] and [001] direction in the case of U_2RhIn_8 and $URhIn_5$ and along the [100] and [110] direction for UIn_3, respectively. Vertical dashed line marks the transition temperature T_N.

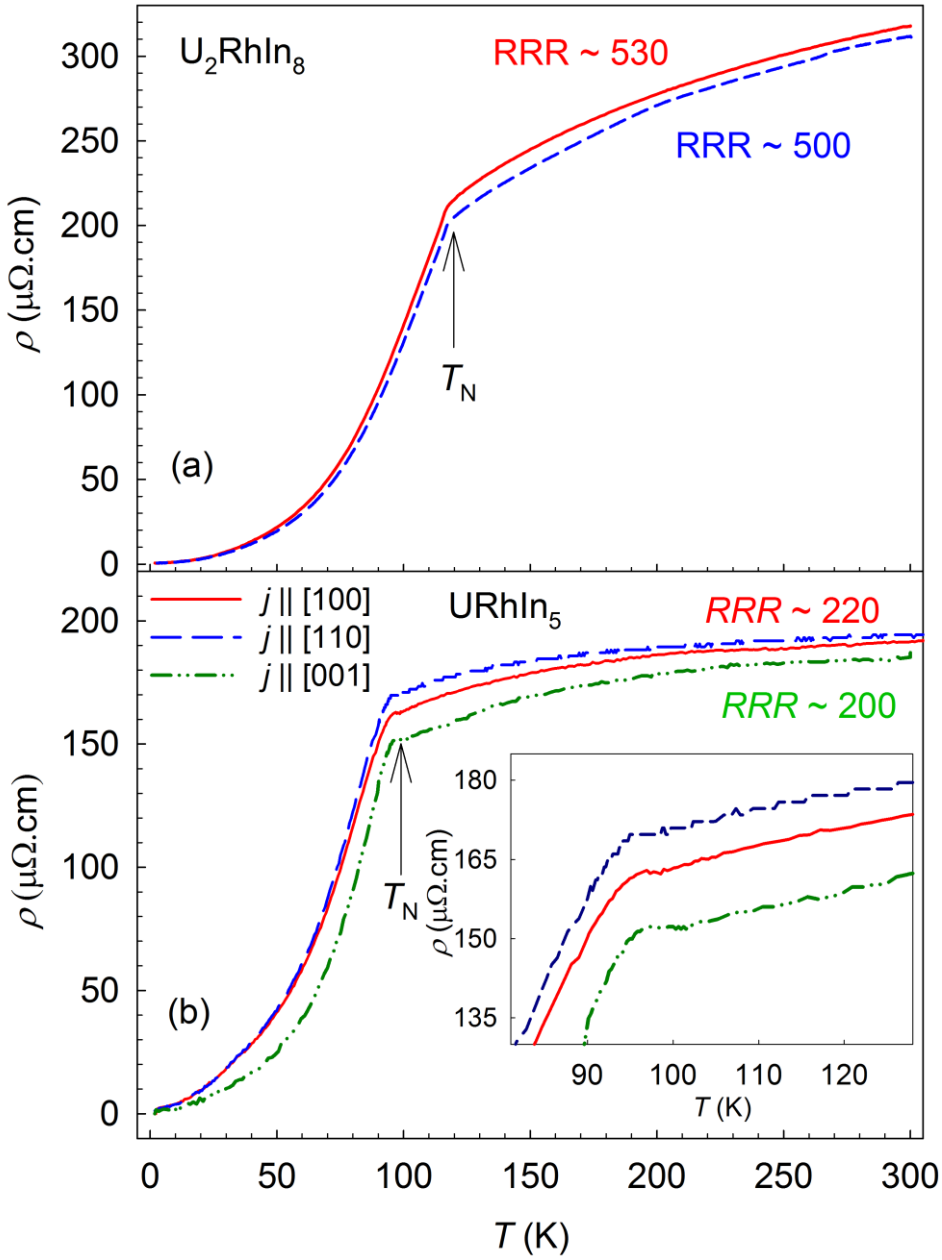

Figure 3: Temperature dependence of the electrical resistivity for electrical current applied along [100] and [110] directions for U_2RhIn_8 (a). The temperature dependence of the electrical resistivity for current applied along the [100], [110] and [001] directions for $URhIn_5$ compound (b). The inset in (b) shows the transition in detail. The arrow marks the onset of the antiferromagnetic transition at T_N = 117 K (T_N = 98 K) for U_2RhIn_8 ($URhIn_5$). One legend applies for both figures.

45èmes Journées des Actinides, April 15–19, 2015, Prague–Průhonice, Czech Republic

Crystal structure and physical properties of Np_2PdIn_8 and Pu_2PdIn_8

Adam Pikul[1], Tomasz Klimczuk[2,3], Jean-Christophe Griveau[3], Eric Colineau[3], Dariusz Kaczorowski[1]

[1] *Institute of Low Temperature and Structure Research, Polish Academy of Sciences, ul. Okólna 2, 50-422 Wrocław, Poland, e-mail: A.Pikul@int.pan.wroc.pl*
[2] *Faculty of Applied Physics and Mathematics, Gdansk University of Technology, ul. Narutowicza 11/12, 80-233 Gdańsk, Poland*
[3] *European Commission, Joint Research Centre, Institute for Transuranium Elements, Postfach 2340, D-76125 Karlsruhe, Germany*

Polycrystalline samples of Pu_2PdIn_8 and Np_2PdIn_8, crystallizing with a tetragonal Ho_2CoGa_8-type structure (space group P4/mmm), were studied by means of magnetic susceptibility, electrical resistivity and specific heat measurements. The temperature-dependent magnetic susceptibility of Pu_2PdIn_8 is almost featureless, while that of Np_2PdIn_8 exhibits a distinct anomaly at 9.5 K that probably manifests an onset of long-range antiferromagnetic ordering. The Pu-based compound shows metallic conductivity, and a moderately-enhanced Sommerfeld coefficient (≈ 150 mJ/(K^2 mol_{Pu})). The low-temperature properties of Np_2PdIn_8 are dominated by the magnetic ordering. The main phase transition is followed by some spin reorientations at about 9 K and 8.5 K. Based on the available experimental data, a tentative magnetic phase diagram of Np_2PdIn_8 was constructed.

Actinide Mediated Catalytic Activation of Heterocumulenes

Moris S. Eisen,[*†] Isabell S. R. Karmel,[†] Matthias Tamm[‡]

[†]*Schulich Faculty of Chemistry, Institute of Catalysis Science and Technology, Technion – Israel Institute of Technology, Technion City, 32000 Israel. e-mail: chmoris@tx.technion.ac.il*
[‡]*Institut für Anorganische und Analytische Chemie, Technische Universität Braunschweig, Hagenring 30, 38106 Braunschweig, Germany*

The activation of heterocumulenes, such as carbodiimides, isocyanates, thioisocyanates and carbon disulfide is an atom efficient, waste free synthetic approach, yielding the respective guanidines and related systems, which find a wide application as synthons in organic synthesis as well as ligands for a variety of transition metals, lanthanides and actinides. Several lanthanide coordination complexes have been shown to be active for the insertion reactions of amines and phosphines into the central NCE (E = N, O, S) linkage of heterocumulenes.[1] In addition, Evans et al. have shown the stoichiometric reactivity of $(C_5Me_5)An(CH_3)_2$ (An = U, Th) toward aliphatic carbodiimides, furnishing mixed pentamethylcyclopentadienyl amidinate actinide (IV) complexes.[2] Hence, it was interesting to investigate the conceptual question whether this process can be incorporated into a catalytic cycle using catalytic amounts of actinide coordination complexes.
Recently, we have reported on the reactivity of mono(imidazolin-2-iminato) actinide (IV) complexes in the catalytic dimerization of aldehydes, displaying a high catalytic activity and selectivity toward the asymmetrically substituted ester, when $[Th(Im^{Dipp}N)(N(TMS)_2)_3]$ was used as catalyst.[3] Therefore, $[Th(Im^{Dipp}N)(N(TMS)_2)_3]$ was used for catalytic activation of carbodimides with primary and secondary amines, phosphines and thiols, yielding the respective insertion products (Scheme 1). In addition, heterocumulene systems, such as PhNCO, PhNCS and CS_2 were also catalytically activated using amines, phosphines and thiols, furnishing the insertion products in high yields under mild conditions.
Scheme 1: Actinide mediated activation of heterocumulenes.

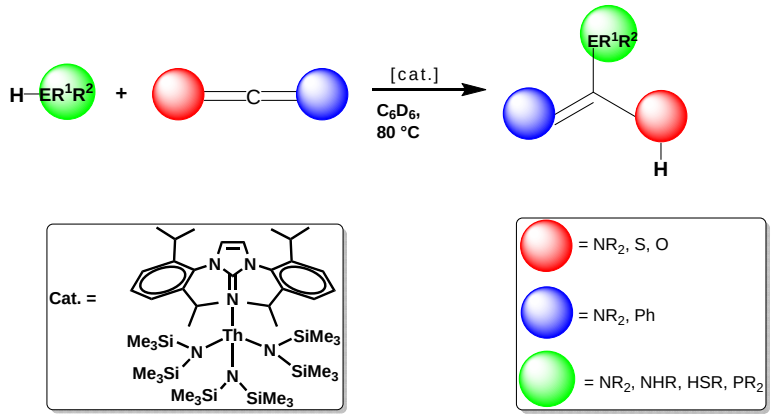

1. Behrle, A. C.; Schmidt, J. A. R. *Organometallics* **2013**, *32*, 1141-1149, and references therein.
2. Evans, W. J.; Walensky, J. R.; Ziller, J. W.; Rheingold, A. L. *Organometallics* **2009**, *28*, 3350-3357.
3. Karmel, I. S. R.; Fridman, N.; Tamm, M.; Eisen, M. S. *J. Am. Chem. Soc.* **2014**, *136*, 17180-17192.

First structural characterization of triscyclopentadienylactinide(iii) derivatives (An: U, Np, Pu)

Olaf Walter, Christos Apostolidis, Michal Dutkiewicz

European Commission, Joint Research Centre, Institute for Transuranium Elements, P.O. Box 2340, D-76125 Karlsruhe, Germany, e-mail: olaf.walter@ec.europa.eu

Triscyclopentadienylactinide(iii) complexes ($Cp_3An(iii)$) are among the oldest well known in the literature described organometallic actinide compounds. There properties have been investigated extendedly and reported since the 1965 [1, 2]. Nevertheless till present there is a lack of structural investigation on these compounds.

In the presentation this gap will be closed by a detailed discussion of the structural features of $Cp_3An(iii)$ comparing them to those of their isosteric and isoelectronic Ln(iii)-complexes.

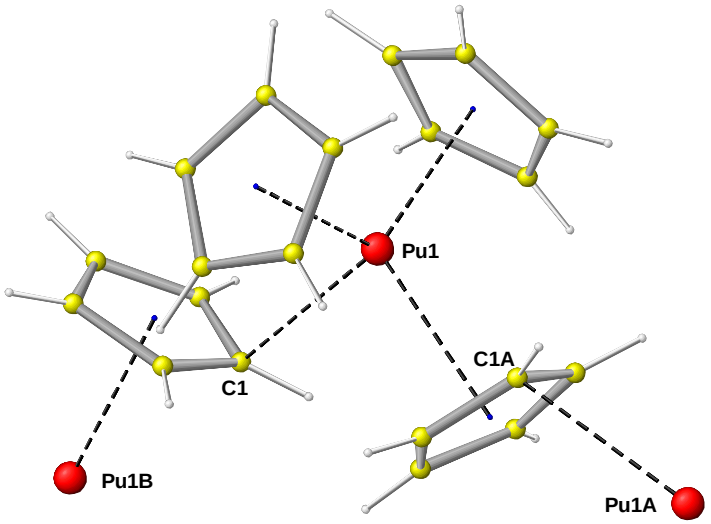

Fig. 1. View to a representative part of the polymeric molecular structure of $Cp_3Pu(iii)$ in the crystal, symmetry generated atom names are indexed with A or B.

References

[1] B. Kanellakopulos, E.O. Fischer, E. Dornberger, F. Baumgärtner, *J. Organomet. Chem.* **24** 507 (1970).
[2] F. Baumgärtner, E.O. Fischer, B. Kanellakopulos, P. Laubereau, *Angew. Chem.* **77** 866 (1965).

Complexation of trivalent actinides with acetate studied by TRLFS and EXAFS spectroscopy

Daniel R. Fröhlich,[1] Andrej Skerencak-Frech,[2] André Rossberg,[3] Petra J. Panak[1,2]

[1] *Institute of Physical Chemistry, Ruprecht-Karls-Universität Heidelberg, Im Neuenheimer Feld 253, 69120 Heidelberg, Germany, e-mail: daniel.froehlich@partner.kit.edu*

[2] *Institute of Nuclear Waste Disposal, Karlsruher Institut für Technologie, PO Box 3640, 76021 Karlsruhe, Germany*

[3] *Institute of Resource Ecology, Helmholtz-Zentrum Dresden-Rossendorf, PO Box 510119, 01314 Dresden, Germany.*

The final disposal of high-level nuclear waste will be performed in deep geological formations. Argillaceous rocks are investigated as potential host rock formations in several European countries (i.e. Belgium, France, Germany, Switzerland). The pore waters of natural clays are known to contain a high variety of dissolved inorganic and organic constituents. Among the dissolved organic matter, low-molecular weight compounds (LMWC) are present at fractions up to 88% [1,2]. The relevant small organic ligands particularly include carboxylic ligands (e.g. formate, acetate, propionate, lactate, etc.). Furthermore, small organic molecules may also be formed by radiolytic degradation of more complex organic compounds (e.g. fulvic and humic acids). Regarding LMWC, acetate is the most abundant ligand in pore waters and can occur at millimolar concentrations.

Due to their long half-lifes, the long-term radiotoxicity of the nuclear waste will be determined by the transuranium elements (Np, Pu, Am). Therefore, a detailed knowledge on the interaction mechanisms between these actinides, the potential host rock and the aquifer is indispensable. Among other processes (e.g. sorption, diffusion), the complexation with small organic ligands is of importance for the solubility and transport of the actinides. Furthermore, these relevant geochemical processes are strongly affected by different system parameters (e.g. pH, Eh, ionic strength, temperature, partial pressure of CO_2, etc.).

Due to the reducing conditions in the near-field of the repository (e.g. due to corrosion of the steel canisters), trivalent actinides (Pu(III), Am(III)) are of particular interest.

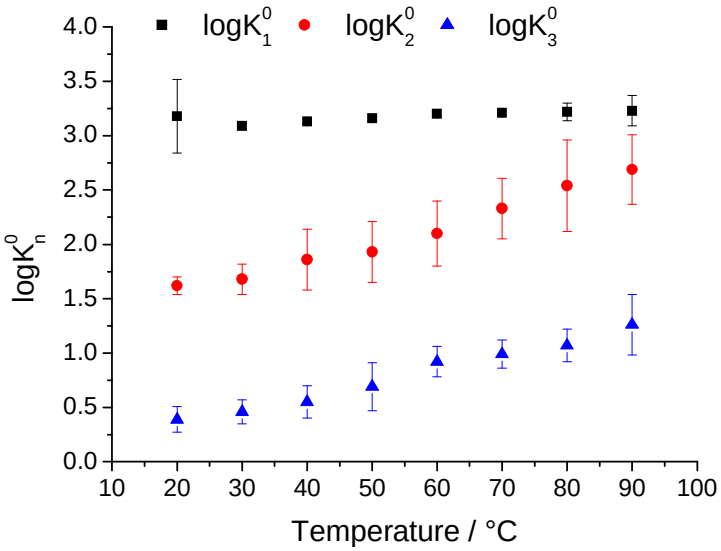

Figure 1: Thermodynamic stability constants for the formation of $[CmAc_n]^{3-n}$ (n = 1-3) as a function of temperature determined in NaCl solution. [3]

In the present work, the thermodynamics for the complex formation of Cm(III) as representative for

trivalent actinides with acetate are studied using time-resolved laser fluorescence spectroscopy (TRLFS). In the first step, TRLFS is used to determine the aqueous speciation of Cm(III) in the presence of acetate as a function of ionic strength and ligand concentration at variable temperature (20 – 90 °C). The stability constants (log K_n^0) and the standard reaction enthalpies and entropies ($\Delta_r H^0_m$, $\Delta_r S^0_m$) of the related complexation reactions are determined for the formation of $[CmAc_n]^{3-n}$ (n = 1-3) according to the specific interaction theory (SIT) and the Van't Hoff equation, respectively. As shown in Figure 1, the thermodynamic stability constants for all observed Cm-acetate species increase continuously with increasing temperature. The related complexation reactions are, thus, endothermic and entropy-driven.

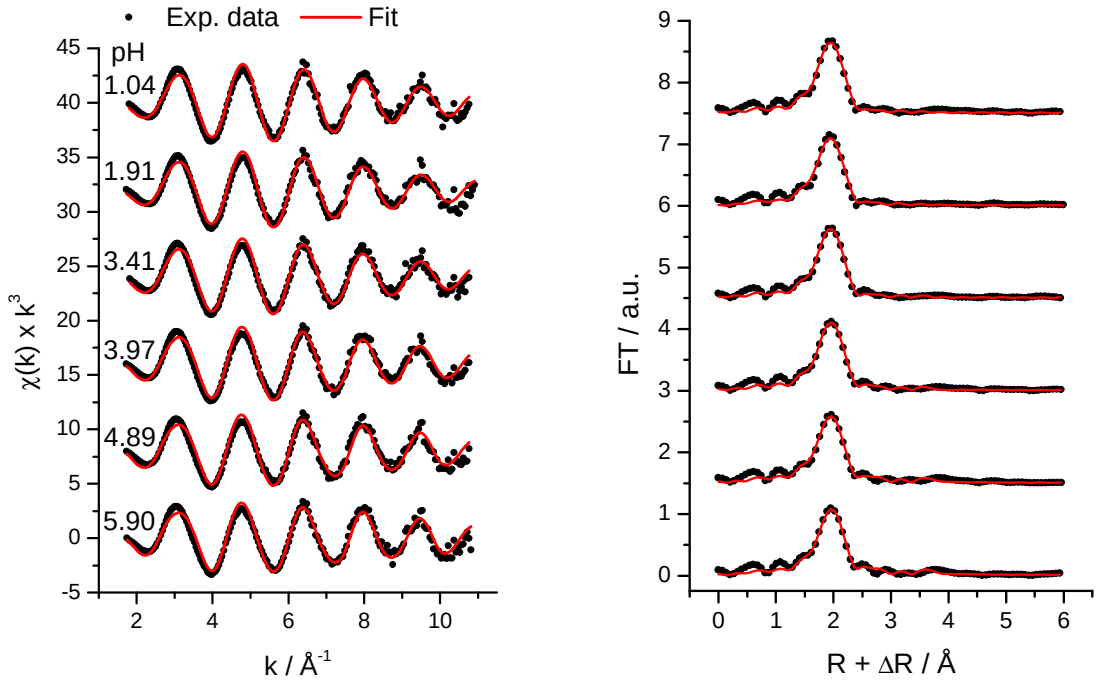

Figure 2: k^3-weighted Am L_3-edge EXAFS spectra as a function of the pH (left) and related Fourier Transforms (right); [Am(III)] = 1 mM, [acetate] = 0.2 M. [4]

Table 1: Fit parameters of the raw k^3-weighted Am L_3-edge EXAFS spectra shown in Figure 2. [4]

Sample		1	2	3	4	5	6
pH		1.04	1.91	3.41	3.97	4.89	5.90
O	N	10.1 (3)	10.1 (4)	10.4 (5)	10.2 (4)	10.7 (5)	10.4 (5)
	R / Å	2.47 (1)	2.47 (1)	2.48 (1)	2.49 (1)	2.49 (1)	2.49 (1)
	σ^2 / Å²	0.009 (1)	0.009 (1)	0.009 (1)	0.009 (1)	0.010 (1)	0.009 (1)
$C_{carboxyl}$*	N	-	-	0.4 (4)	1.0 (3)	1.6 (0.4)	2.0 (4)
	R / Å	-	-	2.78 (7)	2.81 (3)	2.83 (2)	2.84 (1)
C_{distal}**	R / Å	-	-	4.39 (9)	4.41 (4)	4.41 (3)	4.41 (2)
ΔE_0 / eV		-2.0 (3)	-2.1 (3)	-1.6 (4)	-1.0 (3)	-1.0 (4)	-0.3 (4)

The thermodynamic results are complemented by Am-L_3-edge EXAFS measurements to determine the structural parameters of the corresponding Am(III) acetate complexes as a function of the pH value (1 - 6). The raw k^3-weighted Am-L_3-edge EXAFS spectra and related Fourier Transforms are shown in Figure 2, the fit parameters are summarized in Table 1. In all cases, about 10 oxygen neighbors at a distance of 2.47-2.49 Å are found in the first coordination sphere which is in good agreement with oxygen distances reported in the literature for Am(III) and other trivalent actinides in aqueous solution [5]. At pH 1-2, no carbon shells are observed, at higher pH the coordination

number with respect to carbon increases continuously with increasing pH from 0.4 to 2.0. The carboxylic and distal carbon atoms of acetate are located at 2.78-2.84 and 4.39-4.41 Å, respectively. These values are in the same range as An-C distances obtained for acetate complexes with U(VI) ($C_{carboxyl}$: 2.87-2.91 Å [6-8] C_{distal}: 4.36), Np(V) ($C_{carboxyl}$: 2.91-2.93 Å [9]) and Np(VI) ($C_{carboxyl}$: 2.87 Å, C_{dist}: 4.38 Å [9]). Furthermore, the experimental EXAFS spectra have been analyzed using iterative transformation factor analysis (ITFA) to further conform the used structural model.

The present study provides new insights into the complex formation of trivalent actinides. The newly determined thermodynamic data improve the thermodynamic database which is necessary for reliable long-term predictions of actinide geochemistry in a nuclear waste repository. Furthermore, pH-dependent EXAFS measurements provide molecular-level information on the structure of the complexes formed. The data obtained for Am(III) and Cm(III), respectively, can also be used to estimate the behavior of Pu(III).

References

[1] Courdouan, A., Christl, I., Meylan, S., Wersin, P., Kretzschmar, R. (2007a). *Appl. Geochem.* **22**, 1537-1548.
[2] Courdouan, A., Christl, I., Meylan, S., Wersin, P., Kretzschmar, R. (2007b). *Appl. Geochem.* **22**, 2926-2939.
[3] Froehlich, D.R., Skerencak-Frech, A., Panak, P.J. (2014). *Dalton Trans.* **43**, 3958-3965.
[4] Froehlich, D.R., Skerencak-Frech, A., Bauer, N., Rossberg, A., Panak, P.J. (2015). *J. Synchrotron Radiat.* **22**, 99-104.
[5] Allen, P.G., Bucher, J.J., Shuh, D.K., Edelstein, N.M., Craig, I. (2000). *Inorg. Chem.* **39**, 595-601.
[6] Bailey, E.H., Mosselmans, J.F.W., Schofield, P.F. (2004). *Geochim. Cosmochim. Acta* **68**, 1711-1722.
[7] Jiang, J., Rao, L., Di Bernardo, P., Zanonato, P.L., Bismondo, A. (2002). *J. Chem. Soc., Dalton Trans.* **8**, 1832-1838.
[8] Lucks, C., Rossberg, A., Tsushima, S., Foerstendorf, H., Scheinost, A.C., Bernhard, G. (2012). *Inorg. Chem.* **51**, 12288-12300.
[9] Takao, K., Takao, S., Scheinost, A.C., Bernhard, G., Hennig, C. (2009). *Inorg. Chem.* **48**, 8803-8810.

Acknowledgements

All EXAFS measurements have been performed at the Rossendorf Beamline (ROBL, BM20) at the European Synchrotron Radiation Facility (ESRF, Grenoble, France). This work has been supported by the German Federal Ministry of Economics and Technology (BMWi) under contract no. 02E11031.

Radiolysis driven dissolution of UO_2 using synchrotron radiation

L. Costelle,[1] S. Rennie[1], J. E. Darnbrough[1], C. Stitt[1], E. Cocklin[2], C. Lucas[2], R. Burrows[3], H. Sims[4], D. Wermeille[5], J. Rawle[6], C. Nicklin[6], W. Nuttall[7], T. B. Scott[1], G. H. Lander[8] and R. Springell[1]

[1] *Interface Analysis Centre, University of Bristol, Bristol BS2 8BS, United Kingdom, e-mail: leila.costelle@bristol.ac.uk*
[2] *Department of Physics, University of Liverpool, Liverpool L69 7ZE, United Kingdom*
[3]*National Nuclear Laboratory, 102B Stonehouse Park, Sperry Way, Stonehouse, Gloucester GL10 3UT, United Kingdom*
[4]*National Nuclear Laboratory, Harwell Science and Innovation Campus, Oxfordshire OX11 0QT, United Kingdom*
[5]*XMaS, European Synchrotron Radiation Facility, BP220, F-38043 Grenoble Cedex 09, France*
[6]*Diamond Light Source, Harwell Science and Innovation Campus, Harwell OX11 0DE, UK*
[7]*Department of Engineering and Innovation, The Open University, Venables Building, Milton Keynes MK7 6AA, United Kingdom*
[8]*European Commission, Joint Research Centre, Institute for Transuranium Elements, Postfach 2340, D-76125 Karlsruhe, Germany*

High level nuclear waste (HLW) is increasing globally as a consequence of the growing number of operational nuclear power plants, with uranium dioxide (UO_2) accounting for the majority of HLW generated by modern society. However, despite the recent advancement in HLW containment systems, eventual failure may expose the surface of stored UO_2 fuel to ground water [1]. Therefore, it is imperative to understand how UO_2 surface behaves in likely storage environments.

In the present case we study the oxidative dissolution of UO_2 in water. Single-crystal thin films of UO_2 were grown by dc magnetron sputtering. Samples were [001]-oriented UO_2 films, with a nominal thickness of t_{UO2} = 40Å, deposited onto single-crystal [001]-YSZ (yttria-stabilised zirconia) substrates. Substrate heating was used to elevate the growth temperature to ~550 °C, providing thermal energy to improve the crystalline quality, monitored using in-situ reflection high-energy electron-diffraction (RHEED).

UO_2 films were then exposed to water, while simultaneously being illuminated by a high intensity x-ray beam at a synchrotron source, in order to study the direct UO_2/water interaction.

This technique was shown to effectively provide the radiation fields required to split the water into highly oxidising radiolytic products, and to probe the structure of the surface as it is modified by the dissolution process [2]. A finite element calculation of the highly oxidising hydrogen peroxide product suggests that a more complex surface interaction than simple reaction with H_2O_2 is responsible for significant corrosion at the interface of water and UO_2 [3] and this could impact on models of long-term storage of spent nuclear fuel.

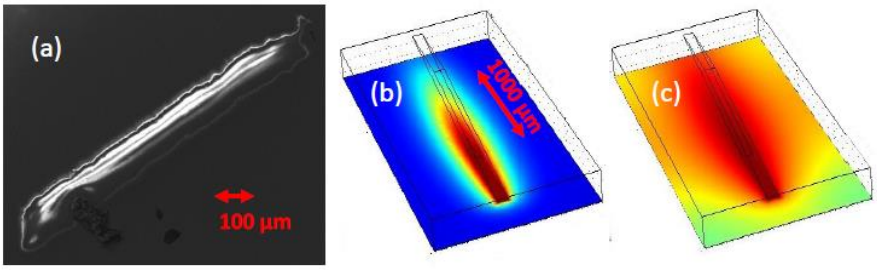

Panel (a) shows an SEM image of a corroded UO_2 single-crystal thin film. Panels (b) and (c) are images representing radiolysis product concentrations close to the beam footprint, as calculated using finite element modelling, including H_2O_2 surface diffusion and bulk diffusion constants, respectively.

References

[1] J. Bruno and R. C. Ewing, *Elements* **2**, 343 (2006).
[2] D. W. Shoesmith, **Nuclear Waste Management Organization** (2007).
[3] Springell *et. al*. **Faraday Discuss.** Accepted Manuscript (2015). DOI: 10.1039/C4FD00254G

45èmes Journées des Actinides, April 15-19, 2015, Prague-Průhonice, Czech Republic

Applications of Laser Spectroscopy for Actinide Detection in Solutions

I.N. Izosimov

Joint Institute for Nuclear Research, 141980 Dubna, Russia, e-mail: izosimov@jinr.ru

The limit of detection (*LOD*) of some lanthanides and actinides in solutions by the time-resolved laser luminescence spectroscopy is up to 10^{-13} mole/liter [1]. The time-resolved laser luminescence spectroscopy technique features selectivity in four parameters: the laser radiation wavelength, measured radiation wavelength, measurement delay with respect to the pulse laser, and measurement time. Unfortunately, Pu, Np, and some U compounds do not produce direct luminescence in solutions, but when excited by laser radiation, they can induce chemiluminescence of some chemiluminogen (luminol in our experiments) [1-3]. Currently, chemiluminescence methods are used for detection of various substances with *LOD* of 10^{-6}-10^{-13} mole/liter [4]. We demonstrated a possibility of using the chemiluminescence method for detection and determination of valence states of Pu, Np, and U. A key problem of chemiluminescence application to detection of lanthanides and actinides in solutions is an increase in the selectivity of detection. Appropriate selectivity of lanthanide or actinide molecules excitation can be reached by initiation of transitions within 4f- or 5f-electron shell, which correspond to visible spectral range of absorbed laser radiation. Since the energy of one-quantum excitation in visible range may be insufficient for initiation of chemiluminescence it was proposed to excite lanthanide or actinide ion by multi-quantum absorption of visible light [1-3].

The use of laser radiation with tunable wavelength allows selective excitation of actinide or lanthanide species with subsequent registration of direct actinide/lanthanide luminescence or chemiluminescence of chemiluminogen initiated by excited actinide/lanthanide molecules [1-3].

The details of multi-step luminescence/chemiluminescence excitation in solutions containing Sm, U, Pu and Np species are considered. It is shown that the multi-step schemes [2,3] of luminescence/chemiluminescence excitation increase both the sensitivity and selectivity of lanthanide and actinide detection.

References

[1] I.N. Izosimov, *Phys. Part. Nucl.* **38**, 177 (2007). DOI: 10.1134/s1063779607020025
[2] I.N. Izosimov, N.G. Firsin, N.G. Gorshkov et al., *Hyperfine Interact.* **227,** 271 (2014). DOI: 10.1007/s10751-013-0990-7
[3] I.N. Izosimov, *Journal of Radioanalytical and Nuclear Chemistry*, (2015). DOI: 10.1007/s10967-014-3601-4
[4] C.Dodeigne, L.Thunus, and R.Lejeune, *Talanta*, **51**, 415 (2000).

Complexation of uranyl with sulphate and selenate in aqueous solution: experimental data and quantum chemical modelling

Jakub Višňák[1,2,3], Aleš Vetešník[1], Jakub Kuba[1], Lukáš Sobek[2,3], Vladimir Sladkov[4]

[1] *Department of Chemical Physics and Optics, Faculty of Mathematics and Physics, Charles University in Prague, Ke Karlovu 3, 121 16 Prague 2, Czech Republic, e-mail: jvisnak@gmail.com*
[2] *J. Heyrovský Institute of Physical Chemistry, Dolejškova 2155/3, 182 23 Prague 8, Czech Republic*
[3] *Department of Nuclear Chemistry, Faculty of Nuclear Sciences and Physical Engineering, Czech Technical University, Břehová 7, 115 19 Prague 1, Czech Republic*
[4] *CNRS, Institute de Physique Nucleaire (IPN), UMR 8608, Université Paris-Sud, 15 rue G. Clemenceau, 91406 Orsay, France*

The uranyl-anion interactions are of both pure chemical and practical importance. Uranyl-sulphate thermodynamical data ($\Delta G°$, $\Delta H°$, $\Delta S°$ of 1:1, 1:2, 1:3 complexes and several ternary uranyl-hydroxo-sulphato complexes) has an important role as an input for the geochemical modelling, e.g. particularly in the pre-mining analyses, modelling of chemical proceses in nuclear energetics and safety studies of radioactive waste repositories. In the latter two cases, uranyl-selenate system is of high importance as well, due to both uranium and selenium elements. ^{79}Se is a long-lived ^{235}U thermal fission product and is a critical radionuclide due to its chemical and radiological toxicity and relatively high mobility. While data for the uranyl-sulphate system were already established [1-14], the information [15-17] of the uranyl-selenate system is still rather sparse, specially when we consider the luminescence spectral data.

The luminescence properties of uranium(VI) allow us to study the UO_2^{2+} - XO_4^{2-} - H_2O speciation (X = S, Se) by the time-resolved laser-induced fluorescence spectroscopy (TRLFS). We used also spectrophotometric (UV-VIS absorption) and the Affinity Capillary Electrophoresis (ACE) as alternative methods.

We prepared several series of solutions differing by the total ligand (SO_4^{2-} or SeO_4^{2-}) concentration within the series and by *pH* and ionic strengths between series. The multilinear principal component analysis of obtained spectrophotometric and TRLFS spectra result in the stability constants (β_m) and individual component spectra (the absorption spectra ($\varepsilon_m(\lambda)$),luminescence spectra ($Z_m(\lambda)$) and the luminescence life-times (τ_m)). While the dependence of β_m on ionic strength (I) provides information about the (to-zero-I) stability constant extrapolated value $\beta_m°$ and Specific Ion Interaction Theory parameters (ε(i,j)),

$$\log \beta_m = \log \beta_m^o + \frac{A\sqrt{I}}{1+Ba\sqrt{I}}\Delta z_m^2 - \sum_k \Delta\varepsilon_{mk} c_k \,, \qquad (1)^1$$

dependence of $\beta_m°$ on temperature provides $\Delta H°$ and $\Delta S°$ thermodynamical data for complex formation reactions of the type (X = S, Se)

$$a\ UO_2^{2+} + b\ XO_4^{2-} + (2c+d)\ H_2O \rightleftarrows [(UO_2)_a(XO_4)_b(OH)_c(H_2O)_d]^{(2a-2b-c)} + c\ H_3O^+, \qquad (2)$$

$$\beta_m \equiv \frac{\left[(UO_2)_a(XO_4)_b(OH)_c(H_2O)_d^{2a-2b-c}\right]\left[H_3O^+\right]^c}{\left[UO_2^{2+}\right]^a\left[XO_4\right]^b}, \qquad (3)$$

[1] Where β_m is defined by molal equilibrium concentrations (3), A and Ba are Debye-Hückel parameters, I is molar ionic strength, $\Delta z_m^2 = \sum_k \nu_{mk} z_k^2$, where ν_{mk} is steciometric coefficient, z_k k-th particle (product or reactant) charge number, c_k its molal concentration and $\Delta\varepsilon_{mk} = \sum_i \nu_{mi}\varepsilon(i,k)$. Summation is over all molecules/particles in m-th chemical reaction.

$$\ln \beta_m^o = \frac{\Delta S_m^o}{R} - \frac{\Delta H_m^o}{RT}, \quad (4)^2$$

The pure component spectra were analysed for chemical and physical implications (e.g. the uranyl group symmetric mode vibrational frequency dependence on ligand concentration) and are prepared for possible use in experimental detection of uranium compounds in natural samples (TRLFS gives detection limit lower than 10^{-8} mol·dm^{-3} U). Since this is still rather preliminary research, we will present up to date just values for a = 1 and c = 0 (1), but further studies are planned.

Preliminary results from the spectrophotometric study of uranyl-selenate system (I = (3.8 ± 0.3) mol·kg$_w^{-1}$, T = (25.0 ± 0.5)°C) are log β_1° = 2.6 ± 0.2 ($UO_2SeO_4^0$) and log β_2° = 3.3 ± 0.2 ($UO_2(SeO_4)_2^{2-}$). TRLFS measurements resulted in log β_1° = 3.05 ± 0.25 (I_1 = 0.05 mol·kg$_w^{-1}$, T = (26 ± 2)°C) and log β_1 = 1.54 ± 0.45, log β_2 = 1.75 ± 0.50 (I_2 = (1.0 ± 0.2) M, T = (25.0 ± 0.5)°C, SIT: log β_1° = 2.8 ± 0,5, log β_2° = 3.0 ± 0.6).

The lower stability constants values for the uranyl-selenate system when compared to suranyl-sulphate system corresponds with SeO_4^{2-} being softer Lewis base than SO_4^{2-} and therefore forming weaker complex with relatively strong Lewis acid – UO_2^{2+} [16].

The UV-VIS absorption spectra of $UO_2(SeO_4)_m^{2-2m}$ have similar shape as corresponding uranyl-sulphate complexes and luminescence spectra of uranyl-selenate complexes show similar trends as corresponding uranyl-sulphate complexes – the peak maxima are more red-shifted with higher number of SeO_4^{2-} ligands m, the distinguishability of luminescence spectra were lower for the higher ionic strength I_2. For this ionic strength the estimates of symmetric vibrational mode of uranyl group in corresponding complex species were derived from the luminescence peak maxima spacing, 870 cm^{-1} for $[UO_2(H_2O)_5]^{2+}$ and 860 cm^{-1} for both $UO_2SeO_4^0$ and $UO_2(SeO_4)_2^{2-}$ (number of coordinated water molecules is to be determined), the corresponding energy of 0→0' transition were estimated as 20 470 cm^{-1} (UO_2^{2+}), 20 330 cm^{-1} (UO_2SeO_4) and 20 270 cm^{-1} ($UO_2(SeO_4)_2^{2-}$). The luminescence life-times (ionic strength I_2) for the corresponding complex species were τ_1 = (2.2 ± 0.7) μs, τ_2 = (4.5 ± 1.0) μs and τ_3 = (8 ± 3) μs).

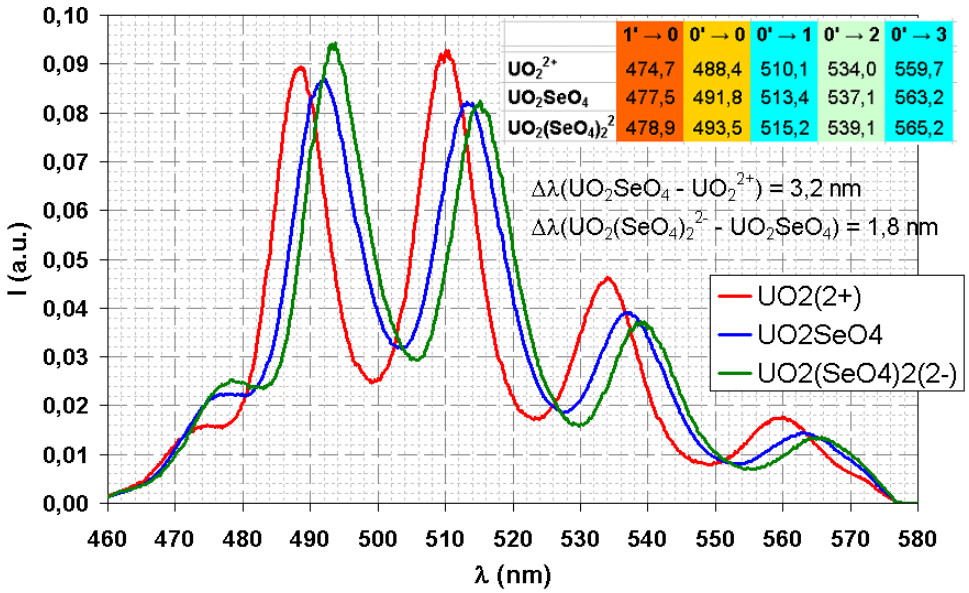

Fig. 1. Noramlized luminescence spectra of UO_2^{2+}, UO_2SeO_4 and $UO_2(SeO_4)_2^{2-}$ (I = 1.0M, T = 25°C).

We have investigated the possibility of quantum chemical modelling of uranyl-sulphate and uranyl-selenate complexes in aqueous solution with the aiming at predicting important

[2] No temperature dependence of ΔH° and ΔS° in studied temperature range (15-45°C) were taken into account here.

thermodynamical and spectral properties from the theory (using both DFT and wave-function based methods) as well. In the first step, presented here, we reproduced and further developed the studies [18-19].

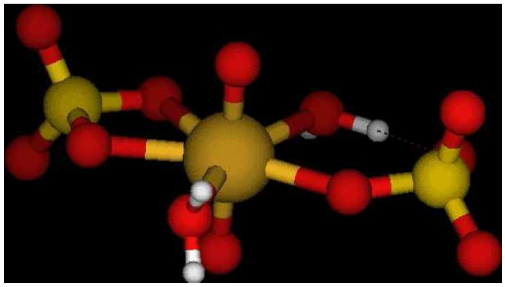

Fig. 2. Diaquabis(sulphato)uranyl(2-) molecule, $[UO_2(H_2O)_2(\eta^1\text{-}SO_4)(\eta^2\text{-}SO_4)]^{2-}$. Ground state geometry optimalisation by the DFT/B3LYP method

References

[1] S. Ahrland: On the complex chemistry of the uranyl ion: V. The complexity of uranyl sulfate, Acta Chem. Scand., **5** (1951) 1151-1167.
[2] S. Matsuo: Sulphate complexes of uranium(VI), J. Chem. Soc. Japan, **81** (1960) 833-836.
[3] D. Banerjea, K. K. Tripathi: Association of uranium(VI) with anions in aqueous perchloric acidic medium, J. Inorg. Nucl. Chem., **18** (1961) 199-206.
[4] R. M. Wallace: Determination of stability constants by Donan membrane equilibrium: The uranyl sulphate complexes, J. Phys. Chem., **71** (1967) 1271-1276.
[5] D. Langmuir: Uranium solution – mineral equilibria at low temperatures with applications to sedimentary ore deposits, Geochim. Cosmochim. Acta, **42** (1978) 547-569.
[6] R. J. Lemire, P. R. Tremaine: Uranium and plutonium equlibria in aqueous solutions to 200°C, J. Chem. Eng. Data, **25** (1980) 361-370.
[7] G. Geipel, A. Brachmann, V. Brendler, G. Bernhard, H. Nitsche, Uranium(VI) Sulfate Complexation Studied by Time-Resolved Laser-Induced Fluorescence Spectroscopy (TRLFS), Radiochimica Acta 75:199-204, 1996.
[8] C. Hennig, A. Ikeda, K. Schmeide, V. Brendler, H. Moll, S. Tsushima, A.C. Scheinost, S. Skanthakumar, R. Wilson, L. Soderholm, K. Servaes, C. Görrler-Walrand, R. Van Deun (2008c), The relationship of monodentate and bidentate coordinated uranium(VI) sulfate in aqueous solution. Radiochim Acta 96: 607-611.
[9] G. Tian, L. Rao: Spectrophotometric and Calorimetric Studies of U(VI) Complexation with Sulfate at 25-70°C. Lawrence Berkeley National Laboratory. 2009, s. 16.
[10] T. Vercouter, P. Vitorge, B. Amekraz, Ch. Moulin, Stoichiometries and Thermodynamic Stabilities for Aqueous Sulfate Complexes of U(VI), Inorg. Chem. 2008, 47, 2180-2189.
[11] A. Vetešník, M. Semelová, K. Štamberg, D. Vopálka: Uranium(VI) sulfate complexation as a function of temperature and ionic strength studied by TRLFS In: Uranium, Mining and Hydrogeolology. Berlin: Springer-Verlag, 2008, p. 623-630. ISBN 978-3-540-87745-5.
[12] D. Vopálka, K. Štamberg, A. Motl, B. Drtinová: The study of the speciation of uranyl-sulphate complexes by UV-Vis absorption spectra decomposition (2010), J Radioanal Nucl Chem, 286:681-686.
[13] J. Višňák, A. Vetešník, K. Štamberg, J. Bok, STUDY OF THE SPECIATION IN THE SYSTEM UO_2^{2+} - SO_4^{2-} - H_2O BY MEANS OF THE UV-VIS SPECTROPHOTOMETRY, Nuclear Chemistry Annual Report 2012, not published yet, added as supplementary info.
[14] H. Moll, T. Reich, C. Hennig, A. Rosseberg, Z. Szabó, I. Grenthe, Solution coordination chemistry of uranium in the binary UO2(2+) - SO4(2-) and the ternary UO2(2+) - SO4(2-) - OH(-) system, a combined EXAFS and O-17 NMR study, Report Jan. 1998-June 1999, Project-Group ESRF-Beamline (ROBL-CRG), FZR-275, Sept. 1999.
[15] J. Fuger, Chemical Thermodynamic properties-selected values, in Gmelin Handbook of inorganic chemistry, 8th ed., Uranium, Supp. Vol. **A6**, Berlin: Springer-Verlag, 1983, *pp.*165-192.
[16] V. Sladkov: Uranyl complexation with selenate at variable temperatures studied by affinity capillary electrophoresis, J Chromatography A, 1276 (2013) 120-125.
[17] P. Lubal, J. Havel: The study of complex eqilibria of uranium(VI) with selenate, Talanta 44 (1997), 457-466.
[18] J. Šebera, *Progress of Advanced methods of study of speciation and description of sorption of actinides: Report for Radioactive Waste Repository Agency (Czech Republic)* **(July 1, 2009)**, 33-42.
[19] S. J. Craw, A. M. Vincent, H. I. Hillier: Ab Initio Quantum Chemical Calculations on Uranyl UO_2^{2+}, Plutonyl PuO_2^{2+}, and Their Nitrates and Sulfates, J. Phys. Chem. 1995, 99, 10181-10185.

Magnetic and lattice excitations in hidden order compound URu_2Si_2

N. P. Butch[1,2,3], M. E. Manley[4], J. R. Jeffries[3], M. Janoschek[5,6], K. Huang[6], M. B. Maple[6], A. H. Said[7], B. M. Leu[7], and J. W. Lynn[2]

[1]*Center for Nanophysics and Advanced Materials, Department of Physics, University of Maryland, College Park, Maryland 20742, USA*
[2]*NIST Center for Neutron Research, National Institute of Standards and Technology, 100 Bureau Drive, Gaithersburg, Maryland 20899, USA*
[3]*Lawrence Livermore National Laboratory, 7000 East Ave., Livermore, California 94550, USA*
[4]*Oak Ridge National Laboratory, Oak Ridge, Tennessee 37831, USA*
[5]*Los Alamos National Laboratory, Los Alamos, New Mexico 87545, USA*
[6]*Department of Physics, University of California-San Diego, 9500 Gilman Drive, La Jolla, California 92093, USA*
[7]*Advanced Photon Source, Argonne National Laboratory, 9700 S. Cass Ave., Argonne, Illinois 60439, USA*
Email: nicholas.butch@nist.gov

Inelastic neutron and x-ray scattering measurements have been used to probe both the magnetic and lattice excitations of the heavy fermion superconductor URu_2Si_2, which is best known for its hidden order phase. The transition into this electronic ordered phase at 17.5 K is marked by an appreciable specific heat anomaly, but to date the actual order parameter is still not agreed upon. Decades of experimental study indicate that the hidden order is highly unusual, and that it does not couple strongly to experimental probes.

In the absence of strong direct evidence for symmetry breaking, we searched for incipient symmetry breaking in both the phonons and magnetic excitations of this compound. We find that the phonons do not show any dramatic temperature dependence, although some notable details will be discussed. We have further extended the measurements of the magnetic excitations to more of reciprocal space. Our new data make it possible to estimate the effective moment responsible for the dynamic susceptibility. Moreover, we demonstrate that the magnetic excitations are signatures of the effects of strong electron correlations, whose overall symmetry is not changed by the hidden order phase transition. This fact suggests that this phase transition does not involve the reduction of spatial symmetry.

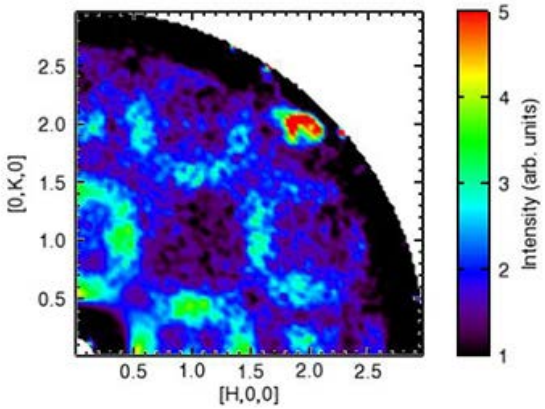

Fig. 1. Magnetic scattering intensity, integrated from 2-8 meV, at 5K in URu_2Si_2. Although the material is in the hidden order phase, the excitations still trace the same reciprocal lattice vectors as they do in the paramagnetic phase, and do not break the high-temperature body-centered tetragonal symmetry. Data were taken at the NCNR on the Disk Chopper Spectrometer using 2.5 A incident neutrons.

References

[1] N. P. Butch, et al., Phys. Rev. B **91**, 035128 (2015)

RXES experiments to explore the 5*f* ground state in URu_2Si_2

H. C. Walker[1], K. O. Kvashnina[2], D. Aoki[3], R. Eloirdi[4], R. Caciuffo[4], and G. H. Lander[4]

[1] *ISIS Facility SFTC - Rutherford Appleton Laboratory, OX11 0QX Didcot, UK*
[2] *ESRF, 38043 Grenoble, France*
[3] *CEA Grenoble, 38054 Grenoble, France*
[4] *European Commission, JRC, ITU, 76125 Karlsruhe, Germany*

A major question in discussing the compound URu_2Si_2 is whether the electronic ground state is $5f^2$ or $5f^3$. To define this ground state we have made resonant x-ray emission spectroscopy (RXES) measurements at the M_4 and M_5 absorption edges of UO_2, USb, UPd_3, and URu_2Si_2. These measurements are similar to those reported recently for U-oxides [1, 2] using the ID26 spectrometer at the ESRF.

The initial excitation is from the core 3*d* shell to the 5*f* empty valence states just above E_F. There is then a decay channel (Mα for the M_5 and Mβ for the M_4) to a state with a hole in the core 4*f* states, before returning to the ground state. These Mα and Mβ fluorescence lines are related to the initial 5*f* ground state. The $M_{4,5}$ transitions are at 3726 and 3555 eV, respectively, so the experiments are with so-called "tender" X-rays, which are strongly absorbed by air, so that spectrometer flight path is filled with He gas [2]. The Mα and Mβ transitions are centered at 3343 and 3173 eV with transitions to *two* states, which are split by the spin-orbit splitting of the 4*f* core states (~10 eV). The final transitions to the ground state have energies of 387 and 378 eV.

The high-energy resolution fluorescence detection XANES data have peaks that are only slightly (– 0.3 eV) displaced from the peak position found in UO_2, showing that all compounds have a greater 5*f* occupation than the $5f^2$ known for UO_2, but the differences are small. These XANES measurements are similar to those performed by Booth *et al.* [3], except that ours are at the $M_{4,5}$ edges, whereas Booth's are at the $L_{2,3}$ edges. Spectroscopy at the $M_{4,5}$ edges probes excitations between the core $3d \rightarrow 5f$ valence states, whereas the $L_{2,3}$ edges are probing transitions $2p \rightarrow 6d$ valence states.

We have examined in detail the Mα and Mβ transitions to the spin-orbit split 4*f* core levels. At the M_4 transition (hole in $3d_{3/2}$ subshell) the Mβ transition is strong to the $4f_{5/2}$ state, but is forbidden to the $4f_{7/2}$ state by the selection rules. However, in the presence of a crystal-field splitting of the ground-state wave functions these selection rules will be modified, and we observe a weak peak (~ 1% of the strong component of the Mβ). Moreover, the peak position is shifted by about 4 eV closer to the $3d_{3/2} \rightarrow 4f_{5/2}$ transition, compared to the two strong (allowed) peaks at the Mα transitions from the M_5 edge. The latter accurately reflects the spin-orbit splitting of the 4*f* core peaks as observed in photoemission experiments [4].

We are currently discussing these results with theorists, and will present the methodology of the experiments and some preliminary conclusions.

References

[1] K. O. Kvashnina *et al.* Phys. Rev. Lett. **111**, 253002 (2013)
[2] K. O. Kvashnina *et al.,* J. of Electron Spectroscopy and Related Phenomena, **194**, 27 (2014)
[3] C. H. Booth *et al.,* Proc. Nat. Academy USA **109**, 10205 (2012)
[4] E. S. Ilton and P. S. Bagus, Phys. Rev. B **71**, 195121 **(**2005**)**

Elastic Response of URu_2Si_2 under Pulsed Magnetic Field

Tatsuya Yanagisawa[1], Taro Murazumi[1], Shota Mombetsu[1], Hiroyuki Hidaka[1], Hiroshi Amitsuka[1], Mitsuhiro Akatsu[2], Shadi Yasin[3], Pham Thanh Cong[3], Sergei Zherlitsyn[3], Jochen Wosnitza[3], Kevin Huang[4], Noravee Kanchanavatee[4], Mark Janoschek[5], M. Brian Maple[4] and Dai Aoki[6,7]

[1] *Department of Physics, Hokkaido University, Sapporo 060-0810, Japan*
[2] *Department of Physics, Niigata University, Niigata 950-2181, Japan*
[2] *Hochfeld-Magnetlabor Dresden, Helmholtz-Zentrum Dresden-Rossendorf, D-01314 Dresden, Germany*
[4] *Department of Physics, University of California, San Diego, La Jolla, CA 92093, U.S.A.*
[5] *Los Alamos National Laboratory, Los Alamos, NM 87545, U.S.A.*
[6] *CEA-Grenoble, F-38000 Grenoble, France*
[7] *Institute for Materials Research, Tohoku University, Oarai 311-1313, Japan*

Heavy-fermion superconductor URu_2Si_2 has been known to show an enigmatic second-ordered phase transition at 17.5 K, so called 'Hidden Order (HO)', whose order parameter has been unsolved since its discovery over 25 years ago [1–3]. Many research efforts have been made to identify the broken symmetry of the phase transition; however, conclusive results have not been obtained yet. Recently, broken fourfold-rotational symmetry about the tetragonal [001] axis and a spontaneous tetragonal-to-orthorhombic lattice deformation in HO were suggested by several experiments [4, 5], however, the interpretation of these experimental results remains controversial [6]. Since ultrasonic measurement can sensitively detect symmetry-breaking lattice instability and electric quadrupole response via electron-phonon coupling, we have measured elastic constants of single-crystalline URu_2Si_2 by means of high-frequency ultrasonic velocity measurement under pulsed magnetic fields up to 68.7 T in wide temperature range from 1.5 K to ~120 K [7]. The combination of the transverse ultrasound (symmetry-breaking strain field) and pulsed magnetic field allows investigating elastic response of URu_2Si_2 in the region where hybridized-electronic state and HO are eliminated by high-magnetic field for $H \parallel [001]$.

Figure 1 shows a comparison of several elastic constants of URu_2Si_2 as a function of magnetic field for $H \parallel [001]$ at 1.5 K. Above the upper phase boundary of HO phase ~35 T at 1.5 K, all ultrasonic modes exhibit successive step-like anomalies up to 39 T, which are related to cascade-like meta-magnetic transitions [8].

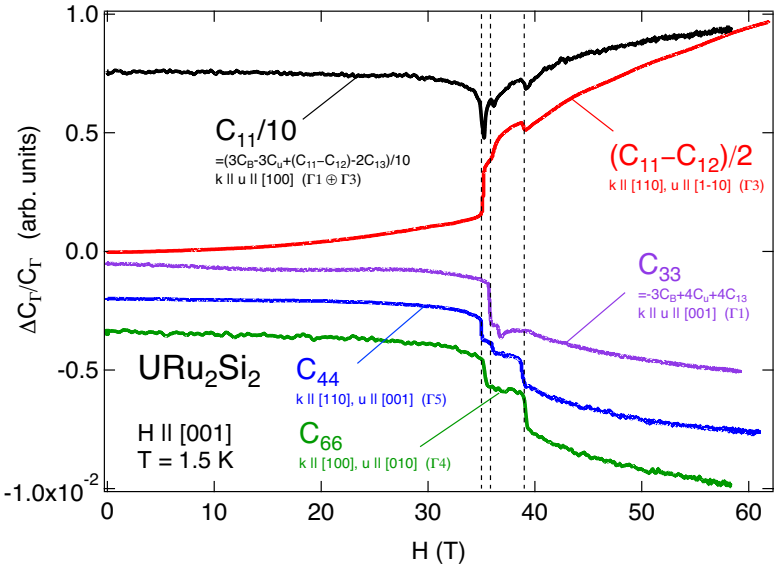

Fig. 1. Magnetic field dependence of elastic constants of URu_2Si_2 for $H \parallel [001]$ at 1.5 K. Dotted lines are guide to the eyes, which indicate three-successive transitions.

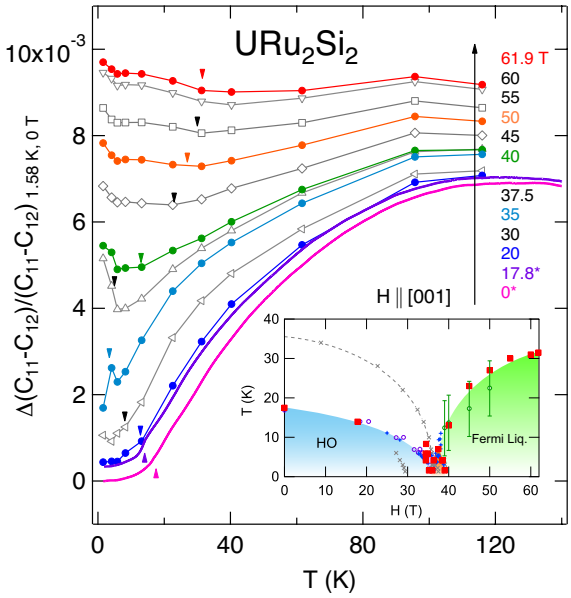

Fig. 2. Normalized elastic constant $(C_{11}-C_{12})/2$ vs. temperature at several fixed magnetic fields H || [001] from 0 to 61.85 T. The curves indicated by a magnetic field with an asterisk, 0 and 17.8 T, have been measured with the conventional method as a basis for the conversion from isotherms to curves at constant fields. Inset shows magnetic field-temperature phase diagram of URu_2Si_2 for H || [001]

Intriguingly, elastic constant $(C_{11}-C_{12})/2$ shows rapid increasing in high magnetic field region, while other transverse ultrasonic modes, C_{44} and C_{66}, show an opposite behavior. It should be noted that the $(C_{11}-C_{12})/2$ mode is the only transverse ultrasonic mode which shows characteristic decreasing (softening) in temperature dependence in low-magnetic field region where the system exhibits a hybridized-electronic state. As shown in Fig. 2, the softening of $(C_{11}-C_{12})/2$ in the temperature dependence is quantitatively recovered at the suppression of hybridized-electronic state and the hidden order in high-magnetic field above 40 T for H || [001]. Since the $(C_{11}-C_{12})/2$ mode corresponds to the elastic response to the (x^2-y^2)-type orthorhombic strain which can conserve volume but breaks Γ_3-lattice symmetry, such clear contrast in the elastic responses and its relation to the hybridized-electronic state strongly suggest that the Γ_3-type orthorhombic lattice instability could result from local-symmetry-breaking band instability via conduction electron to f-electron hybridization and will be linked to the HO parameter of this compound.

References

[1] M. B. Maple, J. Chen, Y. Dalichaouch, T. Kohara, C. Rossel, M. S. Torikachvili, M. W. McElfresh, and J. D. Thompson, *Phys. Rev. Lett.* **56**, 185 (1986).
[2] W. Schlabitz, J. Baumann, B. Pollit, U. Rauchschwalbe, H. M. Mayer, U. Ahlheim, and C. D. Bredl, *Z. Phys. B* **62**, 171 (1986).
[3] T. T. M. Palstra, A. A. Menovsky, J. van den Berg, A. J. Dirkmaat, P. H. Kes, G. J. Nieuwenhuys, and J. A. Mydosh, *Phys. Rev. Lett.* **55**, 2727 (1985).
[4] T. Shibauchi, H. Ikeda, and Y.Matsuda., *Philosophical Magazine* **94**, 3747 (2014).
[5] S. Tonegawa *et al.*, *Nat. Commun.* **5**, 4188 (2014).
[6] C. Tabata, T. Inami, S. Michimura, M. Yokoyama, H. Hidaka, T. Yanagisawa, and H. Amitsuka., *Philosophical Magazine* **94**, 3747 (2014).
[7] T. Yanagisawa, S. Mombetsu, H. Hidaka, H. Amitsuka, M. Akatsu, S. Yasin, S. Zherlitsyn, J. Wosnitza, K. Huang, M. Janoschek, and M. B. Maple, *Phys. Rev. B* **88**, 195150 (2013); T. Yanagisawa, *Philosophical Magazine* **94**, 3775 (2014).
[8] G. W. Scheerer, W. Knafo, D. Aoki, G. Ballon, A. Mari, D. Vignolles, and J. Flouquet, *Phys. Rev. B* **85**, 094402 (2012).

5f-contributions to Fermi surfaces in (Th, U)Ru_2Si_2

Blank line (12 points)

Yoshinori Haga[1], Yuji Matsumoto[2], Naoyuki Tateiwa[1], Etsuji Yamamoto[1], Noriaki Kimura[3], Tomoo Yamamura[4], Zachary Fisk[1,5]

Blank line (12 points)

[1] *Japan Atomic Energy Agency, Tokai, Ibaraki 319-1195, Japan, e-mail: haga.yoshinori@jaea.go.jp*
[2] *Nagoya Inst. Tech, Nagoya, 466-8555, Japan*
[3] *Graduate School of Science, Tohoku University, Sendai 980-8578, Japan*
[4] *Institute for Materials Research, Tohoku University, Sendai 980-8577, Japan*
[5] *University of California, Irvine, California 92697, USA*

Blank line (12 points)

Rare earth and actinide compounds with the tetragonal $ThCr_2Si_2$-type structure have attracted attention because of their intriguing characteristics. Among them, URu_2Si_2 has been a subject of intensive experimental and theoretical studies. URu_2Si_2 is known to exhibit two phase transitions[1]. The first one occurs at 17.5 K with a prominent anomaly in specific heat. Despite intensive research, the order parameter of this phase transition has not been identified [2]. Therefore this 'ordered state' is now called hidden-order. At lower temperature, another phase transition takes place at about 1.4 K, which corresponds to superconductivity with an enhanced effective mass of conduction carrier and anomalous behavior. It is now well established that the superconductivity coexists with the hidden-order state. It is also interesting to note that superconductivity vanishes when hydrostatic pressure transforms into an antiferromagnetic state above the critical pressure of about 1 GPa, indicating that elementary excitation in the hidden order phase most likely provide pairing interaction of unconventional superconductivity [3]. In fact, the detailed analysis of resistivity exponent in the normal state using high-quality single crystals strongly suggest that anomalous scattering component proportional to temperature T is relevant to superconducting transition temperature [4,5]. It is therefore important to characterize the hidden order state and the ground state of 5f electronic state.

Like most of uranium-based magnetic materials, URu_2Si_2 shows Curie-Weiss behavior in the paramagnetic susceptibility, which can be regarded as a signature of the localized 5f states. On the other hand, existence of heavy quasiparticles observed in the normal state strongly suggests an itinerant nature of 5f electrons.

In the present study, we report experimental investigations on the Fermi surfaces property of URu_2Si_2, the reference material $ThRu_2Si_2$ and their alloy by using the de Haas-van Alphen (dHvA) effect. $ThRu_2Si_2$ can be regarded as a typical Th^{4+} metal without 5f electrons. If a localized 5f states is applicable for $U^{4+}Ru_2Si_2$, similar Fermi surfaces are expected because the number of the valence electrons is the same. However, the dHvA frequencies of $ThRu_2Si_2$ are significantly differ from those of URu_2Si_2.[6] One might suggest that comparison has to be made in the 'paramagnetic' state, because the hidden-order transition creates a gap on the Fermi surface. The recent photoemission experiment in the paramagnetic state strongly supports the itinerant picture [7]. It should also be noted that the gap formation is a manifestation of itinerant behavior.

Figure 1 shows examples of dHvA oscillation for dilute (Th, U) Ru_2Si_2 and $ThRu_2Si_2$, and their Fourier transforms [8]. It is demonstrated that the dHvA frequency is unchanged upon introducing 5f electrons in $ThRu_2Si_2$. This is qualitatively different from the Fermi surface evolution in the dilute (La,Ce)Ru_2Si_2 alloys showing typical dilute Kondo effect [9].

For the dilute (Th,U)Ru_2Si_2, non-Fermi liquid like behavior is reported in low temperature properties [10]. The character of 5f electron embedded in the host $ThRu_2Si_2$ therefore might not be reagarded as Fermi liquid. Further experiments are now in progress to fully characterize the electronic state of the dilute systems.

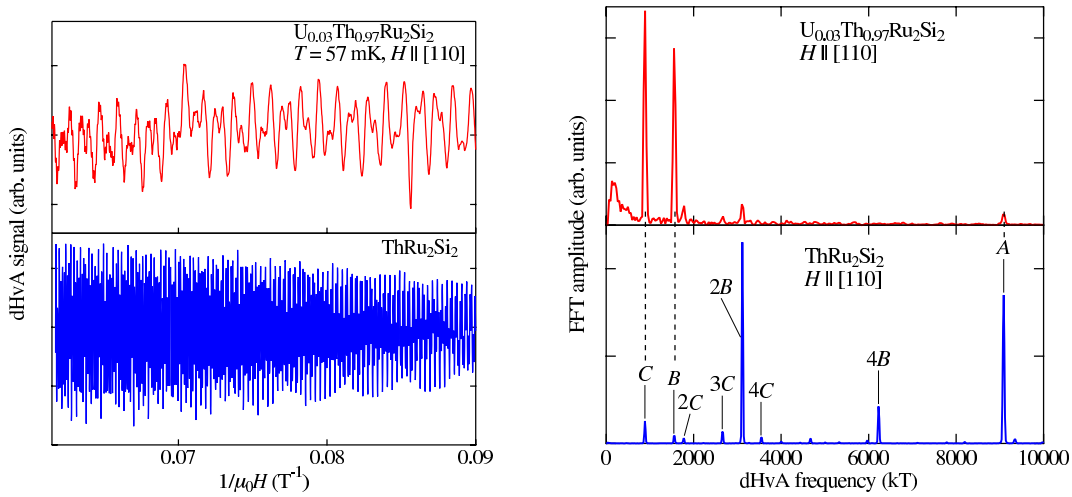

Fig. 1. Examples of dHvA oscillation (left) for dilute (Th, U)Ru_2Si_2 and $ThRu_2Si_2$ and their Fourier transforms (right).

References

[1] T.T.M. Palstra *et al.*, *Phys. Rev. Lett.* **55.**, 2727 (1985).
[2] For a review article, J.A. Mydosh and P.M. Oppeneer, *Rev. Mod. Phys.,* **83**, 1301 (2011) .
[3] H. Amitsuka *et al.*, *J. Magn. Magn. Mater.* **310**, 214 (2007).
[4] T.D. Matsuda *et al.*, *J. Phys. Soc. Jpn.* **80**, 114710 (2011).
[5] N. Tateiwa *et al.*, *Phys. Rev. B* **85**, 054516 (2012).
[6] Y. Matsumoto *et al.*, *JPS Conf. Proc.* **3**, 011096 (2014).
[7] I. Kawasaki *et al.*, *Phys. Rev. B* **83**, 235121 (2011).
[8] Y. Haga *et al.*, to be published.
[9] Y. Matsumoto *et al.*, *J. Phys. Soc. Jpn.* **81**, 054703 (2012).
[10] H. Amitsuka *et al.*, *J. Phys. Soc. Jpn.* **63**, 736 (1994).

Structural and electronic properties of $U_3Fe_4Ge_4$ under pressure

M.S. Henriques,[1,2] D.I. Gorbunov[1,3], A.V. Andreev[1], J. Prchal[4], P. Raison[5], S. Heathman[5], Z. Arnold[1], J.-C. Griveau[5], E. Colineau[5], L. Havela[4], A.P. Gonçalves[2]

[1]*Institute of Physics, ASCR, Na Slovance 2, 182 21 Prague, Czech Republic, e-mail: henriques@fzu.cz*
[2]*CCTN, IST/CFMCUL, University of Lisbon, Nuclear and Technological Campus, P-2695-066 Bobadela, Portugal*
[3]*Dresden High Magnetic Field Laboratory (HLD), Helmholtz-Zentrum Dresden-Rossendorf, D-01314 Dresden, Germany*
[4]*Charles University in Prague, Faculty of Mathematics and Physics, Department of Condensed Matter Physics, Ke Karlovu 5, 121 16 Prague, Czech Republic*
[5]*European Commission, Joint Research Centre (JRC), Institute for Transuranium Elements (ITU), Postfach 2340, 76125 Karlsruhe, Germany*

Recently, a novel itinerant ferromagnet $U_3Fe_4Ge_4$ was characterized [1,2]. It crystallizes in the orthorhombic $Gd_3Cu_4Ge_4$ type of structure (space group *Immm*), in which there are two positions for the U atoms (2*b* for U1 and 4*i* for U2), as shown in Fig. 1. The shortest inter-uranium distances are between the U2 atoms arranged along the *c* axis (3.65 Å), and the second shortest U-U links occur in the (*bc*) plane (3.79 Å). The U atoms form zig-zag chains of alternating U1 and U2 atoms along the *b* direction. $U_3Fe_4Ge_4$ orders at T_C = 18 K and exhibits a strong magnetic anisotropy, in agreement with a two-ion hybridization-induced mechanism. The U magnetic moments are oriented along the *a* axis, perpendicular to the direction where U-U spacing is shorter. The magnetic order in this compound is related exclusively to the uranium sublattice, since iron atoms have no ordered magnetic moment. Due to the strongly itinerant nature of the 5*f* states in $U_3Fe_4Ge_4$, it displays low spontaneous magnetic moment M_s = 0.4 μ_B/U and low U effective magnetic moment not exceeding M_{eff} = 2.46 μ_B/U. As a consequence, the magnetic and electronic properties of this itinerant system are likely to be very sensitive to application of external pressure.

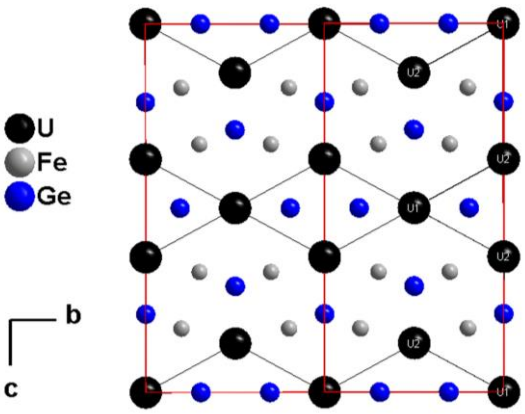

Fig. 1 - Projection of two unit cells of $U_3Fe_4Ge_4$ onto the (*bc*) plane.

Structural, magnetic and electrical properties of $U_3Fe_4Ge_4$ have been studied on a single crystal under hydrostatic pressure. The orthorhombic crystal structure is preserved up to the highest applied pressure (30 GPa). The linear compressibility is strongly anisotropic, the *a* and *b* axes being approximately 3 times softer than the *c* axis (Fig. 2*i*). Contrary to typical uranium intermetallics for which the softest lattice direction is along the shortest inter-uranium links [3], in $U_3Fe_4Ge_4$ the softest lattice direction is along the direction where the 5*f* bonding should dominate, forcing the U moments to be perpendicular to it. The elastic properties are modified considerably in the vicinity of 1 GPa when the *b* axis is transformed from least compressible to most compressible. The bulk modulus is found to be about 150 GPa. In the same pressure range, the elastic anomalies are reflected in the electronic properties that consistently indicate a change of the magnetic ground state from ferromagnetic to antiferromagnetic (Fig. 2*ii* and 2*iii*). This is most clearly seen from the magnetization that tends to zero at low temperatures. Both types of order exhibit a gap in the magnon spectrum, however, it is twice as high for the ferromagnetic state. The magnetoresistance reveals field-induced transitions of different origins in the antiferromagnetic state along the easy and hard magnetization directions. The critical temperatures found from the temperature derivative of the electrical resistivity along *a* ("order-disorder" phase transition at T_a) and *c* ("order-disorder" at T_{c1} and "order-order" phase transition

T_{c2}) lattice directions for pressures up to 3 GPa are systematized in the pressure-temperature phase diagram for $U_3Fe_4Ge_4$ (Fig. 2*iv*).

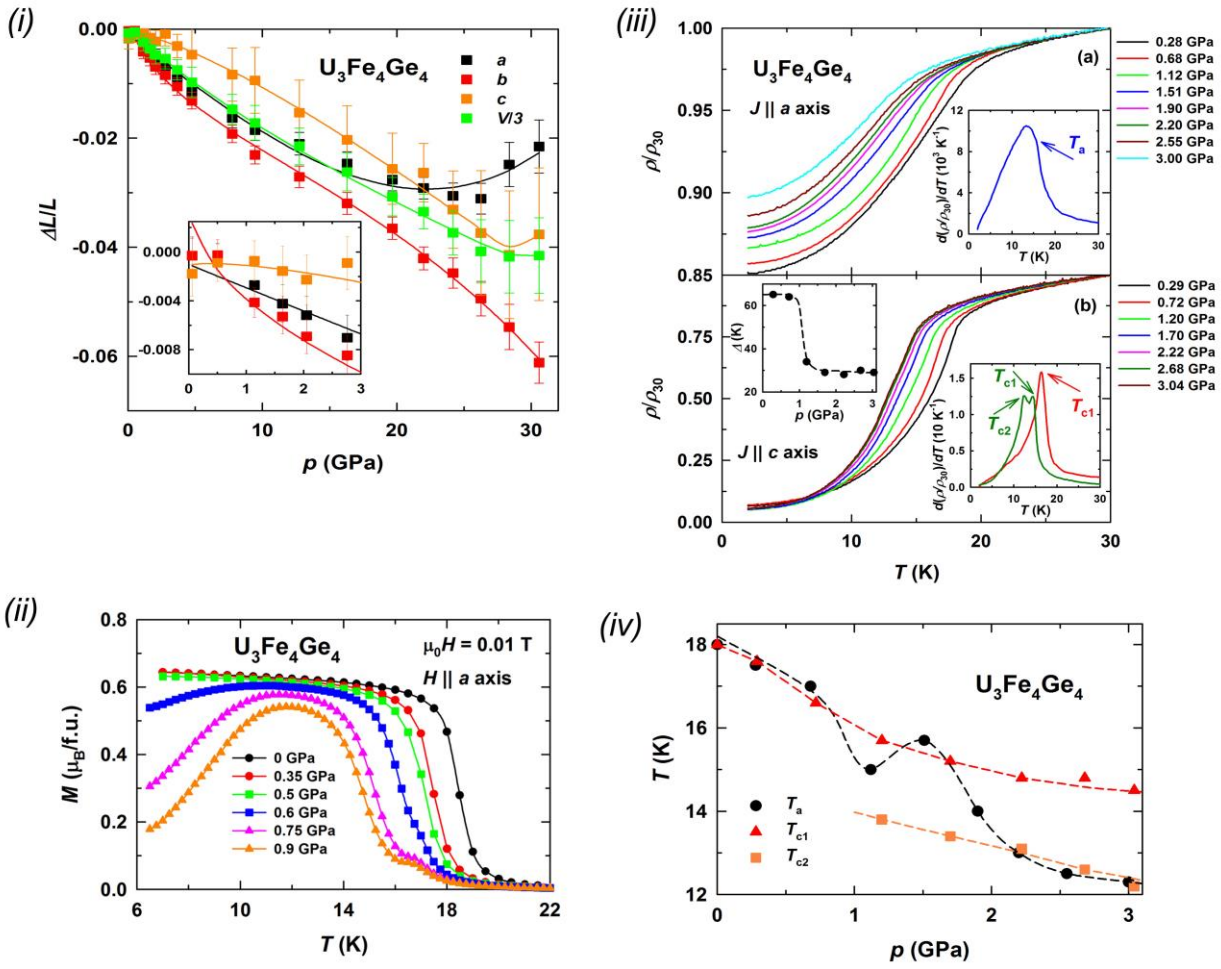

Fig. 2 – (*i*) Pressure dependence of the relative changes of lattice parameters, $\Delta a/a$, $\Delta b/b$, $\Delta c/c$, and volume, $\Delta V/V$, calculated for $U_3Fe_4Ge_4$ from the high pressure X-ray diffraction data. The inset shows the evolution of the relative lattice parameters in the low pressure range. The solid lines are a guide to the eye. (*ii*) Temperature dependence of the magnetization along the *a* axis of a $U_3Fe_4Ge_4$ single crystal in the field of 0.01 T under various pressures. (*iii*) Temperature dependence of the normalized electrical resistivity measured along the *a* (a) and *c* (b) axes of a $U_3Fe_4Ge_4$ single crystal at different pressures. The inset in the upper panel and the lower inset in the lower panel present temperature derivatives of the normalized resistivity at selected pressures. The upper inset in the lower panel shows the pressure dependence of the energy gap in the spin-wave spectrum. (*iv*) Pressure dependence of T_a, T_{c1} and T_{c2} determined from electrical resistivity measurements along the *a* and *c* axes of a $U_3Fe_4Ge_4$ single crystal.

Acknowledgements
The access to infrastructure and support to users provided by the European Commission, DG-JRC, within its "Actinide User Laboratory" program at ITU-Karlsruhe is acknowledged.

References
[1] D. Berthebaud et al., J. Alloys Compd. **554**, 408 (2013).
[2] M.S. Henriques et al., J. Alloys Compd. **555**, 304 (2013).
[3] B.R. Cooper et al., *Handbook on the Physics and Chemistry of the Actinides*, A.J. Freeman and G.H. Lander (Eds.), vol. **2**, 435 (1985) (Elsevier, Amsterdam).

Study of isothermal sections of ternary systems U-*T*-Al (*T*=Ti, Zr)

C. Moussa[1], M. Pasturel[1], H. Noël[1], F. Gouttefangeas[1], L. Joanny[1], B. Stepnik[2], O. Tougait[1]

[1]*Institut des Sciences Chimiques de Rennes, UMR CNRS 6226, Université Rennes 1, Campus de Beaulieu – Bât.10A, 35042 Rennes Cedex, France, email : chantal.moussa@univ-rennes1.fr*
[2]*AREVA-FBFC 69456 Lyon, France*

Both titanium and zirconium belong to column 4 of the periodic table. In consequence, the binary phase diagrams U-Ti and U-Zr show many similarities, such as the formation of complete solid solutions based on their cubic high temperature form [1]. In addition, Ti and Zr show small cross sections of neutron absorption, explaining their uttermost interest as alloying elements to improve the machinability and the used properties of advanced U-metallic fuels [2]. In the frame of the current concern about reduction of ^{235}U-enrichment of fissile materials for civil applications, which is based on the use of dense γ-U(Mo) alloys [3], both Ti and Zr are considered as chemical inhibitors of the interaction with the Al-matrix [4] or diffusion barrier between the fuel and the Al cladding [5]. The knowledge of the interactions between U, T-element (T = Ti, Zr) and Al of the matrix or of the cladding is of noticeable importance. The assessment of the phase equilibria in the U-*T*-Al ternary systems affords a valuable contribution to the understanding of the development of such materials. Up to now, these ternary systems have not been experimentally studied for the whole concentration range. Only the region between Al-UAl_2-$ZrAl_2$ has been reported by Petzow and coworkers [6], and only one ternary phase, UTi_2Al_{20} was identified in the U-Ti-Al system [7]. This presentation will deal with the description of the U-Ti-Al and U-Zr-Al isothermal sections at 1123 K and 923 K for T = Ti and 1073 K and 673 K for T = Zr.

These sections were determined experimentally for compositions covering the whole concentration range of the Gibbs triangles. The synthesis of the samples was carried out by arc-melting the elemental components (U, Al and Ti/Zr). The obtained ingots were then placed into alumina crucibles and introduced in silica tubes sealed under residual Ar atmosphere. After heat-treatments carried out for 3 weeks at least in resistance furnaces, the tubes were quenched in water. All samples were characterized by powder X-ray diffraction (XRD) and energy dispersive spectroscopy coupled to scanning electron microscopy (SEM-EDS). Differential thermal analysis (DTA) was used to define the temperature of phase-transformations.

Despite the similitude of these two elements, the ternary U-*T*-Al, *T* = Ti, Zr, isothermal sections show great differences. For example, our study confirms the formation of one single ternary phase, namely UTi_2Al_{20} in the *3d* element based system, while no ternary has been detected with the *4d* one. This phase, already identified by Niemann et al. [7], has been shown to be a line compound forming via the peritectic reaction **UAl_3 + $TiAl_3$ + L→ UTi_2Al_{20}** at 1365 K **(**Fig. 1)

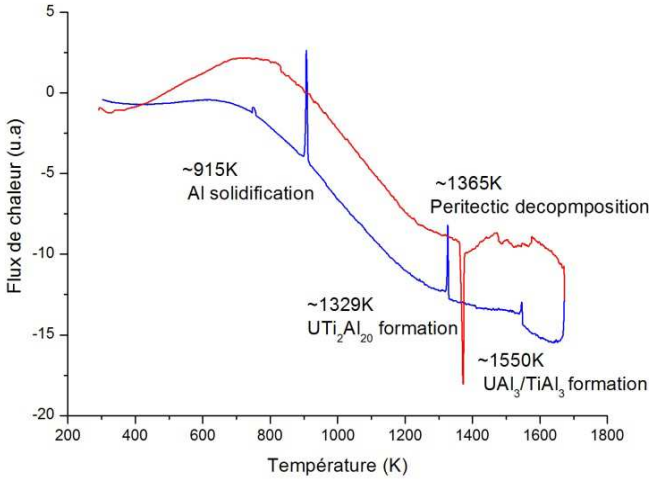

Figure 1: DTA heat flux as function of temperature of UTi_2Al_{20} (5K/min)

The main difference between both systems resides in the substitution mechanisms observed on the extension in the ternary of binary phases. In the case of titanium, an Al/Ti substitution mechanism is observed on many Ti-Al binary phases showing homogeneity ranges, but also on the solid solution $UAl_{2-x}Ti_x$ with $x \leq 0.15(2)$ at 923 K. At the opposite, the U-Zr-Al sections are rather dominated by an U/Zr substitution mechanism, with the occurrence of the solid solutions $U_{1-x}Zr_xAl_2$ and $U_{1-x}Zr_xAl_3$ ranging up to 22(1) and 16.5(10) at.% Zr, respectively, at 1073 K.

At high temperatures, in addition to the full transition metal/uranium substitution rate on the U-(Ti,Zr) boundary, a non negligible solubility of Al is encountered in both γ-U(Ti) and γ-U(Zr) as well as in β-Ti(U) and α-Zr. As expected, the water quenching used in our experiment was not fast enough to retain the cubic γ-U(T), but the microstructure of the quenched samples (fig 2 and 3) is characteristic of the eutectoïd decompositions γ-U(Ti)→ α-U+U_2Ti and γ-U(Zr)→α-U+UZr_2.

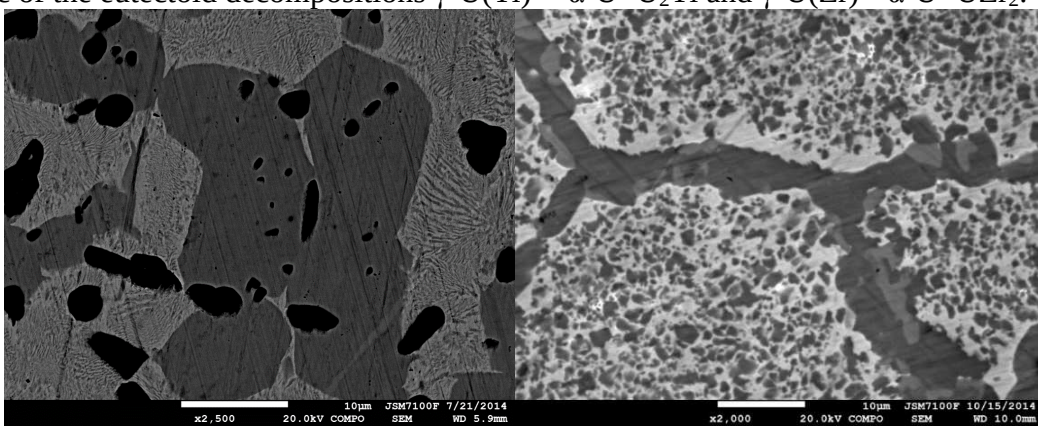

Figure 2a, Back-scattered electron SEM microviews of a) 70U-28Ti-2Al after annealing at 1123 K showing the lamellar morphology of the eutectoid transformation **γU → αU + U_2Ti.** Ti_3Al (black areas), U_2Ti (medium grey areas) and U (light grey areas) and b) of 60U-30Zr-10Al after annealing at 1073 K shows the mosaic microstructure of the eutectoid transformation **γ(U,Zr) → αU + UZr_2.** Zr_2Al (dark grey areas), UZr_2 (medium grey areas) and U (light grey areas)

In conclusion, the isoelectronic titanium and zirconium induce quite different U-T-Al phase diagrams, mainly dominated by different substitution mechanisms. This could be attributed to different metallic radii of these elements, especially because of the closeness of Al and Ti radii and of U and Zr radii. The present study evidence a challenging comprehensive study of the metallurgy of U(Ti) or U(Zr) alloys and their interaction with Al, highlighted by the determined isothermal sections.

References

[1] T.B. Massalski, H. Okamoto, P.R. Subramanian, L. Kacprzak (Eds.), Binary Alloy Phase Diagrams, second ed., ASM International, **1–3** (1990)
[2] I.J. Hastings, R.L. Stoute, j; Nucl. Mater., **37,** 295 (1970)
[3] J.L. Snelgrove, G.L. Hofman, C.L. Trybus, T.C. Wiencek, « Development of Very-High-Density Fuels by the RERTR Program», Proceedings of the International Meeting on RERTR, Seoul, South Korea, (1996).
[4] Y.S Kim, G.L. Hofman, A.B. Robinson, D.M. Wachs, H.J. Ryu, J.M. Park, J.H. Yang, J. Nucl. Mater. **427**, 233 (2012).
[5] E. Perez, B. Yao, D.D. Keiser, Y.H. Sohn, J. Nucl. Mater. **402**, 8 (2010).
[6] G. Petzow, S. Steeb, I. Ellinghaus, J. Nucl. Mater. **4**, 316 (1661).
[7] S. Niemann, W. Jeitschko, J. Solid State Chem. **114**, 337 (1995).

The onset of magnetism in UNi(Zn,Al) system

S. Mašková[1], S. Daniš[1], K. Miliyanchuk[2], O. Stelmakhovych[3], B. Vondráčková[1], L. Havela[1]

[1] *Department of Condensed Matter Physics, Faculty of Mathematics and Physics, Charles University, Prague 2, The Czech Republic, e-mail: maskova@mag.mff.cuni.cz*
[2] *Faculty of Chemistry, Ivan Franko National University of Lviv, 79005 Lviv, Ukraine*
[3] *Department of Life Safety, Ivan Franko National University of Lviv, 79005 Lviv, Ukraine*

UNiZn is the first Zn containing UTX ternary with the ZrNiAl structure type. UNiZn polycrystalline sample was prepared by placing pure elements with the stoichiometry 1-1-1.02 into the quartz tube, which was sealed under argon atmosphere and subsequently inserted into the oven and heated fast to 500 °C, where it was held for 1 hour. After that the sample was heated fast to 1100 °C, where it was held for 26 min and subsequently cooled down at the rate 1 °C/min to 700 °C. At this temperature it was removed from the furnace.

XRD showed that UNiZn crystallizes in the hexagonal ZrNiAl type of structure (*P*-62*m*). The crystal structure parameters are summarized in table 1. The shortest inter-uranium distance (d_{U-U} = 3.43 Å) is in the basal plane, similar to most of other U-compounds with the same structure type.

	UNiZn	UNiAl*	$UNiZnH_{2.3}$#	$UNiZnH_{2.3}$##	$UNiAlD_{2.1}$*
Structure type	ZrNiAl	ZrNiAl	AlB_2	ZrNiAl	ZrNiAl
a (Å)	6.6192	6.733	4.2371	7.339	7.181
c (Å)	4.0586	4.035	3.9520	3.9513	3.989
V (Å^3)	154	158	61.44	184	178
d_{U-U} (Å) *c*-axis	4.06	4.04	3.95	3.95	3.99
d_{U-U} (Å) basal	3.43	3.48	4.21	4.21	4.15

* [1]

Table 1: Structure parameters of UNiZn, UNiAl, $UNiAlD_{2.1}$, and $UNiZnH_{2.3}$ with both types of structure refinement, mentioned in the text. Lattice parameters *a* and *c*, unit cell volume *V* and the shortest inter-uranium distance d_{U-U} are given. The data for UNiAl and its hydride are taken from Ref. 1.

The temperature dependence of magnetic susceptibility indicates that UNiZn has a paramagnetic ground state. Magnetic susceptibility is low (≈ 10^{-8} m^3/mol) but temperature dependent (Fig. 1). Almost identical values in the field of 3 and 6 T evidence the absence of any ferromagnetic impurity. The shape of magnetic susceptibility does not allow us to speculate about any real Curie-Weiss contribution, the temperature variations are simply too weak. UNiZn can be considered as a spin fluctuator with its magnetic properties between two limiting cases, Pauli paramagnet and magnetically ordered material.

The non-magnetic ground state of UNiZn is corroborated by the results of the specific heat studies, which do not reveal any anomaly originating from magnetic order. As the low-temperature data (up to 20 K) exhibit linearity in the C/T vs. T^2 plot, we determined the value of the Sommerfeld coefficient γ using the relation $C = \gamma T + \beta T^3$. We obtained the parameters γ = 94 mJ/mol K^2 and β = 0.579 mJ/mol K^4 (corresponding to Debye temperature Θ_D = 220 K).

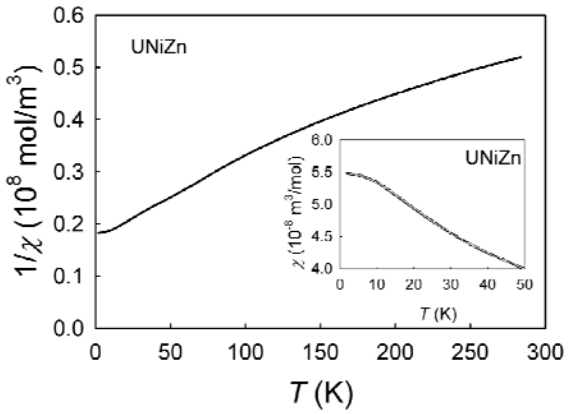

Fig. 1. Temperature dependence of inverse magnetic susceptibility measured in external magnetic field $\mu_0 H = 3$ T. The inset shows the low temperature part of magnetic susceptibility of UNiZn measured in $\mu_0 H = 3$ T.

As UNiZn properties seem to be close to the onset of magnetism we decided to perform the hydrogen absorption experiment. The hydrogenation of UNiZn was performed at hydrogen pressure 120 bar by heating up to $T = 473$ K and subsequent cooling with the rate 0.5 K/min. The amount of absorbed hydrogen estimated from the weight change was found out to be 2.3 H/f.u. The value of absorbed hydrogen is identical to the value for the γ-hydride of UNiAl, namely $UNiAlH_{2.3}$, which points to a similarity to this hydride studied in the past [1,2].

The refinement of XRD data of the hydride is not unambiguous. There are two possible crystal structures. One is the crystal-structure of AlB_2 type (space group *P*6/*mmm*). It is hexagonal with U placed in (0,0,0) and Ni and Zn randomly distributed in (⅓, ⅔, ½). The second possible crystal structure, similar to UNiAl-H, is the same as for the parent compound but with somewhat higher symmetry [2]. We tend to believe that the AlB_2 type is the right one. The obtained lattice parameters and critical U-U distances for different type of structure are summarized in Tab. 1 and compared with UNiAl and its γ-hydride. The shortest inter-uranium distance in the parent compound UNiZn ($d_{U\text{-}U} = 3.43$ Å) was found to be in the basal plane. On the other hand, upon hydrogenation the shortest U-U distance is found along the *c*-axis ($d_{U\text{-}U} = 3.95$ Å) for both possible crystal structures (Model choice does not affect U sites). The crystal lattice is expanded in such way that the shortest U-U distance is now higher than the Hill limit what allows magnetic ordering in the hydride. $UNiZnH_{2.3}$ exhibits a maximum in $\chi(T)$ indicating AF ordering around 55 K. The γ-value increases from 94 mJ/mol K^2 in UNiZn to 100 mJ/mol K^2 in the hydride. This tendency is opposite than for UNiAl (164 mJ/mol K^2 in UNiAl and 60 mJ/mol K^2 in $UNiAlD_{2.1}$ [3]). The possible scenarios explaining opposite tendencies of change of γ-value are apparent from fig. 2. The variation of the γ–coefficient of electronic specific heat is in general expected to culminate somewhere close to the onset of magnetism, which is placed between non-magnetic UNiZn and antiferromagnetic UNiAl (green line in fig.2).

We have synthesized $UNiZn_{0.5}Al_{0.5}$ to prove this statement. $UNiZn_{0.5}Al_{0.5}$ was found to be an antiferromagnet with the Néel temperature $T_N = 10$ K. Certainly the Sommerfeld coefficient of the substituted compound is higher than for the terminal phases (fig.3). We can assume that the scenario represented by the green dashed line in fig. 2 is more probable.

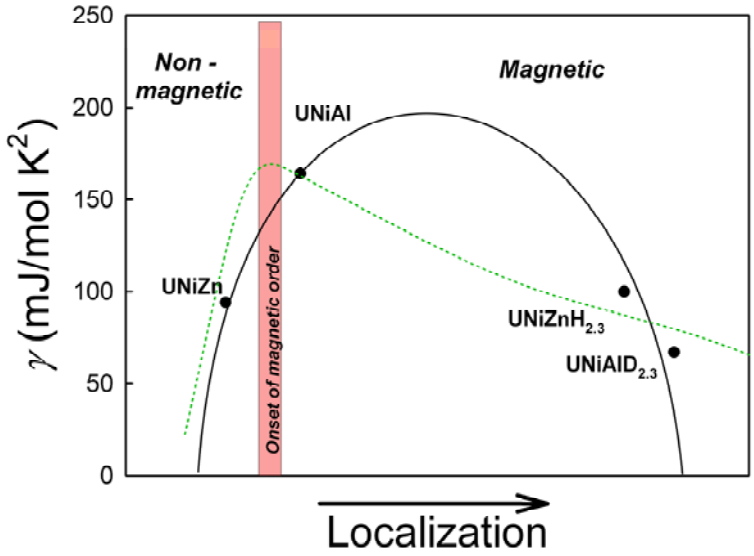

Fig. 2. Schematic representation of localization variations affecting the γ-coefficient. Individual compounds were placed rather arbitrarily on the Localization axis, respecting only the same distance between the precursor and its hydride in both cases. The full and dotted line represent two possible scenarios of the γ-variations.

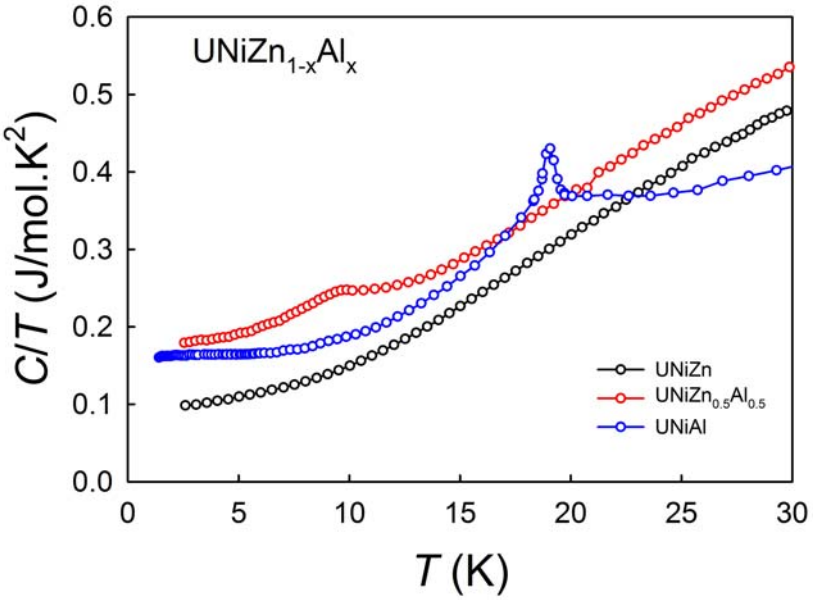

Fig. 3. The low temperature part of the specific heat (in the C/T vs. T representation) of UNiZn compared with $UNiZn_{0.5}Al_{0.5}$ and UNiAl.

The hydrogenation of $UNiZn_{0.5}Al_{0.5}$ was performed at hydrogen pressure 100 bar by heating up to $T = 473$ K and subsequent cooling with the rate 0.1 K/min. The amount of absorbed hydrogen estimated from the desorption experiment was found out to be 2.3 H/f.u. similar to the amount of H absorbed by the terminal phases. Upon hydrogenation the Néel temperature is shifted to $T_N \approx 70$ K (fig. 4). The value of Sommerfeld coefficient of specific heat for the substituted compound indeed falls in between the values for the terminated phases (fig. 5) which is relevant for both presented scenarios.

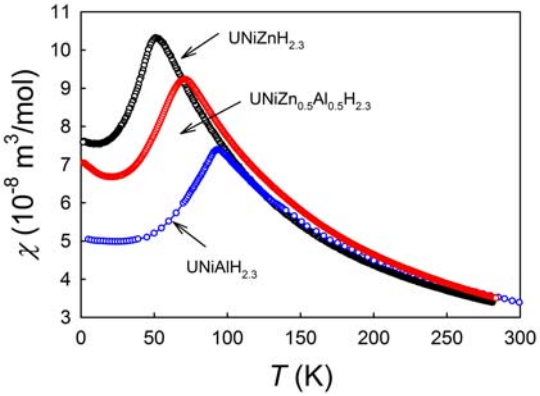

Fig. 4. Temperature dependence of magnetic susceptibility measured in external magnetic field $\mu_0 H = 6$ T.

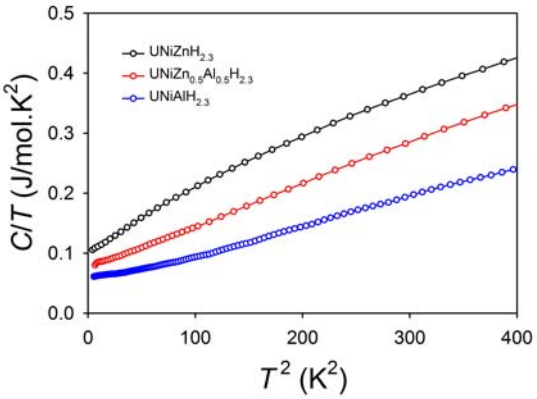

Fig. 5. Comparison of the low temperature part of the specific heat (in the C/T vs. T^2 representation) of $UNiZnH_{2.3}$, $UNiZn_{0.5}Al_{0.5}H_{2.3}$ and $UNiAlH_{2.3}$.

References

[1] H.N. Bordallo, H. Nakotte, A.V. Kolomiets, A. Christianson, L. Havela, A.J. Schultz, H. Drulis, W. Iwasieczko, Physica B 276-278,706 (2000).
[2] T. Yamamoto et al., J. Alloys Compd. **269**, 162 (1998).
[3] L. Havela,K. Miliyanchuk, A. Kolomiets: Int.J.Mat.Res. 100, 1182-1186 (2009).

45èmes Journées des Actinides, April 15-19, 2015, Prague-Průhonice, Czech Republic

Quantum interference phenomena due to disorder in the U_2TSi_3 compounds with AlB_2 type structure

Daniel Gnida, Maria Szlawska, Przemysław Swatek, Piotr Wiśniewski, and Dariusz Kaczorowski

Institute of Low Temperature and Structure Research, Polish Academy of Sciences, P.O.Box 1410, 50-950 Wrocław, Poland; e-mail: D.Gnida @int.pan.wroc.pl

The ternaries U_2CoSi_3 and U_2NiSi_3, crystallizing with a disordered AlB_2-type structure, exhibit cluster-glass (T_f = 7 K) and ferromagnetic (T_C = 27 K) behaviour, respectively. At low temperatures, their electrical transport properties are governed by an interplay of magnetic exchange interactions and quantum interference effects, which inherently result from the in-built crystallographic disorder. For U_2CoSi_3, each component of the electrical resistivity tensor markedly increases below T_f due to weak localization and electron-electron interaction contributions. Similar behaviour appears for U_2NiSi_3 at temperatures below 40 K. However, in the latter case, the electrical resistivity measured along the hard magnetic axis exhibits a clear maximum at T_C, which probably reflects suppression of the weak localization contribution. Remarkably, for both materials, the quantum corrections depend on the direction of external magnetic field with respect to the magnetic axes.

This work was supported by the National Science Center (Poland) under Grant No.2011/03/D/ST3/02351.

Structure and magnetism of UMB_4 (M = V, Cr, Mo, W) uranium borides

A.P. Gonçalves,[1] M.Dias[2], P.A. Carvalho[3], L. Havela[4]

[1] *C2TN, Instituto Superior Técnico, Universidade de Lisboa, Campus Tecnológico e Nuclear, Estrada Nacional 10, 2695-066 Bobadela LRS, Portugal, e-mail: apg@ctn.ist.utl.pt*
[2] *IPFN, Instituto Superior Técnico, Universidade de Lisboa, Av. Rovisco Pais, 1049-001 Lisboa, Portugal*
[3] *ICEMS, Departamento de Engenharia Mecânica, Instituto Superior Técnico, Universidade de Lisboa., Av. Rovisco Pais, 1049-001 Lisboa, Portugal*
[4] *Faculty of Mathematics and Physics, Charles University, Ke Karlovu 5, 12116 Prague, Czech Republic*

The UM'B_4 (M'=*d*-element) uranium borides were reported to exist and to crystallize in three different crystal structures $YCrB_4$-, $ThMoB_4$- and $ErNiB_4$-type [1]. However, their characterization was only preliminary, mainly devoted to crystallographic studies. Magnetization measurements were made just in the 80-300 K temperature range for the V, Mn, Fe, Co compounds, with no signs of magnetic transitions. The existence of superconductivity was also investigated for the Ru and Os borides, but no superconducting transition was observed down to 1.5 K. $UFeB_4$ was characterized by our group, the studies pointing to a predominant $YCrB_4$-type structure (in agreement with the previous results), but with a defective structure compatible with an intergrowth of $YCrB_4$- and $ThMoB_4$-type layers [2]. A paramagnetic behavior was observed in the 2–300 K temperature range. Continuing our investigations, here we present the preparation and study of another part of this family, UMB_4 (M=V, Cr, Mo, W), by means of X-ray powder diffraction, magnetization and specific heat measurements in the 2- 300 K temperature range.

The UMB_4 compounds were prepared by arc-melting followed by annealing at 1000ºC for 300h. Their powder X-ray patterns confirm that the V and Cr borides crystallize mainly in the $YCrB_4$-type structure (S.G. Pbam), while the Mo and W phases essentially adopt the $ThMoB_4$-type (S.G. Cmmm). The unit cell volume of the last two borides is significantly higher than the first two, which is in agreement with previous results that indicate that UM'B_4 borides containing larger transition metals have the tendency to crystallize in the $ThMoB_4$-type structure and those with smaller ones mainly adopt the $YCrB_4$-type [3]. From the point of view of magnetism, all compounds are weak Pauli paramagnets. The specific heat exhibits a strongly non-Debye character for all compounds, which most probably is related to the hardness of the boron sublattice. The γ-coefficient is moderately enhanced, but does not exceed 50 mJ/mol K^2, pointing to the presence of weakly correlated 5*f* states at the Fermi level.

References

[1] P. Rogl, The ternary and higher order systems with actinide elements and boron. In: Handbook on the Physics and Chemistry of the Actinides, A.J. Freeman and C. Keller (Eds.), Elsevier Science Publishers B.V. (1991), pp. 75.
[2] M. Dias, P.A. Carvalho, I.C. Santos, O. Tougait, L. Havela, A.P. Gonçalves, Microsc. Microanal. 19 (2013) 1204.
[3] P. Rogl, H. Nowotny, Uran-haltige Komplexboride, *Monatshefte fur Chemie* 106 (1975) 381.

45èmes Journées des Actinides, April 15-19, 2015, Prague-Průhonice, Czech Republic

Physical properties of an $UFe_{1-x}Sb_2$ single crystal

Antonio P. Gonçalves,[1] Margarida S. Henriques,[1,2] Joao C. Waerenborgh,[1] Ivan Curlik,[3] Sergej Ilʼkovič,[3] Marian Reiffers,[3] Jan Rusz[4]

[1] *C2TN, Campus Tecnológico e Nuclear, Instituto Superior Técnico, Universidade de Lisboa, Estrada Nacional 10, 2695-066 Bobadela LRS, Portugal*
[2] *Institute of Physics, ASCR, Na Slovance 2, 182 21 Prague, Czech Republic*
[3] *Faculty of Humanities and Natural Sciences, Prešov University, 081 16 Prešov, Slovakia, e-mail: marian.reiffers@unipo.sk*
[4] *Department of Physics and Astronomy, Uppsala University, Box 516, 75120 Uppsala, Sweden*

In the present work the crystal structure and electronic properties of the $UFe_{1-x}Sb_2$ compound were studied in a single crystal. XRD confirms that $UFe_{1-x}Sb_2$ crystallizes in the $HfCuSb_2$-type structure. Magnetization, AC susceptibility, specific heat, and electrical transport indicate two consecutive magnetic transitions. According to the AC susceptibility results, the anomalies are connected with an antiferromagnetic state at T_N = 25.5 K that changes to a ferromagnetic ground state at T_C = 21 K. The specific heat in zero field exhibits a small kink at T_N that vanishes with increasing applied magnetic field, which is consistent with the onset of the magnetic transition. The electronic properties exhibit large anisotropy, in agreement with the observed anisotropy in magnetic properties. First principles calculations of electronic structure show an unusually steep local minimum in the density of states right at the Fermi level, providing a starting point for explaining the material's strong anisotropy.

Experimental investigation on the ternary U-Al-Ge system and study of the ternary intermetallic phase $U_3Al_{2-x}Ge_{3+x}$ ($-0.3 \leq x \leq 1.3$)

C. Moussa[1], Z. El Sayah[1], G. Chajewski[2], V. Dorcet[1], A. P. Pikul[2], M. Pasturel[1], O. Tougait[1,3], B.Stepnik[4],

[1]*Institut des Sciences Chimiques de Rennes, UMR CNRS 6226, Université Rennes 1, Campus de Beaulieu – Bât.10A, 35042 Rennes Cedex, France, email : chantal.moussa@univ-rennes1.fr*
[2] *Institute of Low Temperature and Structure Research, ul. Okólna 2, 50-422 Wrocław, Poland*
[3] *Unité de Catalyse et de Chimie du Solide, UMR CNRS 8181, Université de Lille, France*
[4] *AREVA-FBFC69456 Lyon, France*

The interesting electronic properties of U-based intermetallics, such as non-conventional superconductivity, seem to be governed by a subtle balance between the localized and itinerant character of the 5*f* electrons. The U-Al binaries are non-magnetically ordered compounds [1-4], whereas the U-Ge binaries appear somehow with a magnetic character [5, 6]. Therefore, the study of the electronic properties of the pseudo-binary and ternary U-Al-Ge compounds can be attractive. In addition, no systematic investigation of the U-Al-Ge ternary system is available in the literature. $U_3Al_2Ge_3$ is the only ternary phase identified in this system [7]. It crystallizes in a hexagonal structure deriving from the Cr_5B_3 type and orders ferromagnetically below T_c = 63 K [8]. We have thus initiated the assessment of the solid phase relations at 673 K (i.e. below the eutectic temperature of the binary Al-Ge boundary) and at 1173 K (increased diffusion kinetics). The objectives of the project are to correlate the structural and physical properties for well-established compositions and to hypothetically discover novel ternary phases.

The samples were synthesized by arc-melting the elemental components, followed by annealing in sealed silica tubes for dwell periods of 6 weeks at 673 K, or 3 weeks at 1173 K for compositions above 25 at.% U. All samples were characterized by powder X-Ray Diffraction (XRD) and Scanning Electron Microscopy coupled to Energy Dispersive Spectroscopy (SEM-EDS). Phase transitions were determined by Differential Thermal Analysis (DTA). Single crystal X-ray and electron diffractions were used for specific samples to obtain further crystallographic information.

From these results, the equilibrium lines between the different phases were established for these two temperatures. The main features are: (*i*) the solubility of Al and Ge in U at low and high temperature (673K and 1173K) are in agreement with the assessments of Massalski *et al.* on binary systems [9]; (*ii*) the binary phase UAl_4 was not observed in any sample, proving that Ge inhibits the formation of UAl_4, similarly to Si [10]; (*iii*) the solubility of Al was evaluated in the U-Ge binaries to be systematically below approximately 4 at.% at both temperatures, except for UGe_3 which exhibits a complete solubility up to UAl_3.

Only one ternary phase, $U_3Al_{2-x}Ge_{3+x}$, is confirmed. It is not a line compound but it presents an extended homogeneity domain in the range $-0.3 < x < 1.3$. The crystallographic data of this phase was examined by Transmission Electron Microscopy (TEM) for several compositions suggesting the *I4/mcm* space group as reported in [7] rather than the *I4* space group [8], as shown by the systematic extinctions on the [010] zone axis diffraction pattern (fig. 1). The evolution of the magnetic properties of this phase with the Al/Ge substitution confirmed the ferromagnetic ordering with an increase of T_c and μ_{eff} with increasing the aluminium content (see e.g. fig. 2 for $U_3Al_{0.8}Ge_{4.2}$).

This presentation will focus on the phase equilibria in the U-Al-Ge system and the crystallographic properties of the pseudo-binary and ternary phases. An introduction to the magnetic properties along the $U_3Al_{2-x}Ge_{3+x}$ solid solution will be given and further specific heat and transport properties will be discussed by G. Chajewski during this conference.

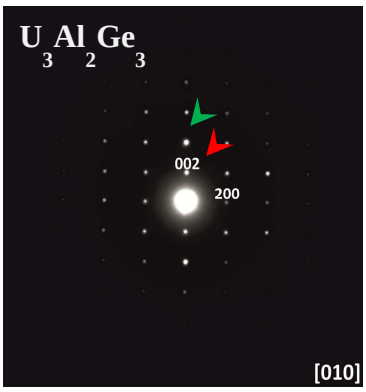

Figure 1 Electron diffraction pattern of $U_3Al_2Ge_3$. Two reflection conditions compatible with the existence of a *c* glide plane are identified: (i) the condition l = 2n along the (00l) direction and (ii) the condition h = 2n and l = 2n on the (h0l) peaks. The latter is only encountered in *I*-centered tetragonal space-groups.

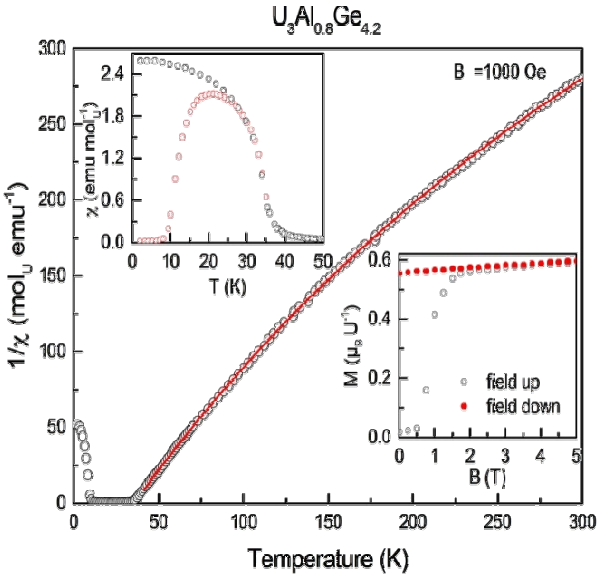

Figure 2 Temperature dependence of $U_3Al_{0.8}Ge_{4.2}$ inverse magnetic susceptibility. This phase is found ferromagnetic with T_C = 34(2) K. The fit of the paramagnetic domain using a modified Curie-Weiss law results in μ_{eff} = 2.28 μ_B, θ_p = 35.4(2) K and χ_0=0.00111(1) emu mol_u^{-1}.

References

[1]: R. J. Trainor, M. B. Brodsky, H. V. Culbert, Phys. Rev. Let., **34**, 1019-1022, (1975)
[2]: M.S. Wire, A. L. Giorgi, Phys. Rev. B, **32**, 1687- 1690, (1985).
[3]: A. L. Cornelius, A. J. Arko, J. L. Sarrao, J. D. Thompson, M. F. Hundley, and C. H. Booth, N. Harrison, P. M. Oppeneer, Phys. Rev. B **59,** 14 473-14 483 (1999).
[4]: K. H. J. Buschow and H. J. van Daal, AlP Conf. Proc. **5,** 1464-1477 (1972).
[5]: C.E.Olsen, J.Appl.Phys., **31,** 340S (1960)
[6]: R. Troć, H. Noël and P. Boulet, Phil. Mag. Part B, 82, 805-824 (2002)
[7]: F. Weitzer, M. Potel, H. Noël, P. Rogl, J. Solid State Chem. **111**, 267-275, (1994).
[8]: P. Rogl, G. André, F. Weitzer, H. Noël., J. Magn. Magn. Mater **191,** 291-300, (1999).
[9]: T.B. Massalski, H. Okamoto, P.R. Subramanian, L. Kacprzak (Eds.), Binary Alloy Phase Diagrams, second ed., ASM International, **1–3,**(1990).
[10]: W.C.Thurber, R.J.Beaver, American Nuclear Society Meeting, (1957) (Pittsburgh).

Formation and structural properties of novel ternary intermetallics U_3TGe_5 with *T*= transition metal of columns 4, 5 and 6.

N. Brisset[1], C. Moussa[1], G. Chajewski[2], H. Noel[1], A. P. Pikul[2], M. Pasturel[1], P. Boulet[3], O. Tougait[1, 4]

1 Institut des Sciences Chimiques de Rennes, UMR CNRS 6226, Université Rennes 1, Campus de Beaulieu, 35042 Rennes Cedex, France, e-mail : brisset.nicolas@univ-rennes1.fr
2 Institute of Low Temperature and Structure Research, ul. Okólna 2, 50-422 Wrocław, Poland
3 Institut Jean Lamour, UMR CNRS 7198, Université de Lorraine, 54011 Nancy, France.
4 Unité de Catalyse et de Chimie du Solide, UMR CNRS 8181, Université de Lille, Campus Scientifique, 59655 Villeneuve d'Ascq.

The anti- Hf_5CuSn_3 (space-group $P6_3/mcm$, no. 193) structure type [1] can be regarded as an ordered variant of the Ti_5Ga_4 type which is adopted by the binary compounds U_5Ge_4 [2], U_5Sn_4 [3] and U_5Sb_4 [*4*]. The ternary derivatives were first observed for the uranium antimonides, U_3TSb_5 with *T*= Ti, V, Cr, Mn [*5*]. This family of antimonides was later expanded to *T*= Sc, Zr, Nb and Hf [*6,7]* but also to the titanium based germanide U_3TiGe_5 and stannide U_3TiSn_5 [*8*].

On a structural point of view, the cell volume varies only slightly with the *T* element within the antimonide family, but in a much larger scale when the *p*-element (*X*) is changed from Sb (442.1 $Å^3$) or Sn (449.2 $Å^3$) to Ge (357.01 $Å^3$) within the U_3TiX_5 series.

Despite these changes in cell volumes, inducing a modification of the U-U and U-Ligand distances, and the evolutions in the electronic configuration upon the substitution of the *T* or *X* element, all these U_3TX_5 intermetallics are ferromagnets with T_c ranging from 65 K for U_3TiSn_5 [*8*] to 160 K for U_3TiSb_5 [*5*].

As this structure can accommodate most of early transition metals, we have attempted to and successfully synthesize the U_3TGe_5 compounds with *T*= V, Cr, Zr, Nb, Mo, Hf, Ta and W.

All samples were prepared by arc-melting under argon atmosphere the constituent elements (purity > 99 % in all cases). Two types of subsequent heat treatments were performed, (*i*) either into sealed silica tubes in electrical resistance furnace at 1173 K for about 200 h or (*ii*) in a high frequency furnace between 1373 and 1773 K for 3 h. Differential Thermal Analyses (DTA) measurements were performed up to 1823 K, with heating / cooling rates from 5 to 20 K min^{-1} under Ar flood. All samples were afterwards analyzed by powder X-ray diffraction (XRD) and by Scanning Electron Microscopy coupled to Energy Dispersive Spectroscopy (SEM-EDS).

For the 8 transition metals investigated, SEM-EDS analyses always evidence after annealing the presence of a phase with different levels of purity, but with elemental composition close to 33.3U-11.1*T*-55.6Ge, as expected for a U_3TGe_5 stoichiometry. Powder XRD confirms the formation of compounds isotypic to U_3TiGe_5. As an example, the XRD pattern and the SEM microview of U_3MoGe_5 are given in Fig. 1.

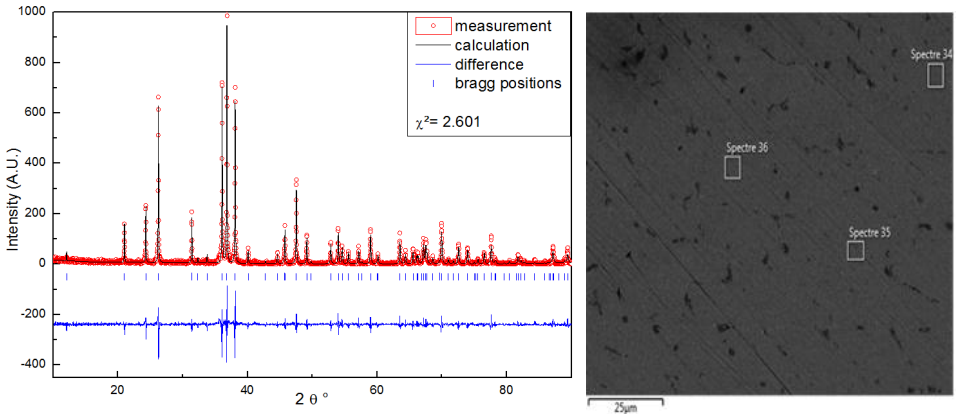

Figure 1 Left panel: X-ray diffraction pattern of U_3MoGe_5 refined with the anti-Hf_5CuSn_3 structure type. Right panel: Backscattered electron mode SEM image showing the formation of U_3MoGe_5 (main grey area) as well as $U_2Mo_3Ge_4$ as an impurity (black dots).

DTA measurements performed on this sample (fig. 2) exhibits characteristic features of a peritectic decomposition upon heating as evidence by a sharp endothermic peak at 1677 K, followed by a broad endothermic shoulder corresponding to the full melting of the sample. This process is reversible upon cooling, even for rapidly solidified samples, justifying the presence of U_3MoGe_5 as majority phase in as-cast samples. Similar thermal behaviours are observed for other U_3TGe_5 samples, suggesting a peritectic formation for all compounds of this series.

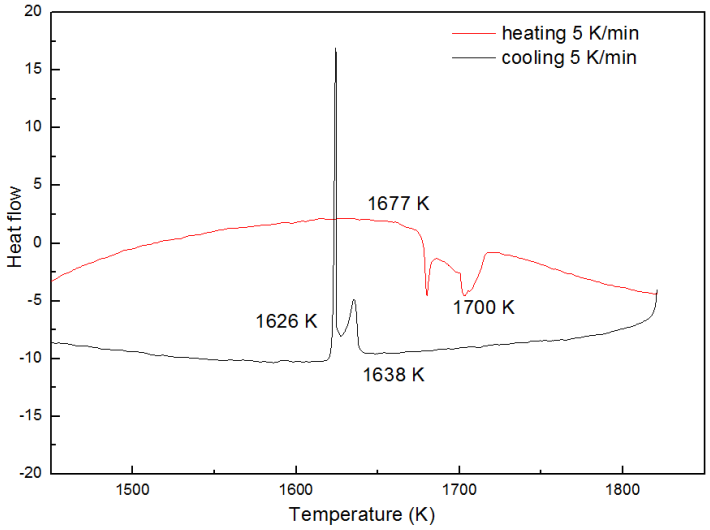

Figure 2: DTA measurement on U_3MoGe_5

Refinements of the lattice parameters by global profile matching, indicate an almost linear and moderate increase of the cell parameters and cell volume with the metallic radius of the transition metal [*9*] , in good agreement with the previous results in the antimonides.

Single crystal X-ray diffraction experiments performed on U_3TGe_5 for *T*=V, Cr and Mo confirmed the anti-Hf_5CuSn_3 crystal structure assigned from powder XRD. Precise atomic positions were thus determined and subsequently reliable U-U and U-*L* (with *L*= *T*, Ge) interatomic distances. The shortest U-U distances are found along uranium zig-zag chains along the *c*-axis. They range between 3.4 and 3.5 Å, which compare the smallest values suggested by Hill for the occurrence of magnetic ordering [*10*].

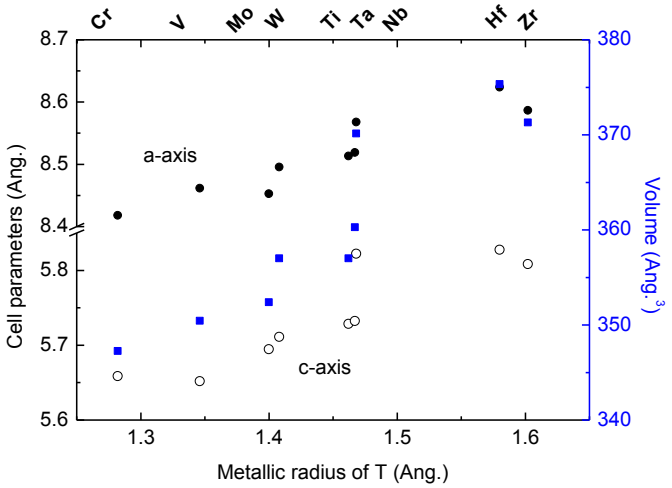

Figure 3: U_3TGe_5 cell parameters (black and empty circles stand for *a* and *b* parameters respectively) and volume variation (blue squares) vs. metallic radius of the transition element.

The magnetic properties measured for the samples with *T*= V, Cr and Mo do not exhibit ferromagnetism but a variety of behaviours, ranging from paramagnetism for *T* = Cr and Mo to antiferro- or ferrimagnetism for *T* = V (fig. 4). In the latter, a large metamagnetic transition is observed above the critical field Hc = 2 T for T = 2 K. In the germanide series, the column of the transition element seems to play a more important role than in the antimonide one.

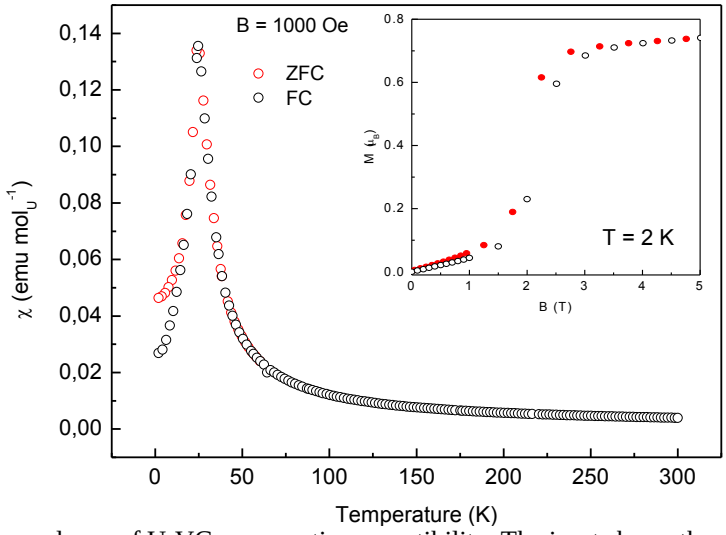

Figure 4 : Temperature dependence of U_3VGe_5 magnetic susceptibility. The inset shows the magnetic field dependence of the magnetization.

In this presentation, we will detail the syntheses of the 8 investigated U_3TGe_5 compounds, their formation path, thermodynamic behavior and structural parameters obtained either by powder or single-crystal diffraction. The magnetic properties for *T* = V, Cr, Mo will be presented and discussed, trying to establish relations with the structural parameter. Details about their low temperature electronic features will be given in a separated contribution presented by G.Chajewski.

[1] W. Rieger, H. Nowotny and F. Benesovsky, *Monatshefte für Chemie* **96**, 232 (1965)
[2] P. Boulet, M. Potel, G. André, P. Rogl and H. Noël, *Journal of Alloys and Compounds* **283**, 41 (1999).
[3] A. Palenzona and P. Manfrinetti, *Journal of Alloys and Compounds* **221**, 157-160 (1995).
[4] J.A. Paixao, J. Rebizant, A. Blaise, A. Delapalme, J.P. Sanchez, G.H. Lander, H. Nakotte, P. Burlet and M. Bonnet, *Physica B* **203**, 137 (1994).
[5] M. Brylak, W. Jeitschko, *Zeitschrift Fur Naturforschung Section B-a Journal of Chemical Sciences* **49**, 747-752 (1994).

[6] A. Mar, O. Tougait, M. Potel, H. Noël, E. B. Lopes,. *Chemistry of Materials* **18**, 4533-4540 (2006).
[7] A. V. Tkachuk, C. P. T. Muirhead, A. Mar,. *Journal of Alloys and Compounds* **418**, 39-44 (2006).
[8] P. Boulet, G. M. Gross, G. André, F. Bourée, H. Noël,. *Journal of Solid State Chemistry* **144**, 311-317 (1999).
[9] E. Teatum, K. A. Gschneidner, J. Waber, *Compilation of calculated data useful in predicting metallurgical behavior of the elements in binary alloy systems*, **2345** (1960) (Los Alamos Scientific Laboratory of the University of California),.
[10] H. Hill, in *Plutonium and other actinides*, Ed. W. Miner (1970)(AIME, New York).

45èmes Journées des Actinides, April 15-19, 2015, Prague-Průhonice, Czech Republic

Physical properties of U_3TGe_5 (T = V, Cr, Mo) and $U_3Al_{2-x}Ge_{3+x}$ ($-0.3 \leq x \leq 1.5$) compounds

G. Chajewski[1], C. Moussa[2], N. Brisset[2], Z. El Sayah[2], V. Dorcet[2], H. Noël[2], M. Pasturel[2], P. Boulet[3], A. P. Pikul[1], D. Kaczorowski[1], O. Tougait[2,4], B. Stepnik[5]

[1] *Institute of Low Temperature and Structure Research, Polish Academy of Sciences, ul. Okólna 2, 50-422 Wrocław, Poland, e-mail: G.Chajewski@int.pan.wroc.pl*
[2] *Institut des Sciences Chimiques de Rennes, Chimie du solide et Matériaux, UMR CNRS 6226, Université Rennes 1, Campus de Beaulieu – Bât.10A, 35042 Rennes Cedex, France*
[3] *Institut Jean Lamour, UMR CNRS 7198, Université de Lorraine, 54011 Nancy, France*
[4] *Unité de Catalyse et de Chimie du Solide, UMR CNRS 8181, Université de Lille, Campus Scientifique*
[5] *AREVA, 10 rue Juliette Récamier 69 456 Lyon Cedex 06, France*

Polycrystalline samples of U_3TGe_5 and $U_3Al_{2-x}Ge_{3+x}$ ($-0.3 \leq x \leq 1.3$), crystallizing in closely related derivatives of the AlB_2-type structure, were studied by means of magnetization, specific heat and electrical resistivity measurements. U_3VGe_5 was found to order antiferromagnetically at about 26 K, while U_3CrGe_5 and U_3MoGe_5 remain paramagnetic at least down to 2 K. All the 3–1–5 phases studied exhibit moderately enhanced electronic specific heat (of about 110–170 mJ/($Kmol_U$)) and temperature dependent electrical resistivity characteristic of spin fluctuators. The $U_3Al_{2-x}Ge_{3+x}$ compounds are ferromagnetically ordered with the Curie temperature decreasing with increasing Ge content from 70 K for $x = 0.3$ down to 27 K for $x = 1.5$.

Local-Fermi-Liquid Behavior in Dilute Uranium Alloys $Th_{1-x}U_xBe_{13}$ ($x \leq 0.11$)

N. Miura[1], T. Yanagisawa[1], H. Hidaka[1], C. Tabata[1],
S. Mombetsu[1], S. Yamazaki[1], Y. Shimizu[2], and H. Amitsuka[1]

[1]*Graduate School of Science, Hokkaido University, Sapporo 060-0810, Japan,*
e-mail: muller@phys.sci.hokudai.ac.jp
[2]*ISSP, The University of Tokyo, Kashiwa 277-8581, Japan*

We have performed magnetic susceptibility χ, electric resistivity ρ, and specific heat C measurements on single-crystalline $Th_{1-x}U_xBe_{13}$ (x = 0, 0.01, 0.07, and 0.11) at low temperature down to 2 K. Both $ThBe_{13}$ and UBe_{13} crystallize in $NaZn_{13}$-type structure (space group: O_h^6) as shown in Fig. 1. UBe_{13} is known as a heavy fermion superconductor (T_c ~ 0.85 K) [2], where 5*f* electrons play a dominant role and various peculiar features have so far been found: a possibility of broken time-reversal symmetry [3], unusual temperature dependence of upper critical field [4], and so on. Despite much research effort, however, there is no consensus concerning the symmetry of the gap structure and the parity of the Cooper-pair. One major reason for the difficulty in understanding the nature of the superconductivity (SC) in UBe_{13} would be the lack of basic information on the unusual metallic behavior observed in the normal state: First, for example, $\rho(T)$ shows a monotonous increase with decreasing temperature from room temperature with double hump-like anomalies [2], which is remarkably different from the conventional behavior in heavy-fermion system. ρ reaches ~ 200 μΩcm just above T_c, and then suddenly drops to zero [2]. Secondly, $C(T)$ shows a $-\ln T$ behavior, which is extremely robust against the magnetic field of over 12 T[4, 6]. Thirdly, $\chi(T)$ shows a $T^{1/2}$ dependence below ~ 10 K, although it obeys normal Curie-Weiss law at high temperature [5, 7]. Some of these features significantly differ from the prediction of Landau's Fermi-liquid (FL) theory and thus referred to as non-Fermi-Liquid (NFL) behavior.

We synthesized dilute uranium alloys $Th_{1-x}U_xBe_{13}$ ($x \leq 0.11$) in order to obtain the following basic information on this system: (i) the valency of uranium ions and the crystalline-electric-field (CEF) energy scheme, in particular, the CEF ground state, (ii) electric correlations on a single-uranium-site, and (iii) the inter-uranium-site correlations. Regarding the point (ii), Cox proposed a theory of unconventional *electric quadrupolar Kondo Effect*, by assuming the non-Kramers doublet Γ_3 to be the CEF ground state.

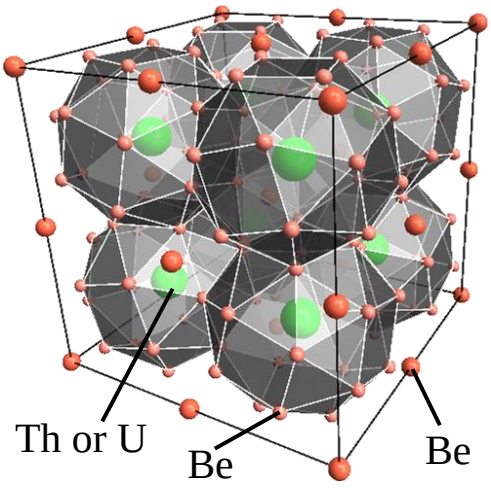

Fig. 1. The crystal structure of $ThBe_{13}$ and UBe_{13}. The lattice constants were previously reported as a ~ 10.394 Å for $ThBe_{13}$ and a ~ 10.256 Å for UBe_{13} [1].

We synthesized single-crystalline $Th_{1-x}U_xBe_{13}$ for compositions x = 0, 0.01, 0.07, 0.11, by using an Al-flux method, which is recognized as a means of growing high-purity single-crystals. Fig. 2 shows the results of powder X-ray diffraction. From the X-ray diffraction analysis, we obtained the lattice constant of a ~ 10.39(1) Å, which is approximately the same as the value of $ThBe_{13}$ reported in the previous study [1]. Secondary phase was not detected within the experimental accuracy of 0.3%. From the x dependence of magnetic susceptibility, we estimated the single-uranium-site contribution to the magnetic susceptibility, χ_f, as shown in Fig. 3. At higher temperatures above ~ 100 K, χ_f obeys the Curie-Weiss law with the effective moment μ_{eff} ~ 3.7(3) μ_B/U, and the Curie-Weiss temperature θ_p ~ –50(5) K. Below ~ 20 K, on the other hand, χ_f exhibits a deviation from Curie-Weiss law and shows a tendency to saturate at a value of χ_f ~ 0.025(5) emu/molU. Figure 4 shows the single-uranium-site contribution to the electric resistivity, ρ_f. It increases with decreasing temperature in the high temperature range above ~ 70 K. This behavior is one of the prominent characteristics of the Kondo effect. Below ~ 70 K, on the other hand, the Kondo-like behavior appears to vanish, showing a gradual decrease in ρ_f with decreasing temperature. Below ~ 20 K, ρ_f is well described by $\rho_0 + AT^2$ with a moderately enhanced A value of ~ 0.1 μΩcm/K^{2}molU. From the specific-heat measurement, we found that the value of C/T at the lowest temperature (~ 1.9K), increases roughly in proportion to x. The rate of increase is estimated to be ~ 0.15(2) J/K^{2}molU (Fig.5). All the measured quantities follow the FL theory, and we didn't find any indication of the NFL behavior suggestive of the quadrupolar Kondo effect in this dilute-alloy system.

The Curie-Weiss law in χ_f, the negative value of θ_p, and the Kondo-like behavior in ρ_f indicate the presence of the Kondo effect above ~ 70 K probably due to a CEF excited level with a magnetic moment. On the other hand, the clear drop in ρ_f below ~ 70 K is definitely different from the conventional single-impurity Kondo effect, which should show ρ_f saturating with the unitary limit as $T \rightarrow 0$. The observed low-T behavior clearly indicates that the Kondo scattering is suppressed below ~ 70 K. Since the system is not a so-called periodic Kondo lattice but a diluted magnetic alloy, we can conclude that a (moderately-heavy) local-Fermi-liquid (LFL) occurs in $Th_{1-x}U_xBe_{13}$ in a different manner from the conventional Kondo effect. We believe that the valency of uranium would be quadrivalent ($5f^2$), and the CEF ground state would be Γ_1 singlet, at least in $Th_{1-x}U_xBe_{13}$ ($x \leq 0.11$). The high-temperature Kondo-like behavior might occur by involving the excited CEF (magnetic) state: Γ_4 or Γ_5. We will discuss the observed LFL behavior in $Th_{1-x}U_xBe_{13}$ ($x \leq 0.11$) and its

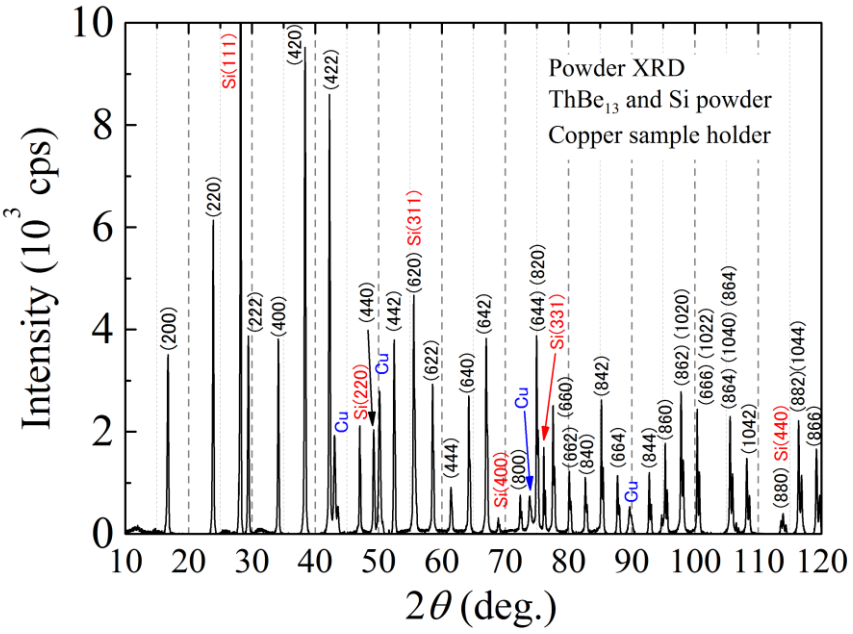

Fig. 2. The result of the powder X-ray diffraction on $ThBe_{13}$. For the purpose of refinement of the analysis, small amount of powdered Silicon were mixed into the sample. Contributions of the copper (sample holder) are also seen. Measurements for other composition x were performed as well.

relationship to the NFL in UBe_{13} in terms of the theoretical predictions based on the competition between two different ground states, a CEF singlet and the Kondo-Yosida singlet [8-10].

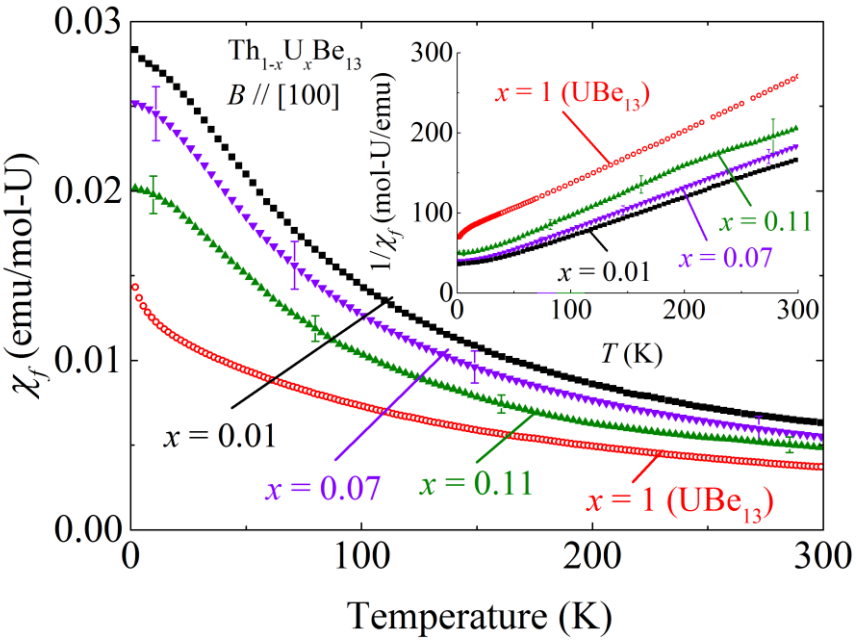

Fig. 3. The temperature dependence of single-uranium-site contribution to the magnetic susceptibility of $Th_{1-x}U_xBe_{13}$ for x = 0.01, 0.07, 0.11. The magnetic susceptibility of UBe_{13} is also plotted. Inset shows the inverse of them. For x = 0.07 and 0.11, we performed plural measurements on different pieces cut out of the same uranium concentration sample. The error bar shows the dispersion of U concentration.

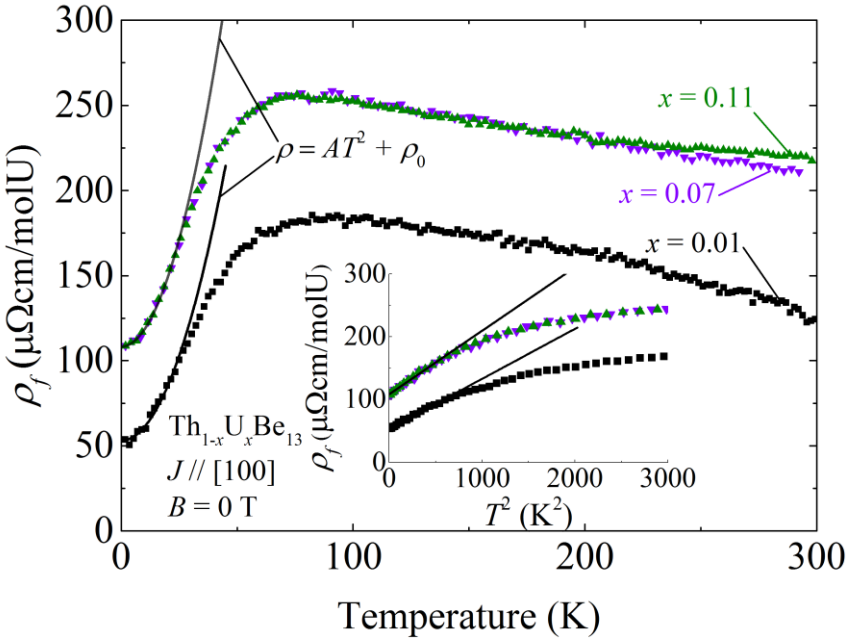

Fig. 4. The temperature dependence of single-uranium-site contributions to the electric resistivity of $Th_{1-x}U_xBe_{13}$ for x = 0.01, 0.07, 0.11. Inset shows T^2 dependence of them. The solid line represents the fitting curve of quadratic T dependence below ~ 20 K.

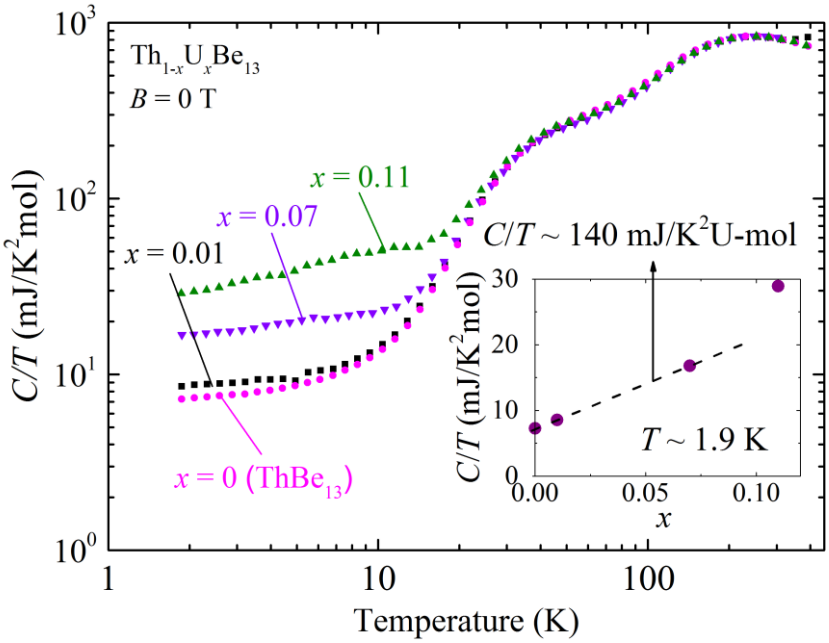

Fig. 5. log T vs log(C/T) of $Th_{1-x}U_xBe_{13}$ for x = 0, 0.01, 0.07, 0.11. Inset shows x dependence of C/T (T ~ 1.9 K).

References

[1] J. S. Kim, B. Andraka, C. S. Jee, S. B. Roy, and G. R. Stewart, *Phys. Rev. B* **16**, 11073 (1990).
[2] H. R. Ott, H. Rudlgier, Z. Fisk and J. L. Smith, *Phys. Rev. Lett.* **50**, 1595 (1983).
[3] R. H. Heffner, J. L. Smith, J. O. Willis, P. Birrer, C. Baines, F. N. Gygax, B. Hitti, E. Lippelt, H. R. Ott, A. Schenck, E. A. Knetsch, and J. A. Mydosh, and D. E. MacLaughlin, *Phys. Rev. Lett.* **65**, 2816 (1990).
[4] M. B. Maple, J. W. Chen, S. E. Lambert, Z. Fisk, J. L. Smith, H. R. Ott, J. S. Brooks, and M. J. Naughton, *Phys. Rev. Lett.* **54**, 477 (1985).
[5] G.R. Stewart, *Rev. Mod. Phys.* **56**, 755 (1984).
[6] P. Gegenwart, C. Langhammer, R. Helfrich, N. Oeschle, M. Lang, J. S. Kim, G. R. Stewart, and F. Steglich, *Physica C* **408-410**, 157 (2004).
[7] M. McElfresh, M. B. Maple, J. O. Willis, D. Schiferl, J. L. Smith, and Z. Fisk, *Phys. Rev. B* **48**, 10395 (1993).
[8] S. Yotsuhashi, K. Miyake and H. Kusunose, *J. Phys. Soc. Jpn.* **71**, 389 (2002).
[9] Y. Shimizu and O Sakai, *J. Phys. Soc. Jpn.* **74**, 27 (2005).
[10] S. Nishiyama, PhD. Thesis (2013), unpublished.

Neutron scattering facilities at PSI and ILL. Case of Study: Novel superconducting and magnetic phases in $CeCoIn_5$ and $Nd_{0.05}Ce_{0.95}CoIn_5$

Jorge Gavilano
Paul Scherrer Institut, Switzerland

We present here the neutron scattering facilities of Paul Scherrer Institut in Switzerland and briefly describe the possibilities open to the users from outside Switzerland. As an example of our studies both at PSI and ILL Grenoble, we discuss the results for the intriguing properties of the tetragonal intermetallic compounds $CeCoIn_5$ and $Nd_{0.05}Ce_{0.95}CoIn_5$ and explore their phase diagrams. These materials display unconventional superconductivity, with *d*-wave symmetry order parameter, that develops below 2.3 K. In the presence of an external magnetic field a large anisotropy of the order parameter is revealed. For $CeCoIn_5$ in fields applied along the basal plane a magnetic phase, the Q-phase, develops at very high fields and low temperatures, within the superconducting phase. The propagation vector of the magnetic structure is $\boldsymbol{q}$ = (0.45, 0.45, ½). Careful analysis of the magnetic domains shows that they are driven by a secondary superconducting phase of probably *p*-symmetry. For $N_{0.05}Ce_{0.95}CoIn_5$ a magnetic phase develops at zero-field with identical propagation vector. However, this magnetic phase has a very different behavior as the Q-phase in $CeCoIn_5$.

Nanostructured Bilayered Uranium Oxide- Iron Oxide Thin Films for Solar Hydrogen Production

Jennifer Leduc, Rajitha Ravithas, Prof. Dr. Sanjay Mathur

Institute of Inorganic Chemistry, University of Cologne, Greinstrasse 6, 50939 Cologne, Germany, jleduc@smail.uni-koeln.de

In order to reduce the amount of uranium waste, its reuse is discussed in the context of semiconductor materials[1] as well as catalysts for thermochemical water splitting[2], destruction of air pollutants[3,4] and CO_2 activation[5]. Herein, we present the generation of uranium oxide materials via plasma enhanced chemical vapor deposition (PE-CVD) and their use in photoelectrochemical water splitting devices. Recently, we have demonstrated the use of substituted heteroarylalkenolates for obtaining air-stable and volatile uranium (IV) and (VI) precursors.[6] Due to its relatively low sublimation temperature (130 °C, 10^{-3} mbar), its moderate decomposition temperature and preformed U=O bonds, hexavalent uranium compound $UO_2(DMOTFP)_2(DMOTFP\text{-}H)$ **1** was used for the PE-CVD experiments.

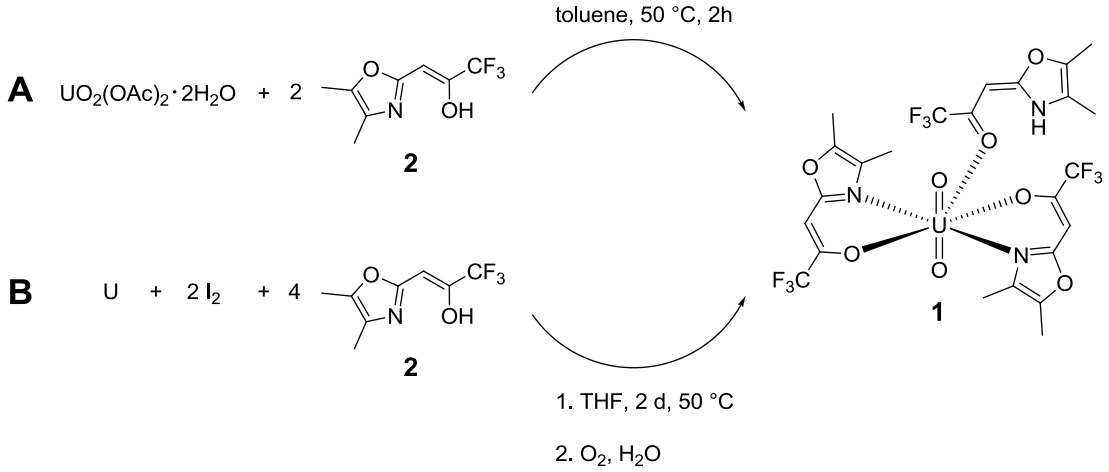

Fig. 1. Two reaction pathways for the synthesis of the uranium (VI) compound **1**.

Since bulk UO_2 and UO_3 materials are unattractive photoelectrodes due their rather low conductivity we deposited uranium oxide thin film nanostructures thus ensuring fast diffusion of the holes to the surface of the photoelectrode and preventing charge recombination with electrons. To avoid dissolution of uranium oxide thin films in basic electrolytes, we coated them with hematite (α-Fe_2O_3) as protective layer via chemical vapor deposition (CVD) using $[Fe(O^tBu)_3]_2$ as precursor.

References

[1] T. T. Meek, v. Roedern, *Vacuum* **83**, 226-228 (2009).
[2] I. Al-Shankiti, Y. Al-Salik, F. Al-Otaibi, H. Idriss, *Top. Catal.* **56**,1129-1138 (2013).
[3] G. J. Hutchings, C. S. Heneghan, I. D. Hudson, S. H. Taylor, *Nature* **384**, 341-343 (1996).
[4] Z. T. Zhang, M. Konduru, S. Dai, S. H. Overbury, *Chem. Commun.*, 2406-2407 (2002).
[5] A. R. Fox, S. C. Bart, K. Meyer, C. C. Cummins, *Nature* **455**, 341-349 (2008).
[6] L. Appel, J. Leduc, C. L. Webster, J. W. Ziller, W. J. Evans, S. Mathur, *Angew. Chem.* **126** (2014).

Exchange bias effect in CaF_2-based UO_2/Fe_3O_4 thin films

Evgeniya Tereshina[1], Zhaohui Bao[2], Ladislav Havela[3], Anna Mackova[4], Thomas Gouder[5], Roberto Caciuffo[5]

[1]*Institute of Physics ASCR, Na Slovance 2, 18221 Prague, Czech Republic.*
[2]*PANalytical B.V., Lelyweg 1 (7602 EA), PO Box 13, 7600 AA Almelo, The Netherlands.*
[3]*Department of Condensed Matter Physics, Faculty of Mathematics and Physics, Charles University, Prague 2, Czech Republic.*
[4]*Tandetron Laboratory, Nuclear Physics Institute of Academy of Sciences of the Czech Republic, Rez near Prague, 25068 Czech Republic.*
[5]*European Commission, Joint Research Centre (JRC), Institute for Transuranium Elements (ITU), Postfach 2340, DE-76125 Karlsruhe, Germany.*

Magnetic exchange bias (EB) effect is a phenomenon resulting from exchange coupling between a ferromagnet and an antiferromagnet at their interface [1]. The EB is set by cooling through the Néel temperature of the antiferromagnet in the presence of the magnetic field. The magnetic hysteresis loop of an exchange-biased bilayer is shifted along the field direction. This property has become of a great technological value for applications in magnetic sensors based on spin-valves or tunnel junctions [2]. Having in mind the strong spin-orbit coupling and enormous magnetic anisotropy displayed by some actinide compounds, we employ uranium-based antiferromagnets to study exchange anisotropy effects in thin magnetic films. The crystal structure and magnetism of bilayers composed of an antiferromagnetic UO_2 (bulk Néel temperature 30.8 K) with ferrimagnetic Fe_3O_4 are investigated in this work. A reference UO_2/Fe sample has been also prepared and studied. We used reactive sputter deposition from metallic U and Fe targets to produce the samples. The samples were grown on commercially available CaF_2 (100) and (111) substrates (CaF_2 has an identical crystal structure and a lattice parameter within 0.5% of UO_2). The stoichiometry of each deposited layer was controlled by X-ray Photoelectron Spectroscopy (XPS). A magnesium cap was deposited for protection on top of each sample. The samples were characterized using X-ray diffraction.

Due to the matching lattice parameters of UO_2 and CaF_2, the films grew epitaxially in the [100] (or [111]) direction when the (100) (or (111)) CaF_2 substrates were used. The structures were further characterized by means of the Rutherford Backscattering Spectroscopy (RBS), which showed no intermixing at the interface (within the depth resolution 1 nm). Very pronounced ion channelling characteristics proved high crystallinity (low defect concentration) of the UO_2 layer, which is actually better than that of the (100) CaF_2 substrate. The spectra obtained showed well-separated signals from UO_2 and magnetite. A channelling was observed also for the Fe_3O_4 layer, but considerably more defects/disorder was found, which could be perhaps related to a combined twinning [3] effect and monoclinic distortion below Verwey transition (120 K), as the samples had been subjected to thermal cycling during the prior magnetic study.

The UO_2/Fe_3O_4 bilayers with magnetic layers grown in different directions were examined using a SQUID magnetometer. Hysteresis loops obtained after field cooling in a magnetic field of 20 kOe showed strong exchange bias with the maximum effect reaching 1600 Oe at 5 K for the UO_2/Fe_3O_4 sample with the thinnest magnetite layer of t_{FM} = 80 Å on a CaF_2 (100) substrate. The EB obtained for the same sample of UO_2/Fe_3O_4 on CaF_2 [111] exceeds this value considerably, 2100 Oe (see Fig. 1). Similar trend was found in the samples with larger t_{FM}'s. Interestingly, exchange bias did not vanish at the bulk Néel temperature of UO_2. Non-zero values of EB were observed up to 125 K. This is in line with our previous study of the $LaAlO_3$-based UO_2/Fe_3O_4 system [3], where exchange bias disappeared at 120 K, i.e. at the Verwey transition temperature in magnetite. At this temperature, the change of the magnetization direction from [111] to [100] takes place.

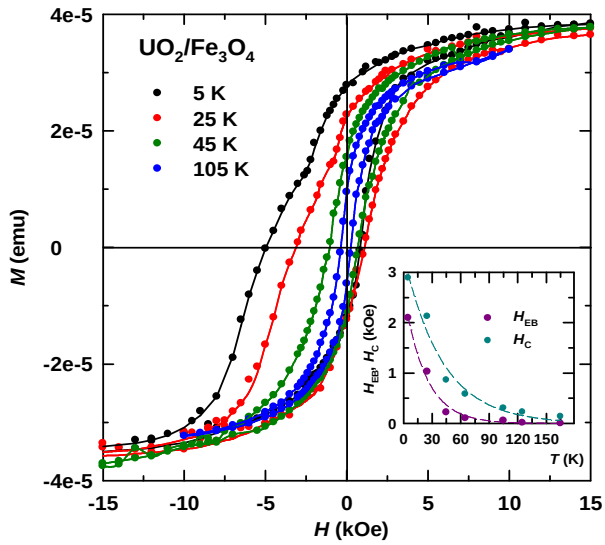

Fig. 1. Magnetization data for the UO_2/Fe_3O_4 bilayer on a CaF_2 (111) substrate with the 80-Å thick layer of magnetite at various temperatures after field cooling in 20 kOe. Inset: exchange bias field and coercive field vs. temperature for the same sample.

The reference UO_2/Fe sample with Fe as thick as approx. 80 Å showed no exchange bias for either [100] or [111] growth directions of UO_2 when measured within the film plane. An order of magnitude smaller effect as compared to UO_2/Fe_3O_4 was found in UO_2/Fe measured in the direction perpendicular to the film plane (perpendicular coupling). This is likely due to polycrystalline nature of the Fe layer and thus, weaker exchange coupling with UO_2 through a rougher surface as compared to Fe_3O_4. Furthermore, Fe itself is a soft magnetic material, while magnetite [3] alone shows a considerable exchange bias and coercivity.

The work has been supported by the Czech Science Foundation under the grant No. 13-25866P. The samples were prepared in the framework of the EARL project of the European Commission Joint Research Centre, ITU Karlsruhe. RBS measurements were carried out at the CANAM infrastructure of the NPI ASCR Rez supported through MŠMT project No. LM2011019.

References

[1] W. H. Meiklejohn AND C. P. Bean, “New magnetic anisotropy”, *Phys. Rev. B* **102**, 1413 (1956).
[2] B. Dieny, V. S. Speriosu, S. S. P. Parkin, B. A. Gurney, D. R. Wilhoit, and D. Mauri, “Giant magnetoresistive in soft ferromagnetic multilayers“, *Phys. Rev. B* **43**, 1297 (1991).
[3] E. A. Tereshina, Z. Bao, L. Havela, S. Daniš, C. Kuebel, T. Gouder, R. Caciuffo, “Exchange bias in UO_2/Fe_3O_4 thin films above the Néel temperature of UO_2”, *Appl. Phys. Lett.* **105**, 122405 (2014).

γ-U phase stabilized by combined T doping (T=Mo, Nb, Pt, Pd, Zr) and ultra-fast cooling

N.-T.H. Kim-Ngan[1,*], M. Paukov[2], S. Sowa[1], M. Krupska[1], I. Tkach[2], L. Havela[2]

[1]*Institute of Physics, Pedagogical University, Podchorazych 2, 30-084 Krakow, Poland*
[2]*Faculty of Mathematics and Physics, Charles University, Ke Karlovu 5, 12116 Prague, Czech Republic*
[*]*E-mail: tarnawsk@up.krakow.pl*

U-T alloys prepared by combined T doping (T=Mo, Nb, Pt, Pd, Zr) and ultrafast cooling have been investigated. UMo15, UPt15, UNb15 alloy (with 15 at. % Mo/Pt/Nb doping) exhibit a stable γ-U phase. However, the pure *bcc* structure was observed only in UMo15 splat [1]. The orthorhomic α-U phase is found to remain in U-Zr alloys with Zr content up to 30 at. %. The main outcome is that by using ultrafast cooling we can reduce the T content for stabilization of the γ-U phase down to room temperature without any additional sample treatment [2].

All U-T splats become superconducting with T_c in the range of 0.6 K – 2.1 K. The conventional BCS superconductivity was observed only in UMo15 alloy consisted of a pure cubic γ-U phase, revealed by an exceptional sharp resistivity jump at 2.1 K and λ-type specific-heat peak at T_c [3,4]. In other alloys, despite of the sharp resistivity jumps in the ρ(T) curves, only broad peaks in the C(T) curves were revealed at the superconducting transition. Our results also indicate that the superconductivity in the pure α-U splat is not a real bulk effect.

All splat-cooled alloys are very stable when exposing to ambient conditions without reversion to an α-U phase. In exposure to the hydrogen atmosphere, the α-U splat easily absorbs hydrogen even at room temperature forming UH_3. The U-T splats can absorb hydrogen only at high hydrogen pressure ($p(H_2) > 4.5$ bar) [5].

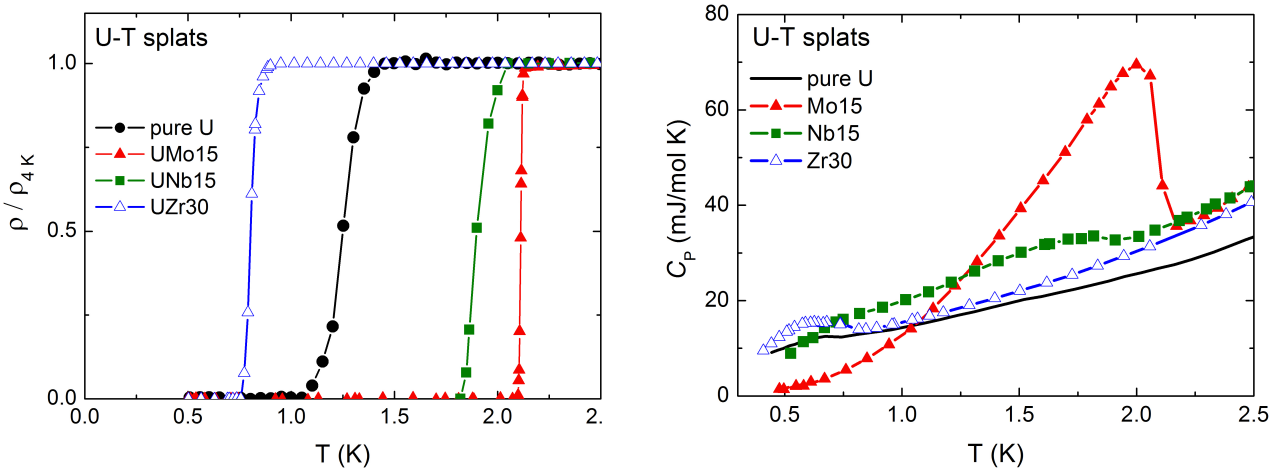

Figure 1. The superconducting phase transition of selected U-T splat-cooled alloys revealed by a resistivity jump and specific-heat anomaly.

Acknowledgement

This work was supported by the Czech Science Foundation under the grants No. P204/12/0285 and P204/10/0330. Experiments were performed at MLTL (http://mltl.eu/) supported within the program of Czech Research Infrastructures (project No. LM2011025). Participation of Krakow group was supported by the Czech-Polish cooperation in the scope of Czech-Polish project 7AMB14PL036 (9004/R14/R15).

References

[1] I. Tkach, N.-T.H. Kim-Ngan, S. Mašková, M. Dzevenko, L. Havela, A. Warren, C. Stitt, T. Scott, *J. Alloys and Compounds* **534**, 101 (2012).
[2] N.-T.H. Kim-Ngan, I. Tkach, S. Maškova, A.P. Goncalves, L. Havela, *J. Alloys and Compounds* **580**, 223 (2013).
[3] I. Tkach, N.-T.H. Kim-Ngan, A. Warren, T. Scott, A.P. Goncalves, L. Havela, *Physica C* **498**, 14 (2014).
[4] N.-T.H. Kim-Ngan, S. Sowa, M. Krupska, M. Paukov, I. Tkach, L. Havela, *Advances in Natural Sciences: Nanosci. Nanotechnol.* **6**, 015007 (2015) (IoP publishing).
[5] I. Tkach, S. Mašková, Z. Matej, N.-T.H. Kim-Ngan, A.V. Andreev, L. Havela, *Phys. Rev. B* **88**, 060407(R) (2013).

In situ XPS study of the evolution of chemical nature on U-Ti alloy surface during vacuum annealing

Peng Shi,[1] Lizhu Luo[2], Xiaolin Wang[1]

[1] *China Academy of Engineering Physics, Mianyang 621900 , Sichuan P. R. China, e-mail: shipeng@caep.cn*
[2] *Science and Technology on Surface Physics and Chemistry Laboratory, P.O. Box 718-35, Mianyang 621907, Sichuan China*

Many factors including reaction temperature, hydrogen pressure, pre-heating, the characteristics of the surface uranium oxide layer, the presence of gaseous impurities species in the hydrogen gas, the sample microstructure and so on would affect the uranium hydriding behavior[1]. It has been reported vacuum annealing could promote the surface reactivity of uranium toward hydriding. The effect of vacuum annealing on uranium has been studied by Thermal Desorption Spectroscopy (TDS)[2] and XPS[3], and is thought owing to the desorption of surface contaminants and modifications of the oxide over-layers. However, little is known about the effect of vacuum annealing on the surface character of U-Ti alloy. In this work, we have employed XPS to reveal the evolution of chemical nature for oxide over-layers on U-0.79Ti surface with vacuum annealing between room temperature and 700 ^{o}C.

The surface covered oxide layer was prepared by exposing the water-quenched U-0.79Ti disks in ambient air for ~24 hours and then transferred into the XPS analysis chamber. The high-energy resolution spectra were collected for the following elements: uranium (U 4f), titanium (Ti 2p), oxygen (O 1s), and carbon (C 1s).

The depth profile of the initial sample, which is collected at different time during the Ar^{+} sputtering, indicated that the surface is initially covered with a hyperstoichiometric UO_{2+x} layer and some organic contamination. No Ti peak is detected.

The results of the XPS spectra collected during the vacuum annealing from R.T to 700^{o}C is shown in Fig. 1. It is found that the UO_{2+x} outer oxide layer starts to be reduced to UO_2 at 200 ^{o}C. Between 300 and 400 ^{o}C, an oxycarbide (UO_xC_y) layer is observed due to the reaction between UO_2 and carbon. Above 500 ^{o}C, UO_xC_y decomposes and the surface covered oxide layer starts to be reduced to the metallic state, meanwhile, a thermal driven segregation of Ti to the surface is also observed above 500^{o}C.

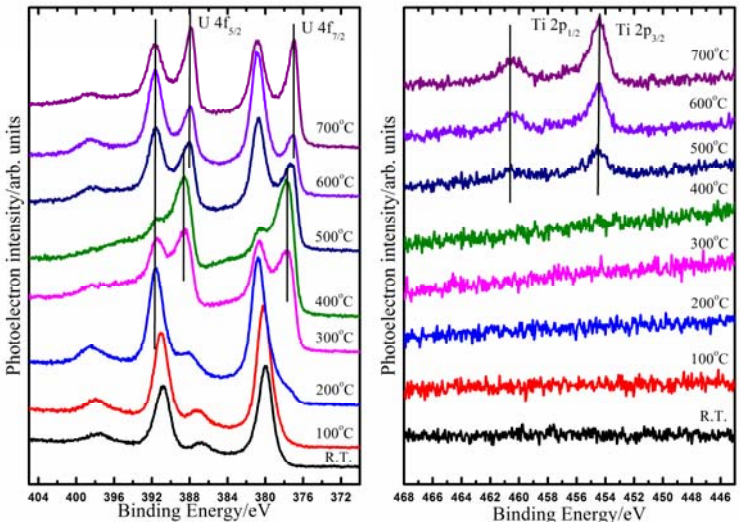

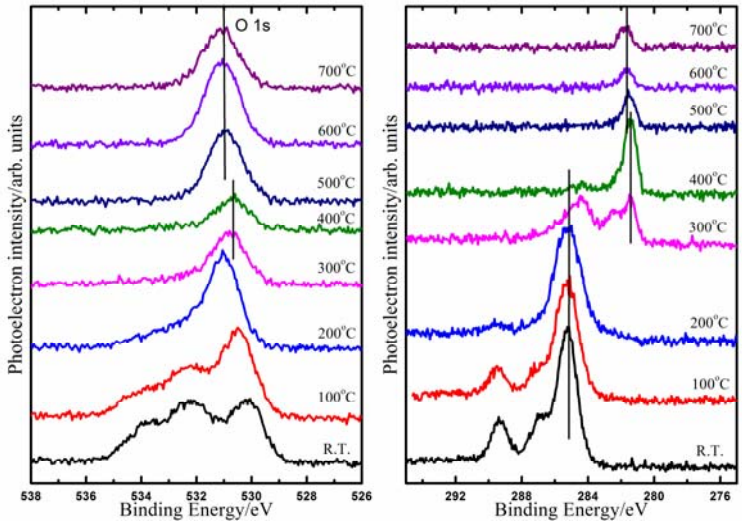

Fig. 1 Change in (a) U 4f ; (b) Ti 2p; (c) O 1s; (d) C 1s photoelectron spectrum from U-0.79Ti alloy by heating in vacuum from R.T to 700°C.

The depth profile which was collected after cooling the sample down to room temperature conformed the the surface segregation of titanium during the vacuum annealing. A possible Ti(C,O) solid solution-type structure was formed on the U-Ti alloy surface during the 500~700°C thermal heat-treatment[4]. And the evolution of the chemical nature of the U-Ti alloy surface during vacuum annealing is summarized in Fig. 2.

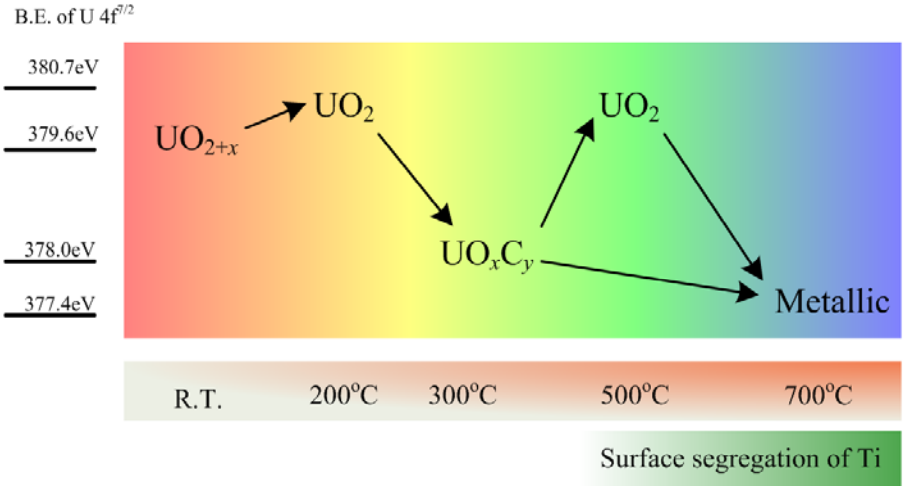

Fig. 2 The evolution of the U-0.79Ti alloy surface character during heating in vacuum.

References

[1] A. Loui, The Hydrogen Corrosion of Uranium: Identification of Underlying Causes and Proposed Mitigation Strategies, Report LLNL-TR-607653(2012), LLNL.

[2] A. Danon, J.E. Koresh, and M.H. Mintz, *Langmuir*, **Vol.**15, 5913–5920 (1999).

[3] J.P. Knowles, I.M. Findlay, D.A. Geeson and S.G. Bazley, *MRS Online Proceedings Library*, **Vol.**1444, 211-216(2012).

[4]J.M. Chappé, A.C. Fernandes, C. Moura, E. Alves, N.P. Barradas, N. Martin, J.P. Espinós and F. Vaz, *Surf Coat Technol,* **Vol.** 206, 2525–2534 (2012).

Hydride Growth Kinetics of U-Nb Alloy — the Role of Strain Energy

Li Ruiwen[1]

China Academy of Engineering Physics, P. O. Box 919-71, 621700 Mianyang, P. R. China, e-mail: ruiwenli@163.com

To study the difference behavior of hydride growth kinetics of U, U-2.5%Nb and U-5.7%Nb(mass fraction), based on the strain energy theory, the deformation, stress and strain energy during the hydride growing were studied by finite element model(FEM), according to mechanical properties of the three U materials. As shown in Fig. 1, around the hydride, the deformation, cracks and ruptures occurred, which are due to the difference of density between UH_3 and U. Because the density of U is 18.9g/cm^3 , and that of UH_3 is 10.9g/cm^3 , accompanying with the volume expanding of formation UH_3, Uranium has been pressured by great much stress, and deformed constantly. The simulation deformation on matrix owing to hydride growing was displayed in Fig.2, which was the same as experiment observation showed in Fig.1. Elastic strain energy of U, U-2.5%Nb and U-5.7%Nb during hydride growth were calculated, seen in table 1.The results show that the formed strain energy due to hydride expansible growth in matrix display much difference for the three U materials. When hydride growing, the order of the strain energy value is U-5.7%Nb>U>U-2.5%Nb, which illuminates that U-2.5%Nb alloy is the most susceptible to hydrogen corrosion, and U is following, U-5.7%Nb the most anti-hydrogen-corrosion. The calculation results about the strain energy agree well with the hydride growth kinetics experimental results, which also show the hydride growth model is correct. The study approves that the formation of large strain energy due to volume change during hydride growing plays a very important role in the growth kinetics.

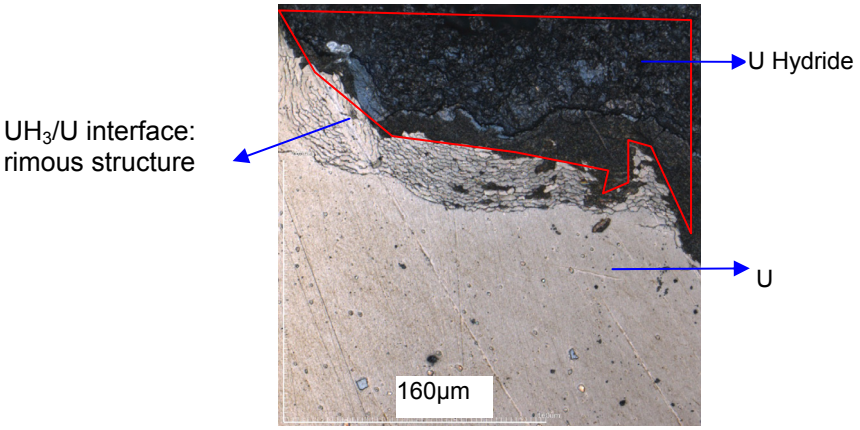

Fig.1 OM observation of deformation at

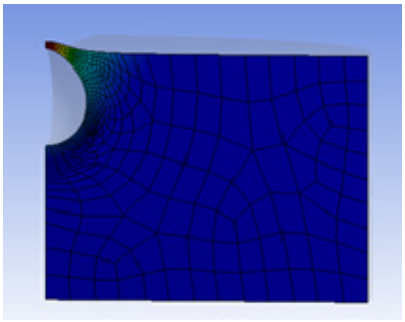

Fig.2 Deformation of hydride growth by FEM simulation

Table 1 Elastic strain energy of U, U-2.5%Nb and U-5.7%Nb during hydride growth

Materials	Max elastic energy/(kJ·mol^{-1})
U	28.3
U-2.5Nb	24.5
U-5.7Nb	63.28

45èmes Journées des Actinides, April 15-19, 2015, Prague-Průhonice, Czech Republic

Structure and magnetic properties of doped UH_3 -based hydrides.

M. Paukov, I. Tkach, Z. Matěj, D. Kriegner, L. Havela

Charles University, Ke Karlovu 5, 12116 Praha 2, Czech Republic, e-mail: Michael.Paukov@gmail.com

Interaction with hydrogen is an important issue related to application of uranium and its alloys. Any contact of α-U with H leads to formation of the stable allotropic form β-UH_3, a dark pyrophoric powder, formed via the metastable α-UH_3. Applications of U metal are typically based on its *bcc* form γ-U, because it is more malleable, ductile and stable with respect to irradiation effects than α-U. It is stable at high temperatures, but it can be retained as pure or in a α–γ composite using a doping (by Mo, Zr, Ti, Nb, Re, Ru, Pd, or Pt). Our aim was to explore the interaction of γ-U with different dopants with hydrogen. We found that U-Mo alloys do not absorb hydrogen at ambient pressure. Pressures of several bar induce a slow process of formation of hydrides, which can be characterized as $(UH_3)_{1-x}Mo_x$, and their structure corresponds to β-UH_3 with a grain size of 1 nm, i.e. almost amorphous phase. They not only retain the ferromagnetism of β-UH_3 ($T_C \approx 165$ K), but the ordering temperature even increases, exceeding 200 K. (Fig. 1.) Magnetic moments also increase, from 0.9 to 1.1 μ_B/U. [1].

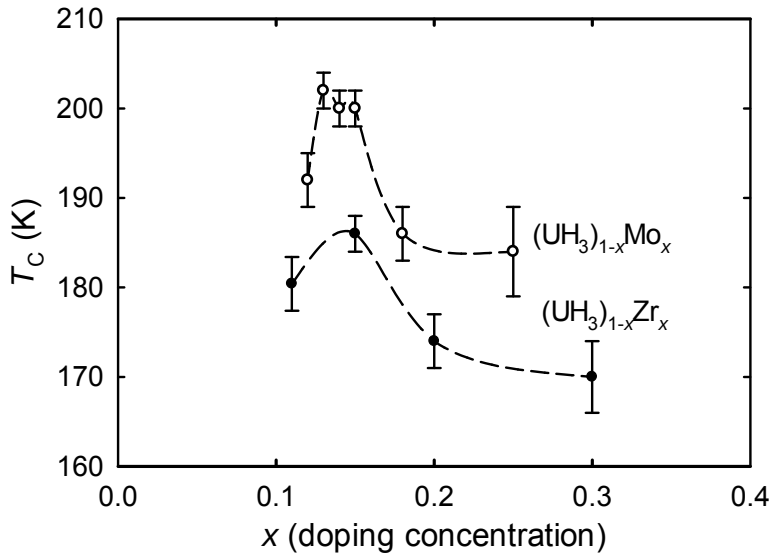

Fig. 1. Concentration dependence of the Curie temperature for the hydrides $(UH_3)_{1-x}Mo_x$ and $(UH_3)_{1-x}Zr_x$

Starting from the U-Zr alloys, we also obtained hydrides $(UH_3)_{1-x}Zr_x$ (analogous to stoichiometry UH_3). For low Zr concentrations we have a mixed crystal structure α-UH_3 and β-UH_3. With increasing x, the α-UH_3 phase, which is the *bcc* U structure filled with H, dominates (Fig. 2.). We assume that unlike smaller Mo atoms, bigger Zr atoms occupy U positions without problem.

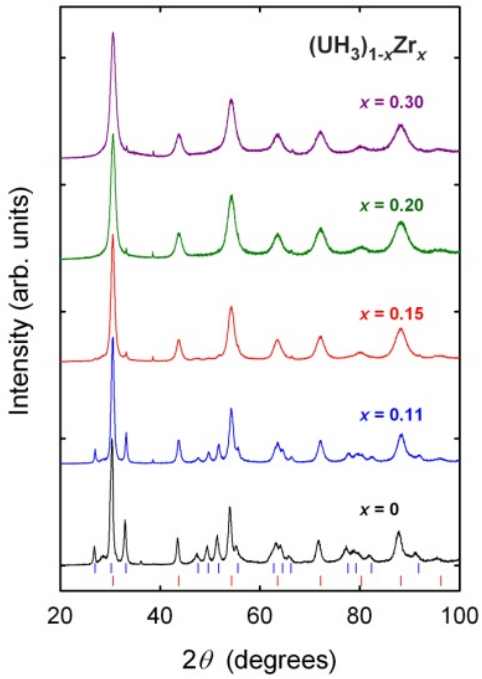

Fig. 2. X-ray diffraction patterns of the $(UH_3)_{1-x}Zr_x$ hydrides (λ =0.1540562 nm).

Our investigation of the hydrides in the α-phase shows that despite different crystal structures and U-U spacing, the properties of the α- and β-phases are very similar. Even T_C exhibits the same type of non-monotonicity, but the values do not exceed 190 K in the Zr case (Fig. 1.).

The coercive force increases with Zr doping up to 6 T for $(UH_3)_{0.70}Zr_{0.30}$, and it is in the same range for the U-Mo hydrides.

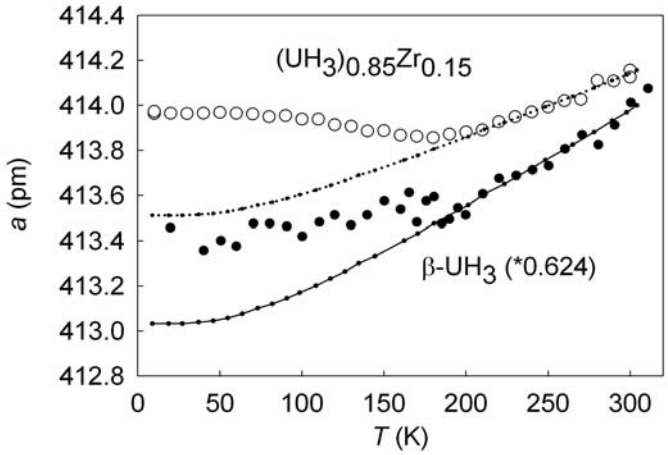

Fig. 3. Temperature dependence of the lattice parameter of $(UH_3)_{0.85}Zr_{0.15}$ compared with β-UH_3, (from Ref. 4) with extrapolated dependence from the paramagnetic state. The data on β-UH_3 are rescaled to match approximately those on $(UH_3)_{0.85}Zr_{0.15}$, which allows to compare mutually the magnetostriction and thermal expansion

To determine the spontaneous magnetostriction, the temperature dependence of the lattice parameter *a* was measured in the range 10 - 300 K using X-ray diffraction (Fig. 3.). The result can be compared with the data of β-UH_3 that was published in [4]. Fig. 3. indicates a large magnetostriction effect below 200 K, amounting to relative volume change $\Delta V/V = 3.2*10^{-3}$.

Besides those two types one has to include also hydrogenation of U_6T (T = Mn, Fe, Co, Ni), which leads to β-UH_3 type of hydrides, with T_C in the similar range below 200 K.

U_6FeH_{17} corresponding to $(UH_{\approx 2.8})_{0.86}Fe_{0.14}$ (magnetic moment 0.79 μ_B/U) and U_6CoH_{18} corresponding to $(UH_3)_{0.86}Co_{0.14}$ (magnetic moment 1.0. μ_B/f.u, i.e. 1.2 μ_B/U) have the Curie temperatures 173 K and 185 K respectively [2,3].

As next, we tested the hydrogenation of double doped samples, i.e. using different dopants besides Mo, which itself guarantees the amorphous structure of the hydrides. We assumed that the amorphous structure must be more accepting diverse sizes of dopant atoms. We indeed obtained the amorphous structure (Fig. 4.) for the hydrides with Ti, Fe, or Zr doping together with Mo, as $(UH_3)_{0.851}Fe_{0.142}Mo_{0.007}$, $(UH_3)_{0.78}Mo_{0.12}Zr_{0.10}$, $(UH_3)_{0.78}Mo_{0.12}Ti_{0.10}$.

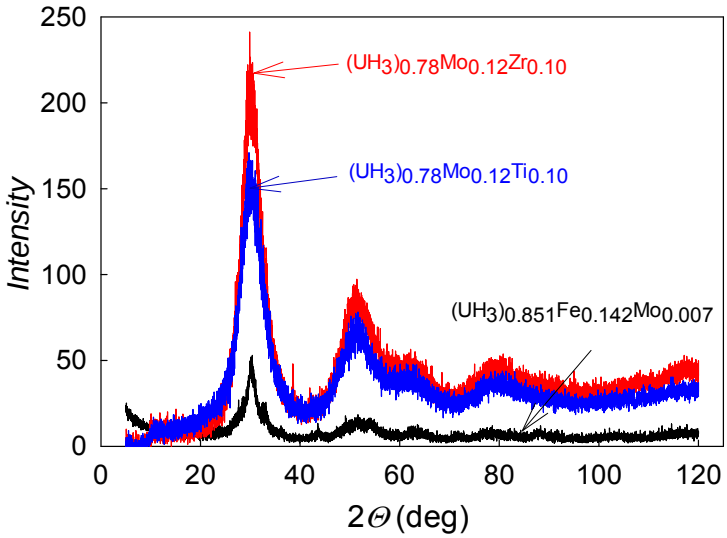

Fig. 4. X-ray diffraction pattern of the amorphous hydrides (λ =0.1540562 nm).

Our investigation of magnetic properties of such double doped hydrides shows ferromagnetic ordering with parameters only weakly depending on the dopants, as illustrated in Fig. 5.

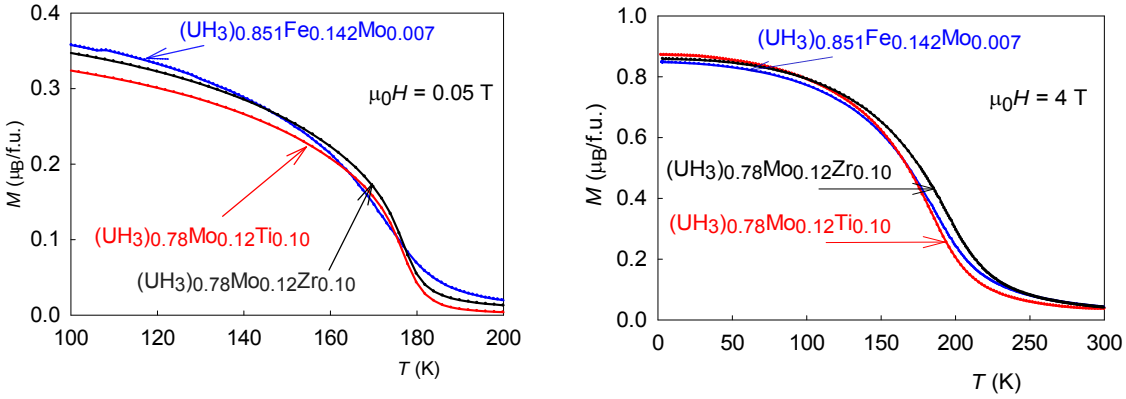

Fig. 5. Temperature dependence of magnetization: left - detail in for low magnetic fields illustrating the Curie temperatures, right - in $\mu_0 H$ = 4 T, illustrating the total magnetization

The addition of Zr enhances T_C more than addition of Ti, addition of Fe broadens the transition and enhances magnetization per U atom. The work will continue to establish limits of stability of the amorphous phase.

References

[1] I. Tkach, S. Maškova, Z. Matěj, N.-T.N. Kim-Ngan, A.V. Andreev, L. Havela, *Phys. Rev. B* **88**, 060407(R) (2013).
[2] H. Drulis et al., *Phys. Rev. B* **52**, 9500 (1995).
[3] A.V. Andreev et al., *Phys. Stat. Sol. (a)* **98**, K47 (1986).
[4] A.V. Andreev, S.M. Zadvorkin, M.I. Bartashevich, T. Goto, J. Kamarád, Z. Arnold, H. Drulis, *J.Alloys Comp.* **267**, 32 (1998).

Covalent and Ionic Bonding In Heavy Metal Oxides

Paul S, Bagus[1] and Connie J. Nelin[2]

[1]*Department of Chemistry, University of North Texas, Denton, TX 76203-5017, USA, Paul.Bagus@unt.edu*
[2]*Consultant, Austin, TX 78730, USA*

There is debate over the importance of covalent and ionic interaction and bonding in heavy metal oxides; in particular, the actinide dioxides, AnO_2. [1-2] This debate needs to be resolved since the nature of the interactions is key to understanding the electronic structure of these oxides. In part, the debate and controversy arise because it is not completely transparent how to assign ionic and covalent character from quantum mechanical calculations of electronic structure. We will show, using novel methods which permit us to make quantitative estimates, that the covalent interactions in oxides of heavier metals are important. These methods are based on the analysis of wavefunctions for embedded clusters which model the bulk oxides; a representative cluster model for fluorite dioxides is shown in Fig. 1. Our analysis includes methods to characterize the extent of the covalent mixing of metal cation and ligand anion orbitals. [3] In these methods, the projection of the wavefunctions of the fragments of the cluster on the wavefunctions of the cluster model of the oxide are used to estimate effective charges. A unique feature of these methods is that they can provide estimates of the uncertainty of the assignments of effective charges to the metal and ligand. These methods have been applied to selected oxides and indicate considerable covalent character in UO_x and CeO_2. [3] A method has also been developed to provide quantitative measures of the energetic importance of these covalent interactions by constraining the variational space in the solution of the equations to determine the optimal orbitals for the cluster models; see Ref. [4] and references therein. This Constrained Space Orbital Variation, CSOV, method has been applied to estimate the energetic importance of covalent interactions, especially for chemisorbed atoms and molecules. [5-6] Here, we report, for the first time, the combination of these two approaches for several different oxides to examine both the extent of the covalent interactions and the importance of the interactions for the stability of the oxides. The systems discussed are chosen to illustrate the importance of various factors including charge state and position of the metal in the periodic table. We acknowledge support for this work by the Geosciences Research Program, Office of Basic Energy Sciences, U.S. DOE.

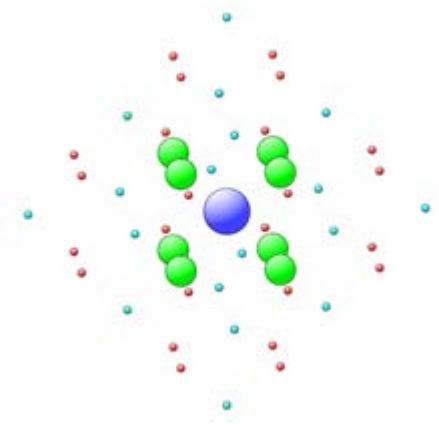

Fig. 1 An embedded cluster to model UO_2 and other dioxides with fluorite structure. The central metal atom and 8 nearest neighbor O atoms are shown as large circles and a sub-set of the embedding charges is shown as small circles.

References

1. I. D. Prodan, G. E. Scuseria, and R. L. Martin, Phys. Rev. B **76**, 033101 (2007).
2. L. Petit, *et al.*, Phys. Rev. B **81**, 045108 (2010).
3. P. S. Bagus and C. J. Nelin, J. Electron Spectrosc. Relat. Phenom., in press (2014).
4. P. S. Bagus and F. Illas, J. Chem. Phys. **96**, 8962 (1992).
5. P. S. Bagus, *et al.*, Phys. Rev. Lett. **100**, 126101 (2008).
6. P. S. Bagus and G. Pacchioni, J. Phys.: Conf. Ser. **117**, 012003 (2008).

45èmes Journées des Actinides, April 15-19, 2015, Prague-Průhonice, Czech Republic

Ab initio theory of magnetic properties of pure and Zr-doped alpha-UH_3

Ilja Turek,[1] Martin Diviš,[1] Ladislav Havela[1]

[1] *Charles University, Faculty of Mathematics and Physics, Ke Karlovu 5, 12116 Praha 2, Czech Republic, e-mail: turek@ipm.cz*

The electronic structure of uranium trihydride, recently prepared in its Zr-doped alpha phase, is studied theoretically by means of up-to-date techniques based on the local spin-density approximation (LSDA). Both the ferromagnetic ground state and a high-temperature disordered-local-moment (DLM) state have been considered. Particular attention has been devoted to magnetovolume phenomena, namely, to the volume dependence of spin and orbital moments of U atoms and to the spontaneous volume magnetostriction. The large volume magnetostriction, observed in experiment, is semiquantitatively reproduced by the calculations, which corroborates the itinerant nature of magnetism of the compound. Further aspects, such as an estimation of the Curie temperature and the effect of Zr doping on magnetic properties, will be briefly discussed as well.

Adsorption of O_2, CO, CO_2 and H_2O on α-U (001) surface: A density-functional theory study

Gan Li,[1] Wenhua Luo[1], Huchi Chen[1]

[1] *China Academy of Engineering Physics, P.O.Box 919-71, 621900, Mianyang, Sichuan, China, e-mail: lgzf1980@163.com*

Introduction

Understanding the interactions of uranium with environmental gases is an important issue due to its relation to environmental corrosion processes. The chemisorption and initial stage of chemical reaction of O_2, CO, $CO_2$and H_2O on clean α-U surface have been investigated experimentally using many surface science techniques such as XPS, UPS, AES SIMS and DRS [1-6]. However there are very few theoretical studies of these oxygen-containing molecules adsorption on α-U surface. With the aim of getting a deeper understanding of the uranium initial oxidation process and mechanism, the geometric and electronic properties of O_2, CO and CO_2 adsorption on α-U(001) surface were investigated by density functional theory calculations.

Computational Method

The calculations were performed using DMol3 under the following conditions: (i) the general gradient approximation (GGA) with the Perdew and Wang functional (PW91), (ii) the double numerical basis plus p-polarization functions (DNP) basis set and (iii) the density functional semi-core pseudo-potential (DSPP). The α-U (001) surface, with a (2×1) surface unit cell, was modeled by repeated five-layer slabs separated by a vacuum of 15 Å, and one adsorbate was placed on the surface, corresponding to the coverage of 0.25 monolayer. Four different adsorption sites: top site, bridge site, hollow1 site and hollow2 site were considered. For the structural optimization and electronic properties calculations, a cutoff radius of 5.1 Å and the k-point of 4×4×1 were used, and the energy, gradient and displacement convergence were set to 10^{-5} Ha, 4×10^{-3} Ha/Å and 3×10^{-3} Å, respectively. To investigate the dissociation barrier of adsorbed molecules, LST/QST protocol was used, which has been well validated to find a transition-state structure. To determine the electronic interaction between the adsorbed molecules and the α-U surface, Mulliken charge transfer and local density of state were calculated.

Results

a) Adsorption of Oxygen Molecule

Dissociative adsorptions of O_2 are significantly favored than molecular adsorptions with adsorption energies of 9.54-10.22 eV, and the dissociated O atoms are apt to occupy the neighboring threefold hollow sites. The U atoms of top layer are found to move upward after adsorption coupled with rumpling of the surface layer, and the larger values of relaxation and rumpling are attributed to the distributing asymmetry of U-O bonding. The ionic part of the U–O bonding plays a significant role in the dissociative adsorption, along with the covalent part due to U 5f/6d and O2p hybridization.

b) Adsorption of Carbon Monoxide molecule

CO molecules are chemisorbed on the hollow sites in different orientations with adsorption energies of 1.78-1.99 eV. Common features of the adsorbed geometries are a tilt of the molecule with C atom closer to the surface and elongation of CO bond due to the population of CO lowest unoccupied $2\pi^*$ orbital by the U electrons. The dissociative adsorption is more energetically favored than molecular adsorption with adsorption energies of 2.71 and 3.08 eV for h1(C)+h2(O) and

h1(C)+h1(O) configurations, respectively. The diffusion barriers of C and O atoms between two neighboring hollow sites are 0.57 and 0.14 eV, respectively, which indicates the on-surface diffusion of O atoms is easier than C atoms.

c) Adsorption of Carbon Dioxide Molecule

CO_2 molecules are chemisorbed on the top, bridge and hollow sites with the formation of $CO_2^{\delta-}$, a charged and bent species, and the degree of C–O bond activation strongly depends on the degree of electron transfer from surface to the adsorbed CO_2. The adsorption energies are 1.24-1.67 eV. The interaction between the U atoms and the CO_2 molecules mainly comes from the population of the CO_2 lowest unoccupied $2\pi_u$ orbital by U electrons with CO_2 $2\pi_u/1\pi_g/3\sigma_u$–U 6d orbital hybridization. The dissociative adsorption energies for the CO_2 adsorbed on the hollow1 and hollow2 sites are 3.15 and 3.13 eV, respectively. The corresponding dissociation barriers are 0.26 and 0.36 eV, respectively, which indicates that the dissociation of adsorbed CO_2 into CO and O occurs easily.

d) Adsorption of Water Molecule

H_2O molecule is preferentially adsorbed on the top site in a flat-lying configuration with the adsorption energy of 0.58 eV. The adsorption interaction is mainly contributed by the overlapping between the $1b_1$ orbital of H_2O and the 6*d* orbital of the top-layer U atom, along with some weak H_2O $3a_1$-U 6*d* mixing. The activation energy for H_2O diffusion between two adjacent top sites is 0.20~0.23 eV, indicating that the on-surface diffusion is easy for H_2O molecule. The OH+H dissociative adsorption is about 1.24~1.39 eV higher in energy than molecular adsorption, together with the dissociation barrier of 0.56~0.62 eV, suggesting that the dissociation of adsorbed H_2O into OH and H can occur under the certain heat activation condition.

References

[1] W. McLean, C.A. Colmenares and R.L. Smith, Physics Review B **25.**, 8-24 (1982).
[2] J. Bloch, U. Atzmony, M.P. Dariel, M.H. Mintz and N. Shamir, Journal of Nuclear materials **105.**, 196-200 (1982).
[3] T. Gouder, C. Colmenares, J.R. Naegele and J. Verbist, Surface Science **235.**, 280-286 (1989).
[4] E. Swissa, J. Bloch, U. Atzmony and M.H. Mintz, Surface Science **214.**, 323-333 (1989).
[5] K. Winer, C.A. Colmenares and R.L. Smith, Surface Science **183.**, 67-99 (1987).
[6] E. Tiferet, S. Zalkind, M.H. Mintz, I. Jacob and N. Shamr, Surface Science **601.**, 936-940 (2007).

Polar Kerr effect and unconventional superconductivity in heavy-fermion metal UPt3

Gertrud Zwicknagl,[1] A. J. Berlinsky[2]

[1] *Institut für Mathematische Physik, Technische Universität Braunschweig, Mendelssohnstr. 3, 38106 Braunschweig, Germany e-mail: g.zwicknagl@tu-bs.de*

[2] *Kavli Institute for Theoretical Physics, University of California, Santa Barbara, CA 93106-4030, USA*

The heavy-fermion metal UPt_3 is an unconventional superconductor exhibiting multiple superconducting phases. The identification of the corresponding order parameters remains a challenge. A key question is whether the superconducting states preserve or break time-reversal invariance.

Starting from realistic models for the heavy quasi-particles we calculate the expected polar Kerr-effect, a key signature of broken time-reversal symmetry. We compare the theoretical predictions for various possible superconducting order parameters symmetries to experimental observations and discuss the implications.

45èmes Journées des Actinides, April 15-19, 2015, Prague-Průhonice, Czech Republic

Thermal expansion and phonon anharmonicity of alpha-plutonium

Filanovich A.N., Povzner A.A.

Ural Federal University, Mira st., 19, 620002, Russia, e-mail: a.n.filanovich@urfu.ru

Alpha-plutonium, which is one of the most important phases of pure plutonium (exists from 0 to ~390 K), exhibits a number of anomalous properties, including strong temperature dependence of the bulk modulus, anomalously high values of the thermal expansion coefficient and Gruneisen parameter. In the present study we show that these anomalies of α-plutonium are caused by its strong phonon anharmonicity. We develop a self-consistent thermodynamic model of α-Pu based on the generalized Debye model, in terms of which we carry out self-consistent calculations of the temperature dependencies of thermal and elastic properties of α-plutonium. In order to account for the effect of the electronic subsystem, we calculate the coefficient of the electronic heat capacity of α-Pu from the results of calculations of its electronic structure and magnetic susceptibility [1].

The self-consistent thermodynamic model is based on the connection of Debye temperature θ with molar volume V and bulk modulus B in the form

$$\theta = \frac{\hbar}{k_B}\left(6\pi^2 N_A^2\right)^{1/3}\sqrt{\frac{3}{\mu}}\Xi^{1/2}B^{1/2}V^{1/6}, \qquad (1)$$

where $\hbar$, N_A are Plank and Avogadro constants, respectively; μ is the molar mass and $\Xi(\sigma)$ is a function of the Poisson coefficient σ. We define the thermodynamic potential (TDP) in the additive form $\Phi = \Phi_0 + \Phi_{ph} + \Phi_{el}$, where $\Phi_0=\Phi_0(P)$ is the "constant" part of TDP, which is temperature independent, but is a function of pressure; $\Phi_{ph}=\Phi_{ph}(\theta(P),T)$ is the molar lattice (phonon) part of TDP and Φ_{el} is the electronic part of TDP. It has been shown in [1] that the electronic densities of states of α-Pu near the Fermi level are rather flat, which results in that the coefficient of electronic heat capacity of α-Pu is almost temperature independent. This enables to utilize the simple form for the electronic part of TDP $\Phi_{el} = -\frac{\zeta T^2}{2}$, where ζ=1.87 mJ/(mol·K^2) is the coefficient of electronic heat capacity obtained from the value of total electron density of states at the Fermi level $g(\varepsilon_F)$=0.79 1/(eV·atom) as calculated in [1]. The phonon part of TDP, responsible for the contribution of acoustic vibrations of a solid, is written in the form:

$$\Phi_{ph} = 3R\left(\frac{3}{8}\theta + T\phi(z)\right), \qquad (2)$$

where $z = \theta/T$ is the inverse reduced temperature and $\phi(z) = \ln(1-e^{-z}) - D(z)/3$ ($D(z)$ is the standard tabulated Debye function). From equations (1) and (2) it follows that the characteristic Debye temperature enters the definition of the phonon part of TDP $\Phi_{ph}=\Phi_{ph}(\theta(P),T)$ and at the same time θ is a function of temperature. Since all the calculated thermal and elastic properties are defined from the phonon TDP $\Phi_{ph}=\Phi_{ph}(\theta,T)$, the change of the simulated values of Debye temperature leads the change of these properties. The simulation of the properties, in turn, leads to renormalization of Debye temperature values. This allows to construct an iterative procedure for the self-consistent calculations of temperature dependencies of θ, thermal and elastic properties and account for the effects of phonon anharmonicity.

For example, one can calculate the molar volume by differentiation of TDP with respect to pressure

$$V(T) = \left(\frac{\partial\Phi}{\partial P}\right)_T = V_0 - \frac{3R\theta\gamma_\theta}{B}\left(\frac{3}{8} + \frac{D(z)}{z}\right) + \frac{\zeta\gamma_\zeta T^2}{2B}, \qquad (3)$$

where V_0 is the volume at T=0 K, the second term is the lattice contribution and the third one is the electronic part. Then it is possible to obtain expression for the volumetric coefficient of thermal

expansion (VCTE)

$$O(T)=\frac{1}{V}\left(\frac{\partial V}{\partial T}\right)_P=-\frac{3R\theta\gamma_\theta}{VB}\{C_{VR}(z)[1-\frac{T}{\theta}\left(\frac{\partial\theta}{\partial T}\right)_P]\frac{1}{\theta}+[\frac{3}{8}+\frac{D(z)}{z}]\cdot[\frac{1}{\theta}\left(\frac{\partial\theta}{\partial T}\right)_P+\frac{1}{\gamma_\theta}\left(\frac{\partial\gamma_\theta}{\partial T}\right)_P-\frac{1}{B}\left(\frac{\partial B}{\partial T}\right)_P]\}+\frac{\varsigma\gamma_\varsigma}{VB}T, \quad (4)$$

where $C_{VR}(z)$ is the standard Debye heat capacity, normalized to $3R$. In the equations above we use the generalized dimensionless Gruneisen parameters, which for a thermodynamic quantity $f=f(T,V)$ at constant temperature and pressure are defined as

$$\gamma_f=\frac{V}{f}\left(\frac{\partial f}{\partial V}\right)_{TP};\qquad \gamma_f^*=\frac{V^2}{f}\left(\frac{\partial^2 f}{\partial V^2}\right)_{TP}. \quad (5)$$

It is clear that the generalized Gruneisen parameter γ_θ of the first order for the Debye temperature up to a sign coincides with the well-known Gruneisen parameter of a solid $\Gamma=-\frac{\partial\ln\theta}{\partial\ln V}$, which characterizes the degree of lattice vibrations anharmonicity

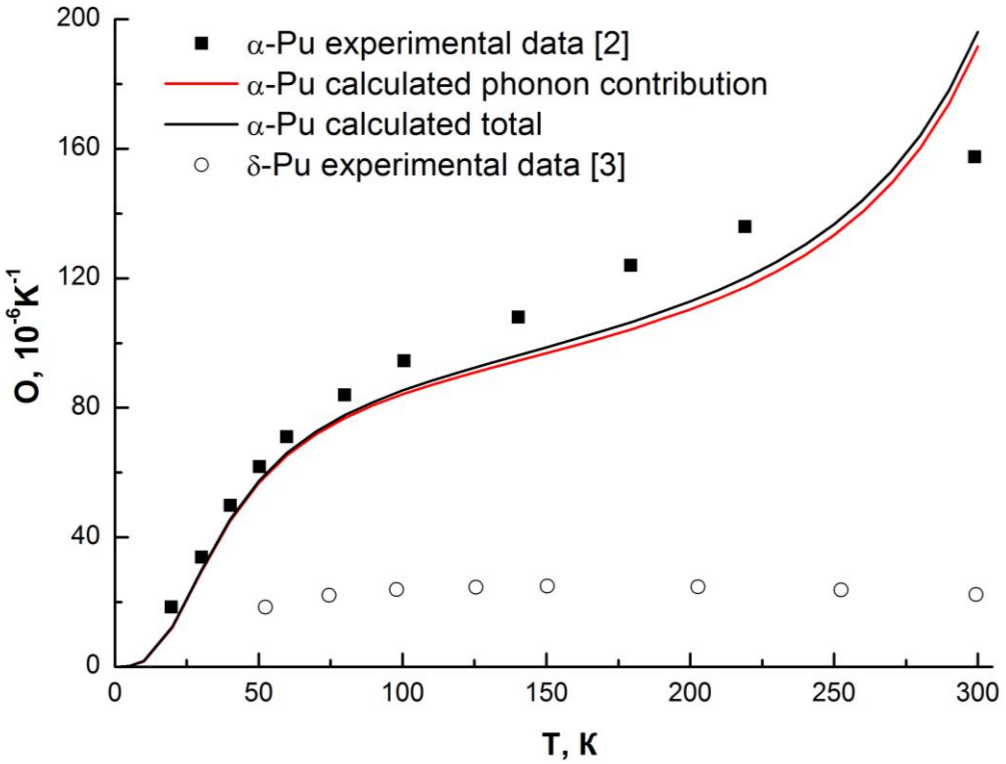

Fig. 1. Volumetric thermal expansion coefficient of plutonium

From Fig. 1 one can see that the experimental data on the volumetric thermal expansion coefficient of α-Pu are almost completely described by the phonon part. Thus, the giant values of VCTE of α-Pu are associated with its large phonon anharmonicity. In addition, from Fig. 1 it is evident that the thermal expansion of α-Pu is considerably higher than of δ-Pu, which points to that the phonon anharmonicity is much stronger in α-Pu.

The strong phonon anharmonicity of α-Pu is further manifested in its Gruneisen parameter Γ shown in Fig. 2. At all temperatures Γ takes values not lower than three, which is typical for systems with strong phonon anharmonicity (for "usual" metals Γ is in the range from 1.4 to 2.4). Previously in [4] Ledbetter et al. have performed a comprehensive analysis of Gruneisen parameter of α-Pu obtained by different methods. This analysis provided a wide spread of Γ values, ranging

from 3.5 to 9.6. From the results of the present study it is evident that the Γ of α-Pu strongly depends on temperature and this explains the wide spread of Γ values presented in [4], which are actually somehow temperature-averaged values, since were obtained from a series of experimental points measured at different temperatures.

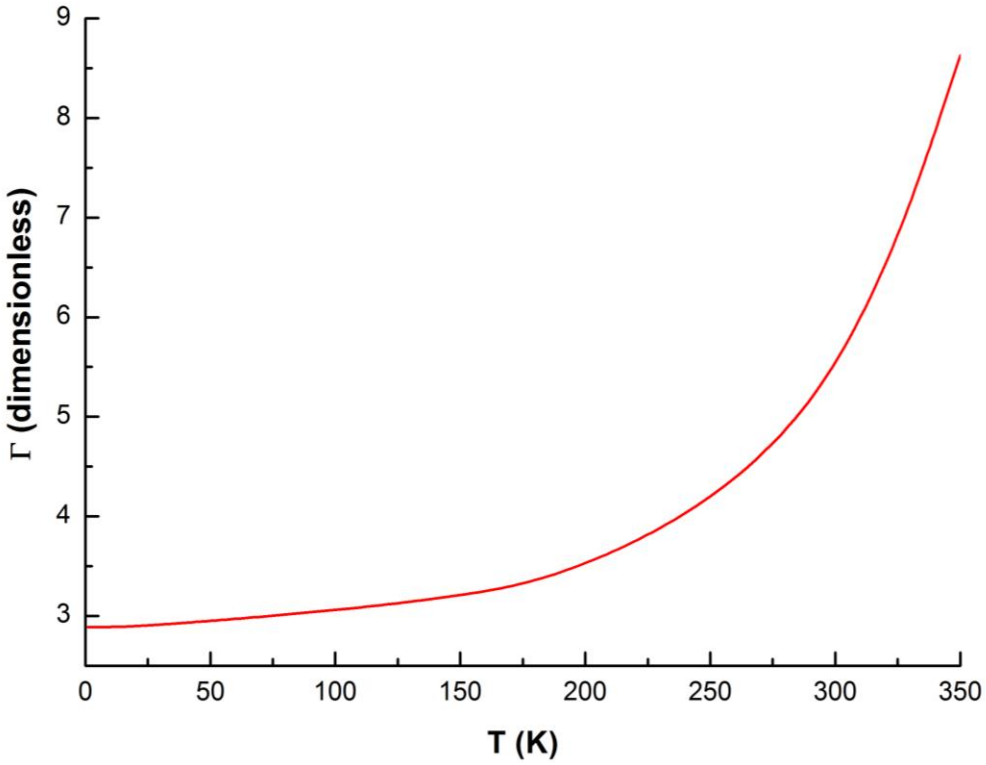

Fig. 2. Gruneisen parameter of α-Pu

It is worth noting that Ledbetter et al. supposed that the large values of α-Pu Gruneisen parameter are induced by the effect of a localized–itinerant f-electron transition. However, as we see from the present study, the large Γ values can completely be explained by the phonon anharmonicity of α-Pu. This anharmonicity is most likely caused by the complex crystal structure of α-Pu – the monoclinic crystal lattice with eight unique positions of plutonium atoms. However, this requires additional investigations.

References

[1] A.A. Povzner, A.N. Filanovich, A.O. Shorikov et al, JETP Letters **99,** 656 (2014).
[2] J.A. Lee et al., Proc. of the 3th Int. Conf. «Plutonium 1965» , p. 176 (1965).
[3] A.C. Lawson et al., Phil. Mag. B. **82**, 1837 (2002).
[4] H. Ledbetter, et al., J. Phys.: Condens. Matter. **22** 165401 (2010).

Calculating vibrational properties of actinides with quantum molecular dynamics

Johann Bouchet, Francois Bottin, Boris Dorado

Commissariat à l'énergie atomique, DAM, DIF, F-91297 Arpajon, France

In density functional theory the thermal vibration of atoms and therefore the free energy are usually obtained via the harmonic or quasiharmonic approximation. Unfortunately, it is well known that this approximation fails for the treatment of lattice dynamics of strongly anharmonic solids. For example, the free energy of dynamically unstable structure at 0 K as the bcc structure of Li, Zr, Ti or U cannot be obtained or the temperature dependence of a soft mode cannot be reproduced. Here we will present how the lattice dynamics of a solid at high temperature can be obtained by means of first-priciples molecular dynamics simulations. Then we will present several examples to show the usefulness of this method : the charge density wave phase transition in uranium, the fcc structure of plutonium and uranium dioxide.

Electronic Structure and Core-Level Spectroscopy of Light Actinide Dioxides

Jindřich Kolorenč

Institute of Physics, Academy of Sciences of the Czech Republic, Na Slovance 2, 182 21 Praha, Czech Republic, e-mail: kolorenc@fzu.cz

The correlated-band theory implemented as a combination of the local-density approximation with the dynamical mean-field theory (LDA+DMFT) is applied to UO_2, NpO_2 and PuO_2 [1, 2]. The calculated band gaps and valence-band spectra are in very good agreement with optical absorption experiments as well as with photoemission spectra. The relatively large hybridization of the actinide 5f shell with the 2p states of oxygen causes a sizable increase of the filling of the 5f orbitals from the nominal ionic configurations with two, three and four electrons to fractional values 2.5, 3.4 and 4.4. This enhancement is compatible with the 4f core-level photoemission spectra [3] but in the same time it appears to disagree with the recent synchrotron experiments that employ the resonant X-ray emission spectroscopy (RXES) and suggest fillings much closer to the nominal integers [4, 5]. This discrepancy is analyzed in the LDA+DMFT framework by an explicit calculation of the RXES spectra for incident photons $\hbar\omega_1$ scanned across the actinide L_3 absorption edge ($2p_{3/2} \rightarrow 6d_{5/2}$) and emitted photons $\hbar\omega_2$ detected at the actinide $L\alpha_1$ line ($3d_{5/2} \rightarrow 2p_{3/2}$).

The LDA+DMFT ground state of UO_2 is a superposition of $5f^2$, $5f^3$ and $5f^4$ configurations with weights 57%, 38% and 5%. The standard interpretation of the RXES spectra builds on the assumption that the spectrum is a superposition of several signals, each corresponding to one configuration of the 5f shell [6, 7]. When this assumption is applied to UO_2 together with the LDA+DMFT ground state, the spectrum shown in figure 1 is obtained. There are two spots at the diagonal of the intensity map, the less intense spot corresponds to the $5f^2$ configuration, the brighter spot at a smaller $\hbar\omega_1$ comes from the $5f^3$ configuration. The intensities of the peaks do not track the actual weights of the configurations because additional effects due to a large width of the 6d band, the structure of the 6d density of states, and the lifetime broadening are all at play. The $5f^4$ state has a too small weight to be discernible.

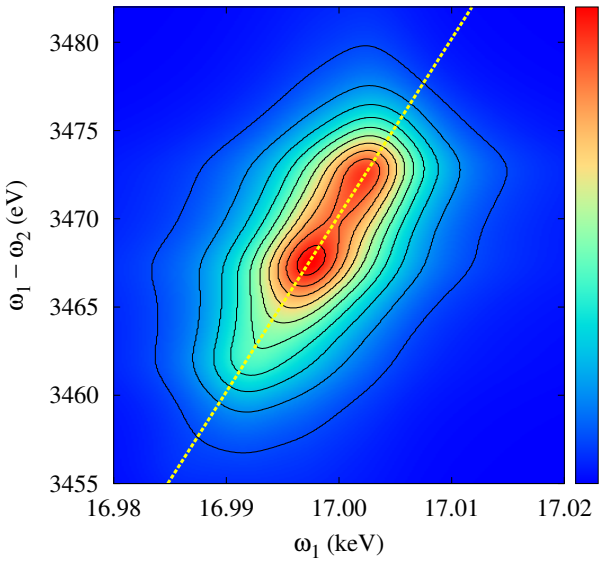

Figure 1: The UO_2 RXES intensity displayed as a contour map with axes corresponding to incident and transferred energies. The calculation employs the standard theory that neglects the effects of hybridization in the intermediate and final states of the RXES process.

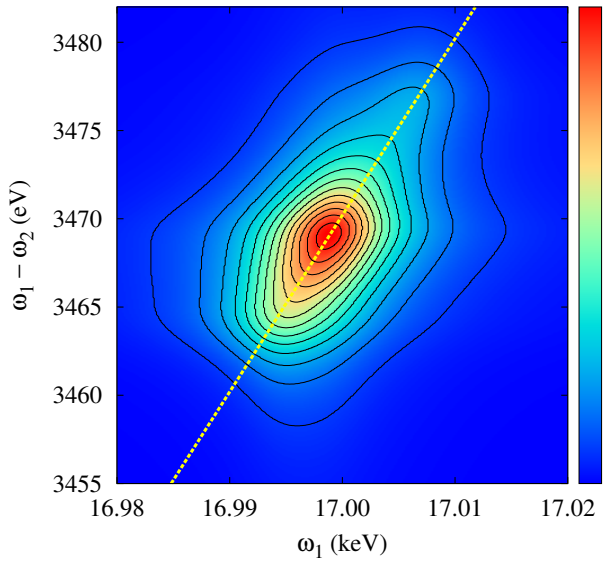

Figure 2: A contour map of the UO_2 RXES intensity calculated with the aid of an improved theory that takes into account the hybridization neglected in figure 1.

Clearly, the spectrum from figure 1 does not match the experimental data that show just a single peak and hence suggest only a single configuration being present in the ground state [4]. This disagreement could mean that the LDA+DMFT modeling of the electronic structure of UO_2 is not accurate. We argue, however, that it is not the LDA+DMFT approximation but the standard method of RXES interpretation that is not sufficiently accurate in this case. A closer inspection of the Kramers–Heisenberg formula, which determines the probability of the two-photon RXES process, reveals that the standard analysis neglects nearly all effects of the hybridization between the 5f shell and the ligand states, and as such it is justified only if the hybridization is weak or if the core-valence interaction is very strong. There is ample evidence that neither of these conditions applies to the actinide dioxides. A more accurate calculation, which takes into account the hybridization, leads to the RXES spectrum plotted in figure 2. There are substantial differences between the spectra in figures 1 and 2. The latter displays essentially a single peak, although it does in fact correspond to the LDA+DMFT ground state with significant weights of two configurations ($5f^2$ and $5f^3$).

References

[1] A. B. Shick, J. Kolorenč, L. Havela, T. Gouder, and R. Caciuffo, Phys. Rev. B **89**, 041109 (2014).
[2] J. Kolorenč, A. L. Kozub, and A. B. Shick, arXiv:1412.2489 (2014).
[3] A. Kotani and T. Yamazaki, Prog. Theor. Phys. Supplement **108**, 117 (1992).
[4] K. Kvashnina, Y. Kvashnin, and S. Butorin, J. Electron. Spectrosc. Relat. Phenom. **194**, 27 (2014).
[5] C. H. Booth, private communication.
[6] C. Booth, Y. Jiang, D. Wang, J. Mitchell, P. Tobash, E. Bauer, M. Wall, P. Allen, D. Sokaras, D. Nordlund, T.-C. Weng, M. Torrez, and J. Sarrao, PNAS **109**, 10205 (2012).
[7] C. Booth, S. Medling, Y. Jiang, E. Bauer, P. Tobash, J. Mitchell, D. Veirs, M. Wall, P. Allen, J. Kas, D. Sokaras, D. Nordlund, and T.-C. Weng, J. Electron. Spectrosc. Relat. Phenom. **194**, 57 (2014).

Search for Hyperstoichiometric Plutonium Oxides from Electronic Structure Calculations

Bingyun Ao

China Academy of Engineering Physics, P.O. Box 919-71, 621900 Mianyang, China, e-mail: aobingyun@caep.cn

Plutonium dioxide (PuO_2), a very important nuclear fuel and surface-corrosion product, had long been recognized as the highest composition binary oxide. Many attempts to prepare higher oxides with strong oxidants such as atomic oxygen, ozone, and nitrogen dioxide were unsuccessful. Despite the possibility of preparing plutonium oxides with the valence states above +4, PuO_2 was still recommended as the standard for the long-term storage of solid-state Pu-based nuclear materials. However, after the discovery by Haschke *et al.*[1] of the higher composition binary oxides in the presence of water, PuO_{2+x} ($0 < x \leq 0.27$), the feasibility of the standard was deeply discussed. Many researchers have conducted direct or indirect experimental measurements on the similar Pu-H_2O systems to find the higher-valence Pu oxides; however, the existence of PuO_{2+x} remains controversial[2-5]. In general, the discrepancies mainly resulted from the extreme difficulties in controlling the sample quality and chemical environments of the radioactive, toxic and highly-reactive materials.

In the processes of exploring hyperstoichiometric Pu oxides, both experimental and theoretical studies mainly focused on the PuO_2–O_2, PuO_2–H_2O, or PuO_2–O_2–H_2O systems. Even for the theoretical studies, the systematic calculation on the reactions of PuO_2 with the possible oxidizing products of radiolysis of H_2O was very limited. Furthermore, the reactions of PuO_2 with other active molecules were scarcely reported. In fact, apart from O_2 and H_2O, there often exist other ingredients in the real chemical environments, and they could have significant impacts on the formation of hyperstoichiometric Pu oxides. Here, the reaction energies of PuO_2 with a series of molecules (e.g., H_2, He, B, C, N_2, O_2, O_3, F_2, Cl_2, H_2O, and their potential radiation-induced radicals and products) are comprehensively predicted using the well-established first-principles DFT+*U* calculations.[6-8] In order to evaluate the validity of the methods, the similar calculations are also performed on UO_2–the analogue of PuO_2.

The calculation results show that hyperstoichiometric U oxides are energetically more favorable than hyperstoichiometric Pu oxides, which is in reasonable agreement with experimental findings. The feasibility of the reaction between F_2 and PuO_2 imply that the existence of higher-valence Pu in PuO_2-based solid-state materials. Radiation-induced free radicals favor the formation of hyperstoichiometric Pu oxides; however, the hyperstoichiometric Pu oxides can transfer into PuO_2 in the presence of the free radicals. In the absence of enough free radicals, among all hyperstoichiometric Pu oxides considered here, only $PuO_2(OH)_x$ cannot directly decompose into PuO_2. Therefore, the formation of hyperstoichiometric Pu oxides is deduced to be driven by radiolysis water rather than pure chemistry, and $PuO_2(OH)_x$, or $PuO_{2+x}H_x$, instead of PuO_{2+x}, are determined to be the experimental observed products in the kinetically favorable chemical conditions. The widely discussed PuO_{2+x} act only as the intermediate products. The potential formation mechanism of hyperstoichiometric Pu oxides is briefly illustrated in Fig. 1.

The interpretation on the stability of these hyperstoichiometric Pu oxides relative to PuO_2 is further substantiated by the analysis of electronic structures. Total and projected density of states (TDOS and PDOS) of PuO_2 and five representative Pu_4O_8X (X = O, F, He, C and OH) are plotted in Fig. 2. With the incorporation of octahedral interstitial atoms, the most remarkable change from the stability point of view is the upward shifting of Fermi energy level (E_F). Although the valence bands (VB) and conduction bands (CB) of Pu_4O_9 and Pu_4O_8C are well separated, the gap states induced by the incorporated atoms are very clear, forming *p*-type and *n*-type semiconductors, respectively. This well-known pinning effect in the field of doped semiconductor implies that octahedral interstitial O and C result in the occurrence of unoccupied states, and thus reduce the

chemical bonding and stability. However, for Pu_4O_8F and Pu_4O_8OH in which F and OH have the formal charge of –1, there are no any unoccupied states resulted from F and OH, indicating that both chemically binds with PuO_2 host and the unoccupied states in Pu_4O_9 can be balanced by H as shown in Fig. 2.(c). The results strongly demonstrate that Pu_4O_8X in which the formal charge of X is –1 is relatively more stable. We find that $Pu_4O_8(OH)_2$ is energetically more favorable than PuO_2. Based on the deduction, incorporating more than two OH into Pu_4O_8 seems to be feasible. However, the larger lattice expansion and distortion result in the severe deviation from the nature of Pu_4O_8; therefore, the possibility is reasonably excluded.

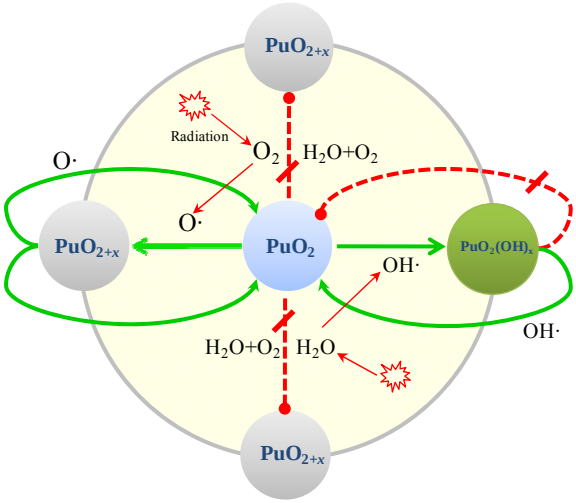

Fig. 1. Potential formation mechanism of hyperstoichiometric Pu oxides. Hyperstoichiometric Pu oxides cannot form by the direct reaction with O_2, H_2O and the mixture of O_2 and H_2O. However, the oxides can form by the reaction with radiation-induced O· and HO· free radicals. In the absence of enough free radicals, PuO_{2+x} will decompose into PuO_2; however, $PuO_2(OH)_x$ will not.

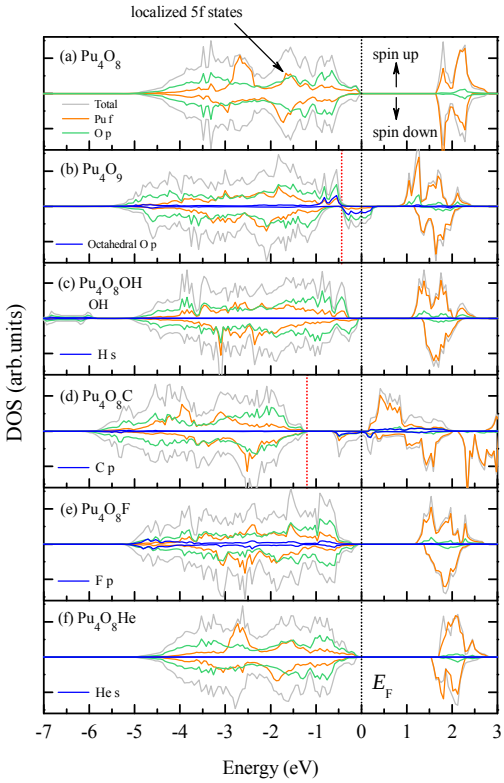

Fig. 2. Density of states (DOS) and Projected density of states (PDOS) of Pu_4O_8, Pu_4O_9 and other four typical Pu_4O_8X (X = OH, C, F and He). Fermi energy (E_F) is scaled to zero energy and marked by the black dotted line. For the sake of comparison, one can shift the intrinsic E_F (marked by the red dotted lines) of artificial Pu_4O_8 in Pu_4O_9 and Pu_4O_8C to zero energy.

References

[1] J.M. Haschke, T.H. Allen and L.A. Morales. Reaction of PuO_2 with water: formation and properties of PuO_{2+x}. *Science* **287**, 285 (2000).
[2] P. Martin, S. Grandjean, M. Ripert, M. Freyss, P. Blanc and T. Petit. Oxidation of plutonium dioxide: an X-ray absorption spectroscopy study. *J. Nucl. Mater*. **320**, 138 (2003).
[3] T. Gouder, A. Seibert, L. Havela and J. Rebizant. Search for higher oxides of Pu: A photoemission study. *Surf. Sci*. **601**, L77 (2007).
[4] J.D. Farr, R.K. Schulze and M.P. Neu. Surface chemistry of Pu oxide. *J. Nucl. Mater*. **328**, 124 (2004).
[5] P.A. Korzhavyi, L. Vitos, D.A. Andersson and B. Johansson. Oxidation of plutonium dioxide. *Nat. Mater.* **3**, 225 (2004).
[6] B. Ao, X. Wang, P. Shi, X. Ye, X. Lai and T. Gao. First-principles LDA+*U* calculations investigating the lattice contraction of face-centered cubic Pu hydrides. *J. Nucl. Mater*. **424**, 183 (2012).
[7] L. Huang and B. Ao. Non-Fermi-liquid behavior in cubic phase $BaRuO_3$: A dynamical mean-field study. *Phys. Rev. B* **87**, 165139 (2013).
[8] B. Ao, R. Qiu, H. Lu, X. Ye, P. Shi, P. Chen and X. Wang. New insights into the formation of hyperstoichiometric Pu oxides. Submitted to *J. Phys. Chem. C* (2014).

Distinct ultrafast dynamics of itinerant and localized magnetic moments in gadolinium

K. Carva,[1] P.M. Oppeneer[2], S. Wienholdt[3], D. Hinzke[3], and U. Nowak [3]

[1] *Charles University in Prague, DCMP, Ke Karlovu 5, CZ-12116, Prague, Czech Republic, e-mail: karel.carva@mff.cuni.cz*

[2] *Department of Physics and Astronomy, Uppsala University, P.O. Box 516, 75120 Uppsala, Sweden*
[3] *Fachbereich Physik, Universitat Konstanz, 78457 Konstanz, Germany*

Femtosecond lasers allow to observe magnetization dynamics on unprecedently short timescale. Recently an interesting ultrafast magnetization dynamics has been observed in rare-earth based systems with 2 ferrimagnetically ordered sublattices. A complete reversal of magnetization in GdFeCo alloy can be achieved with a linearly-polarized laser pulse, without the help of external field, circular polarization of the laser pulse [1] or any other direct source of angular momentum. Time-resolved XMCD observations have provided detailed information on the evolution of individual sublattice magnetizations: Fe magnetization is reverted first and for a time around 1ps the originally anti-parallel sublattices are ordered parallel to each other [2].

Crucial feature of the system is the fact that most magnetic momentum in the system originates from Gd 4f orbitals, which lie deep below the Fermi level and are not accessed by the pump laser. Therefore the magnetization of these orbitals cannot be assumed to be the same on femtosecond timescale. More detailed view can be obtained by studying pure Gd alone. Recent experimental data on Gd provide magnetooptical signal of the 4f and 5d moments separatedly and reveal distinct dynamics as predicted. Their dynamics differ by one order of magnitude with decay constants of 14 vs. 0.8 ps.

We calculate exchange interaction between the atomic moments as well as the intraatomic exchange between Gd 4f and 5d orbitals to allow mapping the problem to an effective orbital-resolved Heisenberg Hamiltonian. The instability of Gd 5d moment is an important component of the process and is studied too. A subsequent simulation based on the Landau-Lifschitz-Gilbert equation has shown magnetization dynamics of 4f and 5d orbitals, which is in reasonable agreement with the experiment. For GdFeCo the simulation has reproduced the switching behavior [3]. We have shown that the exchange coupling between 4f and 5d states in Gd is sufficient to revert the large magnetic moment of Gd 4f shell on a picosecond time scale [3]. Our simulation is in agreement with a recent finding that the crucial part of magnetization dynamics is disipationless, driven by exchange interaction[1].

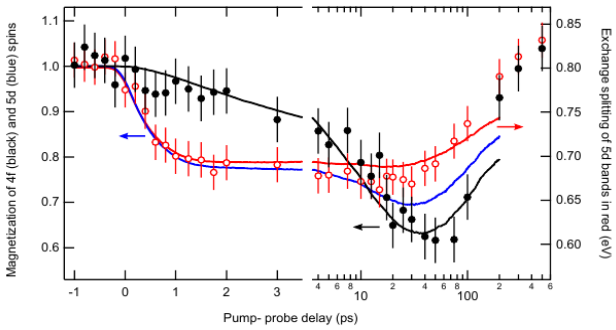

Fig. 1. Orbital-resolved spin dynamics in gadolinium. Circles: experiment by M. Weinelt, FU Berlin; lines: spin dynamics simulation

References

[1] Bergeard et al., Nature Communications **5**, 3466 (2014).
[2] I. Radu et al., Nature **472**, 205 (2011).
[3] S. Wienholdt, D. Hinzke, K. Carva, P. M. Oppeneer, and U. Nowak, Phys. Rev. B **88**, 020406(R) (2013).

Relative stability of possible ThT_2Al_{20} structures (where T= *3d* transition metal)

A. Uziel[1,2], D. Fuks[1], L. Meshi[1,2]

[1] *Department of Materials Engineering, Ben-Gurion University of the Negev, Beer-Sheva 84105, Israel*

[2] *Ilse Katz Institute for Nanoscale Science and Technology, Ben-Gurion University of the Negev, Beer-Sheva 84105.*

Strong interlinkage exists between the physical/chemical properties-chemical composition and crystal structure of the materials. In order to gain improved properties - composition and/or structure should be changed. Such researches are normally done either via theoretical route (i.e. prediction) or experimental (i.e. trial and error). Experimental route is time and resource consuming. Prediction is not always possible, especially when system of an interest exhibits complex electronic structure. ThT_2Al_{20} (when T-transition metal) is an example of such systems. It belongs to the AT_2Al_{20} family of alloys (where A-actinide/lanthanide) which were studied in [1-5, for example] with a purpose to find aluminides with possible heavy fermion properties. Studied alloys (see Figure 1 which summarizes the reported compositions) consisted of single phase cubic (*Fd-3m* space group, $Cr_2Mg_3Al_{18}$ structure type [1–5]) aluminide. It can be concluded from Figure 1 that phases, reported to exist with $Cr_2Mg_3Al_{18}$ structure type, where formed with almost all A-atoms. Transition metals were either not studied fully or cubic AT_2Al_{20} structures did not form with all T atoms. Thus, it is enough to choose one type of A (here Th was chosen as a representation of actinide/lanthanide atoms) and check systematically if specific aluminide with specific structure will form with all possible transition metals.

In a previous study, performed in our group [6], ThT_2Al_{20} systems (with T-*3d* transition metal) were studied systematically, varying T from Ti to Fe. Cast alloys were heat treated for long period of time (~3 weeks) at 800°C, in order to attain the most stable ternary Al-rich phases. It was found that cubic, $Cr_2Mg_3Al_{18}$-type structure forms in ThT_2Al_{20} systems when T=Ti and V (existence of $ThCr_2Al_{20}$ cubic phase was reported earlier in [5]), while with T=Mn and Fe, cubic structure does not form, despite the prolonged heat treatment. Instead, orthorhombic, $YbFe_2Al_{10}$-type structure forms in ThT_2Al_{10} stoichiometry together with Al matrix.

Current research was undertaken with a purpose to explain these results. Calculations based on Density Functional Theory (DFT), incorporated in WEIN2K software [7], were performed. Final goal was to determine the energy of each structure (cubic vs. orthorhombic) at each ThT_2Al_{20} alloy (when T-*3d* transition metal). The results of calculations were in perfect match to the experimental data. There is a symmetry breakage point of the energetically favorable ternary Al-rich structure as a function of atomic number (Z) of the 3d transition metal. When Z=22-24 – cubic structure is energetically favorable. When Z=25 (and 26) symmetry breaks and orthorhombic phase becomes more energetically favorable. The obtained tendency in the change of the relative stability of competing phases is explained in terms of Theory of Coordination Compounds [8].

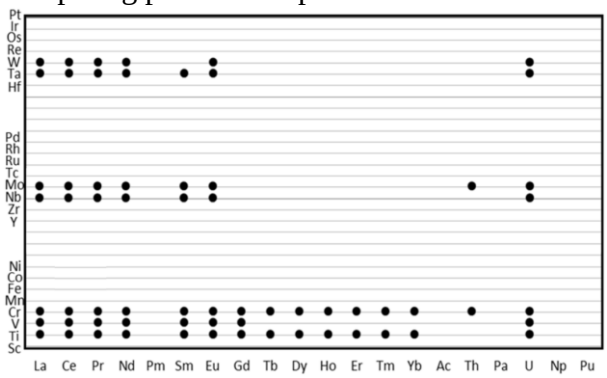

Fig 1. Summary of the $Cr_2Mg_3Al_{18}$-type structures reported to exist with AT_2Al_{20} stoichiometry (A = actinide or lantinide and T is the transition metal). Data was taken from the information available in [9].

References

[1] S. Niemann and W. Jeitschko, "Ternary Aluminides AT_2Al_{20} (A = Rare Earth Elements and Uranium; T = Ti, Nb, Ta, Mo, and W) with $CeCr_2Al_{20}$-type structure", *J. Solid State Chem.*, vol. 114, pp. 337–341, 1995.

[2] I. Halevy, E. Sterer, M. Aizenshtein, G. Kimmel, D. Regev, E. Yahel, L. C. J. Pereira, and A. P. Goncalves, "High pressure studies of a new ternary actinide compound UV_2Al_{20}", *J. Alloys Compd.*, vol. 319, no. 1–2, pp. 19–21, 2001.

[3] Y. Verbovytsky, K. Łatka, and K. Tomala, "The crystal structure and magnetic properties of the GdV_2Al_{20} and $GdCr_2Al_{20}$ ternary compounds," *J. Alloys Compd.*, vol. 442, no. 1–2, pp. 334–336, 2007.

[4] M. J. Kangas, D. C. Schmitt, A. Sakai, S. Nakatsuji, and J. Y. Chan, "Structure and physical properties of single crystal $PrCr_2Al_{20}$ and CeM_2Al_{20} (M=V, Cr): A comparison of compounds adopting the $CeCr_2Al_{20}$ structure type," *J. Solid State Chem.*, vol. 196, pp. 274–281, 2012.

[5] L.G. Akselrud, V. Davydov, P.Y. Demchenko, O.I. Bodak, P. Starodub, "Crystal structure of the $DyCr_2Al_{20}$, $ThCr_{1.825}Al_{20}$ and $ThMo_{1.69}Al_{20}$ Compounds", *Ser. Khim.*, vol. 46, no. 86-89, 2005.

[6] A. Bram, A. Venkert and L. Meshi, "Towards prediction of crystal structure of Al-rich intermetallides formed in Al-T-A systems", In: 44th Journées des Actinides and 10th SPCA.; 2014 April 22-29; Ein-Gedi, Dead sea Israel. Abstract nr 3.

[7] P. Blaha, K. Schwarz, G.K.H. Madsen, D. Kvasnicka and J. Luitz, "WEIN2K, An Augmented Plane Wave + Local Orbitals Programme For Calculating Crystal Properties, Technische Universitat, Wein, Vienna, Austria, 2001.

[8] S. S. Zumdahl and S. A. Zumdahl, "Chemistry", chapter 21*:* Transition Metals and Coordination Chemistry 942-995, 7th edition, Ed. R. Stratton Houghton Mifflin Company Boston New York**,** 1056 pages, 2007.

[9] "PDF4+", commercial database of the International Center for Diffraction Data (ICDD), 2014.

Interplay between electronic and magnetic degrees of freedom in UT_2Zn_{20} (T = Fe, Ru, Os, Co, Rh, Ir)

Przemysław Swatek and Dariusz Kaczorowski

Institute of Low Temperature and Structure Research, Polish Academy of Sciences,
P.O. Box 1410, 50-950 Wrocław, Poland
e-mail: P.Swatek@int.pan.wroc.pl

Ternary intermetallic compounds UT_2Zn_{20} (T = d-electron transition metal) crystallize with a cubic structure of the $CeCr_2Al_{20}$-type (space group $Fd\bar{3}m$). The U and T atoms are located inside cages made by Zn atoms only. All these phases are paramagnetic moderately-enhanced Kondo lattices, showing some tendency towards magnetic ordering that increases on changing the component from Fe to Ru to Os, and then from Co to Rh to Ir. By combination of the tight-binding linear muffin-tin orbital method (TB-LMTO) and the full-potential local-orbital method (FPLO), we demonstrate that the strength of interaction between the 5*f* electrons and conduction electrons significantly depends on the T-*d* band filling. The calculated electronic band structures of UT_2Zn_{20} comply with the experimentally observed gradual strengthening along the series of short-range magnetic fluctuations, and support the scenario of the competition between Kondo effect and RKKY exchange interactions.

Synthesis and physical properties of $A_{0.8}V_2Al_{20}$ (A = Th, Np, Pu) ternary actinide aluminides

Michał J. Winiarski,[1,*] Eric Colineau[2], Jean-Christophe Griveau[2], Konrad Wochowski[3], Piotr Wiśniewski[3], Tomasz Klimczuk[1]

[1] *Faculty of Applied Physics and Mathematics, Gdansk University of Technology, Narutowicza 11/12, 80-233 Gdansk, Poland*
[2] *European Commission, Joint Research Centre (JRC), Institute for Transuranium Elements (ITU), Postfach 2340, 76125 Karlsruhe, Germany*
[3] *Institute for Low Temperature and Structure Research, Polish Academy of Sciences, Post Office Box 1410, 50-950 Wrocław, Poland*
** - presenting author, e-mail: mwiniarski@mif.pg.gda.pl*

Polycrystalline samples of three novel intermetallic cage compounds containing actinide elements were synthesized using the arc-melting method. A sequential melting technique was developed to ensure a good homogeneity of the samples with high Al content.

Crystal structure studies were performed using powder x-ray diffraction and Rietveld refinement method. $Th_{0.8}V_2Al_{20}$, $Np_{0.8}V_2Al_{20}$, $Pu_{0.8}V_2Al_{20}$ crystallize in $CeCr_2Al_{20}$-type structure [1], with actinide elements positioned in the centres of oversized icosahedral Al cages (Wyckoff symbol 8*a*). The substoichiometry of the position was inferred from the previous studies on UV_2Al_{20} by Halevy *et al.* [2], where UAl_4 impurity phase was found in the x-ray diffraction pattern.

Specific heat and magnetic susceptibilities of the samples were measured in low temperatures. The radiative self-heating phenomenon was limiting the lowest temperature achievable for Np and Pu samples. Results show no magnetic ordering phenomena down to 2.5 K for Pu and 2.1 K for Np. Specific heat results obtained for $Th_{0.8}V_2Al_{20}$ were used as a non-magnetic reference. The Sommerfeld coefficient of the specific heat of the Np-containing material is 109(1) J mol-Np^{-1} K^{-2} being significantly higher than for the $Pu_{0.8}V_2Al_{20}$ (39(1) J mol-Pu^{-1} K^{-2}).

The new materials show a negative dependency of lattice constants on covalent radii of the actinides. This behavior is opposite to the trend observed for $CeCr_2Al_{20}$-type aluminides containing rare-earth metals. The difference between the two groups should arise from the itinerant behavior of 5*f* electrons of actinides as opposed to localized character of lanthanide 4*f* electrons.

Several $CeCr_2Al_{20}$-type superconductors are known, with critical temperatures up to 1 K. $Np_{0.8}V_2Al_{20}$ is a promising material for search of Neptunium superconductors. Up to date only two Np-based superconductors are known: $NpPd_5Al_2$ and $Np_{1+x}Mo_6Se_8$, with the Np 5*f* electrons in the latter compound most probably not contributing to the superconducting state [3]. $NpPd_5Al_2$ remains the only one, where 5*f* states are known to contribute to superconductivity.

Acknowledgements

The access to the infrastructures of JRC-ITU and financial support provided by the European Commission within its Actinide User Laboratory" program is acknowledged.

The high purity Np metal required for the fabrication of the compound was made available through a loan agreement between Lawrence Livermore National Laboratory and ITU, in the framework of a collaboration involving LLNL, Los Alamos National Laboratory, and the US Department of Energy.

References

[1] P. I. Kripyakevich and O.S. Zarechnyuk, Dopovidi Akademii Nauk Ukrainskoi RSR Seria A **30**, 364 (1968)
[2] I. Halevy, E. Sterer, M. Aizenshtein, G. Kimmel, D. Regev, E. Yahel, L. C. J. Pereira, and A. P. Goncalves, Journal of Alloys and Compounds **319**, 19 (2001).
[3] J.-C. Griveau and E. Colineau, Comptes Rendus Physique **15**, 599 (2014).

PuCrO3 compound: synthesis, structural and thermodynamic

J. Léchelle [1], R.C. Belin [1], P.M. Martin [1], C. Martial [1], A.Pieragnolia [1], R. Thomas [1], G. Cécilia [1], P.J. Valenza [1], J.C. Richaud [1], M. Reynaud [1], A.C. Scheinost [2]

[1] *CEA, DEN, MAR, DTEC, SECA, LCC, 13108 Saint-Paul-lez-Durance, France, e-mail: Jacques.lechelle@cea.fr*
[2] *Helmholtz-Zentrum Dresden-Rossendorf, Institute of Resource Ecology, D-01314 Dresden, Germany*

The synthesis of $PuCrO_3$ compound starting from metallic and/or sesquioxide chromium and PuO_2 powder mixtures in stoichiometric ratios has been studied at different temperatures under atmospheres with a varying oxygen potential (Ar, Ar + 5% H2, Ar + 5% H2 + 850 vpm H_2O). The structure of the polycrystalline perovskite compound $PuCrO_3$ was investigated by means of an X-ray powder pattern fitting. A Rietveld analysis was performed using the computer software JANA 2000. $PuCrO_3$ crystallizes in the orthorhombic space group Pbnm with a = 549.58(3) pm, b = 771.99(3) pm and c = 543.97(3) pm. A XAS study gave oxidation states +III for both chromium and plutonium. The heat capacity of $PuCrO_3$ was measured by means of a differential scanning calorimeter (DSC) in the temperature range of 373–1373 K. Debye temperature as well as electronic defect energies have been fitted from these measurements. Enthalpy increment, entropy and free energy function of PuCrO3 have been calculated from the measured heat capacity and estimated data as a function of temperature.

A New Approach for the Incorporation of Dilute Self-Irradiating Defects in Thin Films

Tzvi Templeman[1], Eyal Yahel[3], Itzhak Kelson[2] and Michael Shandalov[3]

1Department of Materials Engineering, and Ilse Katz Institute for Nanoscale Science and Technology, Ben-Gurion University, Beer Sheva 84105, Israel

2School of Physics and Astronomy, Tel-Aviv University, Tel-Aviv 84105, Israel

3Department of Physics, Nuclear Research Center Negev, P.O. Box 9001 Beer Sheva, Israel

We present a new method to produce a model system for the study of radiation damage in non-radioactive materials. The method is based on homogenously incorporating ^{228}Th ions in PbS thin films using a small volume chemical bath deposition (CBD) technique. The common way to alloy metals with radioactive elements is by melting pure elements, which requires considerable amounts of radioactive material with its safety consequences such as high sample activity. Regarding Actinides, their activity and toxicity require special measures such as glovebox for their handling. Controlled doping of the thin films with (very) small amounts (100-200ppm) of radioactive elements such as thorium is expected to provide a unique path for studying radiation damage in materials without the need of sealed enclosure.

As a first stage, we developed CBD process for controlled doping of PbS thin films (~100 nm thick) with the stable isotope ($t_{1/2}$~10^6 years), ^{232}Th. Next, we developed CBD process for controlled doping of PbS thin films with active ^{228}Th isotope, using different deposition parameters, due to ^{228}Th daughters presence in solution. This was achieved by altering deposition parameters such as temperature, pH, reagent concentrations and time.

The ^{228}Th-doped films were characterized using x-ray diffraction, which indicated a single phase material. Film morphology and thickness were determined using scanning electron microscopy (SEM). Energy dispersive spectroscopy (EDS) mapping in the analytical transmission electron microscope (A-TEM), x-ray photoelectron spectroscopy (XPS) depth profiles and a-autoradiography indicated that the Th ions were homogeneously distributed throughout the films, suggesting Pb substitution by Th ions in the crystal lattice. The properties of the PbS(^{228}Th) film activity were investigated by using alpha-spectroscopy and gamma-spectroscopy. The resulting films show promise as a model system for the analysis of dilute defect systems in semiconductor thin films.

Martensitic Phase Transformation Inhibition in Pu-1.9 at.% Ga

Jason R. Jeffries,[1] Mark A. Wall[1], and Patrick G. Allen[1]

[1] *Materials Science Division, Lawrence Livermore National Laboratory, Livermore, CA USA*

While the metastable, retained δ-phase of Pu-1.9 at.% Ga is generally the observed phase of this system at room temperature, decreasing temperature will elicit a martensitic phase transformation to the α′-phase, which has a nearly 18% smaller lattice volume than the δ-phase. This phase transformation is characterized by uncommon kinetics, but it also shows a strong sensitivity to previous heat treatment schedules [1-3]. If a specimen of Pu-1.9 at.% Ga is cycled through the δ–α′ transformation and α'–δ reversion without a sufficient high-temperature annealing treatment, then the volume fraction of the α'-phase formed on cooling will rapidly decrease with increased cycling. A simple hypothesis to explain this behaviour is that the δ–α′ transformation produces significant lattice defects, dislocations, or strains that are retained even through the α'–δ reversion process. In this scenario, subsequent transformations would then occur in a field of increasing dislocation density, which is presumed to be detrimental to the δ–α′ transformation. However, no detailed experimental investigations exist to quantify any detailed behavior or existence of these putative transformation-inhibiting defects.

Here we report experiments using differential scanning calorimetry (DSC) combined with transmission electron microscopy (TEM) that reveal some of the effects of annealing that overcome this phase transformation inhibition. Samples were thermally cycled through the δ–α′ transformation and α'–δ reversion such that the final cooling run showed no phase transformation. DSC measurements were then used to quantify the time and temperatures necessary to destroy the remnant factors inhibiting subsequent phase transformation. Following this characterization, TEM studies were performed to examine the microstructure of a sample before annealing—in a condition that would impede phase transformation—and after annealing. The results indicate a substantially higher dislocation density before annealing, pointing to a microstructural origin for phase transformation inhibition.

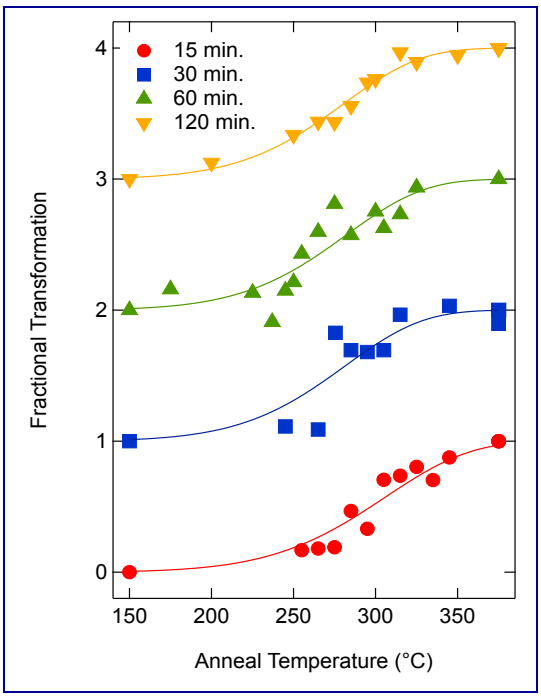

Fig. 1. Annealing treatments for a thermally cycled alloy of Pu-1.9 at.% Ga for different hold times and temperatures. Solid lines are fits to the data using a "stretched" Arrhenius equation.

This work was supported by the Science Campaign at Lawrence Livermore National Laboratory. Lawrence Livermore National Laboratory is operated by Lawrence Livermore National Security, LLC, for the U.S. Department of Energy, National Nuclear Security Administration under Contract DE-AC52-07NA27344.

References

[1] S. S. Hecker, D. R. Harbur, and T. G. Zocco, *Prog. Mater. Sci.* 49, 429 (2004).

[2] K. J. M. Blobaum, C. R. Krenn, M. A. Wall, T. B. Massalski, and A. J. Schwartz, *Acta Mater.* **54**, 4001 (2006).

[3] J. N. Mitchell, F. J. Freibert, D. S. Schwartz, and M. E. Bange, *J. Nucl. Mater.* **385**, 95 (2009).

Nuclear Fuel Cycle with METMET and Composite Fuel: Materials, Technology and Advantages

Aleksei Savchenko, Valentin Ivanov, Gennady Kulakov, Ksenia Lipkina, Oleg Uferov

A.A. Bochvar Institute of Inorganic Materials (VNIINM), 123060, P.O.BOX 369, Rogova St. 5A, Moscow, Russia, e-mail: sav-alex111@mail.ru

1. Introduction

Currently fuel cycle options for thermal and fast reactors are considered only with the use of container type UO_2, MOX or metallic fuel [1-4]. While closing the fuel cycle has been the general aim for several decades, progress towards that goal has been slow. On this way some limitations exists – low uranium density of UOX and MOX, degradation the Pu isotopic vector from cycle to cycle in thermal reactors as well as complicated fabrication technology and low irradiation resistance of fuel for fast reactors [5-8]. Additionally, we have not still optimized reprocessing technology for container type fuel.

The other disadvantages of pelletized uranium-oxide fuel are the high operating central temperature and low serviceability under transients. All these problems encourage us search for other types of fuel taking into consideration novel fuel developments as well as fuel designs.

We suggest replacing the container design fuel rod, for which possibilities are practically exhausted, to dispersion type fuel elements [9-12]. The dispersion type fuel is known to have a high irradiation resistance and better thermal conductivity, hence low operating temperatures and high burn-ups can be achieved [13, 14].

Structurally the dispersion fuel meat consists of uniformly distributed higher density fuel granules of U-Mo, U-Nb-Zr or U_3Si alloys that are metallurgically bonded between themselves and to fuel cladding with specially developed Zr-based matrix alloys [15] having the melting temperatures of 790–860°C. A fuel form retains controllable porosity in the range of 14- 22% to accommodate fuel swelling (Fig. 1). As applied to thermal reactors the novel METMET fuel will have much better neutronics characteristics which in the end will reduce the cost of produced electrical energy.

The same approach might be applied to designing fast reactor fuels using a more environmentally clean production process [16, 17]. In this case the conversion ratio of novel fuel is higher than that of MOX fuel and is at the level of more high density metal fuel.

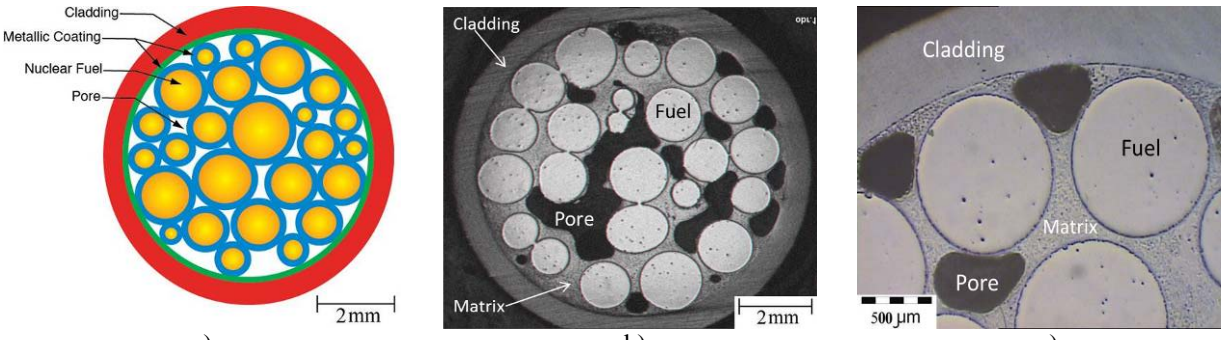

a) b) c)

Fig. 1. Schematic presentation of composite fuel (a); micro and macrostructures of composite fuel (b) U-Mo + Zr matrix alloy; (c) U-Zr-Nb + Zr matrix alloy. Conditions: t = 850°C and τ = 60 s, fuel column length: 1200 mm.

2. Design and Fabrication Process of Advanced METMET Fuel for VVER, PWR, RBMK, CANDU (HWPR)

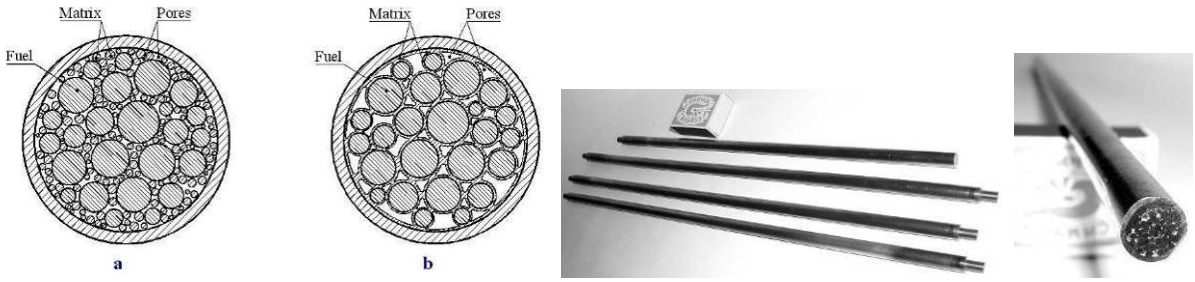

Fig. 2. Schematic cross-section representation of fuel element fabricated by capillary impregnation method; (a) as vibroloaded; (b) as capillary impregnated and appearance of fuel elements produced by capillary impregnation method

Dispersion type fuel element with high uranium content can be produced by capillary impregnation method [9]. It involves vibrofilling a zirconium cladding of a fuel element with blended fuel and matrix granules (fig. 2a) and a capillary impregnation – a short-term (1-5 minutes) anneal at 840–910°C (fig. 2b). At those temperatures zirconium matrix alloy melts down and under capillary forces moves into gaps between fuel granules as well as the space between fuel and cladding resulting in metallurgical bonds which promotes a high thermal conductivity of a fuel meat.

Properties of fuel compositions are presented in Table 1 and microstructures in Fig. 1, 3.

Dispersion Fuel		**U_3Si**	**U-9Mo**	**U-1.5Mo-1.0Zr**	**U-5Nb-5Zr**	**U-3Nb-1.5Zr**	***UO_2 pellet***
U content in fuel form (under the cladding, g/cm^3) at volume fraction of fuel	66%	9.6	10.7	11.9	9.8	11.34	***8.5***
	72%	10.45	11.7	12.9	10.7	12.37	
Increase of U content (in comparison with UO_2 pellet), %		13-24	26-38	42-55	15-26	35-47	-
Thermal conductivity at 500 °C, W·m^{-1}·K^{-1}		19	22	24	18	21	***2-4***
Interaction layer after annealing at 750 °C for 6000 h, μm		7-10	10-15		15-25		
Corrosion rate in water at 330^{0}C (g/m^{2}h)		0.03	0.05		0.02		

Tab 1: Properties of fuel compositions

In the fuel elements the volume fraction of the fuel is 66-72 %. Hence, with the use of high uranium content fuel the uranium content reaches 9.5-12.9 g·cm^{-3}. High thermal conductivity of the fuel compositions which combines with the metallurgical bond with the cladding is available, ensures the low operating temperature in the fuel element centre (cold fuel). Fuel compositions due to Zr alloy matrix show high corrosion resistance. Aqueous corrosion rate at 330 °C is 0.02-0.05 g·m^{-2}·h^{-1} [10-12].

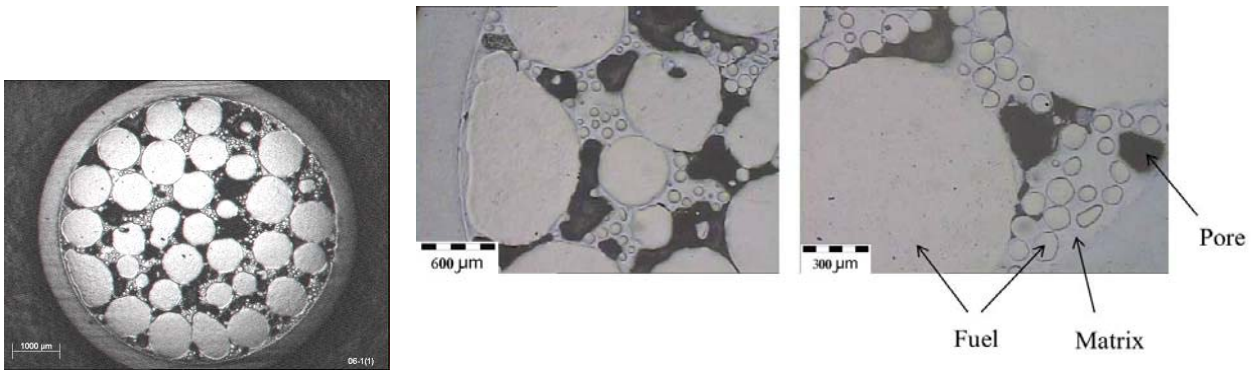

Fig. 3. Micro and macrostructure of modified METMET fuel composition with higher uranium content (72% volume fraction of fuel under the cladding) [12]

Basic advantages of METMET fuel for use in thermal reactors (PWR, BWR, VVER, and CANDU):

1. High uranium content (9.5 – 12.9 g/cm^3) within fuel element cladding, that is 25-50 % more than the uranium content of the standard PWR, BWR and VVER-1000 fuel rods, which allows the uranium enrichment of fuel to be reduced or the burn-up to be increased. It is also improves the neutronics characteristics and safety of a reactor.

The use of novel composite fuel increases the breeding ratio. The higher density fuel reduces the hydrogen-to-heavy metal ratio in the reactor which results in a harder spectrum in which breeding is more effective [18]. This is illustrated in Fig 4 where dependence Reactivity versus burn-up for PWR assembly using standard pelletized oxide fuel in comparison with composite fuel is presented [19]. It is clearly seen that composite fuel refers to the fuel of higher reactivity.

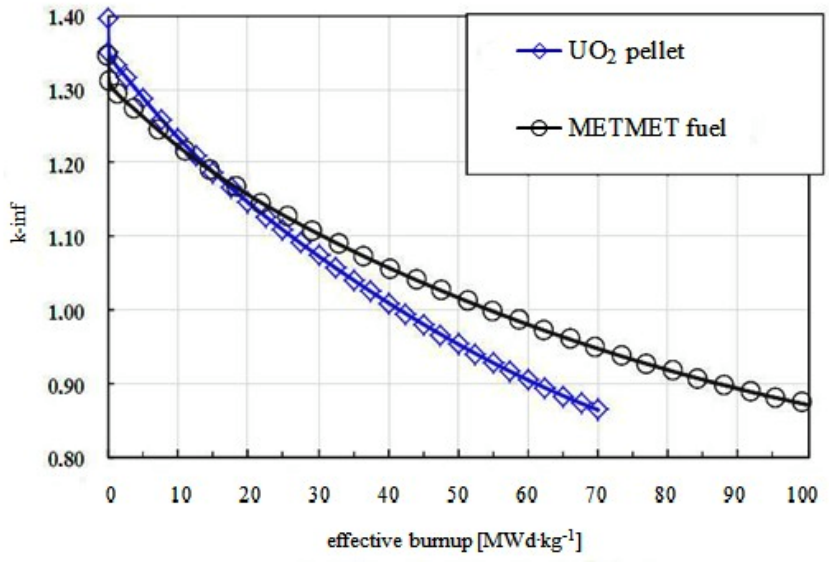

Fig. 4. K-inf versus effective burn-up for UO_2 and composite fuel at 4.95% initial enrichment

Generated of Uranium large quantities of Plutonium involved in the process of fission, leads to significant savings of enriched uranium, which in the end favourably affects the economics of nuclear power. The conversion ratio increases from 0.55 to 0.7. Therefore the prolongation of the company will be more than 30% in effective days (up to 500 additional effective days), or uranium enrichment can be reduced from 4.95 to 3.7% (Fig. 5-6).

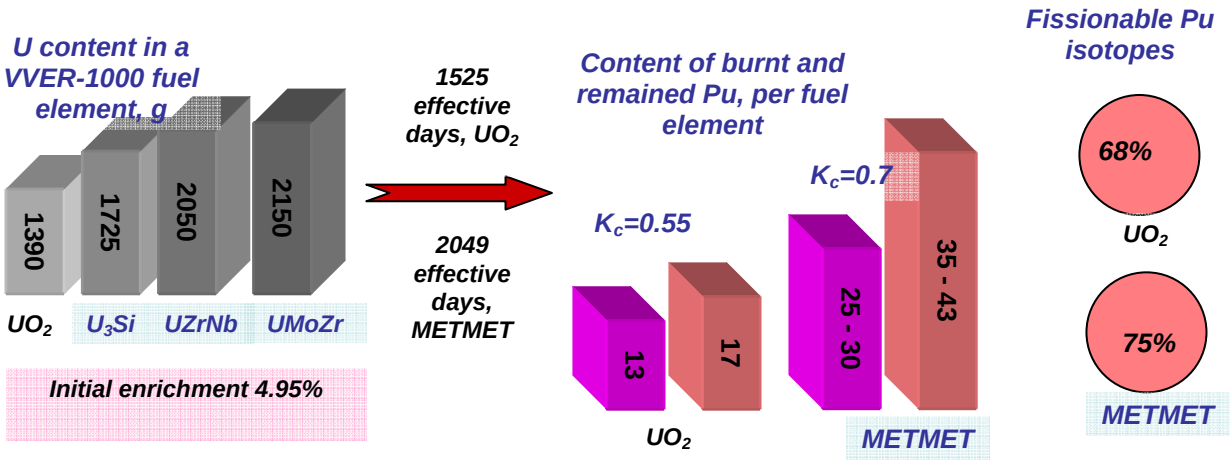

Fig. 5. Comparative assessed neutron-physical characteristics of novel composite (METMET) and dioxide uranium fuel for VVER-1000 reactor at burn-up of 65 MWd/kgU

The advantage of the fuel higher reactivity might be used to increase the time between refueling, in other words, to increase the Unit Capacity Factor (UCF). In this case instead of a year or a year and a half fuel cycle at two year cycle becomes feasible.

At the life time end the plutonium content reaches 2-3% instead of 1.3% in a uranium dioxide pellet. Due to the higher density fuel the total Pu content in fuel element is 2.5-3 times higher and makes up 43 g per a single fuel element. In this case if fissionable Pu isotopes make up 68-70 % in spent UO_2, their content in the novel fuel is 75-78 %. In other words, after reprocessing the plutonium content will be sufficient for fabricating a factor of 3 more MOX fuels than in case of the standard fuel which is very important in closing the nuclear fuel cycle (Fig. 6).

Aside from this due to the specific features of the design the novel fuel might be reused in RBMK, CANDU reactors after minimal reprocessing (without the chemical reprocessing of fuel).

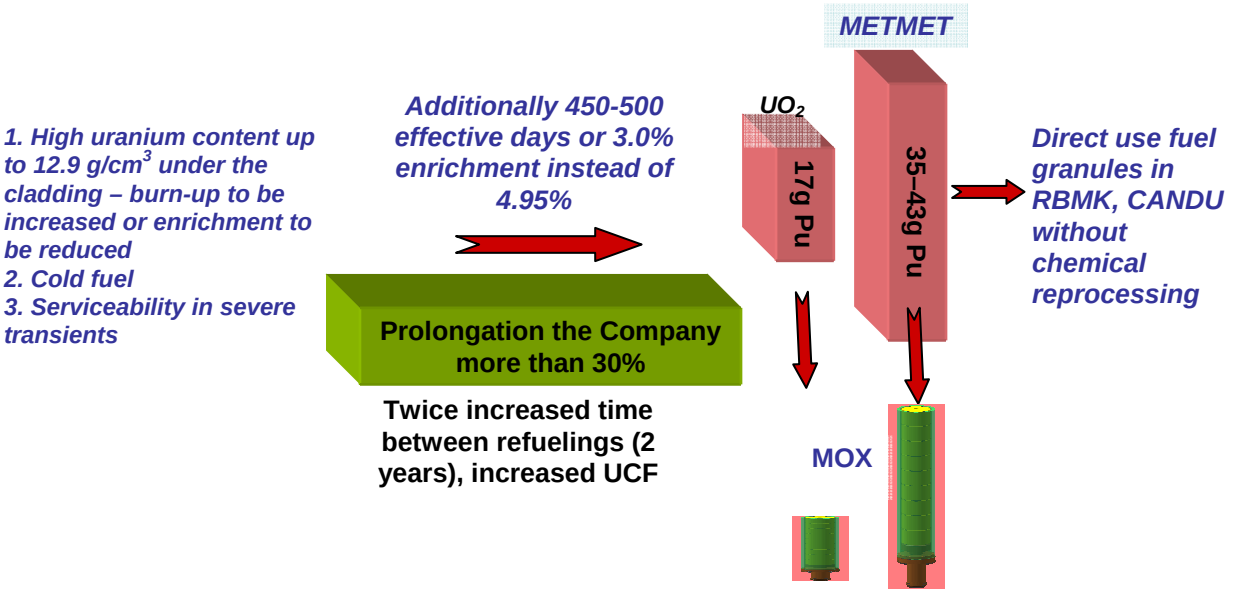

Fig. 6. Advantages of using novel dispersion type high density uranium fuel (METMET) in VVER-1000 type reactor

2. Low temperature of the fuel, which satisfies the requirements to cold fuel.

3. The porosity in the fuel meat will allow the accommodation of swelling up to the burn-up of 1.0 g-fiss/cm^3, which in terms of the standard VVER-1000 fuel rod corresponds to 120 MW*d/kgU.

4. Metallurgical bond between the fuel and cladding makes fuel elements serviceable under severe transients. It leads to optimization of Nuclear Plant operation conditions *a*nd improvements

of their operation reliability and safety.

These advantages of novel generation fuel might result in the increasing of economic efficiency and degrease of the cost of electric power.

3. Design and Fabrication Process of Alternative to MOX Composite U(Th)-PuO_2 Fuel for PWR, VVER, CANDU (HWPR)

The major approach to fuel element development consists of individual operations used to fabricate a fuel element with uranium meat and to fill it with plutonium dioxide powder which minimizes dust producing operations in a fuel element fabrication [11, 16, 17].

At the first stage under conventional conditions of a plant a fuel element frame of dump uranium bonded with Zr matrix alloy is fabricated using described above capillary impregnation method. The fuel meat open porosity is to be increased up to 25 – 30% (Fig. 7). In this way a porous uranium meat (frame fuel element) is created that has the uranium content of 9.0 – 9.5 g/cm^3 and the thermal conductivity of 16-18 W/m·K. Then, through the fuel column via open pores the standard plutonium dioxide powder up to 100 μm fraction is introduced The PuO_2 powder is manufactured by the already mastered methods, viz., the pyrochemical one or using the GRANAT type process etc. Then a fuel element is sealed. In this way plutonium dioxide granules located in the pores of a heat conducting uranium fuel frame (Fig. 7) [16].

The advantages of composite fuel element as an alternative to the MOX one are:

1. The process of the fuel element fabrication is environmentally more friendly due to degrease the quantity of technologic operations with plutonium.
2. The higher uranium content of a fuel element, hence, the higher conversion ratio.
3. Low temperature of fuel (cold fuel).
4. Serviceability under transient conditions.
5. Possibility of Pu isotopes separation.

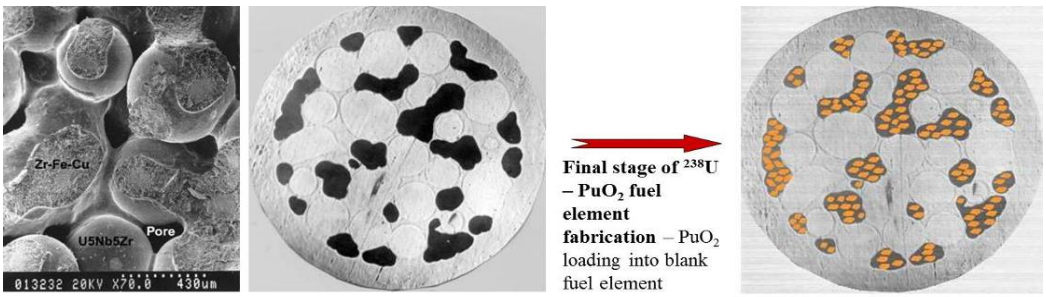

Fig. 7. Process flow diagram composite fuel fabrication [17].

Microstructure of composite fuel, where UO_2 is used in place of PuO_2 is illustrated in Fig. 8. In this option granules of Zr matrix and UO_2 were loaded simultaneously into fuel element cladding before annealing.

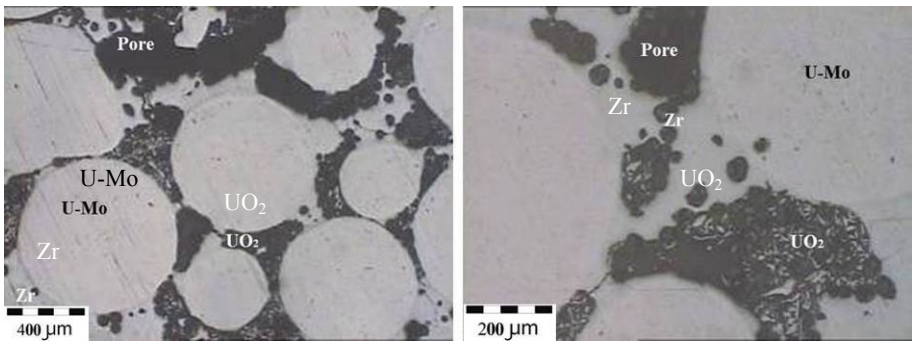

Fig.8. Microstructure of composite fuel (UO_2 is used in place of PuO_2) [12, 17]

This approach can be also implemented with the use of Th granules in place of dump uranium alloy granules. In this case the conversion ration increased. For CANDU reactors it is exceeds 1. Therefore this type of reactor can reach the burn up of 100 MW·d/kgU. Then the fuel granules may be extracted out of a fuel element via crushing the fuel meat and reused without the chemical reprocessing of fuel.

Mechanism of composite fuel operation in thermal reactors: first, PuO_2 burns-up in the metmet fuel form while Pu is generated in the metmet fuel that first serves as a breeding blanket and then begins to burn-up. Consequently, the components of the composite fuel have different Pu isotopic compositions at the cycle end. The plutonium dioxide powder will basically accumulate non-fissionable isotopes while in the metmet fuel – fissionable species. Hence, at the average MOX fuel burn-up of 45 MW d kg^{-1}, the metmet fuel will contain 75 % fissionable isotopes while in PuO_2 there will be only 42 % (Table 3). Through mechanical separation of the metmet frame from the PuO_2 powder the composite fuel may be used many times at a high efficiency in this way, saving natural uranium. In MOX fuel at the above burn-up the concentration of fissionable isotopes makes up only 55%, hence, its re-use is economically not beneficial.

Initial fuel MOX or PuO_2 powder (for composite)	MOX pellets	Spent composite U-PuO_2 fuel		
	Spent MOX fuel	In metmet granules	In PuO_2 powder	Average Pu^{239}+Pu^{24} [1]
66%	55%	75%	42%	58%

Tab 2. Assessed quantities of fissionable Pu isotopes in composite and MOX fuel of VVER-1000 operated on three year cycle as applied to fuel cycle closing.

It has also to be noted that in the composite fuel the burn-up is distributed about equally between the PuO_2 powder and the granules of uranium alloys therefore the mechanically extracted granules will contain about two times less fission fragments having a high parasitic neutrons capture.

Novel composite fuel allows the separation of the newly generated fissile plutonium from burnt one without chemical processes with repeated use in PWR or CANDU reactors, which simplifies the closing of the nuclear fuel cycle. Hence in comparison to MOX we can multiply use of generated Pu in spent fuel and instead of partial recycling implement full recycling which drastically reduces the fuel waste.

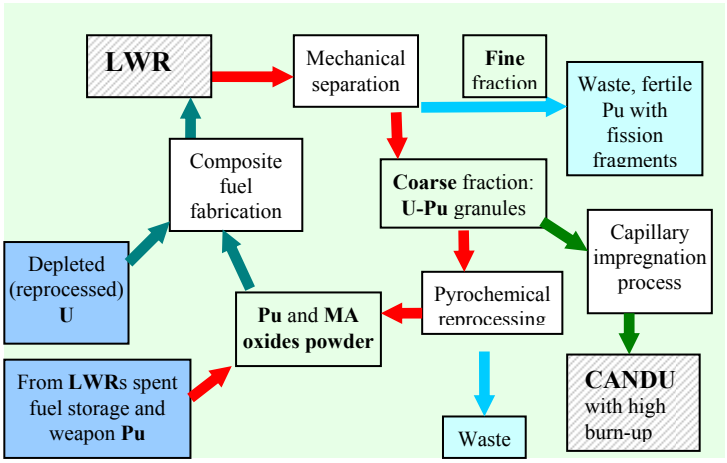

Fig. 9. LWR fuel cycle with composite fuel and multiply recycling of Pu

Thus, using novel concept based on high density dispersion and composite fuel we can implement the closed U-Pu cycle in thermal reactors – as the fuel available to these reactors may be increased by ~48% (18% in case of MOX) (Fig. 9). The remained Pu fissile isotopes can be used from the accumulated in thermal reactors spent fuel.

4. Reprocessing of U METMET and U(Th)-PuO_2 Composite Fuels

Hydro-metallurgical reprocessing was considered in a first step. The proposed U metmet fuels dissolve in hot nitric acid as the content of Zr matrix alloy in the fuel meat is low, with only 10-15% of the fuel material volume. Due to the large volume fraction of the intermetallic phases available in the Zr matrix alloy structure, the U metmet dissolves in nitric acid but not as rapidly as the uranium fuel itself.

The other option for fissile phase separation without chemical reprocessing would be the application of a simplified methodology derived from the DUPIC process. First, as for the DUPIC process fission gases are removed from the fuel by heating. Then a fuel element is subjected to a light deformation. Zr alloy matrix bridges between fuel granules are destroyed due to brittleness of Zr matrix alloy and fuel element content is emptied and phases are separated on a sieve. Finer fractions of the zirconium matrix alloy are separated from coarser granules of metallic fuel that also contain the generated Pu. This U-Pu alloy from cladding granules can be used repeatedly for RBMK and CANDU reactors using fuel elements obtained by the capillary impregnation method as they have a high content of generated Pu (2%), with high fissile ratio.

The same approach can be implemented for the U(Th)-PuO_2 composite fuel. The basic difference of such fuel is the separate arrangement of depleted uranium alloy and PuO_2 powder. Consequently, their burn-up and Pu isotope composition differ in the phases of the composite fuel, since the fissile Pu of the PuO_2 almost fully burns and it contains low quality Pu isotopes prior to reprocessing. The metal fuel builds up Pu with high value fissile isotopes. Hence, at the opposite of the standard design of homogeneous MOX fuel elements, for which separation of fissile isotopes in Pu is difficult, they are initially separated in the proposed novel cermet fuel. Therefore, the separation of fissile elements may be carried out without chemical processes.

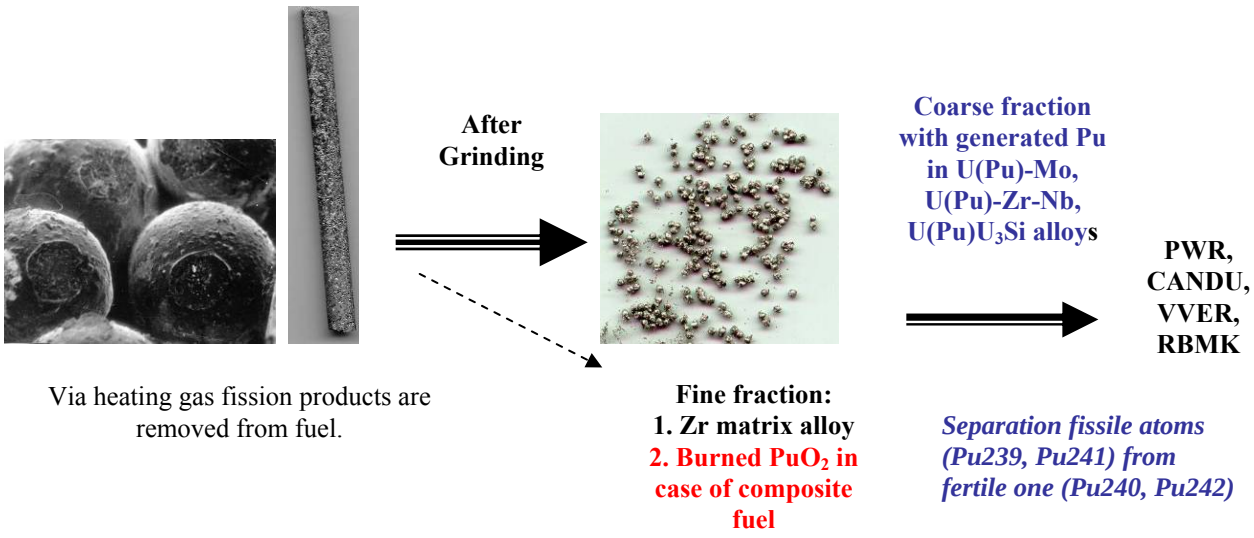

Fig. 10. Novel fuel reprocessing without chemical processes with fissile phase separation and repeated use in PWR, CANDU, VVER, RBMK reactors: Bridges between particles of a frame fuel element; its appearance without cladding and individual granules of frame fuel (U-2Mo-1Si) after crushing and sieving. Out-of-pile investigations [8]

Thus, the novel composite fuel does not require grinding and pulverization of the burnt pellets, as is required for DUPIC: an intricate process of manufacturing new fuel pellets from high activity powder. Moreover, in the new process the valuable fissile Pu isotopes (^{239}Pu and ^{241}Pu) are mostly separated from ^{240}Pu and ^{242}Pu.

This approach makes fuel reprocessing easier and more environmentally friendly, which simplifies the closing of the nuclear fuel cycle.

5. Design of Fuel Element for Fast Reactors and to Burn MA

For fast reactors the same design and process are used, but to enlarge the plutonium dioxide fraction in a fuel element the porosity is increased to 30 – 38 % (Fig. 11) and in place of zirconium claddings the steel ones are employed. The zirconium matrix alloy coating that results from the capillary impregnation at the inner surface of a cladding protects it from interacting with both fuel and fission products [16-17].

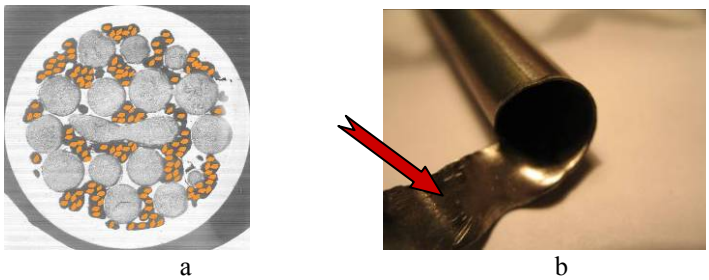

a b

Fig. 11. Structure of composite U-PuO_2 fuel meat for fast reactors and MA incineration (a), internal zirconium alloy coat at inner surface of steel cladding (b) [16-17]

For consumption of MA a powder of their oxides is filled in instead of plutonium dioxide. If the fuel meat does not contain fuel (zirconium granules are used) a version of an inert matrix fuel element results (IFM) to burn up both Pu and MA in thermal or fast reactors [20-22].

The composite fuel retains the advantages inherent in metallic and ceramic types of fuel. Since the contribution into the total burn-up is made not only by the metallic fuel at the final irradiation stage as plutonium is generated, but also by plutonium dioxide at the initial irradiation stage, the total swelling of the metallic fuel is reduced due to a less build-up of fission fragments in it.

The suggested U-PuO_2 composite fuel having a high conversion factor and thermal conductivity like metallic fuel does not interact with a fuel cladding since Zr matrix coats the cladding and protects against fuel-cladding interaction. Fabrication technology is simple and environment-friendly.

Microstructure of such composite fuel, where UO_2 is used in place of PuO_2 is illustrated in Fig. 12. In this option granules of Zr matrix and UO_2 were loaded simultaneously into fuel element cladding before annealing (capillary impregnation).

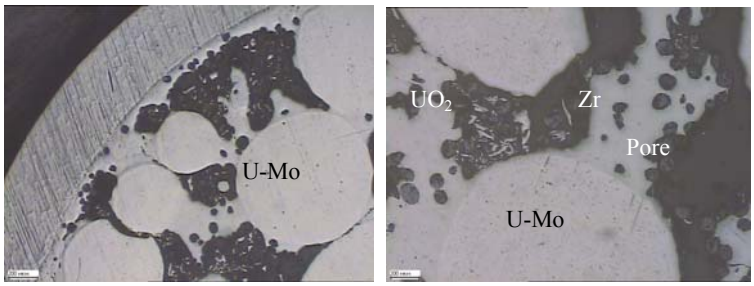

Fig. 12. Microstructure of composite fuel (UO_2 is used in place of PuO_2) [17-18]

Major advantages of composite U-PuO_2 fuel for fast reactors:

These include:

- High contents of U and Pu compared to MOX fuel and hence a high conversion ratio, which makes it feasible to close the nuclear fuel cycle.
- Lower damage of fuel by fission products and, hence, lower swelling compared to that of U-Pu-Zr fuel.
- The novel fuel is a dispersion type fuel, therefore, the existence of a metallurgical bond between fuel and cladding not only decreases fuel temperature, but also protects fuel cladding from interaction with fuel and fission products.
- High fabrication adaptability and ecology of production – actually the main part of the fuel element fabrication is carried out under conventional conditions and only the final operation of fuel element fabrication needs remote implementation. In this case PuO_2 is used as a powder not as pellets. All this minimizes process operations that involve Pu and make fuel element fabrication environmentally clean.
- After irradiation spent fuel can be mechanical separated into high and poor quality, in other words, into fissile and fertile Pu that may increase the re-used of Pu.

Mechanism of composite fuel operation in fast reactors

It should be noticed that composite fuel includes both an active core with PuO_2 powder and an inner blanket with U blank fuel, since U and Pu have initially a separate arrangement. Moreover, in the U alloy granules Pu generates much higher than in the outer blanket due to more intensive neutron flux.

Initial fuel MOX or PuO_2 powder (for composite)	MOX pellets	Spent composite U-PuO_2 fuel		
	Spent MOX fuel (10% at. burn-up)	In metal frame (granules) (2.5% at. burn-up)	In PuO_2 powder (33% at. burn-up)	Average (Pu^{239}+Pu^{241})
66%	63%	88%	39%	64%

Tab 3. Assessed quantities of fissionable Pu isotopes in composite and MOX fuel in sodium fast reactors and 10% at. burn-up (MOX) as applied to fuel cycle closing.

First, PuO_2 powder burns up inside the METMET fuel frame while Pu is generated in the METMET fuel that first serves as a breeding blanket and only then begins to burn up. Therefore, plutonium dioxide powder will basically accumulate non-fissionable isotopes while the METMET fuel fissionable species. We can receive practically weapons grade Pu in the U alloy granules with atomic burn-up of 2-3%, and 8-10% of the generated Pu. However, in PuO_2 powder we can achieve the burn-up of 33% with poor isotopic Pu composition and high quantities of MA as well as 80% of fission fragments. Then, without chemical reprocessing, using only mechanical methods we can separate the high quality product from the poor one.

Design of fuel elements to burn MA

To burn up MA in IFM of thermal or fast reactors instead of pelletized fuel element with YSZ $(Er,Y,Pu,Zr)O_2$ a novel fuel design is suggested having on isolated location of powder of PuO_2 or MA in the fuel minielements Fig. 13 [23-26]. Fuel element completed by fuel minielements (thin ***steel*** or Zr claddings) that are placed inside a fuel element. Fuel minielements is sealed. This design fully complies the requirements for 'Rock Fuel'. In this way the quantity of dust producing technologic operations is minimized. Fuel elements are fabricated by impregnation or capillary impregnation methods using a molten Al or Zr matrix alloys. This type of fuel design shall extend the burn-up, lower down the fuel temperature, accommodate swelling and make a fuel element serviceable under transient conditions.

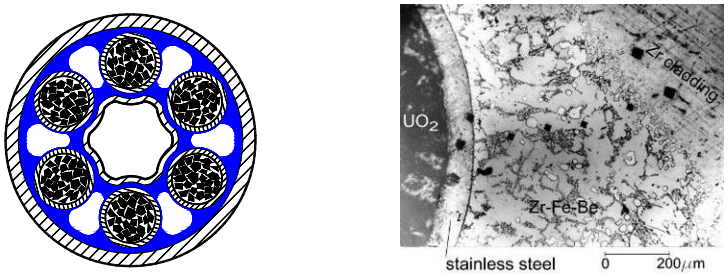

Fig. 13. Fuel element design with fuel minielements for MA incineration [11]

Peculiarities of closing fuel cycle with composite fuel in fast reactors

Generally, the fuel cycle with composite fuel does not have any principal differences with the existing fuel based on an implementation of pelletized fuel for fast reactors. Some peculiarities do exist, however, that lead to the minimizing of radioactive waste (Fig. 14).

First, by mechanical separation, spent fuel is separated on the basis of high quality (U granules) and poor quality (PuO_2 powder). High quality fuel (fissile Pu isotopes) can be used again after pyrochemical reprocessing in fast reactors, or without reprocessing coarse granules can be used as feedstock for fuel fabrication Plant producing fuel elements for thermal reactors using capillary impregnation technology.

Fuel of the low quality (PuO_2 powder) of poor Pu isotopic composition, including fission fragments and MA can be used for IMF fabrication with the above mentioned design followed by incineration in thermal or fast reactors with direct geological disposal as (Rock fuel). Thus, the proposed fuel cycle looks more effective from the point of minimizing radioactive wastes and reused of the generated Pu.

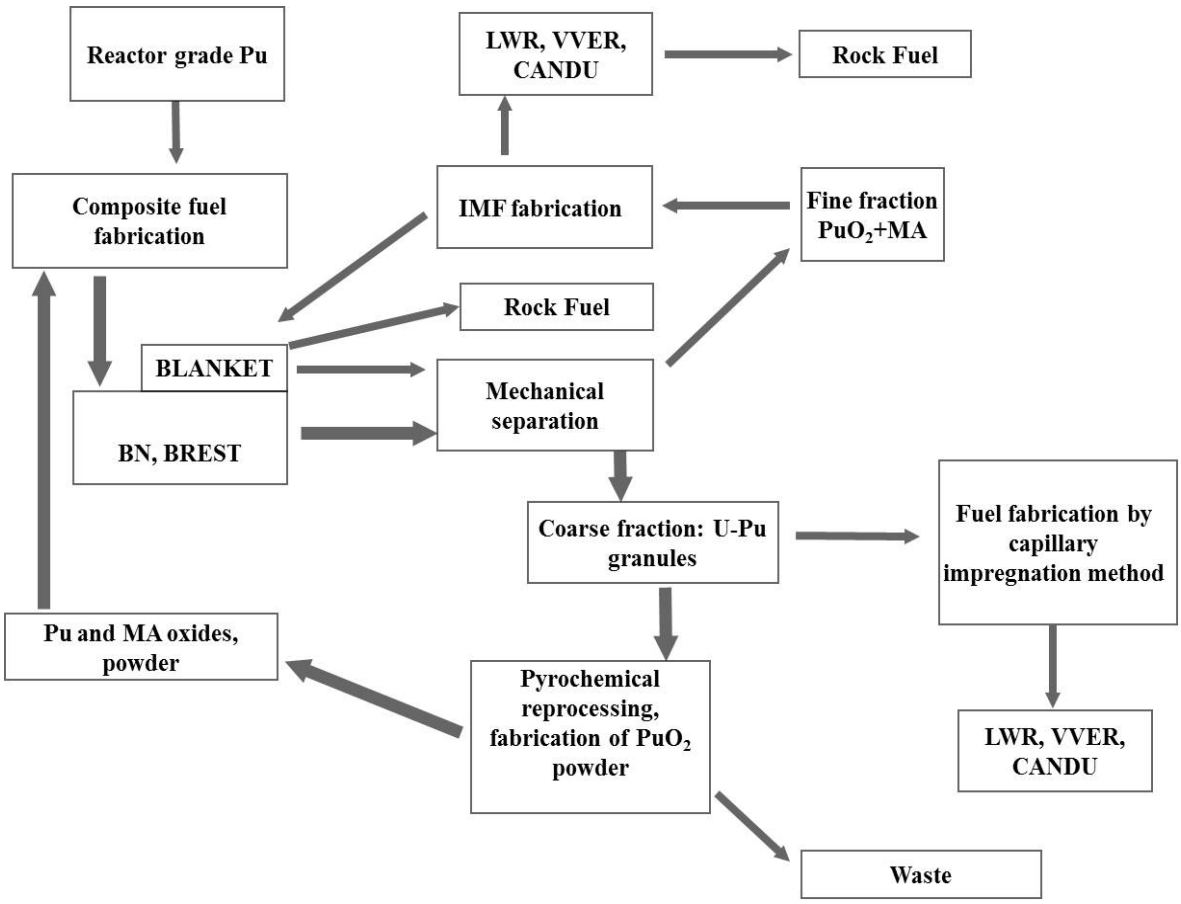

Fig. 14. Peculiarities of closing fuel cycle with composite fuel.

6. Conclusion

A possibility is considered for use in thermal and fast reactors in place of the base container type UO_2 or MOX fuel, the dispersion type fuel elements (high uranium content fuel, U-Mo, U-Nb-Zr, U_3Si with Zr alloy matrix - METMET). The use of the novel fuel in thermal reactors might result in 500 additional effective days prolongation of the campaign of fuels or in a reduced enrichment of fuel which leads to natural uranium saving as well as to increasing the conversion factor. Additionally Pu content increases more that twice in comparison with uranium dioxide pellet that makes novel fuel form to be of a potential promise for use in PWR reactors, which would considerably simplify the closing of the nuclear fuel cycle.

On the basis of METMET fuel composite U-PuO_2 fuel (an analogue of MOX) can be fabricated where depleted uranium alloy and dioxide plutonium powder have initially separate arrangement. Due to this as compared to MOX fuel the new one features higher thermal conductivity, higher uranium content, hence, high conversion ratio does not interact with fuel cladding and is more environmentally clean. Composite fuel is intended for use in fast or thermal reactors as it features higher characteristics in comparison to metallic or MOX fuel.

Novel approach to reprocessing of composite fuel is demonstrated, which allows the separation of uranium from burnt plutonium as well as the newly generated fissile plutonium from burnt one without chemical processes with repeated use in fast, PWR or CANDU reactors, which simplifies the closing of the nuclear fuel cycle. Hence in comparison to MOX we can multiply use of generated Pu in spent fuel and instead of partial recycling implement full recycling which drastically reduces the fuel waste.

Thus, the novel concept of using novel dispersion type METMET (composite) fuel in thermal or fast reactors might in future replace the currently existent approach based on the application of pelletized UO_2 or MOX fuel.

References

[1] United States Department of Energy Strategic Plan, DOE/CF-0067, May 2011. http://energy.gov/sites/prod/files/2011_DOE_Strategic_Plan_.pdf
[2] G. Ledergerber, S. Valizadeh, J. Wright, M. Limbäck, L. Hallstadius, D. Gavillet, S. Abolhassani, F. Nagase, T. Sugiyama, W. Wiesenack, T. Tverberg, "Fuel Performance Beyond Design – Exploring the Limits", Proceedings of 2010 LWR Fuel Performance/TopFuel/WRFPM Orlando, Florida, USA, September 26-29, 2010, Paper 0112.
[3] M. Arslan, A. Marincic; A. Niquille; J. Dodelier, "MOX in reactors, present and future", Global Conference September 6-10, 2009. Paris, France.
[9] M. Arslan, J. Krellmann; J. Pierre Gros, "MOX fuel recycling, present status and prospects", Global Conference Paris, France, 6-10 September, 2009.
[5] D. Crowfard, Fuels for sodium-cooled fast reactors: US perspective, J. Nucl. Mater. 371 (2007) 202-231.
[6] P. Millet, "Fast Breeder Reactors: Fuels", in Encyclopedia of Materials: Science and Technology, Elsevier Ltd., p. 2843 (2001).
[7] H. Tsai, "Behavior of mixed-oxide fuel elements during an overpower transient", J. Nucl. Mater. 204, (1993) 217-227.
[8] G.L. Hofman, L.C. Walters, T.H. Bauer, "Metallic Fast Reactor Fuels", Progress Nucl. Energy, 83(31), 1997.
[9] A. Savchenko, A. Vatulin, I. Konovalov, A. Morozov, V. Orlov, O. Uferov et. al, Dispersion type zirconium matrix fuels fabricated by capillary impregnation method, J. Nucl. Mater., 362 (2007) 356-363.
[10] A. Savchenko, I. Konovalov "METMET Fuel with Zirconium Matrix Alloys", in: Proceedings of the 7th International Conference on WWER Fuel Performance, Modelling and Experimental Support (WWER-2007), 17-21 September 2007, Albena (Bulgaria), 247-258.
[11] A. Savchenko, A.V. Vatulin, I.I. Konovalov, A.V. Morozov, V.I. Sorokin, S.V. Maranchak, Fuel of Novel Generation for PWR and as Alternative to MOX Fuel, Journal of Energy Conversion & Management, 51 (2010) 1826-1833.
[12] A.M. Savchenko, A.V. Vatulin, G.V. Kulakov, K.V. Lipkina, et al., Peculiarities of fuel cycle with advanced composite fuel for thermal reactors, (2013) ***Progress in Nuclear Energy*** [in press, available online http://www.sciencedirect.com/science/article/pii/S014919701300200X]
[13] M. Bonnet, S. Baldi, J Porta, Progress in core and cermet fuel modelling to calculate severe accidents, Prog. Nucl. Energy 38 (2001) 387-390.
[14] C Degueldre, J.M Paratte, Concepts for an inert matrix fuel, an overview, J. Nucl. Mater., 274 (1999) 1-6.
[15] A. Savchenko, A. Vatulin, A. Morozov, G. Kulakov, A. Laushkin, S. Maranchak, Y. Konovalov, E. Malamanova, Zirconium matrix alloys as innovative material for different types of fuel, Prog. Nucl. Energy, 57 (2012) 138-144.
[16] A.M. Savchenko, A.V. Vatulin, I.I. Konovalov, E.M. Glagovsky, O.I. Uferov, A.V. Morozov, New Concept of Designing Pu and MA Containing Fuel for Fast Reactors, J. Nucl. Mater., 385 (2009) 148-152.
[17] A.M. Savchenko, A.V. Vatulin, O.I. Uferov, E.M. Glagovsky, I.I. Konovalov, A.V. Morozov, V.I. Sorokin, New Concept of Designing Combined Fuel for Fast Reactors with Closing Fuel Cycle, in: Proceedings of the 10th US-Russian Workshop on "Fundamental Properties of Plutonium" 12-16 July 2010, Moscow (Russia) 271-278..
[18] Bo Feng, Eugene Shwageraus, Benoit Forget, Mujid S. Kazimi, Light Water Breeding with Nitride Fuel, Prog. Nucl. Energy, 53 (2011) 862-866.
[19] Y. Takada, Y. Shimazu, A Study on Nuclear Characteristics of METMET Fuel, Proceedings of the Third International Symposium on Innovative Nuclear Energy Systems (INES-3), 31 October – 3 November 2010, Tokyo, Japan.
[20] A.M. Savchenko, A.V. Vatulin, E.M. Glagovsky, I.I. Konovalov, A.V. Morozov, A.V. Kozlov, S.A. Ershov, V.A. Mishunin, G.V. Kulakov, V.I. Sorokin, A.P. Simonov, Z.N. Petrova, V.V. Fedotov, Main Results of the Development of Dispersion Type IMF at A.A. Bochvar Institute, J. Nucl. Mater., 396 (2010) 26-31.
[21] A.M. Savchenko, A.V. Vatulin, A.V. Morozov, I.V. Dobrikova, S.A. Ershov, S.V. Maranchak, Z.N. Petrova, Y.V. Konovalov, IMF with low melting point zirconium brazing alloys, J. Nucl. Mater., 352 (2006) 334-340.
[22] Lipkina, K., Savchenko, A., Skupov, M., Glushenkov, A., Vatulin, A., Uferov, O., Ivanov, Y., Kulakov, G., Ershov, S., Maranchak, etc, Metallic inert matrix fuel concept for minor actinides incineration to achieve ultra-high burn-up, Journal of Nuclear Materials, volume 452, issue 1-3, year 2014, pp. 378 – 381
[23] V.M. Oversby, C.C. McPheeters, C. Degueldre, J.M. Paratte, Control of civilian plutonium inventories using burning in a non-fertile fuel, *J. Nucl. Mater. 245 (1997) 112*
[24]J . Porta, J.-Y. Doriath, Toward very high burnups, a strategy for plutonium utilization in pressurized water reactors, *J. Nucl. Mater. 274 (1999) 153*
[25] R.P.C. Schram, R.R. van der Laan, F.C. Klaassen, K. Bakker, T. Yamashita, F.Ingold, The fabrication and irradiation of plutonium-containing inert matrix fuels for the 'Once Though Then Out' experiment, *J. Nucl. Mater. 319 (2003) 118*
[26] M.A. Pouchon, M. Nakamura, C. Hellwig, F.Ingold, C. Degueldre, Cermet sphere-pac concept for inert matrix fuel, *J. Nucl. Mater. 319 (2003) 37*

A thermal analytical study of the phase stability of unalloyed and alloyed plutonium.

S. M. Ennaceur

AWE, Metallurgy group, Aldermaston, Reading RG7 4PR - email: Sue.ennaceur@awe.co.uk

The focus of this work was to investigate the phase stability of two homogeneous fully δ-phase stabilised plutonium gallium alloys of different composition, a Pu-1 at% Ga alloy and a Pu-2 at% Ga alloy, following low temperature treatment and applied pressure.

On cooling the alloys to subambient temperatures, a partial transformation of the δ-phase to α-phase occurs [1]. This phase is referred to as α'-phase as it differs from the α-phase of the unalloyed plutonium in that its lattice is expanded by the gallium atoms occupying substitutional positions [2]. A number of comprehensive studies have reported that the α'-phase, which is induced by low temperature conditioning in Pu-2at% Ga alloys, will revert directly to the δ-phase via a martensitic cascading transformation mechanism, which is evidenced by a series of endothermic peaks [3,4,5]. In contrast, the transformation back to δ-phase of α'-phase induced in Pu-1at% Ga alloys following low temperature treatment, has been shown to occur via competing mechanisms: direct path of α'-phase to δ-phase (martensitic) and indirect α'-phase to β-phase to γ-phases and to δ-phase (following a series of nucleation and growth mechanisms) (Fig 1). Isothermal XRD experiments combined with simulations (CALPHAD method) revealed that the competition between direct and indirect reversion of α'-phase back to δ-phase, appeared to be governed by time dependant gallium diffusion [6,7]. Thermodynamic calculations showed that the direct reversion path would become more favourable as a function of increase in heating rate which would afford less time for the gallium atoms to diffuse.

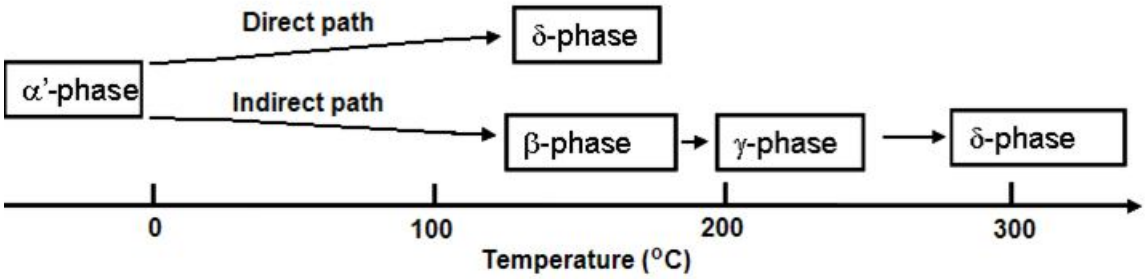

Figure 1. Diagram showing the competing direct and indirect reverse transformation paths of low temperature induced α'-phase back to the δ-phase.

This study has demonstrated how differential scanning calorimetry (DSC) can be used advantageously, to differentiate between the different mechanisms and transformation paths of α'-phase induced in Pu-1at% Ga alloys, following low temperature treatment. The isothermal and athermal character of the different mechanisms can been used to distinguish between them and therefore by conducting recovery anneals, inducing isothermal transformation and optimising the heating rates for each transformation, a different mechanism (a martensitic or a nucleation and growth mechanism) and transformation path (direct or indirect) may be favoured [8]. Determining the transformation path allows the impact of induced α'-phase in a δ-phase stabilised alloy to be evaluated. It provides an understanding as to whether the induced α'-phase transforms directly back to the δ-phase and therefore only has a short lived impact on the material properties of the alloy or if it is likely to cause a greater and longer term impact by requiring heating to higher temperatures (360°C) and several phase transformations to revert back to the δ-phase.

On subjecting the alloys to compressive pressure from 100-300MPa, a significant percentage of α'-phase was induced in the Pu-1at% Ga alloy specimens, whereas no detectable levels of α'-phase were recorded in specimens of the Pu-2at% Ga alloy. However on thermally cycling the specimens from ambient to temperatures within the β-phase stability range, α'-phase was detected in the Pu-2at% Ga alloy as well. Furthermore a significant increase in α'-phase was recorded as both alloys were subjected to an increasing number of thermal cycles (Fig 2). The increase in α'-phase content reached a plateau after a given number of cycles for each of the alloys. The Pu-2at% Ga alloy does not appear to have initially transformed under the compressive stress applied. However there is a hidden impact in that the alloy has been seeded with α'-phase embryos that grow to produce increasing amounts of α'-phase when given sufficient stimulus. The transformation of δ-phase to α'-phase initiated by compressive pressure in the 100–300MPa range has the characteristics of a martensitic mechanism with the α'-phase forming by short busts which appears to be stress driven. The stress to drive the transformation is generated on heating the specimens through the α'-phase to β-phase transformation and on cooling the specimens through the β-phase to α'-phase transformation, with the associated large volume changes. The transformation of the α'-phase, induced by compressive pressure in the 100–300MPa range and thermal cycling, back to the δ-phase in the Pu-1at% Ga and Pu-2at% Ga alloys followed an indirect path [9].

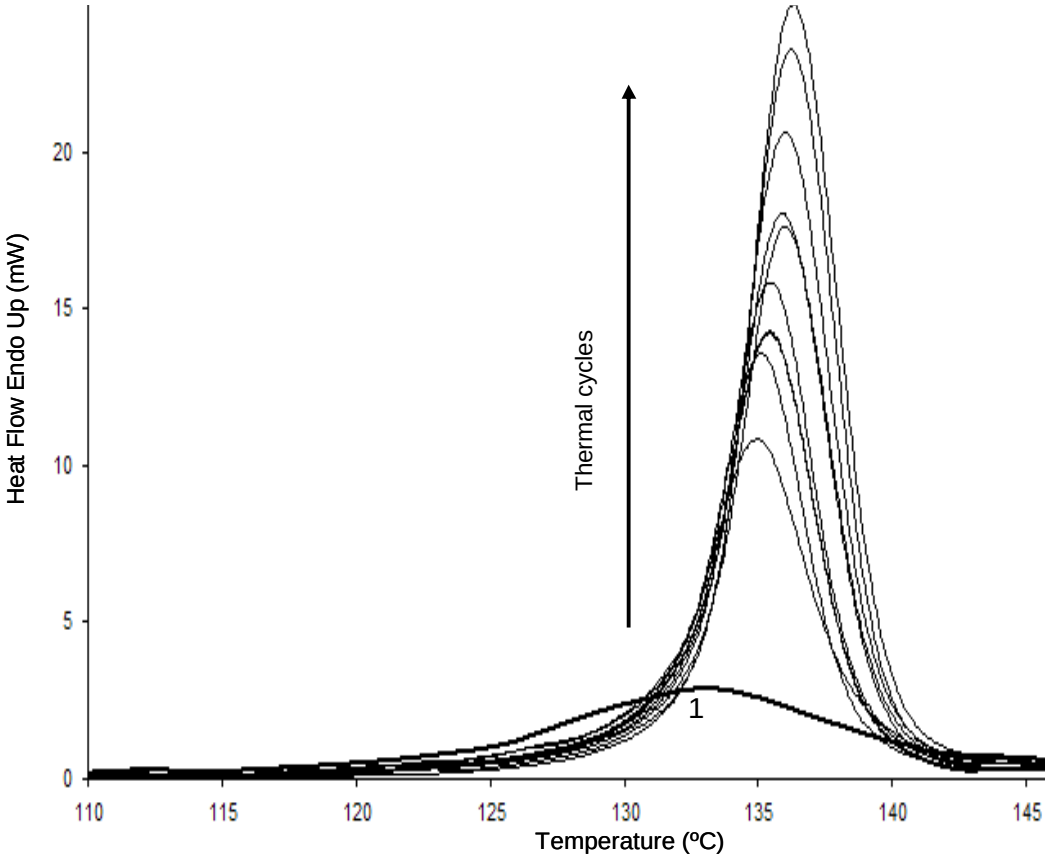

Figure 2. DSC thermograms for a same specimen of Pu-1at% Ga alloy revealing an increase in α'-phase as a function of thermal cycling after the specimen was subjected to compressive stress < 300MPa.

On increasing the compressive pressure to 600±50MPa, the percentage of α'-phase induced in the Pu-1at% Ga alloy showed a significant increase. However on thermally cycling the specimens the α'-phase content decreases to comparable levels as that obtained for the lower pressure regime followed by thermal cycling. In excess of 20% of the α'-phase which transformed on heating to the β-phase (following the indirect transformation path) appears to have reverted back to the δ-phase on cooling to ambient temperatures. Increasing the compressive pressure to

600±50MPa in specimens of Pu-2at% Ga alloy induced α'-phase to form. Thermal analysis revealed that two different transformations were occurring with a portion of the α'-phase formed in the Pu-2at% Ga alloy, transforming directly back to the δ-phase and the remainder transforming to the β-phase (indirect path) (Fig 3). Furthermore on cooling the specimens to ambient temperatures about 50% of the β-phase formed appeared to have reverted back to the δ-phase. It would appear that the α'-phase formed as a consequence of the increase in compressive pressure has different degrees of stability which would be dependant on the microenvironment of the α'-phase particles formed and the capacity of the δ-phase matrix to accommodate the induced α'-phase [9].

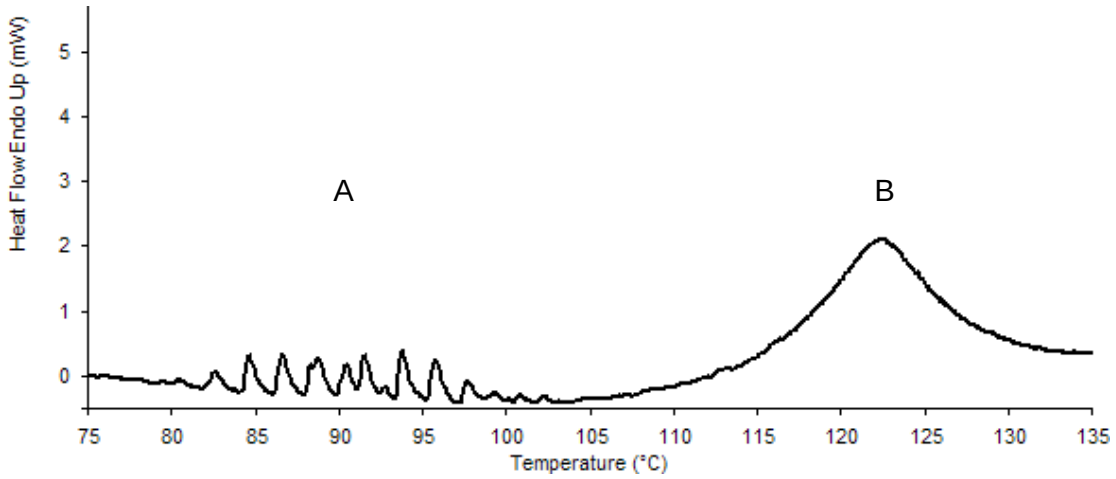

Figure 3. DSC thermogram revealing (A) the direct α'-δ phase (burst) transformation and (B) indirect α'-phase transformation in a specimen of the Pu-2at% Ga alloy after being subjected to compressive stress of 600±50MPa.

[1] A. Goldberg, R.L. Rose and J. C. Shyne, Effects of stress and plastic deformation on the transformation of the delta phase in a Pu-1at% Ga alloy, J. Nucl. Mater., 55 (1975), 33.

[2] S.S Hecker, D.R. Harbur and T.G. Zocco, Phase stability and phase transformations in Pu-Ga alloys, Progress in material Science, 49, (2004), 429.

[3] J.R. Jeffries, K.J.M. Blobaum, M.A. Wall and A.J. Schwartz, Reproducible phase transformation in a single Pu-1.9 at% Ga specimen, J. Nucl. Mater., 384, (2009), 222-225.

[4] K.J.M. Blobaum, C.R. Krenn, J.N. Mitchell, J.J. Haslam, M.A. Wall, T. B. Massalski, A. J. Schwartz, Evidence of transformation bursts during thermal cycling of a Pu-Ga alloy, Metall, Mater, Trans. 37A (2006), 567-577.

[5] J.N. Mitchell, M. Stan, D. S. Schwartz and C. J. Boehlert, Phase stability and phase transformations in plutonium and plutonium-gallium alloys, Metall, Mater, Trans. 35A (2004), 2267-2278.

[6] B. Ravat, B. Oudot, A. Perron, F. Lalire and F. Delaunay, phase transformations in PuGa 1at% alloy, Study of whole reversion process following martensitic transformations, J. Alloys and compounds, 580, (2013), 298-309.

[7] A. Perron, B. Ravat, B. Oudot, F. Lalire, K. Mouturat and F. Delaunay, phase transformations in Pu-Ga alloy, Synergy between simulations and experiments to elucidate direct and indirect

reversion competition, Acta. Mater., 61, (2013), 7109.

[8] S. M. Ennaceur, Phase stability of α'-phase in a Pu-1 at% Ga alloy following low temperature treatment, Thermochim. Acta, 593, (2014), 22-29.

[9] S. M. Ennaceur, Impact of compressive pressure on the phase stability and transformation behaviour of d-phase stabilised plutonium alloys, Thermochim. Acta, 601, (2015), 17-28.

Characterization of minor actinide doped uranium oxide fuels: Raman spectroscopy approach

M. Naji, D. Manara, O. Benes, J-Y. Colle, R. Konings

European Commission, Joint Research Centre, Institute for Transuranium Elements, P.O. Box 2340, 76125 Karlsruhe, Germany
Mohamed.naji@ec.europa.eu, Dario.manara@ec.europa.eu

The versatility of Raman scattering spectroscopy and its ability to provide structural information of even small-size objects allowed its application to radioactive environments. The investigation of nuclear fuel (UO_2, mixed actinide systems) and spent nuclear fuel by Raman spectroscopy began to be widely used in numerous laboratories.[1, 2] This has been usually carried out by connecting the Raman spectrometer with an optical head or a microscope inside a radioactive shielded cell through an optical fiber. In fact, this approach allows the measurement of highly radioactive samples but in turn limits the flexibility of the Raman analysis on one hand and becomes more expensive on the other hand (high maintenance costs due to radiation damage of the set-up) .

In order to overcome these drawbacks, JRC - ITU has recently developed a new technique allowing the measurement of radioactive samples without the nuclearisation of any part of the Raman spectrometer, just by local confinement, in an alpha-radiation shielded cell, of the nuclear materials in order to protect the user against ingestion or incorporation.[3]

In this paper, we present a simple local confinement approach and we report a Raman study of incorporated minor actinides (MA), that is, Np, Am in uranium dioxides. These materials (U, Am)O_2 and (U,Np)O_2 are currently object of many studies due to their potential use as special nuclear fuel for the transmutation of minor actinides and the consequent significant reduction of the spent fuel long-term activity. Presence of oxygen defects, stability of fluorite structure with the Am, Np content will be discussed. Energy dependence of different Raman active modes and resistance to oxidation under laser beam will be also exposed.

References

[1] C. Jégou, R. Caraballo, S. Peuget, D. Roudil, L. Desgranges, M. Magnin, *Journal of Nuclear Materials* **2010**, *405*, 235.
[2] G. Guimbretière, L. Desgranges, A. Canizarès, R. Caraballo, F. Duval, N. Raimboux, R. Omnée, M. R. Ammar, C. Jégou, P. Simon, *Applied Physics Letters* **2013**, *103*.
[3] M. Naji, J.-Y. Colle, O. Beneš, M. Sierig, J. Rautio, P. Lajarge, D. Manara, *Journal of Raman Spectroscopy* **2015**, (submitted).

Charge distribution in doped uranium dioxide

L.Desgranges,[1] G.Baldinozzi[2], G.Dottavio[1], Y.Pontillon[1]

[1] *CEA,DEN,DEC F-13108 Saint-Paul-lez-Durance, France, e-mail: lionel.desgranges@cea.fr*
[2] *SPMS, LRC Carmen, CNRS Ecole Centrale Paris, 92290 Châtenay-Malabry,*

Because it is the most used nuclear fuel, uranium dioxide has received attention for more than fifty years. In the last ten years, the increase in calculation capacities made it possible to achieve first principles calculations of its electronic structure and to derive a correct simulation of many of its thermodynamic properties. However simulation of actual irradiated fuel with the same level of accuracy requires modelling the transfer of electronic charges that occurs in UO_2 when it is irradiated and chemically doped by fission products. In most studies it is widely admitted that uranium dioxide could incorporate large amounts of 3+ cations produced by fission without any change in its crystalline structure because the 3+ cations take U^{4+} position and the charge mismatch is compensated by the formation of U^{5+} or oxygen vacancies.

In this contribution we demonstrate that this assumption is not true in the case of the U-Nd-O system. A miscibility gap was evidenced in this system for Nd concentration as low as 6 at % [1]. Thus the existence of two coexisting phases with different contents in oxygen and neodymium for a sample having $(U,Nd)O_{2\pm x}$ composition implies that a different mechanism for charge transfer should be considered for each phase. The coexisting phases in the miscibility gap have different cell parameters that were modelled with ionic radii of Nd^{3+}, U^{4+} ,U^{5+}, O^{2-} and V_O [2]. In the thermodynamic modelling of U-Nd-O phase diagram, the miscibility gap arises from positive exchange Gibbs energy, notably between U^{5+} and Nd^{3+} [2]. In both cases U^{5+} oxidation state plays a key role. U^{5+} incorporation in UO_2 can also be viewed through the analysis of the U_4O_9 crystalline structure in which it is associated to clusters of interstitial oxygen atoms [3].

These results suggest that 3+ cation incorporation in UO_2 would not be a simple substitution on uranium crystalline site and could be associated with the existence of complex defect clusters.

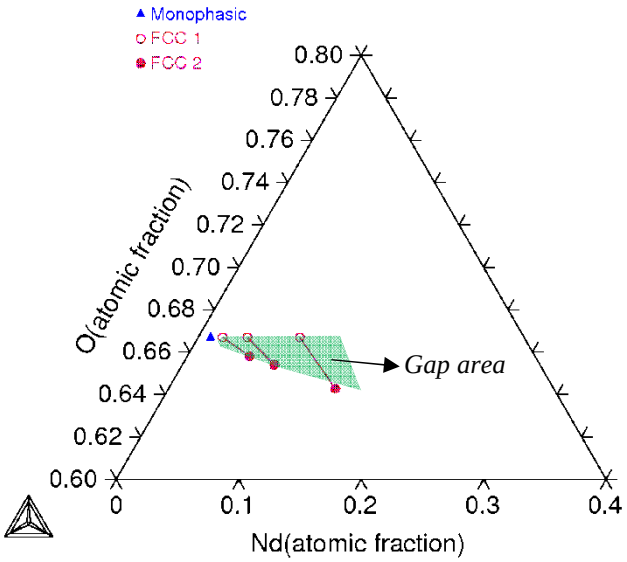

Fig. 1. Miscibility gap in U-Nd-O system (experimental results) [1]

References

[1] G. Dottavio et al. Progress in Nuclear Energy 72 (2014) 22-26
[2] G. Dottavio et al. J. Nucl. Mater 458 (2015) 394–405
[3] L. Desgranges et al. Inorg. Chem. 489 (2009) 7585–7592

Hydrothermal Synthesis of Actinide Dioxide at Low Temperature and Their Physicochemical Studies

T. Yamamura[1], K. Shirasaki[1], D.X. Li[2], Y. Homma[2]

[1] *Institute for Materials Research, Tohoku Univ.[1], 2-1-1, Katahira, Aoba, Sendai, Miyagi 980-8577, Japan, e-mail: yamamura@imr.tohoku.ac.jp*

[2] *Oarai Center, Institute for Materials Research, Tohoku Univ.[1], Oarai, Ibaraki 311-1313, Japan*

Hydrothermal synthesis in supercritical water is widely used for the production of nanoparticles of single and complex metal oxides [1]. During our study to apply thehydrothermal synthesis of UO_{2+x} in terms of the preparation of the nuclear fuel, a control of the crystalline form, particle size, and O/U ratio was achieved under the supercritical condition of 347°-226 atm [2]. In our recent study, the preparation of UO_{2+x} was found to proceeds under very mild condition of down to 60° by the addition of a certain type of aldehyde (Fig. 1) to U(IV) solution [3]. The product of UO_{2+x} obtained at low temperatures shows a larger value of non-stoichiometry x (Fig. 3) and also an inclusion of organic components: the component was found as $UO_{2.1}(C_5H_5O_{2.5})$ for cyclohexylcalbaldehyde as additive. From the susceptibility measurements, the product obtained at 450°C ($x \sim 0.06$) shows a contribution of paramagnetic U^{5+}, in contrast to that obtained at 140°C ($x \sim 0.12$) shows a contribution of diamagnetic U^{6+} (Fig. 2) . The low-temperature hydrothermal synthesis with aldehyde will motivate us to a new challenge not only for a new fabrication method of the nuclear fuel, but also for a preparation method of inorganic-organic hybrid materials.

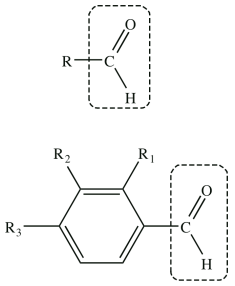

Figure 1: Aldehydes studied in this study

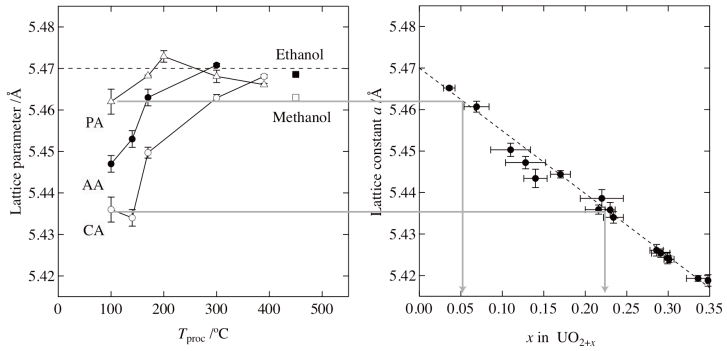

Figure 2: Lattice parameters determined for samples prepared with vairous additives and temperatures and their comparison with previous report [4]

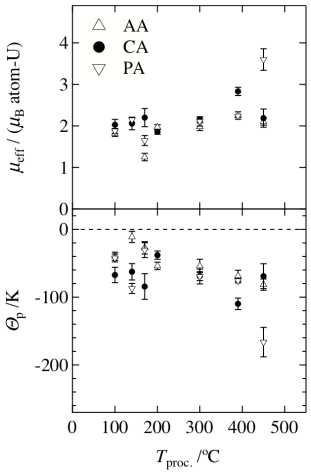

Figure 3: Effective magnetic moments obtained by MCW analysis (top) and Weiss-temperature (bottom)

References

[1] T. Adschiri, K. Kanazawa, K. Arai, *J. Am. Ceram. Soc.*, **75** 1019 (1992).
[2] T. Yamamura *et al.*, PCT/JP2009/055458 (2009).
[3] T. Yamamura *et al.*, PCT/JP2011/064954 (2011).
[4] V. A. Alekseyev, L. A. Anan'yeva, R. P. Rafal'skiy, *Int. Geology Rev.*, **23** 1229 (1981).

Thermochemisty of reactor materials: actinide oxides and fission compounds

Emily E. Moore, and Rudy J.M. Konings

European Commission, Joint Research Centre, Institute for Transuranium Elements, P.O. Box 2340, 76215-Karlsruhe, Germany, e-mail: emily.moore@ec.europa.eu

The thermochemistry of the actinide elements is a key component to understanding the behaviour of nuclear fuel components for reactor safety. The most common fuel types are in the form of actinide oxide species, namely UO_2 and a mixed $(U,Pu)O_2$. Minor actinide inclusion in the form of neptunium and americium are also considered to ease the burden of waste toxicity. These complexes have been the subject of various reviews [1,2] conducted by agencies including the international atomic energy agency (IAEA) and nuclear energy agency (OECD/NEA), who continues to pursue the topic with respect to newly developed data. These reviews present an important basis as the physical properties of reactor materials are determined by their chemical makeup and state. The main focus of these works is to create a comprehensive assessment of available thermodynamic data such as formation enthalpies, standard entropy and heat capacity data, as tabulated and reviewed in [3]. Properties such as the volatile nature of the actinide complexes as well as other fission products (FP's) play a principle role in being able to predict possible outcomes of gaseous release into the atmosphere (i.e. source term) in the case of an accident scenario. Many computational models rely on the chemical thermodynamic descriptions of fuel components and FP's as their behaviour is influenced by variations in temperature, pressure and composition. This work aims to further the current state of assessed data by providing an update and overview of currently available experimental data. A critical review, analysis and assessment of this data provide an important reference bank for these materials. The assessment will be based on fundamental thermodynamic functions including entropy, enthalpy and the Gibbs energy function of the systems. Experimental measurements of incremental enthalpies and heat capacities, equilibrium pressures and constants as well as formation energies and dissociation pressure allow for a complete description at equilibrium for a wide range of temperatures and compositions of the phases of the multicomponent systems considered. The systems under investigation include the fuel components such as UO_2, PuO_2, AmO_2 (and their elemental counterparts), in addition to fission products or containment materials (Zr, Tc, Se, Te) etc. and their oxide compounds. Experimental techniques such as various calorimetric methods (drop, adiabatic, differential scanning and combustion) as well as Knudsen effusion, mass spectrometry and dissociation pressure measurements are considered for their thermodynamic properties and evaluated based on consistency using the third-law method. Gas phase properties are calculated using spectroscopic measurements and molecular constants, at times ab initio techniques are taken into account where data is lacking or completely unavailable.

References

[1] J. Fuger, V.B. Parker, W.N. Hubbard and F.L. Oetting. *The Chemical Thermodynamics of Actinide Elements and Compounds*, IAEA, (1983)

[2] R. Guillaumont, T. Fanghänel, V. Neck, J. Fuger, D.A. Palmer, I. Grenthe and M.H. Rand *Update on the Chemical Thermodynamics of Uranium, Neptunium, Plutonium, Americiuum and Technetium (2003) (Elsevier)*

[3] E.H.P. Cordfunke and R.J.M. Konings,*Thermochemical Data for Reactor Materials and Fission Products,* (1990) (North Holland).

Magnetic properties and superconductivity of americium metal under pressure

Povzner A. A., Volkov A. G., Golubeva L. R.

Ural Federal University, Mira str. 19, 620002 Ekaterinburg, Russia
e-mail: a.a.povzner@urfu.ru

According to the rule of Hill [1] the electronic system of phase of metallic americium - AmI is related to the crossover region of superconductivity and magnetism. Its magnetic susceptibility sharply increases with decreasing temperature near the critical temperature (T_c). With increasing pressure there are four phases of americium AmI (dhcp), AmII (fcc), AmIII (Fddd) and AmIV (Pnma) [2]. The superconductivity, the temperature of which is strongly dependent on the applied pressure [3], is observed in all of these phases. However the question of the mechanism of superconductivity in phases of americium still remains open even for normal phase.

In the present study, the temperature dependence of the magnetic susceptibility is investigated with respect to the possibility of singlet pairing of f-electrons by means of the paramagnons exchange in the framework of the spin-fluctuation theory and models of the electronic structure of the americium phases obtained in the approximation LDA + U [4]. The calculation is carried out in the framework of the Hubbard model, where Hamiltonian is written in terms of the operators of spin and charge densities:

$$H = \sum_{\mathbf{k}\sigma} \varepsilon_{\mathbf{k}} a^{+}_{\mathbf{k},\sigma} a_{\mathbf{k},\sigma} + U \sum_{\mathbf{q}} \left| \mathbf{S}_{\mathbf{q}} \mathbf{e}_{\mathbf{q}} \right|^2 - U \sum_{\mathbf{q}} \left| N_{\mathbf{q}} / 2 \right|^2 , \qquad (1)$$

where $\varepsilon_{\mathbf{k}}$ is one-electron spectrum, $a^{+}_{\mathbf{k},\sigma}\left(a_{\mathbf{k},\sigma}\right)$ is the birth (annihilation) operator of electrons with quasi-impulse **k** and spin quantum number σ, U is the Coulomb interaction between electrons, $\mathbf{S}_{\mathbf{q}}$ is the Fourier transform of the operator of the spin-density vector of the electrons, $\mathbf{e}_{\mathbf{q}}$ is the random unit complex vector along the quantization axis of the Fourier transform of the spin density operator, $N_{\mathbf{q}} = \sum_{\sigma} N_{\mathbf{q},\sigma}$, $N_{\mathbf{q},\sigma} = \sum_{\mathbf{k}} a^{+}_{\mathbf{k},\sigma} a_{\mathbf{k}+\mathbf{q},\sigma}$ is the Fourier transform of the density operator of electrons per site, **q** is quasi-impulse.

The calculation of the normal and anomalous Green's functions has been carried out in approximation of homogeneous local fields in the perturbation theory:

$$G_{k,\sigma} = G^{(0)}_{k,\sigma} + \xi^2_{\perp} G^{(0)}_{k,\sigma} F^{(\sigma\bar{\sigma})}_{k,\sigma} \sum_q \left(F^{(\sigma\bar{\sigma})}_{k+q}\right)^{+} + G^{(0)}_{k,\sigma} \left(F^{(\sigma\bar{\sigma})}_{k}\right)^{+} \sum_q \left(\overline{\left|\delta\xi_{q,\perp}\right|^2} \right) F^{(\sigma\bar{\sigma})}_{k+q} -$$
$$- G^{(0,l)}_{k,\sigma} F^{(\sigma\bar{\sigma})}_{k} \sum_q \left(\left(\overline{\left|\delta\xi_{q,z}\right|^2} \right) + \left(\overline{\left|\delta\eta_{q}\right|^2} \right) \right) \left(F^{(\sigma\bar{\sigma})}_{k+q}\right)^{+} , \qquad (2a)$$

$$F^{(\uparrow\downarrow)}_{k} = \sum_{\sigma} \sigma U M F^{(\sigma\bar{\sigma})}_{k} G^{(0)}_{k,\sigma} + \xi^2_{\perp} G^{(0)}_{k,\uparrow} G_{-k,\downarrow} \sum_q F^{(\uparrow\downarrow)}_{k+q,l} + G^{(0)}_{k,\uparrow} F^{(\uparrow\downarrow)}_{k} \sum_q \left(\overline{\left|\delta\xi_{q,\perp}\right|^2} \right) G_{k+q,\downarrow} -$$
$$- G^{(0)}_{k,\uparrow} G_{-k,\downarrow} \sum_q \left(\left(\overline{\left|\delta\xi_{q,z}\right|^2} \right) + \left(\overline{\left|\delta\eta_{q}\right|^2} \right) \right) F^{(\uparrow\downarrow)}_{k+q} , \qquad (2b)$$

where $\overline{(...)}$ is procedure of averaging at the corners, $G^{(0)}_{k,\sigma}$ is Green's electron function of the normal phase, $\delta\xi_{q,\gamma} = \sum_q \delta\xi_{\nu,\gamma} \exp(iq\nu)$, ξ_{ν} is the stochastic exchange field, η_{ν} is the stochastic charge field.

The critical temperature is estimated as the temperature of the appearance of a nonzero solution of the system (2) in the lowest approximation in the anomalous averages:

$$T_C = Um_{\perp}^2 \left[\frac{U\left(\sum_{\alpha=\pm1} \alpha g_0\ (\mu + Un/2 + \alpha Um)\right)^2}{\sum_{\alpha=\pm1} g_0\ (\mu + Un/2 + \alpha Um)} - 2\kappa m^2 \right]. \qquad (3)$$

where m is the mean square amplitude of the fluctuations of the spin density of f-electrons, ($m_{\perp}$ is the mean square amplitude of the fluctuations of the transverse components of the spin density of f-electrons), $g_0(\varepsilon)$ is the density of f-states, μ is the chemical potential, κ is the spin stiffness coefficient of f-subsystem, n is the number of electrons, $n^{(ef)} = \sum_{\alpha=\pm1} \alpha \int g_0(\varepsilon) f(\varepsilon - \mu - \alpha Um + Un/2) \Big/ 2$, $f(\varepsilon-\mu)$ is the Fermi-Dirac function.

To estimate the magnetic susceptibility the term of the form $\mathbf{hS}_0$, that describes the Zeeman shift of the electron energies, should be added to the Hamiltonian (1), where $\mathbf{h}$ is vector of magnetic field, expressed in units 2μB (μB is Bohr magneton):

$$\chi(T) = \chi^{(f)} + \sum_{l=s,p,d} \chi^{(l)} + \chi^{(f)}_{orb}, \qquad (4)$$

where l=s,p,d, $\chi^{(l)} = 2g_0^{(l)}(\mu)$ is the paramagnetic susceptibility of s-, p- and d-electrons, $\chi^{(f)} = 2U^{-1}\left(1 - D_{0,f}^{-1}\right) D_{0,f}$ is the paramagnetic susceptibility of f-electrons ($D_{0,f}^{-1}$ is the inverse exchange enhancement factor of the paramagnetic susceptibility of f-electrons), $\chi^{(f)}_{orb} = \sum_{\alpha,\alpha'(=\pm1)} \frac{n_f \left[N - n_f\right]}{\left[N\left(\delta + Um(\alpha - \alpha')\right)\right]}$ is the orbital susceptibility (N is the magnitude of the orbital degeneracy of the f-band states, n_f is the filling of the f-band, δ is the average energy separation between the energies of the multiplets of the f-band).

The results of calculations for critical temperatures of different phases are listed in comparison with the experimental data in Table 1, where V_0 is the volume at atmospheric pressure.

Table 1.

Phase of americium	$V(p)/V_0$	p, GPa	T_c, K	T_c, K (experiment [3])
AmI	1	0	0,8	0,7
AmII	0,83	8	2	2,15
AmIII	0,76	11	1,8	1,8
AmIV	0,61	20	1,3	1,4

Figure 1 shows the results of the calculation of the magnetic susceptibility of americium under pressure: 0 GPa (AmI), 8 GPa (AmII), 11 GPa (AmIII) and 20 GPa (AmIV).

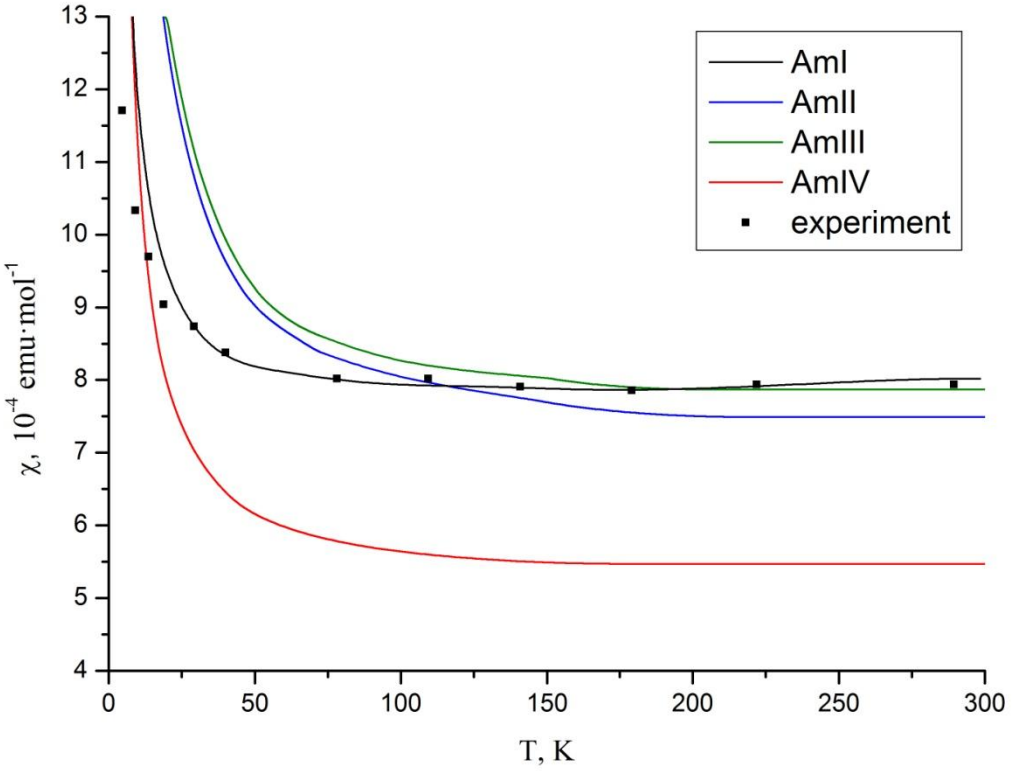

Fig. 1. Temperature dependence of the magnetic susceptibility $\chi(T)$ of americium in phases AmI, AmII, AmIII and AmIV compared with experimental data [5] on the magnetic susceptibility of AmI (p = 0 GPa).

From a comparison the theoretical results of calculations of T_c and the temperature dependence of the magnetic susceptibility it follows that in phase AmI critical temperature is higher than the temperature of the magnetic singularity of $\chi(T)$ dependence, which reflects the suppression of magnetic instability by Cooper pairing through paramagnons. The magnetic instability (to the formation of magnetically ordered ground state) disappears in phases AmII, AmIII, AmIV.

References

[1] K. T. Moore, G. van der Laan, *Rev. Mod. Phys* **81** (1), 235 (2009).
[2] S. Heathman, R.G. Haire, T.Le Bihan et al., *Phys.Rev.Lett* **85** (14), 2961-2964 (2000).
[3] J.-C. Griveau, J. Rebizant, G.H. Lander et al., PRL/V0.0-es2005jan-079 (2005).
[4] A.V. Lukoyanov, A.O. Shorikov, V.B. Bystrushkin et al., *J. Phys.: Condens. Matter* **22**, 495501 (2010).
[5] B. Kanellakopulos, A. Blaise, J. M. Fournier et al., *Solid State Communications* **17**, 713 (1975).

Correlated oscillations of the magnetic anisotropy energy and orbital moment anisotropy in thin films: the role of quantum well states

Leonid Sandratskii

Max Planck Institute of Microstructure Physics, Halle, Germany , e-mail: lsandr@mpi-halle.de

We report the first-principles study of the correlated oscillating behavior of the magnetic anisotropy energy (MAE) and orbital moment anisotropy (OMA) as the functions of the thickness N of the Fe film. The work is motivated by recent experimental studies combining photoemission, XMCD, and magnetic anisotropy measurements. In agreement with experiment, both MAE(N) and OMA(N) show oscillating behavior that has its origin in the formation of the 3d quantum well states (QWS) confined in the films. We demonstrate that the main contribution to the oscillation amplitude comes from the surface layer. This is unexpected feature of the phenomenon consisting in the peculier dependence of the physical quantities on the thickness of the film. We explane this effect by different ±m polarizability of different spatial parts of the QWS (m is magnetic quantum number of the atomic 3d orbitals). The ±m polarizability is caused by the spoin-orbit coupling (SOC) and is the origin of the atomic orbital moments. We demonstrate that the band structure of the bulk Fe cannot be used for the interpretstion of the 3d-QSW in the thin films. A detailed poin-by-point analysis in the 2D BZ shows that the contribution of the Gamma point, contrary to a rather common expectation, is not decisive in the formation of the oscillations.

Combining symmetry arguments and direct calculations we demonstrate that orbital moments of the electronic states possess non-zero transverse components orthogonal to the direction of the spin magnetization. The account for this feature is crucial in the point-by-point analysis of the OMA. On the basis of the calculations for the noncollinear spin configurations we suggest interpretations of two interesting experimental findings: fast temperature decay of the oscillation amplitude in MAE(N) and unexpectedly strong spin mixing of the intial states of the photoemission process.

Electronic properties of UT_2Al_{20} (T = d-electron element) compounds

Przemysław Swatek, Maja Kleinert and Dariusz Kaczorowski

Institute of Low Temperature and Structure Research, Polish Academy of Sciences,
P.O. Box 1410, 50-950 Wrocław, Poland
e-mail: P.Swatek@int.pan.wroc.pl

Nearly all the so far known aluminides UX_2Al_{20} (X = Ti, V, Nb, Ta, Cr, Mo, and W), crystallizing with the cubic $CeCr_2Al_{20}$-type crystal structure, were characterized in the literature as weak Pauli paramagnets. In striking contrast, the isostructural phase UMn_2Al_{20} was reported to order ferromagnetically due to the presence of magnetic moments on the manganese atom sites. In this contribution, we present the results of our calculations from first principles in the local density and local-spin density approaches, employing the full-potential local-orbital method within the density functional theory. The majority of aluminides UX_2Al_{20} exhibit very similar Fermi surface topology and similar, slightly enhanced, values of the density of states (DOS) at the Fermi level, which account well for the experimentally observed electronic contributions to their heat capacity. In contrast, DOS of the compounds with T = Cr, Mn is considerably enhanced, in accord with strong spin fluctuations that govern the ground states of both materials. The electronic structures of the UX_2Al_{20} phases will be compared with those of a few counterparts from the RX_2Al_{20} (R = La, Ce, Yb) series.

Crystal Growth and Low-Temperature Magnetic Properties of UAu_2Si_2

C. Tabata[1], S. Shimmura[1], N. Miura[1], H. Saito[1], H. Hidaka[1], T. Yanagisawa[1], Y. Ihara[1], and H. Amitsuka[1]

[1] *Graduate School of Science, Hokkaido University, N10W8 Kita-ku, Sapporo 060-0810, Japan*
e-mail: c.tabata@phys.sci.hokudai.ac.jp

The 1-2-2 uranium intermetallic compounds with $ThCr_2Si_2$-type crystal structure show various ground-state properties such as exotic magnetic order, heavy fermion states, hidden order and superconductivity. UAu_2Si_2 belongs to the 5d-family of UT_2Si_2 (T = transition metals), and has been classified as a heavy-fermion compound with a ferromagnetic ground state [1]. However, there are only 5 experimental reports on polycrystalline samples, and no further detailed 5f-electronic property has been investigated so far. Moreover, there is significant discrepancy in explanations of an upturn anomaly in the magnetic susceptibility at around 45 K, which is higher than the ferromagnetic ordering temperature T_o = 20 K [2,3]. In order to resolve the controversy and clarify the 5f-electronic properties of this compound, we have performed X-ray diffraction, magnetization, specific-heat and electrical-resistivity measurements on polycrystalline UAu_2Si_2 and on its isostructural nonmagnetic counterpart $ThAu_2Si_2$.

Our experiments have revealed that the magnetic anomaly at ~ 45 K can be attributed to a magnetic impurity, because the anomaly is seen only in the magnetic susceptibility and easily saturated by magnetic field. We found that some of the behaviours observed below T_o in the above quantities are not simply be described as usual ferromagnetic properties. As the field is increased, the magnetization shows a distinct cusp anomaly at T_o (Fig. 1) and the specific-heat jump at T_o becomes not broad but more pronounced (Fig. 2). Besides, an upturn-anomaly at T_o in the resistivity suggests opening of an energy gap on a portion of Fermi surface. We strongly suggest from the observations that the phase transition at T_o will be intrinsically antiferromagnetic, not simply ferromagnetic as reported previously. This speculation seems to be consistent with our preliminary results of ^{29}Si-NMR experiments.

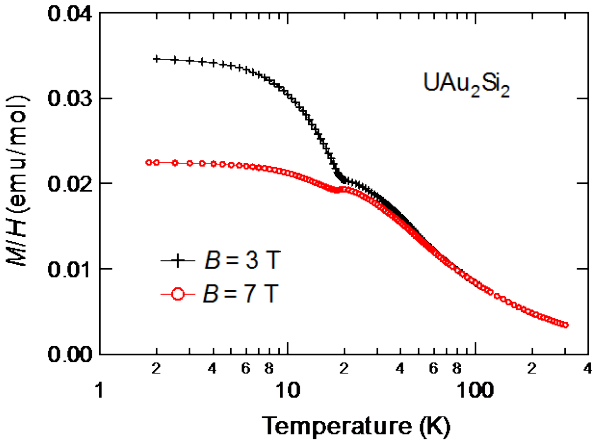

Fig. 1. Temperature dependence of magnetization divided by magnetic field of UAu_2Si_2.

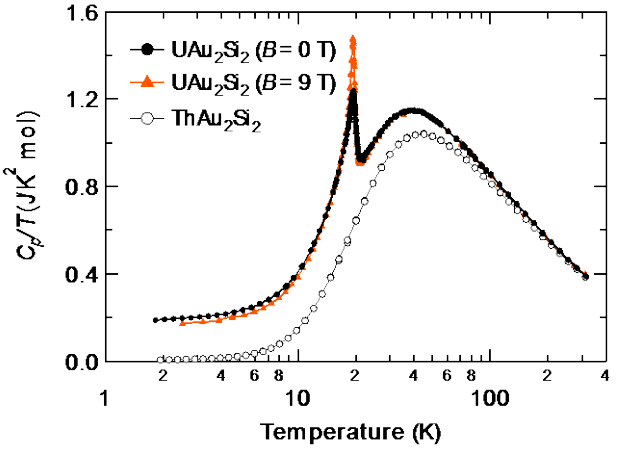

Fig. 2. Specific heat divided by temperature of UAu_2Si_2 and $ThAu_2Si_2$.

References

[1] K. J. Lin et al., Solid State Comm. 103, 185 (1997).
[2] L. Rebelsky et al., J. Appl. Phys. 69, 4811 (1991).
[3] M. S. Torikachvili et al., J. Magn. Magn. Mater. 104-107, 69 (1992).

Single crystal growth and magnetic properties of $U_3Co_4Ge_7$ and $U_3Co_2Ge_7$

Klára Uhlířová, Martin Diviš, Jiří Pospíšil, Stanislav Daniš, Vladimír Sechovský

Charles University in Prague, Faculty of Mathematics and Physics, Department of Condensed Matter Physics, Ke Karlovu 5, 121 16 Prague 2, Czech Republic

$U_3Co_4Ge_7$ and $U_3Co_2Ge_7$ have been prepared as single crystals by solution growth from tin flux. Several small crystals were grown from nearly stoichiometric amounts of U, Co and Ge from (40-50)-fold excess of Sn. The products were characterized by means of X-ray Laue single-crystal analysis, X-ray powder diffraction and EDX spectroscopy. $U_3Co_4Ge_7$ crystallizes in the tetragonal structure (I4/mmm) with lattice parameters a = 4.116 Å and c = 27.49 Å and $U_3Co_2Ge_7$ possesses the orthorhombic structure (Cmmm) with a = 4.151 Å, b = 24.98 Å, c = 4.160 Å. The crystal structures of the two compounds are closely related. Consequently, always some microscopic $U_3Co_4Ge_7$ regions have been found in the $U_3Co_2Ge_7$ samples by the EDX analysis. Reciprocal effect was not observed.

The crystals of $U_3Co_4Ge_7$ and $U_3Co_2Ge_7$ were studied by measurements of the magnetization, ac susceptibility and heat capacity on the PPMS and MPMS facilities (Quantum Design). All measurements clearly document ferromagnetism in $U_3Co_4Ge_7$ below T_C = 21 K. The second phase transition at 20.5 K, previously reported from studies of polycrystals[1], has not been confirmed neither on single-crystal nor polycrystalline samples. The magnetization and magnetic susceptibility measurements revealed strong magnetocrystalline anisotropy. The *c*-axis has a strong ferromagnetic contribution to the magnetization and was found to be the easy-magnetization direction. The value of the saturated magnetic moment in the easy direction was found to be μ_{sat} = 0.9 μ_B/U. The magnetization starts to saturate at the magnetic field of 0.35 T, and the spontaneous magnetization μ_s = 0.77 μ_B/U has been determined. The *a*-axis is the hard magnetization direction; the magnetic susceptibility is much smaller and exhibits a weak temperature dependence, the magnetization at 2 K is linear up to 7 T reaching magnetic moment μ = 0.07 μ_B/U. No spontaneous magnetization was observed in the hard magnetization direction. The susceptibility above 100 K can be described by a Curie-Weiss law with the following values of the effective moment and paramagnetic Curie temperature: μ_{eff} = 2.5 and 3.5 μ_B/U, θ_p = 20 and -190 K for the *c*- and *a*- axis components, respectively. A clear peak in the temperature dependence of the specific heat was observed indicating the presence of the magnetic phase transition at T = 21 K. The Sommerefeld coefficient γ = 100 mJ/mol-U K^2 has been determined.

$U_3Co_2Ge_7$ shows onset of magnetic ordering at 40 K; another transitions were observed at 20 K and 10 by *ac* susceptibility measurements. The transition at 20K is ascribed to impurity, the previously mentioned phase $U_3Co_4Ge_7$. The *c*-axis is the easy magnetization direction with the saturated magnetization μ_{sat} = 1 μ_B/U at 2 K. The magnetization curves show anomalous behavior; the virgin curve goes far out of the hysteresis loop and reaches higher value of saturated magnetization. The metamagnetic-like transition above 4 T offers speculations about the ground-state antiferromagnetism which is converted to ferromagnetic ordering in higher magnetic fields but cannot be restored when removing the applied magnetic field. This effect vanishes at about 10 K [].

References

K. Uhlirova, M. Divis, J. Pospisil, S. Danis, and V. Sechovsky, J Phys Soc Japan, 81, 9, (2012)

AlB_2-type related crystal structure of $UNiZnH_{2.3}$

K. Miliyanchuk[1], S. Mašková[2], S. Daniš[2], O. Stelmakhovych[3], B. Vondráčková[2], A.V. Kolomiets[2,3], L. Havela[2]

[1] *Department of Inorganic Chemistry, Faculty of Chemistry, Ivan Franko National University of Lviv, Kyryla i Mefodiya St. 6, 79005 Lviv, Ukraine, k_miliyanchuk@lnu.edu.ua*
[2] *Department of Condensed Matter Physics, Faculty of Mathematics and Physics, Charles University, Prague 2, The Czech Republic*
[3] *Department of Life Safety, Ivan Franko National University of Lviv, Doroshenka St. 41, 79000 Lviv, Ukraine*
[4] *Department of Physics, Lviv Polytechnic National University, Bandera St. 12, 79013 Lviv, Ukraine*

A large family of equiatomic ternary compounds crystallizing in the ZrNiAl structure type (ordered ternary variant of the Fe_2P type) includes numerous U*TX* compounds, where *T* is a late transition metal and *X* a *p*-block metal. So far, no representatives with Zn have been reported. Here we present the results on synthesis and crystal structure of UNiZn compounds and its hydride.

UNiZn polycrystalline sample was prepared by placing pure elements with the stoichiometry 1-1-1.02 into the quartz tube, which was sealed under argon atmosphere and subsequently inserted into the oven and heated fast to 500°C, where it was held for 1 hour. After that the sample was heated fast to 1100°C, where it was held for 26 min, and subsequently cooled down at the rate 1 °C/min to 700°C. At this temperature it was removed from the furnace. Hydrogenation of UNiZn was performed at hydrogen pressure 120 bar by heating up to $T = 473$ K only and subsequent cooling with the rate 0.5 K/min. It turned out that such conditions are not only sufficient for hydrogenation, but the amount of absorbed hydrogen estimated from the weight change is 2.3 H/f.u.

UNiZn crystallizes in the hexagonal ZrNiAl type of structure ($P\bar{6}2m$). The crystal structure parameters are summarized in the table. The shortest inter-uranium distance ($d_{U\text{-}U}$ = 3.43 Å) is in the basal plane, similar to most of other U-compounds with the same structure type. Hydrogenation leads to anisotropic crystal lattice expansion ($\Delta a/a$ = 10.9 %, $\Delta c/c$ = -2.6 %, $\Delta V/V$ = 19.7 %) with concomitant symmetry increase.

The powder diffraction pattern obtained for $UNiZnH_{2.3}$, exhibiting smaller number of reflections, clearly indicated the symmetry increase and could be indexed in the space group *P*6/*mmm* with the lattice parameters a = 4.2371(4) Å, c = 3.9520(5) Å. The transition from the space group $P\bar{6}2m$ to *P*6/*mmm* can be achieved via the shift of Ni1 atoms to the same plane as Ni2 atoms, followed by the formation of regular hexagonal nets containing Ni and Zn atoms. This modification would mean the realization of ternary ordered variant of AlB_2 structure type. The resulting unit cell for the space group *P*6/*mmm* is three times smaller compared to the one for $P\bar{6}2m$; the translation vector in the *c*-direction remains the same, whereas $a_{P\text{-}62m}/a_{P6/mmm} = \sqrt{3}$. One should keep in mind that due to the close atomic numbers of Ni and Zn their X-ray scattering cross-sections are almost equal and allocating both Ni and Zn in the presence of heavy uranium atoms is rather uneasy. The table provides the results of the crystal structure refinement for $UNiZnH_{2.3}$ in the AlB_2 structure type, assuming the statistical mixture M = 0.5Ni+0.5Zn occupying the sites inside the trigonal prisms formed by uranium atoms. However, if we assume that the hydride crystallizes with the structure directly related to the ZrNiAl structure type observed for the precursor, we may expect the ternary ordered derivative of AlB_2 structure type, namely the LiBaSi type. In this structure, the nets between the uranium layers consist of hexagons formed by strictly alternating atoms of Ni and Zn. Such an ordering would result in the realization of the space group $P\bar{6}m2$. However, this suggestion can be proved merely in the case Ni and Zn atoms can be distinguished.

Crystal structure parameters for UNiZn and $UNiZnH_{2.3}$

Compound	UNiZn	$UNiZnH_{2.3}$
Structure type	ZrNiAl	AlB_2
Space group	$P\bar{6}2m$ (189)	$P6/mmm$ (191)
Pearson symbol	$hP9$	$hP3$
The unit cell parameters a (Å) c (Å) V (Å^3)	 6.6178(2) 4.0596(1) 153.976(8)	 4.2371(5) 3.9519(6) 61.44(1)
Atomic coordinates	U (0.5747(3),0,0) Ni1 (1/3,2/3,1/2) Ni2 (0,0,0) Zn (0,220(2),0,1/2)	U (1a) (0,0,0) M (2d) (1/3,2/3,1/2)
Atomic displacement parameters (Å^2)	B_U = 1.44(5) B_{Ni1} = 2.0(3) B_{Ni2} = 2.0(3) B_{Zn} = 3.1(2)	B_U = 2.61(4) B_M = 2.67(9)
$d_{U\text{-}U}$ (Å) ∥c-axis $d_{U\text{-}U}$ (Å) basal	4.06 3.43	3.95 4.21
Reliability factors R_B; R_p (%)	 10.9; 6.79	 7.93; 6.10

M = 0.5Ni+0.5Zn

The volume expansion of $UNiZnH_{2.3}$ is almost 20 %. It realizes as a large expansion in a direction (10.9%), whereas the c-axis even shrinks (by 2.7 %), which can be compared with UNiAl (6.7% increase in a, 1.1% decrease in c for $UNiAlD_{2.1}$, $\Delta V/V$ = 12.7%). The compressibility anisotropy (or to some degree equivalent anisotropy of thermal expansion) of UNiZn and its hydride are therefore of a primary importance and corroborate existence of basic rules relating the U-U coordination with elastic anisotropy, and perhaps even with magnetic anisotropy if magnetic structure would be determined.

Thermal expansion and magnetostriction in UNiGa

Jan Prokleška, Martin Míšek, Jiří Kamarád, Jiří Prchal, Vladimír Sechovský[1]

[1] *Charles University in Prague, Faculty of Mathematics and Physics, DCMP, Ke Karlovu 5, Prague, 121 16, Czech Republic, e-mail: prokles@mag.mff.cuni.cz*

Its properties puts UNiGa on the top of the most investigated uranium compounds. Huge anisotropy, rather rich magnetic phase diagram, based on the different stacking of ferromagnetic (FM) sheets along the c-axis with its sensitivity to alloying and pressure builds up a wide playground for testing theoretical and experimental approaches.

UNiGa undergoes several magnetic phase transition in the vicinity of TN (~39K) going from incommensurate AF phase through several commensurate magnetic phase to the ground state characterized by the (++-+--) stacking [1]. With application of magnetic field (~0.7T) along the c-axis at low temperatures it undergoes transition to FM state.

In this work measurements of thermal expansion and magnetostriction measurements on single crystal sample by means of dilatometry will be present, followed by discussion of results with respect to the uniaxial and hydrostatic experiments .

References

[1] Prokeš, K., et al.,Journal of Applied Physics, **79**, 6396 (1996)

Magnetic properties of $U_2(Fe,Ni)_2Sn$ intermetallics and their hydrides

A.V. Kolomiets[1,2], S. Mašková[2], L. Havela[2]

[1] *Department of Physics, Lviv Polytechnic National University, 12 Bandera Str., 79013 Lviv, Ukraine*
[2] *Department of Condensed Matter Physics, Faculty of Mathematics and Physics, Charles University in Prague, Ke Karlovu 5, 121 16 Prague 2, Czech Republic*

$U_2(Fe_x,Ni_{1-x})_2Sn$ form a continuous series of the isostructural tetragonal compounds (Mo_2FeB_2-type, space group *P*4/*mbm*). U_2Ni_2Sn (T_N = 26 K) is an antiferromagnet with T_N = 26 K and U_2Fe_2Sn is non-magnetic. The increase of the iron content from x_{Fe} = 0 to 0.2 leads to the monotonous decrease of the Néel temperature, and the compounds with x_{Fe} > 0.2 are non-magnetic. The suppression of the magnetic ordering in $U_2(Fe_x,Ni_{1-x})_2Sn$ is accompanied by the behavior resembling the non-Fermi liquid state when the concentration dependence of the Sommerfeld coefficient comes through a steep maximum at x_{Fe} = 0.2. The temperature dependence of the specific heat at the critical Fe concentration $U_2(Fe_{0.2},Ni_{0.8})_2Sn$ has the upturn below 6 K, which could be interpreted as the crossover from the weakly-interacting spin fluctuations to the paramagnon regime around 3 K. The width of the possible NFL region could be estimated as +/-2 K since the low-*T* upturn in the specific heat is clearly observed for x_{Fe} = 0.20 and 0.21 but it disappears for x_{Fe} = 0.17.

Hydrogenation of $U_2(Fe_x,Ni_{1-x})_2Sn$ leads to the absorbtion of about 2 H atoms per f.u by all studied intermetallics with x_{Fe} = 0…0.8, which retain the original crystal structure despite the volume increase by 7% to 9.5%. Magnetic exchange is stronger in the hydrides as evidenced by the increase of the Néel temperature in U_2Ni_2Sn-H up to 87 K and the ferromagnetic ordering of $U_2(Fe_{0.8}Ni_{0.2})_2Sn$-H at T_C = 30 K. Noteworthy, the magnetic ordering of the hydrides is affected by the Fe content variation in very similar way as in the parent compounds with the critical concentration also around x_{Fe} = 0.2, although the hydrides with x_{Fe} > 0.2 are ferromagnets with almost constant $T_C \approx$ 30 K. No upturn of the low-temperature specific heat at x_{Fe} = 0.2 has observed in the hydrides. The Sommerfeld coefficients in the studied hydrides drop by at least 30% after the hydrogenation.

According to the neutron diffraction and Mössbauer studies of the Ni-based compound only the uranium atoms carry the magnetic moments of 1.05(5) μ_B/U and they are arranged collinearly in the basal plane [1]. It was also suggested that the *f-d* rather than the *f-f* hybridization has the dominating effect on the magnetic interactions in U_2Ni_2Sn. Then, considering the strengthened magnetic exchange and the reduced electronic contribution to the specific heat, one can conclude that the *f-d* hybridization is weakened in $U_2(Fe_x,Ni_{1-x})_2Sn$ upon hydrogenation.

References

[1] F. Bouree *et al.*, J. Magn. Magn. Mater., 138 (1994) 307-313.

Synthesis, structural and physical properties of a novel intermetallic compound $U_3Fe_2Ge_7$

M.S. Henriques[1,2], D.I. Gorbunov[1,3], A.V. Andreev[1], J.C. Waerenborgh[2], M. Pasturel[4], M. Dušek[1], Y. Skourski[3], L. Havela[5], A.P. Gonçalves[2]

[1]*Institute of Physics, ASCR, Na Slovance 2, 182 21 Prague, Czech Republic*
E-mail: andreev@fzu.cz
[2]*CCTN, IST/CFMCUL, University of Lisbon, Nuclear and Technological Campus, P-2695-066 Bobadela, Portugal*
[3]*Dresden High Magnetic Field Laboratory (HLD), Helmholtz-Zentrum Dresden-Rossendorf, D-01314 Dresden, Germany*
[4]*Institut des Sciences Chimiques de Rennes, Chimie du Solide et Matériaux, Université Rennes 1, UMR CNRS 6226, 263 Avenue du Général Leclerc, 35042 Rennes, France*
[5]*Charles University in Prague, Faculty of Mathematics and Physics, Department of Condensed Matter Physics, Ke Karlovu 5, 121 16 Prague, Czech Republic*

$U_3Fe_2Ge_7$ is the latest discovered intermetallic compound crystallizing in the orthorhombic isotype $La_3Co_2Ge_7$ (space group *Cmmm*). The last converging lattice parameters for $U_3Fe_2Ge_7$ from the single crystal data refinement were a = 4.171(5) Å, b = 24.990(5) Å and c = 4.157(5) Å. The asymmetric unit for $U_3Fe_2Ge_7$ consists of seven different atomic sites (two for U, one for Fe and four for Ge) with full occupancy. A scheme of the unit cell and of the uranium sublattice is presented in Fig. 1.

$U_3Fe_2Ge_7$ orders ferromagnetically as follows from the temperature dependence of the magnetization, M (inset in Fig. 2). The specific heat, C_p, indicates that the Curie temperature is T_C = 62 K and the Sommerfeld coefficient is γ = 150 mJ mol^{-1} K^{-2} (upper panel in Fig. 3). Above T_C the specific heat can be fitted using the Debye integral (red line in Fig. 3). The magnetic order also affects the electrical resistivity, ρ, whose temperature derivative displays a sharp maximum at T_C (lower panel in Fig. 3). At low temperatures both, C_p and ρ, identify a gap in the magnon spectrum of about 20 K. The corresponding fit to ρ is shown by the orange line in Fig. 3.

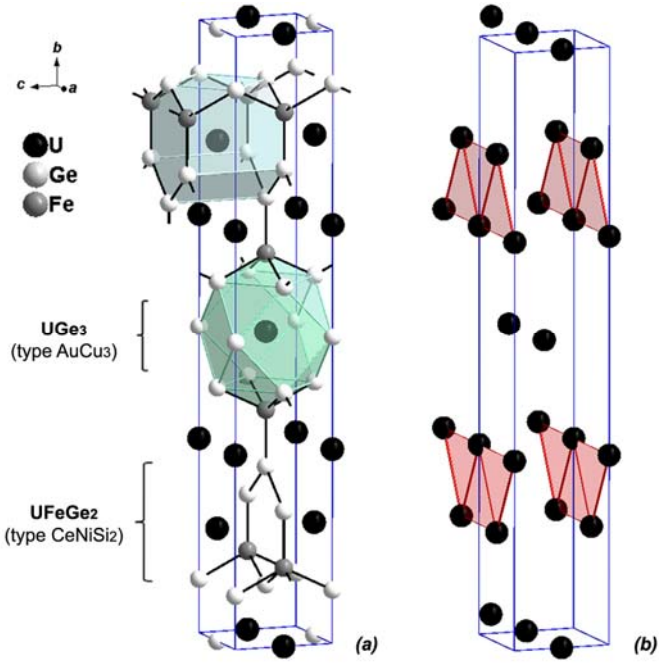

Fig. 1. (*a*) Unit cell of $U_3Fe_2Ge_7$ and coordination polyhedra for the U1 (green) and U2 (cyan) atoms. The structure can be seen as a stacking of layers of $UFeGe_2$ and UGe_3 along the *b* axis. (*b*) Uranium sublattice showing the zigzag coordination of the U2 atoms (a second unit cell was added along the *a* direction).

As typical uranium intermetallics, $U_3Fe_2Ge_7$ exhibits a strong uniaxial anisotropy. Measurements in static (up to 14 T) and pulsed (up to 60 T) magnetic fields indicate that the magnetic moments lie along the *c* axis with the spontaneous magnetic moment M_s = 3.3 μ_B/f.u. at 2 K. A strong anisotropy is present in the (*ab*) plane as well. An S-shape anomaly is observed along the *a* axis in an applied magnetic field and is reminiscent of a first-order magnetization process (FOMP). This is a type-I FOMP since immediately above the transition the magnetization reaches the easy-axis value (and even slightly exceeds it). The presence of the FOMP is outstanding since it provides a tool for description of the magnetic anisotropy despite its enormous energetic strength making its direct measurement impossible for $U_3Fe_2Ge_7$. A FOMP can be described using the relation

$HM_s = 2K_1\frac{M}{M_s} + 4K_2\left(\frac{M}{M_s}\right)^3 + 6K_3\left(\frac{M}{M_s}\right)^5$, where K_1, K_2 and K_3 are the second-, fourth- and sixth-order anisotropy constants, respectively. By fitting the experimental curves we obtained the following anisotropy constants at 2 K: K_1^a = 1.47 MJ/m^3 and K_2^a = -0.34 MJ/m^3 (K_3 = 0 for type-I FOMP). The constants decrease gradually with temperature. We should, however, underline that this anisotropy constants are obtained from the magnetization curve along the *a* axis (marked by the index "*a*") which is not the hardest axis in $U_3Fe_2Ge_7$. Estimation of K_1 from the magnetization curve along the hardest *b* axis yields a much larger value (K_1^b = 4.4 MJ/m^3) at 2 K.

Although $U_3Fe_2Ge_7$ displays strong magnetic anisotropy reflecting involvement of U in its magnetism, a Mössbauer study indicates that the Fe sublattice also carries a magnetic moment of about 0.2 μ_B per Fe atom. Assuming collinear ferromagnetic arrangement of the U and Fe sublattices, we can estimate the magnetic moment of the uranium sublattice as about 1 μ_B per U atom. This value is considerably larger than in other U-Fe-Ge intermetallics (0.5 μ_B/U in U_2Fe_3Ge [1] and 0.4 μ_B/U in $U_3Fe_4Ge_4$ [2]), but lower than in binary UGe_2 (1.5 μ_B/U [3]).

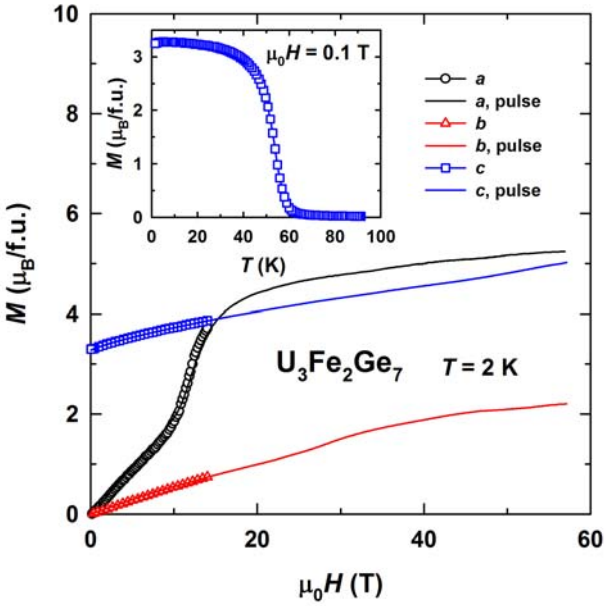

Fig. 2. Magnetization curves of a $U_3Fe_2Ge_7$ single crystal in static and pulsed magnetic fields at 2 K. The inset shows the temperature dependence of the magnetization in 0.1 T along the *c* axis.

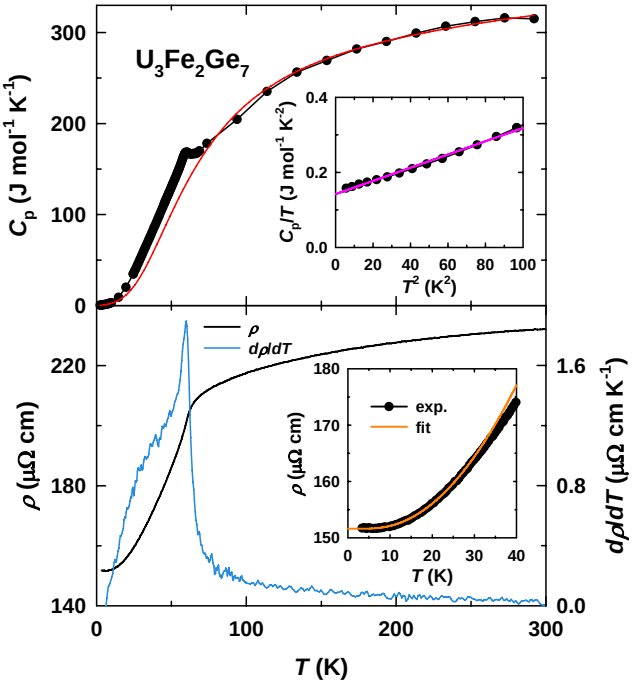

Fig. 3. Temperature dependence of the specific heat and electrical resistivity of a $U_3Fe_2Ge_7$ single crystal. The upper inset shows the $C_p/T(T^2)$ function and the lower inset the $\rho(T)$ function and its fit at low temperatures.

Acknowledgements

The work was supported by the Program of Czech Research Infrastructures (project no. LM2011025). We acknowledge also the support of HLD at HZDR, member of the European Magnetic Field Laboratory (EMFL).

References

[2] M.S. Henriques et al., J. Alloys Comp. 555 (2013) 304.
[1] M.S. Henriques et al., J. Phys.: Condensed Matter 25 (2013) Art. No. 066010.
[3] S.S. Saxena at al., Nature 406 (2000) 587.

A new thin-film approach to making nuclear fuel research accessible.

A M Adamska, W Liu, T Scott, O Payton, L Picco

Interface Analysis Centre, School of Physics, University of Bristol, HH Wills Building, Tyndall Avenue, BS8 1TL, Bristol, UK, *e-mail: am.adamska@bristol.ac.uk*

The UK nuclear industry is currently in a state of change. There are requirements to shut down and decommission existing nuclear facilities which have reached the end of their useful life, alongside requirements to maintain the existing operating facilities, safety manage nuclear waste in the long term and embark on a new build programme to underpin national energy supply. This has placed a significant demand on both current technology and the available experienced nuclear human resources within the industry. The most pressing challenges such as threat to maintaining the existing level of safety and/or security need to be addressed through nuclear research. However, undertaking nuclear research requires especially designed laboratories/facilities, safety procedures, and trained people to handle radioactive materials. This means there are high technical and 'safety barriers to entry' for people wanting to conduct nuclear research. A new thin-film approach provides a unique opportunity for fabrication and analysis of new generation nuclear fuel materials, which significantly reduces experimental risk and limitations. Thin film of uranium and related compounds samples may be used as a useful ultra-low radioactivity experimental surrogate for bulk systems [1]. They exhibit no easily detectable radioactivity and are therefore exempt from transport restrictions. In addition, thin films pose a particular benefit for studying a material. The high surface area to volume ratio means that it is possible to reduce the dimensionality such that surface effects are much more easily observable than for bulk samples. Such simplified 'model' surfaces can be exposed to different environmental conditions (gases, radiation, and temperature) and subsequently used to predict material properties and changes in their bulk counterparts. More fundamentally, the thin film approach to studying of actinide compounds may lead to better understanding of 5f electron systems. Thin film technology can also be used to isolate compounds or phases that may be more difficult to synthesise or even unknown in the bulk.

Polycrystalline and single crystals of uranium-oxide or uranium-alloy thin films – potential next generation nuclear fuel materials have already been grown using ultra-high vacuum DC magnetron sputtering [2-3]. Some of the arising single-crystals of UO_2 have been tested with heavy ion irradiation, simulating the conditions in the heart of a nuclear reactor core. The induced radiation damage was studied using a cutting-edge Electron-Backscatter Diffraction technique, revealing that significant recrystallization and development of a discrete surface nanostructure had occurring in the films. Recently, a new technique for synthesis of polycrystalline thin films has been employed. Fig. 1 and 2 show the columnar growth of an electrodeposited uranium oxide thin film on a nickel substrate produced for potential solar cell applications.

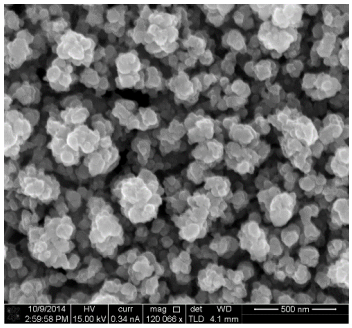

Fig. 1. Secondary electron image of UO_2 thin film electodeposited on Ni-substrates.

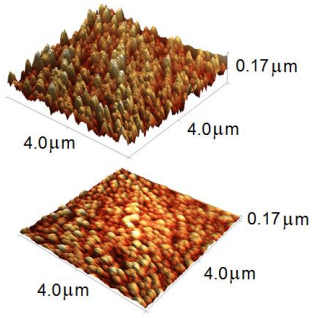

Fig. 2. High-speed AFM micrograph of UO_2 thin film electodeposited on Ni-substrates.

References

[1] A Seibert, S Stumpf, T Gouder, D Schild D and M A Denecke, *Actinide Nanoparticle Research: Actinide This films as Surface Models*, Ed. S N Kalmykov, M A Denecke, Springer-Verlag Berlin Heidelberg, 275-313 (2011).
[2] A M Adamska, R Springell and T B Scott, *Thin Solid Films* 550, 319-325 (2014).
[3] A M Adamska, T B Scott, R Springell, A Warren, L Pico and O Payton, *J. Phys. D: Appl. Phys*. 43, 315301 (2014).

Method for Low Atomic Number Sub-Micronic Film Production for keV Electron Scattering Measurements

M. Geller[1,2], I. Orion[1], A. Givon[1] G. R. Castro[3,4], J. Rubio-Zuazo[3,4] and E. Tiferet[2]

[1] *Department of Nuclear Engineering, Ben-Gurion University of the Negev, Beer-Sheva 84105, ISRAEL, e-mail: Presenting.iorion@bgu.ac.il*
[2] *Nuclear Research Center-Negev (NRCN), Beer Sheva 84190, ISRAEL*
[3] *Spanish CRG BM25-SpLine at the European Synchrotron Radiation Facility, Grenoble, FRANCE*
[3] *Instituto de Ciencia de Materiales de Madrid, Madrid, SPAIN*

Attenuating mediums, targets and barriers made of sub-micron layers with low average atomic number (Low Z) and minimal surface density that decreases elastic scattering and absorption of radiation are required for many applications with low energy experiments in physics, biology and chemistry and can be used for surface studies, electron interactions with matter researches, radiation attenuation, etc.

This work describes the development and characterization of sub-micron Lexan polymer foils with low Z for two new IMFP (Inelastic Mean Free Path) estimation methods validation experiments. 120÷240 nm Lexan layers were developed and fabricated from 1.56, wt.% solution by using Spin Coating on glass substrates.

The sub-micron layers were characterized by AFM and CSI, for thickness, roughness and levelness (Fig. 1). Roughness found to be, overall 10 ± 1 nm rms, local 1.0 ÷ 2.4 nm rms, total thickness change within ± 7.5%. To test the foil and its suitability for IMFP, "Total Current Measurement" experiment, 177 nm Lexan foil was coated with 7 nm gold layer and irradiated under 1÷15 keV SEM electron beam in a comparative experiment to one that was conducted in the past with Polyimide Quantomix® foil [1] (Fig. 2).

The integral electron current attenuation was measured and same behavior for both foils was observed, meaning, energy shift from inelastic scattering and typical attenuation form to a measured thickness. As the foil was well characterized, threshold values needed for the experiments were set. Foil durability was tested by attempt to penetrate it with the electron beam without success. Observation with HR SEM revealed no findings.

A first step of “Wide Spectrum" experiment was performed at ESRF. The spectrum on Lexan showed the signal peak, as well as the multi inelastic scattering peak (MIC peak) similar to previous measurements on carbon films [2]. The Lexan photoelectrons spectrum is shown in Fig. 3.

This work supported the suitability of the developed Lexan foil, for SEM experiments, and allows the continuing of "Total Current Measurement" experiments to evaluate IMFP as well as being an essential landmark in approving the foil for "Wide Spectrum" ongoing study at the ESRF synchrotron.

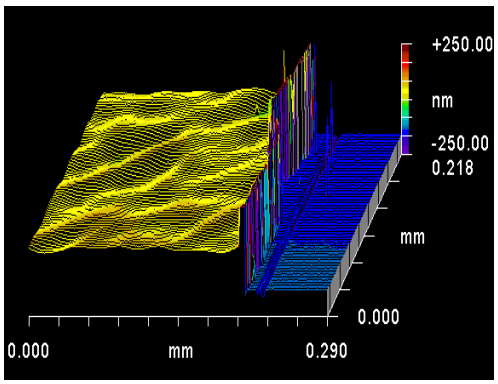

Fig. 1 CSI image of typical 0.2 x 0.2 mm Lexan film.

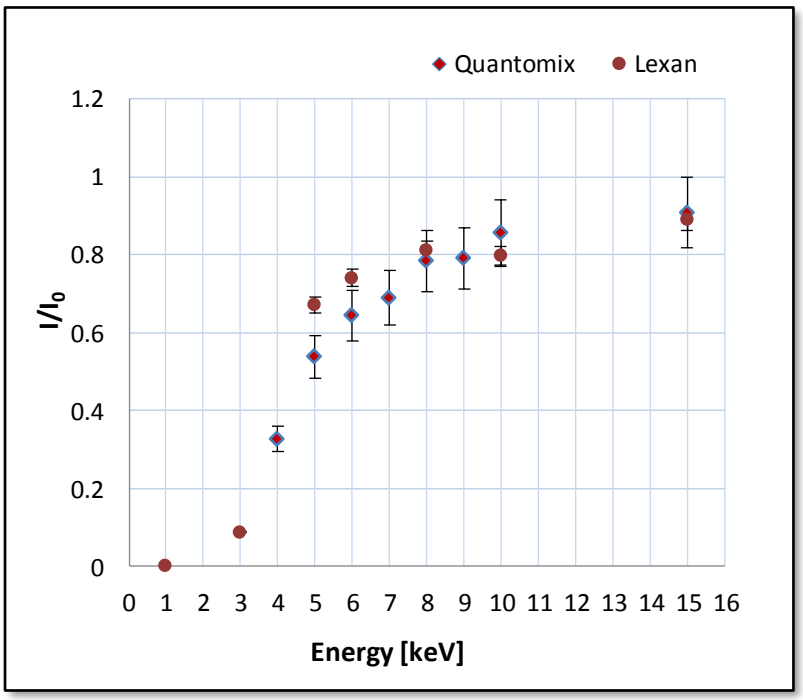

Fig. 2 Total Current experiment results for 177 nm Lexan foil was coated with 7 nm gold layer in SEM compared to 177 nm Polyimide Quantomix® foil results.

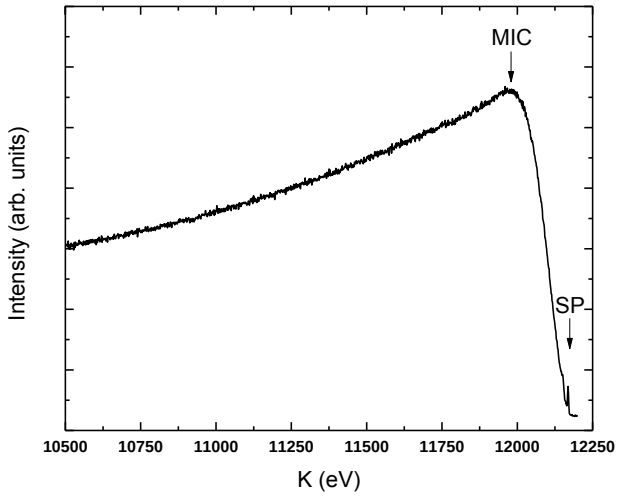

Fig. 3 The Lexan photoelectrons spectrum from the experiment at the ESRF synchrotron.

References

[1] A. Givon, E. Tiferet, I. Yaar and I. Orion, "Measurements and Simulations of Electron Transport through Polystyrene and Polyimide", Bilateral Workshop of the JRC-IAEC cooperation, Ein-Gedi, Israel May 2-6, (2010).
[2] A. Givon, E. Tiferet, G. R. Castro, J. Rubio-Zuazo, E. Golan, I. Yaar and I. Orion, "Hard x-ray photoelectron spectroscopy study of electron spectral structure beyond the known signal electron peak". J. Chemistry and. Chemical Engineering 7 pp. 601-605 (2013).

Small Volume Chemical Bath Deposition of Thorium-Alloyed and Thorium-Doped PbS Films

Michael Shandalov[1], Tzvi Templeman[2], Itzhak Kelson[3] and Eyal Yahel[1]

[1]*Department of Physics, Nuclear Research Center Negev, P.O. Box 9001 Beer Sheva, Israel*
[2]*Department of Materials Engineering, and Ilse Katz Institute for Nanoscale Science and Technology, Ben-Gurion University, Beer Sheva 84105, Israel*
[3]*School of Physics and Astronomy, Tel-Aviv University, Tel-Aviv 84105, Israel*

An addition radioactive element such as thorium to thin films is expected to provide a unique path for studying radiation damage in materials. As first part of this work, we developed a small volume chemical bath deposition (CBD) process for controlled alloying of PbS thin films (~100 nm thick) with the stable isotope ($t_{1/2}$~10^6 years), ^{232}Th. Small volume CBD technique is mandatory in order to decrease the use of Th precursor solution. In contrast to our previous work[1], we were able to drastically increase Th concentration in the films (up to ~7 at%). This was achieved by addition of sodium citrate into deposition solution, which extended Pb ions complexation in solution and allowed to obtain thicker films with higher Th concentration. Next, we developed small volume CBD process for controlled doping of PbS thin films with active ^{228}Th isotope, using different deposition parameters, due to ^{228}Th daughters presence in solution. This was achieved by altering deposition parameters such as temperature, pH, reagent concentrations and time.
The morphology and the thickness for all films were determined using scanning electron microscopy (SEM). X-ray photoelectron spectroscopy (XPS) depth profiles in ^{232}Th-alloyed PbS films indicated homogeneous ^{232}Th distribution in the films, and considerable amounts of oxygen were detected in the films as well. Presence of oxygen is explained by compensation of Pb^{2+} vacancies created in PbS lattice due to oxidation state difference between Pb^{2+} and Th^{4+} ions, by O^{2-} in the films. ^{228}Th-doped films were characterized using x-ray powder diffraction (XRD), which indicated a single phase material. Alpha-autoradiography confirmed homogeneous distribution of ^{228}Th ions throughout the films. The properties of the PbS(^{228}Th) film activity were investigated by using alpha-spectroscopy and gamma-spectroscopy. The resulting films show promise as a model system for the analysis of dilute defect systems in semiconductor thin films.

References

[1] M. Biton, A. Shamir, M. Shandalov, N. Arad-Vosk, A. Sa'ar, E. Yahel, and Y. Golan, *Thin Solid Films* **556**, 223 (2014).

Volatile and Air-Stable Uranium (IV) Precursors for Application in Gas Phase Deposition Processes

Rajitha Ravithas, Kavita Singh Ghotra, Lisa Rathgeber, Jennifer Leduc, Prof. Dr. Sanjay Mathur

Institute of Inorganic Chemistry, University of Cologne, Greinstrasse 6, 50939 Cologne, Germany, jleduc@smail.uni-koeln.de

Uranium complexes with fluoride-[1], borohydride-[2], amide-[3], silazane-[4], alkoxide-[5] and acetyl acetonate[6] ligands are known to be volatile but are not suitable for CVD processes due to different reasons: they are either unsuitable for safe long-term storage, thermally unstable, decompose under air or are sensitive to UV/Vis light. Recently, we have demonstrated the synthesis of air-stable, volatile uranium (IV) and (VI) compounds as well as their gas phase conversion to uranium oxide films.[7] Herein we present the use of heteroarylalkenolates with elongated perfluoroalkyl chain as well as the use of tetradentate enaminon ligands for obtaining novel uranium (IV) complexes with enhanced volatility.

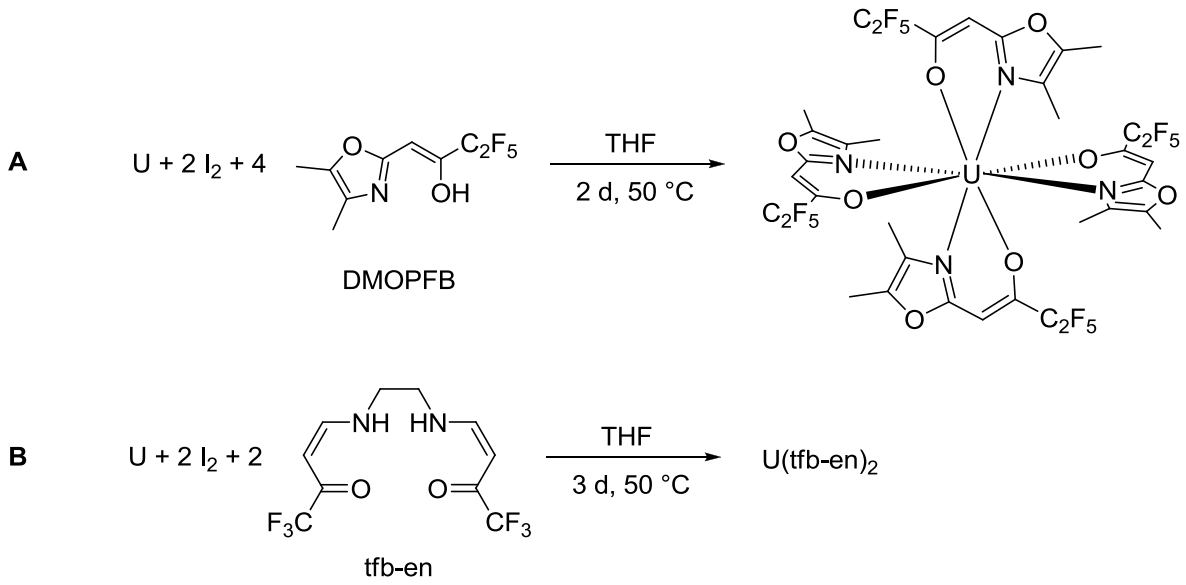

References

[1] F. G. Brickwedde, H. J. Hoge, R. B. Scott, *J. Chem. Phys.* **16**, 429–436 (1948).
[2] M. Ephritikhine, *Chem. Rev.* **97**, 2193 (1997).
[3] R. G. Jones, G. Karmas, G. A. Martin Jr., H. Gilman, *J. Am. Chem. Soc.* **78**, 4285 (1956).
[4] J. C. Berthet, M. Ephritikhine, *Coord. Chem. Rew.* **83**, 178-180 (1998).
[5] S. Fortier, G. Wu, T. W, Hayton, *Inorg. Chem.* **47**, 4752 (2008).
[6] R. Guilard, A. Dormond, M. Belkalem, J. E. Anderson, Y. H. Liu, K. M. Kadish, *Inorg. Chem.* **26**, 1986 (1987).
[7] L. Appel, J. Leduc, C. L. Webster, J. W. Ziller, W. J. Evans, S. Mathur, *Angew. Chem.* **126** (2014).

Magnetic and thermal properties of $CeNi_{1-x}Co_xGe_2$

Molčanová Zuzana[1], Mihalik Marián[1], Mihalik Matúš[1], Zentková Mária[1], Kavečanský Viktor[1], Briančin Jaroslav[2]

[1] *Institute of Experimental Physic, SAS, Watsonova 47, 04001, Košice, Slovakia, molcanova@saske.sk*
[2] *Institute of Geotechnics SAS, Watsonova 49, 04001, Košice, Slovakia*

In our contribution we present results of magnetization, AC susceptibility and specific heat measurements of $CeNi_{1-x}Co_xGe_2$ heavy fermion system ($0 < x < 1$) which were prepared by arc melting and grown by optical floating zone method in four mirror furnace. The parent compound $CeNiGe_2$ is an antiferromagnetic Kondo system that orders magnetically at T_N = 3.9 K and undergoes a spin structure rearrangement at T_1 = 3.2 K [1] while $CeCoGe_2$ is a nonmagnetic heavy-fermion Kondo compound with j = 5/2 ground state and large Kondo temperature T_K > 200 K [2]. Heat capacity measurements revealed double peak at magnetic phase transition with T_N = 3.6 K and T_1 = 3.0 K (Fig 1.). AC susceptibility measurements showed that the phase transition from the paramagnetic to the antiferromagnetic state was suppressed to lower temperatures with an increasing concentration of Co (insert of Fig 1.). The maximum of the transition temperature of $CeNiGe_2$ has been detected around 3.8K for x = 0. The Neel temperature decreased to 3.5K in the case x = 0.01. In the case of the substitution with x = 0.05 the Neel temperature decreases to 2.6K. In temperature range from 300K to 200K, the inverse susceptibility is linear and can be fitted with the Curie – Weiss law for all samples. The effective magnetic moment μ_{eff} for each compound has approximately the same value 2.55μ_B and the paramagnetic Curie temperature θ changes from -5.59 to -80 K.

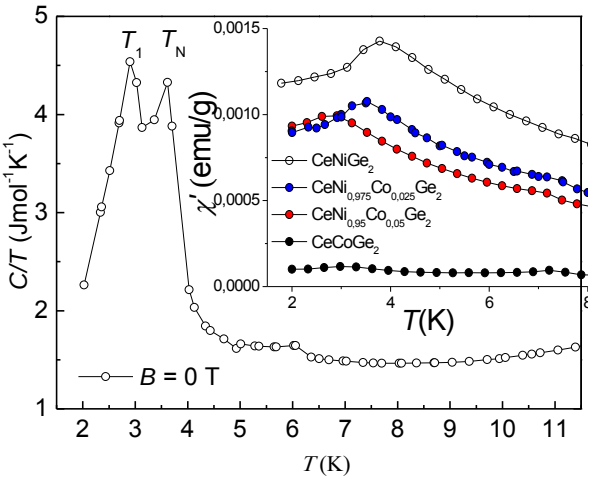

Fig. 1 Maxima related to magnetic phase transition in heat capacity for $CeNiGe_2$. The insert shows maxima in real part of AC susceptibility.

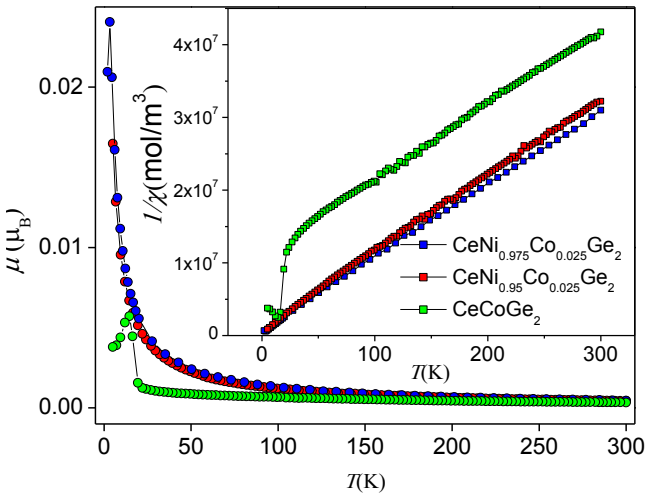

Fig. 2 Temperature dependence of magnetization. The insert shows inverse susceptibility.

References

[1] A.P. Pikul et al. Journal of Physics:Condensed Matter, Vol 16 (2004) 6119
[2] E. D. Mun et al. Physical Review B 69 (2004) 085113

Statistical analysis of UH_3 initiation sites using Electron Backscatter Diffraction (EBSD)

Antonios Banos[1], *Camilla Stitt*[1], *Tom Scott*[1]

[1]*Interface Analysis Centre, University of Bristol, BS2 1TL, England, email: ab13306@bristol.ac.uk*

The detrimental effects of radionuclide release caused by uranium hydride (UH_3) ignition when exposed to air are well known and established [1]. Hydride is found to form on the uranium surface in a spot wise manner nucleating at low energy sites (twin boundaries, grain boundaries, inclusions etc.) where physisorption, dissociation and absorption is assumed to be easier and more favourable. It is thus logical to examine the reaction at the very initial stages where hydride sites are nucleating and in the early stages of growth. At this early stage, growth spots can be very small, even submicron sized (small diameter family), or depending on the controlling influences, large enough to be easily observable (>50μm). In both cases, there is a need to verify that these nucleation spots are indeed UH_3 sites. Secondary Ion Mass Spectrometry (SIMS) has allowed us to quickly verify and locate hydride spots across the corroded Uranium surface by mapping UH^+ ion clusters; characteristic ion fragments produced by Gallium ion-sputtering of the sample surface on the regions where hydride was suspected to form (Fig.1b).

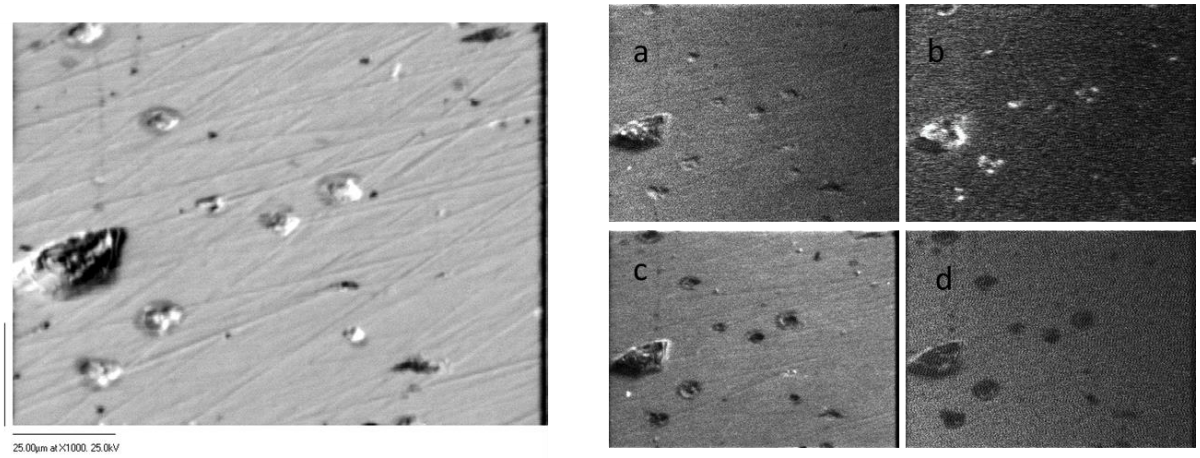

Figure 1: SEM image of a spot-hydrided and pre electropolished uranium surface. Mass spectra for a) Uranium (238) b) UH (239) c) UO (254) d) UO_2 (270).

To evaluate the preferential location of growth sites we have used Focus Ion Beam milling (FIB) to produce sectional cuts through every spot within a defined area and then observe the cross section

face at high magnification (Fig.2). However, this method is long-lasting especially for nucleation densities that exceed 500 spots per mm^2.

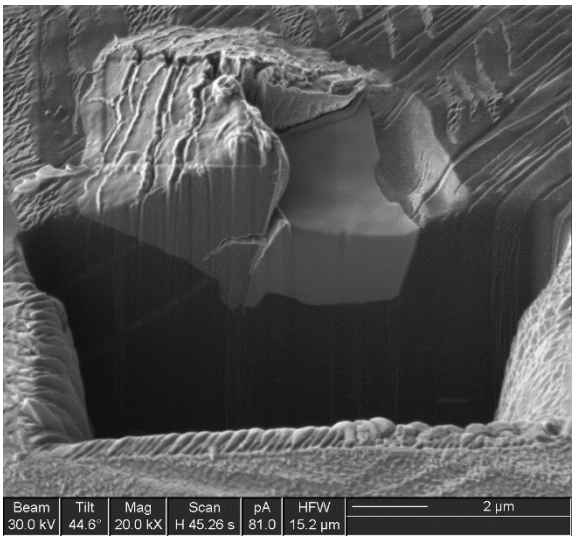

Figure 2: FIB sectioning on an initially intact hydride forming at the margins of a carbide inclusion. Twin boundaries can be easily seen passing through the centre of the nucleation spot.

This issue was overcome by direct ion-sputtering of the hydrided surface up to the stage where the grain structure was revealed and the sputtering depth has not exceeded the depth of the hydride nuclei causing them to vanish (Fig.3). Of course, this procedure is feasible only for preparations involving chemical etching (i.e electropolishing) which result in a pristine and non-damaged surface as compared to the mechanically damaged outer layer of a polished sample.

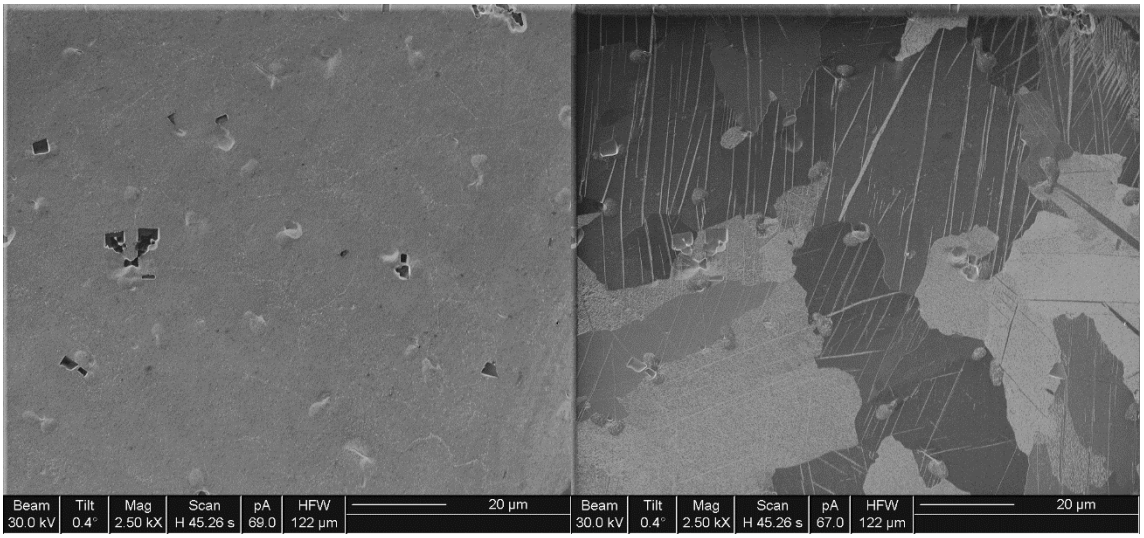

Figure 3: FIB images of a spot hydrided surface a) before ion-sputtering and b) after ion-sputtering for 5 minutes (6600pA).

By using ion-sputtering on a hydrided surface we were able to gain information about the preferential sites of hydride growth semi-quantitatively. However, to obtain quantitative microstructural and crystallographic information about the preferential sites of hydride initiation we have used Electron Backscatter Diffraction (EBSD). Following a step by step method of preparation, good EBSD patterns maybe produced for a hydrided uranium surface (Fig.4).

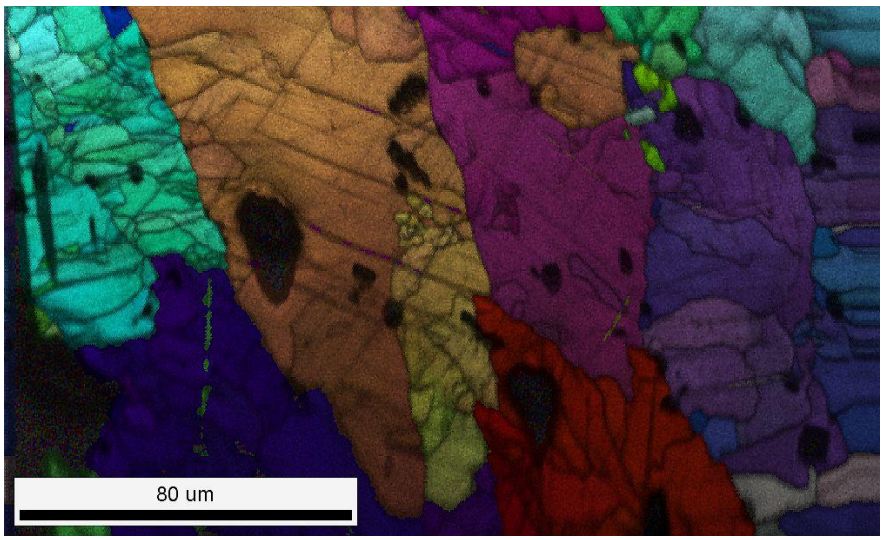

Figure 4: IQ + IPF map of a spot hydrided uranium sample. Large diameter and small diameter hydride spots are forming mainly around grain and twin boundaries.

Such an analytical approach permits statistical analysis of hydride nuclei location for Magnox-U containing chiefly Fe, Al and C impurities. From the analysis it was found that on an electrochemically etched surface, nucleation of UH_3 occurred predominantly at high angle grain and twin boundaries.

References

[1] Bazley, S. (2012). *The influence of hydrogen pressure and reaction temperature on the initiation of uranium hydride sites* (Vol. Volume 211). Solid State Ionics.

In Situ X-ray diffraction measurements of U-0.1w%Cr oxidation

S. Zalkind, G. Refaelov, I. Halevy, T. Livneh, D. Schweke

Nuclear Research Center-Negev, POB 9001, Israel, *e-mail: s_zalkind@yahoo.com*

Understanding the corrosion fundamentals of uranium alloys are essential for handling and long term disposal of spent nuclear fuels. *In-situ* X-ray diffraction was utilized to study the oxidation kinetics of U-0.1w%Cr under 3 PSI oxygen atmosphere and temperature range 90-150^{o}C. The oxide thickness formed on the surface during oxidation was evaluated from the attenuation of the metallic uranium diffraction peaks. This method allows to follow the oxidation kinetics of different crystallographic uranium plains at the surface.

Fig.1 presents XRD spectra taken during oxidation at 150^{o}C, illustrating the attenuation of the metallic U peaks and the development of the UO_2. Oxide thicknesses vs. time, as obtained for the indicated temperatures and for the different crystallographic metal plains are presented in fig. 2. A difference in the oxidation rates was found depending on the crystallographic orientation, the (112) being the fastest and (002) the slowest to oxidize. Fig. 3 presents the oxidation rates of the uranium (111) plain at the different temperatures. It is noticeable that the oxidation starts with a parabolic kinetic rate and when the oxide thickens breakaway and linear rates are observed. The reaction rates have strong temperature dependence and activation energies of $Q_{parabolic}$=17.5 kcal/mol and Q_{linear}=19 kcal/mol were evaluated using Arrhenius plot.

Complementary SEM analyses were performed on the oxidized surface, as presented in fig. 4. It can be seen that the oxide thickness is in very good agreement with the XRD calculations. Uranium carbides (UC) are found to accelerate oxidation around them.

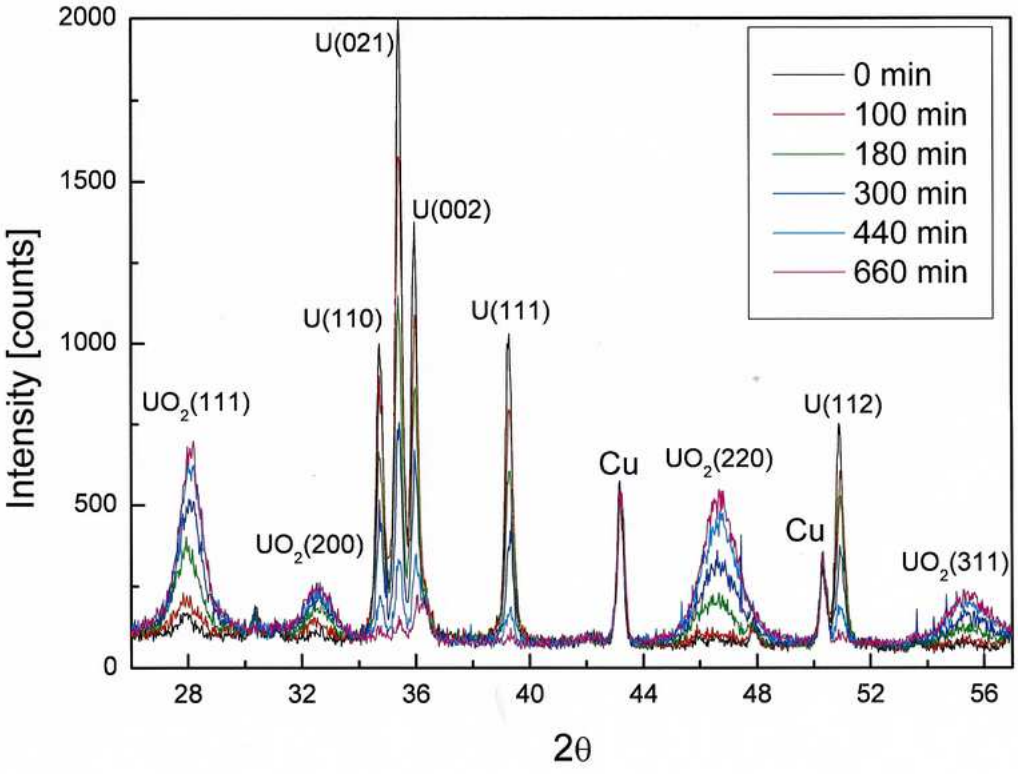

Fig. 1. XRD spectra taken in-situ during oxidation at 150^{o}C.

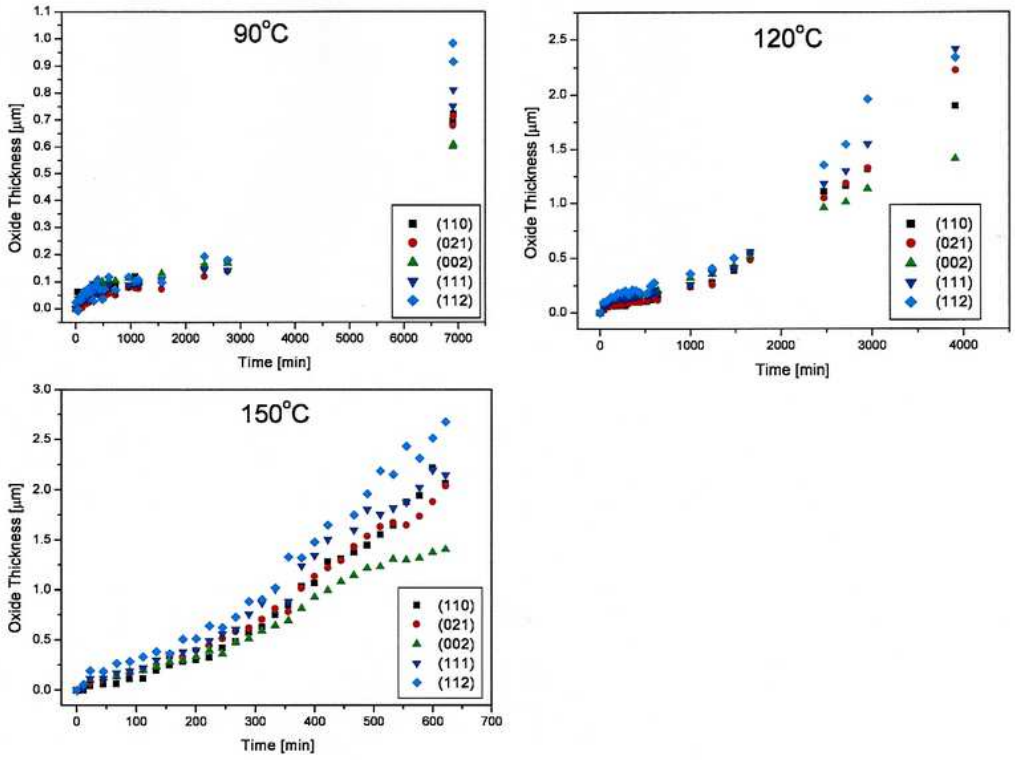

Fig. 2. Oxide thicknesses vs. time, as obtained for the indicated temperatures and for the different crystallographic metal plains.

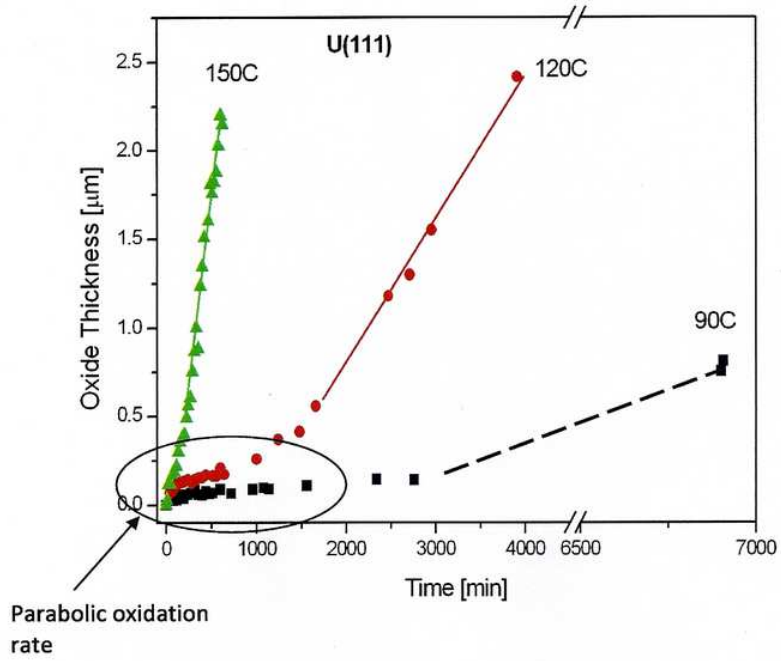

Fig. 3. The oxidation rates of the uranium (111) plain at the different temperatures. The initial parabolic kinetic rate and breakaway and linear oxide growth are indicated.

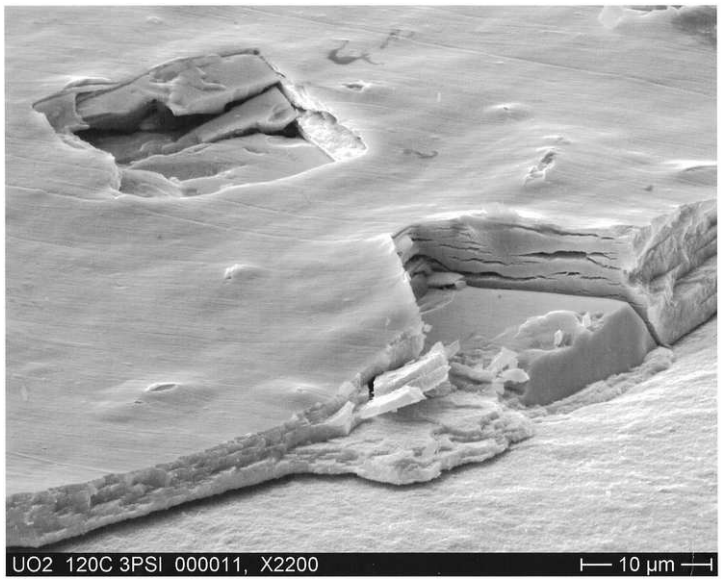

Fig. 4. SEM micrograph taken after oxidation at 120^{o}C. Uranium carbides are sites for preferred oxidation.

Structure and magnetism of UMB_4 (M = V, Cr, Mo, W) uranium borides

A.P. Gonçalves,[1] M.Dias[2], P.A. Carvalho[3], L. Havela[4]

[1] *C2TN, Instituto Superior Técnico, Universidade de Lisboa, Campus Tecnológico e Nuclear, Estrada Nacional 10, 2695-066 Bobadela LRS, Portugal, e-mail: apg@ctn.ist.utl.pt*
[2] *IPFN, Instituto Superior Técnico, Universidade de Lisboa, Av. Rovisco Pais, 1049-001 Lisboa, Portugal*
[3] *ICEMS, Departamento de Engenharia Mecânica, Instituto Superior Técnico, Universidade de Lisboa., Av. Rovisco Pais, 1049-001 Lisboa, Portugal*
[4] *Faculty of Mathematics and Physics, Charles University, Ke Karlovu 5, 12116 Prague, Czech Republic*

The UM'B_4 (M'=*d*-element) uranium borides were reported to exist and to crystallize in three different crystal structures $YCrB_4$-, $ThMoB_4$- and $ErNiB_4$-type [1]. However, their characterization was only preliminary, mainly devoted to crystallographic studies. Magnetization measurements were made just in the 80-300 K temperature range for the V, Mn, Fe, Co compounds, with no signs of magnetic transitions. The existence of superconductivity was also investigated for the Ru and Os borides, but no superconducting transition was observed down to 1.5 K. $UFeB_4$ was characterized by our group, the studies pointing to a predominant $YCrB_4$-type structure (in agreement with the previous results), but with a defective structure compatible with an intergrowth of $YCrB_4$- and $ThMoB_4$-type layers [2]. A paramagnetic behavior was observed in the 2–300 K temperature range. Continuing our investigations, here we present the preparation and study of another part of this family, UMB_4 (M=V, Cr, Mo, W), by means of X-ray powder diffraction, magnetization and specific heat measurements in the 2- 300 K temperature range.

The UMB_4 compounds were prepared by arc-melting followed by annealing at 1000ºC for 300h. Their powder X-ray patterns confirm that the V and Cr borides crystallize mainly in the $YCrB_4$-type structure (S.G. Pbam), while the Mo and W phases essentially adopt the $ThMoB_4$-type (S.G. Cmmm). The unit cell volume of the last two borides is significantly higher than the first two, which is in agreement with previous results that indicate that UM'B_4 borides containing larger transition metals have the tendency to crystallize in the $ThMoB_4$-type structure and those with smaller ones mainly adopt the $YCrB_4$-type [3]. From the point of view of magnetism, all compounds are weak Pauli paramagnets. The specific heat exhibits a strongly non-Debye character for all compounds, which most probably is related to the hardness of the boron sublattice. The γ-coefficient is moderately enhanced, but does not exceed 50 mJ/mol K^2, pointing to the presence of weakly correlated 5*f* states at the Fermi level.

References

[1] P. Rogl, The ternary and higher order systems with actinide elements and boron. In: Handbook on the Physics and Chemistry of the Actinides, A.J. Freeman and C. Keller (Eds.), Elsevier Science Publishers B.V. (1991), pp. 75.
[2] M. Dias, P.A. Carvalho, I.C. Santos, O. Tougait, L. Havela, A.P. Gonçalves, Microsc. Microanal. 19 (2013) 1204.
[3] P. Rogl, H. Nowotny, Uran-haltige Komplexboride, *Monatshefte fur Chemie* 106 (1975) 381.

Synthesis and thermal characterization of uranium carbide materials for ISOL targets

Stefano Corradetti[1], Mattia Manzolaro[1], Alberto Andrighetto[1], Pierluigi Zanonato[2], Daniele Scarpa[1], Alberto Monetti[1], Massimo Rossignoli[1], Roberto Silingardi[1]

[1] *INFN-Laboratori Nazionali di Legnaro, Viale dell'Università 2, 35020 Legnaro (Pd), Italy*
e-mail: stefano.corradetti@lnl.infn.it
[2] *Università di Padova, Dipartimento di Scienze Chimiche, Via Marzolo 1, 35131 Padova, Italy*

In the framework of the ActiLab [1] Work Package in ENSAR, a project within the 7th Framework Program of the European Commission, synthesis and characterization of different uranium carbides was carried out.

These materials were designed to be used as innovative targets for ISOL (Isotope Separation On-Line) facilities for the production of Radioactive Ion Beams (RIBs) [1], to be used for nuclear physics, astrophysics, medicine and materials science studies and applications.

The work here presented was in particular performed in the R&D laboratories of the SPES Project [2], a new ISOL facility now under construction, in collaboration with the other laboratories involved in the ActiLab WP (CERN, IPNO, GANIL, PSI).

The material synthesis was carried out starting from UO_2, graphite and phenolic resin mixtures pressed to form cylindrical pellets, which were then heated up to 1700 °C in a high vacuum furnace (P ~ 10^{-6} mbar). Prior to mixing it with the other reagents, UO_2 particle size was reduced by means of a vibratory micromill and selected using sieves.

Other materials, either UC or UC_2-based, were synthesized in other laboratories and sent to the SPES labs in the framework of the collaboration.

Thermal characterization consisted of emissivity direct measurements performed on all the samples and conductivity estimations on one material type using the technique reported in [3], developed at INFN-LNL to study refractory materials for the SPES target. The experimental setup to perform conductivity measurements, shown in fig.1, is based on a graphite crucible, heated by Joule effect, which by radiation induces thermal gradients in a cylindrical sample suspended above it, inside a high vacuum chamber. The measurement of the temperature gradient in specific positions of the sample top surface, and the comparison of these data with a numerical model developed in ANSYS®, results in the estimation of thermal conductivity by means of the inverse analysis method [3]. Emissivity measurements were obtained on the same setup, placing the samples directly on top of the heating crucible.

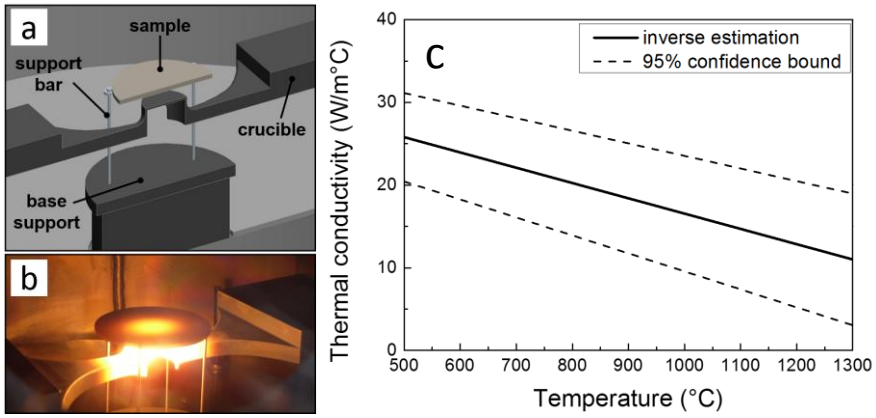

Fig. 1. a) CAD view of the setup for thermal conductivity measurements, b) setup during operation, c) k vs.T estimation.

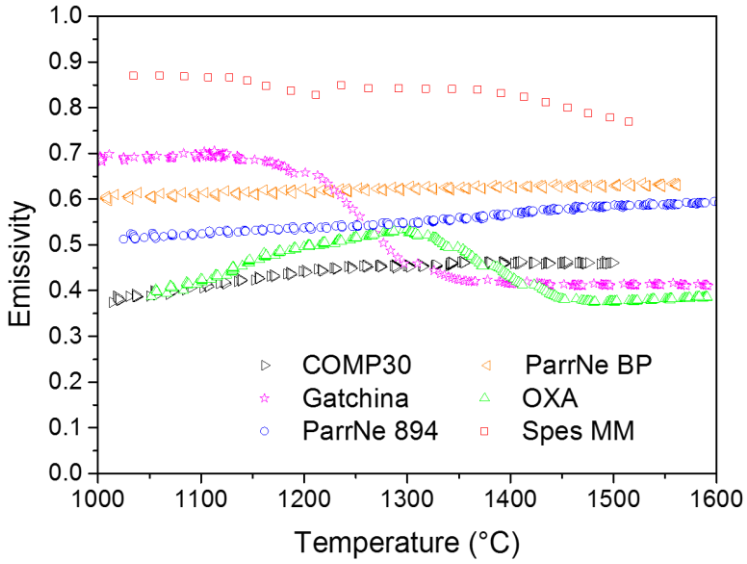

Fig. 2. Emissivity measurements of different uranium carbide-based materials.

Acknowledgements

Authors would like to thank all the people directly involved in the ActiLab collaboration: T. Stora, A. Gottberg, H. Franberg-Delahaye, J. Grinyer, C.Lau, S.Tusseau-Nenez, I. Gunther-Leopold, M. Martin.

References

[1] T. Stora, Nucl. Instrum. Methods Phys. Res., Sect. B **317**, 402 (2013).
[2] A. Andrighetto, G. Bisoffi, G. Bassato, L. Calabretta, M. Comunian, S. Corradetti, P. Favaron, F. Gramegna, G. La Rana, A. Lombardi, M. Maggiore, M. Manzolaro, A. Monetti, G. Prete, M. Rossignoli, D. Scarpa and J. Vasquez, AIP Conf. Proc. **1491**, 58 (2012).
[3] M. Manzolaro, S. Corradetti, A. Andrighetto and L. Ferrari, Rev. Sci. Instrum. **84**, 054902 (2013).

Neutron diffraction investigation of the eutectoid decomposition of γ-U(Mo) powder produced by magnesiothermic reduction

Guillaume Champion,[1] Mathieu Pasturel,[1] Florence Porcher,[2] Xavière Iltis,[3] Olivier Tougait[1]

[1] *Institut des Sciences Chimiques de Rennes, Chimie du Solide et Matériaux, UMR CNRS 6226, Campus de Beaulieu, bât. 10A, 35042 Rennes Cedex, France, e-mail: mathieu.pasturel@univ-rennes1.fr*

[2] *Laboratoire Léon Brillouin, UMR12 CEA-CNRS, Bât. 563 CEA Saclay, 91191 Gif sur Yvette Cedex, France*

[3] *CEA Cadarache,DEN/DEC, 13108 Saint-Paul-Lez-Durance Cedex, France*

Due to their high uranium density and good irradiation stability, cubic γU(8Mo) alloys are the most promising candidates for the fuel conversion of research and test reactors. Post irradiation examinations pointed out, among other [1,2], a major role of the decomposition reaction γU(8Mo) → U_2Mo + αU occurring below the eutectoid temperature of 585°C, on the fission gases behaviors and fuel-matrix interactions.

In order to better understand the decomposition process, it has been followed at 450°C by neutron diffraction (ND) for γ-U(8Mo) powder obtained by magnesio-reduction [3]. The decomposition kinetics are compared to the microstructure of the powder, examined by scanning electron microscopy, electron backscattered diffraction and transmission electron microscopy.

The results of ND pattern sequential refinement and the microstructural features, showing a clear relationship between the chemical homogeneity of the starting material and its resistance to decomposition, will be presented.

[1] A. Leenaers et al., *J. Nucl. Mater.* **2011**, *412*, 41.
[2] S. Van den Berghe *et al.*, *J. Nucl. Mater.* **2008**, *375*, 340.
[3] G. Champion *et al*., Adv. Eng. Mater., **2013**, 15, 257.

Thermodynamic properties of U in Ga-Sn eutectic alloy

Maltsev Dmitry,[1] Volkovich Vladimir,[1] Yamshchikov Leonid[1]

[1] *Ural Federal University, 19 Mira Str., Ekaterinburg, 620002, Russia*
e-mail: d.s.maltsev@gmail.com

Pyrochemical reprocessing of spent nuclear fuels (SNF) employing molten salts and liquid metals as working media is considered as a possible alternative to the existing solvent extraction (PUREX) process. High radiation resistance and thermal stability of molten salts and liquid metals are the main advantages, which allow reprocessing irradiated fuel from the fast neutron rectors with a high burn-up after relatively short cooling time.

Gallium–tin eutectic has one of the lowest melting points (m.p. 293.5 K) amongst gallium containing binary alloys. A wide temperature region of the liquid state makes Ga-Sn alloy quite attractive for the pyrochemical technologies. Knowing the main thermodynamic characteristics of uranium in both molten salts and liquid metals is necessary for achieving efficient separation of SNF elements.

The aim of the present work was studying the behaviour of uranium in the Ga-Sn based alloys and determining thermodynamic characteristics: activity, activity coefficients, and solubility of uranium.

Activity of uranium was determined in alloys based on Ga-Sn, Ga and Sn using the electromotive force (EMF) method. Uranium in the studied temperature range (298–1073 K) undergoes two phase transformations. In the present study for the thermodynamic measurements γ-uranium and super cooled liquid uranium were chosen as the standard states. The method of intermetallic compound (IMC) precipitation from the oversaturated alloys was employed to obtain uranium solubility directly from concentration of uranium in an alloy at a chosen temperature. Uranium activity coefficients in these liquid metals were determined from the difference between experimentally measured activity and solubility values.

To determine uranium activity the EMF measurements of the following galvanic cell were performed between 573 and 1073 K:

$$(-)\ U \mid LiCl\text{-}KCl\text{-}CsCl\text{-}UCl3 \mid U + Me\ (+), \qquad (1)$$

where Me is the low melting metal (Ga, Sn or Ga-Sn eutectic). Uranium metal acted as the reference electrode. Low melting ternary LiCl-KCl-CsCl eutectic (57.5 mol. % LiCl and 16.5 mol. % KCl, m.p. 536 K) was used as the solvent salt. Solubility of uranium in pure Ga and in the Ga-Sn eutectic alloy was measured in a wider temperature range of 296–1073 K employing the IMC precipitation method. All experiments were carried out in high-pure argon (99,998%) atmosphere.

1. Activity of uranium in alloys with Ga-Sn and Sn

X-ray powder diffraction analysis showed the existence of UGa_3 and USn_3 intermetallic phases in the solid alloy samples obtained in U-Ga-Sn and U-Sn alloys, respectively.

Activity of γ -U and super cooled liquid uranium in Ga-Sn-U alloy were calculated from the results of EMF measurements and are described by the following equations (at 571–1016 K):

$$\lg a_{\gamma}\text{-}U_{(Ga\text{-}Sn)} = 3.17 - 8.91\cdot10^{3}\cdot T^{-1}\ (\pm0.18) \qquad (2)$$
$$\lg a_{l}\text{-}U_{(Ga\text{-}Sn)} = 3.51 - 9.39\cdot10^{3}\cdot T^{-1}\ (\pm0.18) \qquad (3)$$

Activity of γ-uranium in binary U-Sn alloy was determined by [6] from EMF measurements at 813–1117 K. In the present study uranium activity in alloys with Sn was determined in a wider

temperature range of 573–1073K. The results obtained for γ-uranium and super cooled liquid uranium in U-Sn alloy in this temperature range is adequately described by the following equations:

$$\lg a_{\gamma\text{-U(Sn)}} = 3.11 - 8.79\cdot10^{3}\cdot T^{-1} \ (\pm 0.18) \quad (4)$$
$$\lg a_{\text{l-U(Sn)}} = 3.11 - 8.79\cdot10^{3}\cdot T^{-1} \ (\pm 0.18) \quad (5)$$

The data obtained in this work for U-Ga alloys are in a good agreement with previously reported [6]. Below 900 K our results are slightly different from those found in the literature. It may be connected with difficulties of measurements due to small solubility of uranium in pure tin at these temperatures.

Comparison of γ-uranium activity in U-Ga [5], U-Ga-Sn and U-Sn alloys, Fig. 1, shows that uranium activities in these alloys are essentially identical and they do not depend on the phase composition.

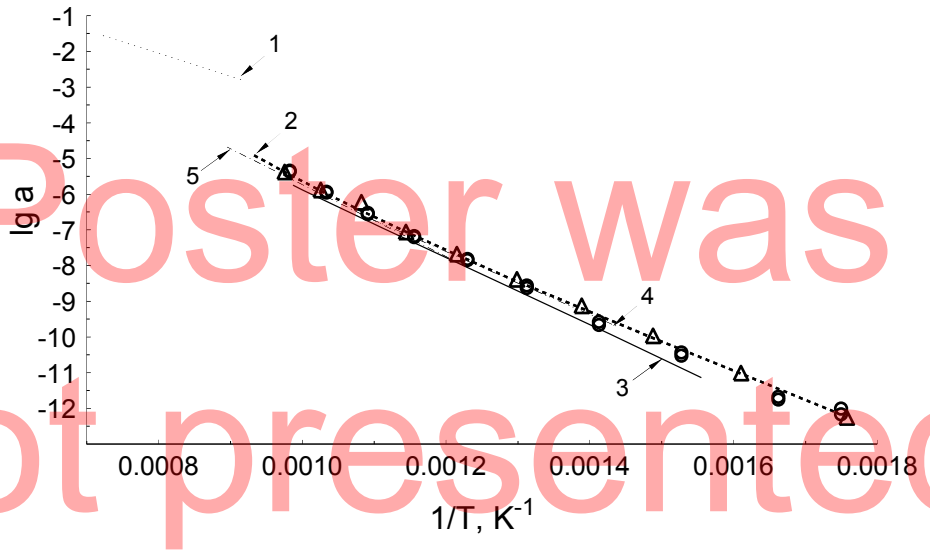

Fig. 1 - Activity of γ-U in U-Sn, U-Ga and U-Ga-Sn alloys. Symbols show the results obtained in the present work for the alloys based on Ga-Sn (○), Sn (Δ). Dashed lines show the literature data: 1-4 – U-Ga [1-3, 5], 5 – U-Sn [6].

2. Activity coefficients of uranium in alloys with Ga-Sn, Ga, Sn

The uranium activity coefficients were obtained as different between activity and solubility of uranium in the alloy under study at chosen temperature.

The obtained temperature dependence of activity coefficients for γ-uranium and super cooled liquid uranium in Ga-Sn eutectic alloy can be well described by the following expressions at 570-1016 K:

$$\lg\gamma_{\gamma\text{-U(Ga-Sn)}} = 0.07 - 1.43\cdot10^{3}\cdot T^{-1} \ (\pm 0.18) \quad (6)$$
$$\lg\gamma_{\text{l-U(Ga-Sn)}} = 3.39 - 6.52\cdot10^{3}\cdot T^{-1} \ (\pm 0.18) \quad (7)$$

The temperature dependence of uranium activity coefficients in liquid gallium was derived from different of uranium activity in gallium [5] and uranium solubility in gallium obtained in present work at the same temperature. This dependence for γ-uranium and super cooled liquid uranium can be described by following equations at 298-800 K:

$$\lg\gamma_{\gamma\text{-U(Ga)}} = 2.42 - 5.32\cdot10^{3}\cdot T^{-1} \ (\pm 0.42) \quad (8)$$
$$\lg\gamma_{\text{l-U(Ga)}} = 2.77 - 5.81\cdot10^{3}\cdot T^{-1} \ (\pm 0.31) \quad (9)$$

In this work we did not obtain solubility of uranium in liquid tin. Therefore extrapolated temperature dependence of uranium solubility in tin [6] was used to derive the activity coefficients of uranium in this metal in the wide temperature range of 569 – 1025 K. The obtained results for γ-uranium and super cooled liquid uranium can be well described by the following expressions:

$$\lg\gamma_{\gamma\text{-U(Sn)}} = 2.62 - 6.13\cdot10^{3}\cdot T^{-1} + 1.00\cdot10^{6}\cdot T^{-2}\ (\pm0.21) \qquad (10)$$
$$\lg\gamma_{l\text{-U(Sn)}} = 2.96 - 6.61\cdot10^{3}\cdot T^{-1} + 1.00\cdot10^{6}\cdot T^{-2}\ (\pm0.21) \qquad (11)$$

Uranium activity coefficients in Ga-Sn based alloys determined in the present work are very close to those in U-Ga alloys and lower than in U-Sn system. This difference increases with lowering the temperature, Fig. 2.

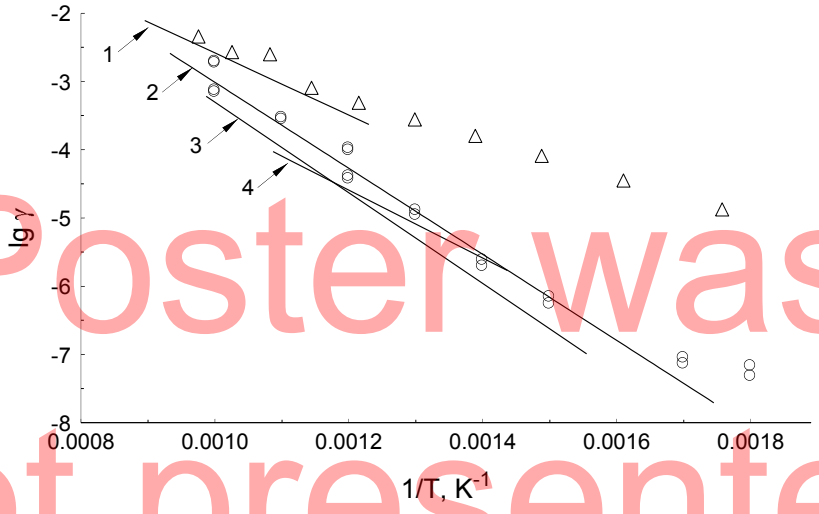

Fig. 2 Activity coefficients of γ-U in liquid alloys with tin, Ga-Sn eutectic, and gallium. Symbols show the results obtained in the present work for the alloys based on Ga-Sn (○), Sn (Δ). Lines show the literature data: 1 U-Sn [6], 2-4 U-Ga [5, 1,2]

3. Solubility of uranium in pure Ga and Ga-Sn eutectic alloys

The temperature dependence of uranium solubility in Ga-Sn eutectic alloy can be described by two linear equations (Fig. 3):

$$\lg X_{U(Ga\text{-}Sn)} = -2.79 - 1.46\cdot10^{3}\cdot T^{-1}\ (\pm0.66)\ (20 - 203\ ^{0}C) \qquad (12)$$
$$\lg X_{U(Ga\text{-}Sn)} = -0.02 - 2.77\cdot10^{3}\cdot T^{-1}\ (\pm0.37)\ (203 - 803\ ^{0}C) \qquad (13)$$

The temperature dependence of uranium solubility in Ga can be described by two following linear equations (Fig. 3):

$$\lg X_{U(Ga\text{-}Sn)} = -2.55 - 1.20\cdot10^{3}\cdot T^{-1}\ (\pm0.49)\ (23.5 - 274\ ^{0}C) \qquad (14)$$
$$\lg X_{U(Ga\text{-}Sn)} = 0.33 - 2.89\cdot10^{3}\cdot T^{-1}\ (\pm0.33)\ (274 - 800\ ^{0}C) \qquad (15)$$

In the studied temperature range uranium solubility in the Ga-Sn eutectic is very similar to the data obtained for U-Ga system, however there is a slight difference at a lower temperature range (297 – 524 K). Also at higher temperatures, the solubility of uranium in in the Ga-Sn alloy is close to that in pure tin but U solubility in Sn drops very fast with lowering the temperature [Fig.3].

The fact that only UGa3 intermetallic compound was found in cooled two-phase U-Ga-Sn alloys indicates that, al least at lower temperatures, uranium predominantly interacts with gallium.

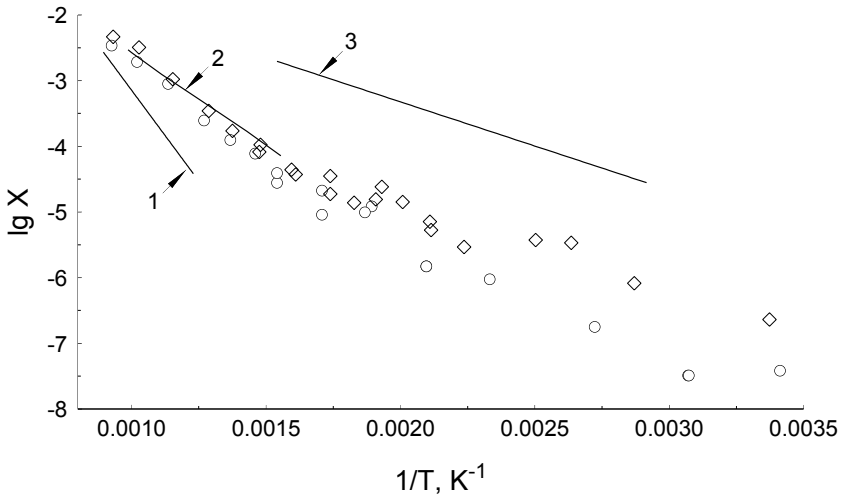

Fig 3 - Solubility of uranium in liquid alloys with tin, Ga-Sn eutectic and gallium. Symbols show the results obtained in the present work for the alloys based on Ga-Sn (○), Ga (◊). Lines show the literature data: 1 U-Sn [6], 2-3 U-Ga [1, 4]

References

[1] I. Johnson, H.M. Feder, *Thermodynamics of Nuclear Materials*, IAEA, Vienna, pp. 319-331 (1962)
[2] V.A. Lebedev, V.M. Seregin, A.M. Poyarkov, I.F. Nichkov, S.P. Raspopin, *Zh. Fiz. Khim.*, **47**, 712 (1973).
[3] C.B. Alcock, J.B. Cornish, P. Grievenson, *Thermodynamics*, **vol. 1**, IAEA, Vienna, pp. 211-230 (1966).
[4] J.R. Johnson, M.G. Chasanov, *Trans. ASM*, **vol. 56**, p. 272 (1963).
[5] Volkovich et.al., *Journal of Nuclear Materials*, **vol. 438,** pp. 94–98 (2013)
[6] V.A. Kadochnikov, V.A. Lebedev, I.F. Nichkov, and S.P. Raspopin, *Russ. Metall.*, **vol. 4**, pp. 61-63 (1976).

45èmes Journées des Actinides, April 15-19, 2015, Prague-Průhonice, Czech Republic

The Use of Finite-Element Modelling to Increase the Average Cooling Rate for the Plutonium Casting Furnace

Dr. Vijay Varsani,[1]

AWE, Aldermaston, Reading, Berkshire, RG7 4PR [1], e-mail: vijay.varsani@awe.co.uk

Non-equilibrium solidification leads to a segregated as-cast plutonium microstructure containing two phases (α and δ phase). As a result the castings are homogenised usually for hundreds of hours. Segregation depends on a number of factors which include diffusion co-efficient of the alloying element in the different phases, the average cooling rate and average dendrite arm spacing. The calcium silicate insulation material and the thickness of the graphite furniture used in the casting process are thought to severely limit the average cooling rate. A Finite-Element model of the plutonium casting process was developed to explore ideas in which the cooling rate could be increased further. By removing the insulation material, replacing the soldered heating coils with brazed coils and reducing the mould wall thickness the average cooling rate could be increased by up to 332%.

Assessment of the behaviour of metallic uranium during encapsulated product evolution

Haris Paraskevoulakos[1], Camilla Stitt[1] ,Tom B. Scott[1]

[1] *Interface Analysis Centre, HH Wills Physics Laboratory Tyndall Avenue, BS8 1TL Bristol, United Kingdom, e-mail: cp13846@bristol.ac.uk*

The safe long term containment of radioactive waste is an essential goal for the UK nuclear community. Within the UK radioactive waste inventory, metallic uranium fuel and its associated Magnox cladding are key 'reactive' materials requiring long term containment. Currently, this intermediate level waste (ILW) is encapsulated in cementitious materials and stored in stainless steel canisters [1]. Recently, significant volumetric expansion has been observed around the circumference of some of these canisters. The suspected reason for this expansion is the corrosion of the encapsulated metal as it reacts with the water present in the cement pores [2]. The arising corrosion products of uranium (uranium oxide/hydride) can occupy a significantly greater volume compared to the parent metal (around 2 times larger) [3]. This increasing internal pressure can lead to extensive grout cracking, when its strength (tensile and compressive) is exceeded. Furthermore, the transmitted stresses throughout the whole volume of the grout cause strains which are finally imposed on the encasing steel canister causing the formation of bulges.

Figure 1: Crack pattern as a result of tensile strength excess at the point of steel's yielding initiation. Massive cracks are shown in red colour.

In the event of an ultimate system's failure expressed by steel fracture, radioactive material could be released in atmosphere posing significant environmental threat. Besides, if pyrophoric uranium hydride forms within the grout environment a radioactive fire may occur as a result of oxygen influx through the failed encapsulated system. The latter scenario threatens the safe long term transport and disposal of the ILW drums. Consequently, the association of the corrosion extent with the mechanical degradation of the encapsulants; i.e the grout cracking and steel distortion magnitude, is essential to evaluate the risk of potential system's failure.

Finite element (FE) modelling, laboratory experimental work and synchrotron X-Ray/neutron diffraction and tomography are the tools employed to shed some light in the interior failure mechanisms of the ILW system. Finite element modelling can prove to be a useful predictive tool in terms of determining the strain state within the grout bulk and the surrounding stainless steel. 2d and 3D models with embedded metal bars have been created. The corrosion – induced volume expansion is simulated using the displacement method around the uranium edges. Crack pattern and Von Mises stress distribution can indicate the level of material degradation at all different steps of loading; i:e at different levels of corrosion (Fig.1). The outputs of the analyses indicate that the

grout's failure may occur very rapidly for low levels of uranium corrosion. Yielding of steel takes place later while most of the grout is crushed.

However, numerical analyses should be validated against experimental work to be efficient as the models are based on specific simplifications and assumptions. Accelerated corrosion tests are currently performed to test the validity of the FE models. Miniaturised ILW canisters with encapsulated uranium in grout are created and allowed to react under hydrogen exposure in suitable pressure – temperature conditions to initiate corrosion. A high magnification camera set up is used to monitor crack initiation and propagation resulting from corrosion – induced volume expansion (Fig.2). A laser scanning technique shall be used for displacement profiling around the circumference of the stainless steel. Time resolved corrosion extent measurements are obtained and linked with the crack initiation, surface cracking and other critical stages of the system's degradation.

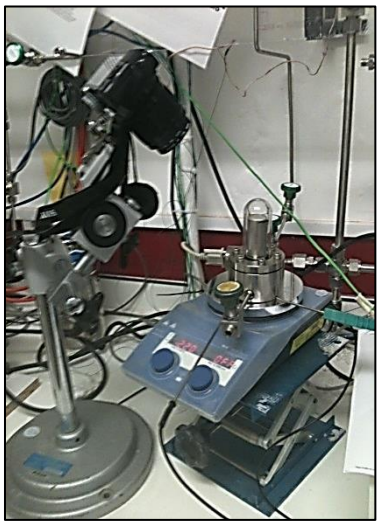

Figure 2: Miniaturised ILW drum system being corroded in the lab.

This specific experimental set up doesn't allow visualization of the interior of the canister, though. It is essential to reveal the mechanisms of corrosion (morphology, characterization of the corrosion products) as well as the interior crack initiation and propagation in order to fully understand the deterioration process. Besides, it is not yet proven that hydride can form in a completely constrained environment, even in an artificial environment. Thus, "seeing inside the box" is required. Studies of uranium corrosion in grout have found that attempts in air or a glove box to physically open the system and directly access the corrosion products can result in their vigorous exothermic chemical transformation, altering the system's behaviour and affecting the results [4]. An alternative non – destructive method to visualize the interior of the canister is using high energy synchrotron X – Rays to directly observe the corrosion state and the cracking behaviour. The latter has already been successfully performed in Diamond Light Source in non-confined systems (uranium – grout). X – Ray diffraction can allow characterization of the arising corrosion products to finally determine if hydride can form (Fig.3a). X – Ray tomography may provide full 3D visualization of a particular area around the uranium region in order to detect cracks and obtain information about the morphology of the corrosion products (Fig.3b) [4]. Relevant proposals have been sent to allow us study the online corrosion occurring inside a miniaturised ILW drum, representing a real ILW package. Neutron and gamma Ray tomography is also planned to be conducted in order to estimate the possibility of investigating larger scale drums efficiently.

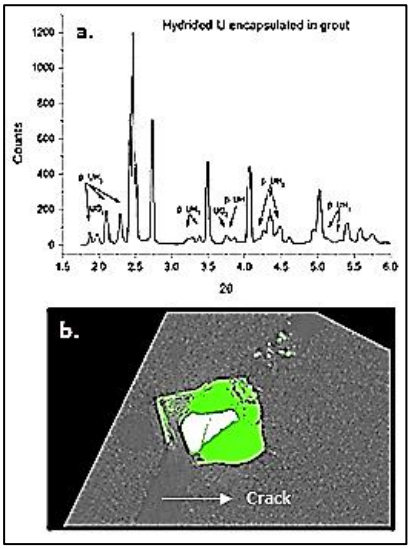

Figure 3: a) XRD pattern of hydrided uranium – grout system, b) Radiograph obtained illustrating the parent metal (light grey), the corrosion products (green) and grout (dark grey. Crack is also shown.

Temperature and time depend changes in speciation of radionuclides sorbed on crystalline rock samples

Yulia Konevnik, Elena Zakharova, Konstantin Martynov

[1] *IPHE RAS, Leninskiy prospect 31, Moscow, Russia 119071 e-mail: leonenko@gmail.com*

An area in gneissic rock near Krasnoyarsk has been chosen as one of the probable sites for a deep geological repository of high level radioactive wastes [1].

The kinetics of light actinides (U (VI), Np(V), Pu(IV) and Am(III)) and some fission products (Cs (I), Sr(II)) sorption from modeling groundwater by gneiss and dolerite collected from the above-mentioned site were evaluated at temperatures of 20 ºC and 90 ºC with different times of contact. Speciation of sorbed radionuclides and its time and temperature depend changes were studied using a modified Tessier's procedure of sequential extraction.

Rising temperature decreases Cs uptake and decrease part of residual fraction with increasing acid soluble one for all studied rock samples. Both of this fractions are strongly bound and such redistribution does not lead to decreasing safety of repository. Neptunium and uranium distribution coefficients, Kd, used in migration forecast increase several times with rising temperature from 20 ºC to 90 ºC. All other radionuclides have not shown significant increasing of uptake with temperature.

Speciation of sorbed radionuclides shows that for all studied radionuclides excluding Cs part of strongly bound fractions increase with rising temperature. Temperature depend changes are more pronounced than time depend.

Distribution of sequential extraction fractions either doesn't significantly change with time or part of strongly bound fractions increases or fraction related to iron oxides increases with decrease of all other fractions.

This shows that radioecological safety of repository will increase with time.

References

[1] Anderson E.B., Belov S.V., Kamnev E.V., Kolesnikov I. Yu., Lobanov N.F., MorozovV.N., Tatarinov V.N. Underground isolation of radioactive wastes. // M. «Gornaya kniga»,

p-25

Study of Cleanup Procedures for Contaminated Areas: Evaluation of Rubidium as a Surrogate to Cesium

Ronen Bar-Ziv, Ofra Paz-Tal, Eitan J.C. Borojovich, Roni Chakhmon, Itzhak Halevy and Ilan Yaar

Nuclear Research Center Negev, POB 9001 Beer Sheva 84190, Israel

Introduction:

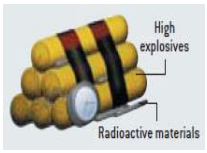

A radiological weapon, or radiological dispersion device (RDD), is designed to spread radioactive materials (^{137}Cs, ^{60}Co, ^{241}Am, ^{252}Cf, ^{192}Ir, ^{238}Pu, ^{90}Sr, ^{226}Ra, etc) over a large area, in order to cause severe contamination. The dispersed radioactive material can be strongly bound to surfaces if not effectively removed shortly after the event.

An effective decontamination agent for such cases is the commercial polymer Decongel-1101[1]. It can be applied onto contaminated surfaces by brushing or spraying. Upon drying, it forms stable films that can be peeled off the surface, together with most of the contaminating materials.

One of the most dangerous isotopes that can be used to produce a RDD is ^{137}Cs[2], therefore, it is important to examine the effectiveness of the polymer DeconGel-1101 in removing it. Working with ^{137}Cs in large scale experiments presents some difficulties, hence It was suggested to replace ^{137}Cs with the short lived radioisotope ^{86}Rb (~18.6 days). This isotope is a good surrogate for ^{137}Cs, having similar chemical properties and migration behavior.

[1] http://decongel.com/documents/1101%20Product%20Data%20Sheet%20v080612.pdf (Last accessed on 18.1.14).
[2] J.L.Conca, J.R. Wischnewsky and M.D. Johnson, Reducing the Threat of a Serious 137Cs Dirty Bomb, Proceedings of the DHS Conference; Working Together – Research & Development Partnerships in Homeland Security, the Seaport Hotel and World Trade Center, Boston, MA, April 27-28 (2005).

The goal:

Verifying whether ^{86}Rb can serve as a surrogate to ^{137}Cs in the development of cleanup procedures for large contaminated areas.

Methodology:

Combustion reaction

ANALYSIS

1. Natural Rb and Cs chloride salts (1ml) were spread on two different types of coupons (5X5cm^2), displaying porous and non-porous surfaces. The first made of Type II Portland cement and the second made of "Hebron" type marble. The concentrations of the chloride salts solutions were 0.1, 1, 10, 50 and 100 g/l, respectively.
2. After drying of the coupon surfaces, DeconGel-1101 was applied manually.
3. After 24 hours, the dry polymer was peeled off and mineralized in a combustion bomb containing 10 ml 0.1N HNO_3.
4. Concentrations of Rb and Cs in the 0.1N HNO_3 solutions were determined by suppressed ion chromatography.

Results:

Linear fit of the Cs to Rb Decontamination factor. Data taken from a non- porous ("Hebron" marble) surface cleaned with DeconGel-1101

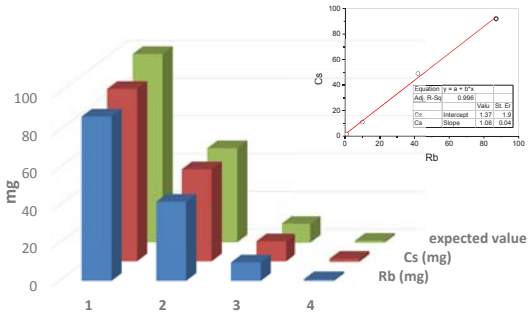

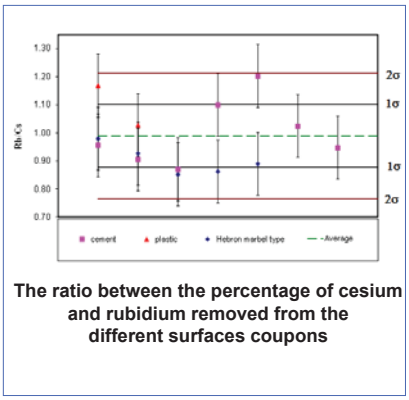

The ratio between the percentage of cesium and rubidium removed from the different surfaces coupons

Decontamination of porous (concrete) surface with DeconGel-1101 (XRF measurements)

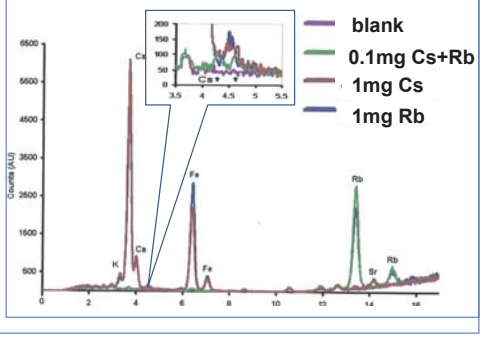

Conclusions:

1. The results obtained in this study point out that rubidium behave similarly to cesium in all surfaces tested, as expected from their chemical properties (some random variations have been observed which are within the limits of the experimental error), Hence ^{86}Rb may serve as a surrogate to ^{137}Cs in cleanup procedures of large contaminated areas experiments.
2. The chelating agents in the commercial DeconGel-1101 used is non-selective and extracts other metals such as Fe, Ca, etc, from concrete surfaces.
3. .The decontamination efficacy seems to be affected strongly from the surface type (porous or non-porous material)

Optimization of aerial survey of radiation in outdoor and indoor environments

Field of research
Engineering

PIs
Dr. Itzhak Halevy – NRCN
Dr. Amir Hen – NRCN
Dr. Shai Arogeti – BGU

Scientific background
Aerial radiation survey is the method of choice of first responders to a major nuclear incident. Aerial survey produces real time data that enables on line risk assessment and situation awareness. Large scale aerial radiation survey systems such as the SPARCS (USA) in Figure 1 (a) and Air RAM-2000 (Israel) are available and been used on various fixed wing airplanes and helicopters. All those systems require significant resources to operate and to maintain functionality for time of need. Also the large scale systems do not solve the problem of high accuracy and high resolution contamination estimation specifically in confined environments such as urban or indoor scenarios expected in Radiation Dispersal Device (RDD) attack.

a. SPARCS

b. Casper UAV

c. Mikro-Kopter UAV

Figure 1 – Platforms for Airborne Radiation Survey

To achieve the ability to monitor and assess contamination and its' risks with high accuracy the aerial monitoring system should have the following properties: (a) high sensitivity that will allow the shortest possible measurement time needed to collect the required statistics (sensor sensitivity) (b) the system should have the ability to "hold station" with high accuracy (c) the system should have the ability to measure its' altitude above ground with the required precision (sensor to source distance correction).
The 1st requirement can be divided into two interleaved technical issues, the airborne sensor (payload) its' sensibility and sensitivity which translate to size, weight and power requirements and the flying platform characteristics, specifically, station keep ability, endurance and power efficiency.

Analytical and simulative work has that proposes an algorithm for radioactive contamination estimation out of airborne survey data has been carried out at the NRCN and awaits validation with real world data. Number of test survey flight that were made both by a fixed wing drone (Casper UAV Figure 1 (b)) and a hexacopter platform (Mikro-Kopter Figure 1 (c) and Figure 2) show the feasibility and limitations of the airborne survey by small scale UAVs . The test surveys emphasized the inherent limitations of the platform and payload combinations and the need to optimize both.

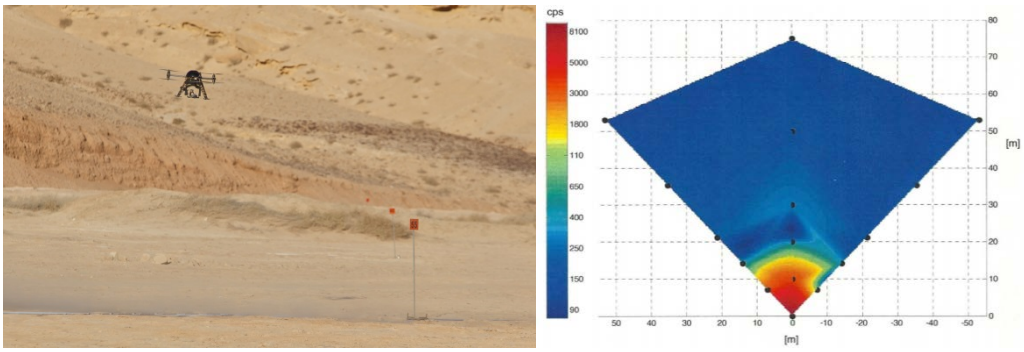

Figure 2 – Contamination Survey using a QuadCopter UAV and results obtained in a 12 minutes flight

Motivation

While large scale airborne radiation survey systems exists they cannot answer the need for high accuracy survey required in radiation dispersal scenarios both in indoor and outdoor environments following an RDD attack. With recent advances in the civilian the drone field, it becomes apparent that this gap in survey ability can be bridged by employing small scale drones of various types. Those drones employ high level of autonomy and it is evident that automatic operation and smart survey patterns can be employed with high level of confidence. The main drawback of small scale drones is their operation time (endurance) versus useful payload weight. While fixed wing small scale drones can achieve substantial air time to pay load weight they cannot achieve the slow flight or hover characteristics needed for high accuracy survey. Therefore an optimization of the radiation sensor (sensitivity vs. weight) and carful platform selection is needed to provide a real world applicative high accuracy airborne survey system.

Research goals

The goal of the research is to produce a parametric selection function for the survey system and to achieve a real world demonstration of optimal aerial survey system of radiological contamination in outdoor and indoor environments.

The research will focus on the optimization of the sensor and flying platform. The research aims to produce an optimized parametric selection function which will help to quantize the engineering tradeoffs of detector sensitivity versos platform performances. A benchmark will be established and validated through simulations, calibration measurements using sealed radiation sources and with data from various platforms and sensors combinations.

Tetrakiscyclopentadienyl-actinide(IV)-complexes (Cp_4An): structures and reactivity against Broensted acidic compounds

Christos Apostolidis, Olaf Walter, Michal Dutkiewicz, Alfred Morgenstern

European Commission, Joint Research Centre, Institute for Transuranium Elements, P.O. Box 2340, D-76125 Karlsruhe, Germany, e-mail: christos.apostolidis@ec.europa.eu

The organometallic complexes [Cp_4An] (An: Th, U, Np, Pu) of the 4-valent actinides are among the first organometallic compounds of these elements which have been synthesised and described in the literature [1-4].
They can be prepared relatively easily by metathesis reaction in high yields. Kinetic shielding of the nuclei by the four organometallic Cp-ligands in a tetrahedral arrangement around the central metal contributes to their resulting good stability.
However, under careful control of the reaction conditions reaction with Broensted acidic compounds might proceed to well defined organometallic products exhibiting interesting spectroscopic and magnetic properties.
An example of the presented chemistry is given in the scheme 1, the reactions will be presented on Th, U, and Np, respectively.

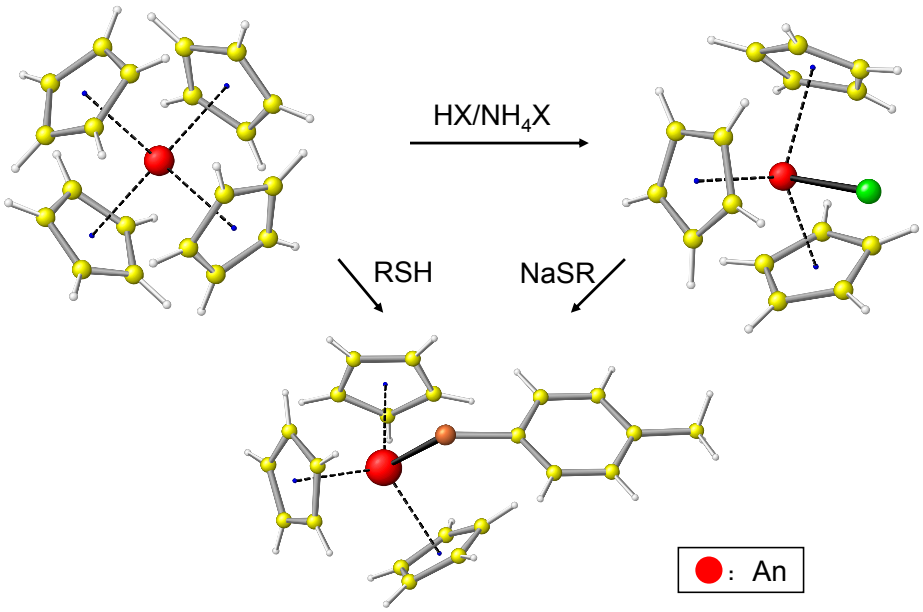

Scheme 1: Cp_4An, conversion into Cp_3AnX, both starting material for the synthesis of Cp_3AnX derivatives of via salt metathesis or via direct reaction with Broensted acidic compounds.

References

[1] E.O. Fischer, Y, Hristidu, *Z. Naturforsch., Teil B*, **17**, 276 (1962)
[2] E.O. Fischer, A. Treiber, *Z. Naturforsch., Teil B*,**17**, 275 (1962)
[3] F. Baumgärtner, E. O. Fischer, B. Kanellakopulos, P. Laubereau, *Angew. Chem. Int. Ed. Engl.*, **7**, 634 (1968)
[4] F. Baumgärtner, E. O. Fischer, B. Kanellakopulos, P. Laubereau, *Angew. Chem. Int. Ed. Engl.*, **8**, 202 (1969)

About protonated uranyl oxalate species. Affinity capillary electrophoresis data.

Sladkov Vladimir

CNRS, Institute de Physique Nucleaire (IPN), UMR 8608, 15 rue G. Clemenceau, 91406, Orsay, France, e-mail:sladkov@ipno.in2p3.
[2] Université Paris-Sud, Orsay, France

The interaction of U(VI) with oxalic acid is of great interest. It deals not only with a fundamental knowledge, but also with the migration of U(VI) species in the environment, as oxalic acid is one of the products of the degradation of natural organic matter and can form the complex species with U(VI).

The focus of this project is to obtain information about the existence of protonated uranyl oxalate species by using affinity capillary electrophoresis. The protonated complex species of uranyl oxalate are difficult to identify by physical methods [1]. In this project the mobilities of U(VI) are measured in aqueous acid solutions, containing oxalic acid at different concentrations. The observed U(VI) mobility is found to decrease with increasing ligand concentration added to the background electrolyte. The obtained data do not allow to confirm the existence of protonated uranyl oxalate species in aqueous solutions in range of pH from 1,5 to 2,5.

References

[1] W. Hummel, G. Anderegg, L. Rao, I. Puigdomenech and O. Tochiyama *Chemical Thermodynamics of Compounds and Complexes of U, Np, Pu, Am, Tc, Se, Ni and Zr with selected organic ligands.* Ed. F.J. Mompean, M. ILLemassene and J. Perrone, **vol. 9**, 1088 pages (2005) (Elsevier, Amsterdam).

CO_2 mitigation and production of methanol over bimetallic copper-lanthanides/actinides oxides catalysts

C.O. Soares[1], A.P. Gonçalves[1], Ana C. Ferreira[1,2], T. Almeida Gasche[1], J.B. Branco[1]

[1]*Centro de Ciências e Tecnologias Nucleares (C2TN) IST-UL, Campos Tecnológico e Nuclear, Estrada Nacional 10 ao Km 139.7 2695-066, Bobadela-Loures, Portugal*

[2]*Centro de Química e Bioquímica - FCUL, Campo Grande, 1749-016 Lisboa, Portugal*

**e-mail: cybelle@ctn.ist.utl.pt*

Introduction

There is growing concern about the emission of greenhouse gases (GHG), namely CO_2, CH_4 and NOx. A way to mitigate its effects implies their use as reagents aiming the production of value-added chemicals such as hydrocarbons and alcohols [1]. The production of CH_3OH became a major target addressing two major problems: depletion of fossil fuels and GHG effect. Actinides and lanthanides based catalysts were already applied with success in the partial oxidation of CH_4 and other catalytic reactions evolving hydrocarbons [2-5] as well as CH_3OH synthesis [6].
Herein, CO_2 and CH_4 were used as reagents for the production of CH_3OH over Cu combined to *f* elements catalysts.

Experimental

The bimetallic oxides supported in alumina were prepared by co-precipitation method, as described elsewhere [1b]. The intermetallic compounds containing *f*-block elements (IC) were obtained by the arc melting technique [7]. In order to obtained the bimetallic oxides, some of IC suffer a controlled oxidation under air (Air Liquide, O_2:N_2 = 20:80 (vol%), purity 99.995%). All prepared catalysts were characterized by XRD and SEM.
The catalytic tests for methanol production were carried out at 50 bar in a stainless steel reactor. Mass flow controllers were used to control CH_4 (Air Liquide, purity 99.9995%), CO_2 (Air Liquide, purity 99.9995%), H_2 (Air Liquide, purity 99.9995%) and He (Air Liquide, purity 99.9995%) flows. Unless otherwise stated, a gaseous mixture with a CO_2 / H_2 / CH_4 (1:3:1 mol/mol/mol) was used and the reaction studied with an adequate Gas Hourly Space Velocity (GHSV, mL of CO_2/g of catalyst.h) of 40000 mol_{CO2} /g_{Cat}.h.

Results and discussion

Preliminary results show that bimetallic oxides obtained from IC are more active than commercial Cu based catalysts (Alfa Aesar) for the production of CH_3OH using CO_2, CH_4 and H_2 as reagents at 50 bar and 250 ºC (Fig.1).

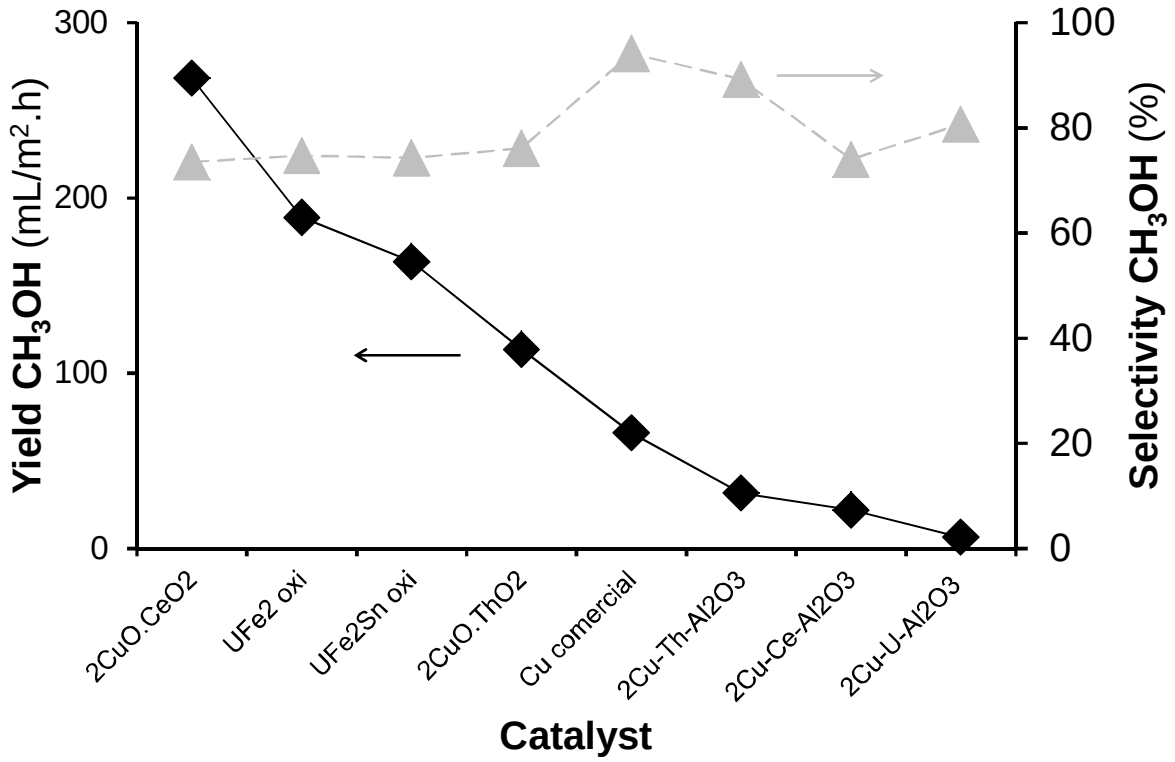

Figure 1. Activity and selectivity for the production of methanol using CO_2 / H_2 / CH_4 (1:3:1 mol/mol/mol) as reagents at 250 ºC, total pressure of 50 bar and a gas hourly space velocity (GHSV) of 40000 mol_{CO2} /g_{Cat}.h.

Ongoing characterization show that the bimetallic oxides are better described as a d metal oxide embedded in a matrix of lanthanide or actinide oxides where the existence of a synergism with the *f* block element phase [4] can explain the higher activity for methanol formation.

Acknowledgements: this work was supported by FCT under contract number PTDC/AAG-TEC/3324/2012. Ana C. Ferreira thanks FCT for her PhD grant (SFRH/BD/69942/2010).

References

[1]a) L. Shi; G. Yang.; K. Tao; Y. Yoshiharu; Y. Tan; N. Tsybaki, *Accounts of Chemical Research*, **2013**, *46*, 1838-1847; b) A Urakawa, A. Bansode; *Journal of Catalysis*, **2014**, *309*, 66-70.

[2] A.C. Ferreira; A. P. Gonçalves; T. Almeida Gasche; A.M. Ferraria ; A.M.B. Rego; M.R. Correia; A.M. Bola; J.B. Branco, *Journal of Alloys and Compounds* **2010,** *497*, 249-258.

[3] J.B. Branco; D. Ballivet-Tkatchenko; A. C. Matos, *Journal of Molecular Catalysis A: Chemical* **2009,** *307*, 37-42.

[4] A. C. Ferreira, A. P. Gonçalves, T. Almeida Gasche, A. M. Ferraria, A. M. Botelho do Rego, M. R. Correia, J. B. Branco, *Journal of Alloys and Compounds*, **2010**, *489*, 316-323.

[5] Z. R. Ismagilov, S. V. Kuntsevich, N. V. Shikina, V. V. Kuznetsov, M. A. Kerzhentsev, V.A. Ushakov, V. A. Rogov, A. I. Boronin, V. I. Zaikovsky, *Catalysis Today*, **2010**, *157*, 217-222.

[6] E.G. Baglin, G. B. Atkinson, L. J. Nicks, *Ind. Eng. Chem. Prod. Res. Dev.*, **1981**, *1*, 87-90.

[7] J. B. Branco, T. Almeida Gasche, A. P. Gonçalves, A. Pires de Matos; *Journal of Alloy and Compounds 323-324*, **2001**, 610-613.

Neptunium(IV) Coordination Chemistry and Spontaneous Reduction in a Flexible Small-cavity Macrocycle

Michał S. Dutkiewicz[a,b], Olaf Walter[a]*, Joy H. Farnaby[b], Christos Apostolidis[a] and Polly L. Arnold[b,]*

[a] *European Commission, Joint Research Centre, Institute of Transuranium Elements, E06 Unit Actinide Research, P.O. Box. 2340, D-76125 Karlsruhe, Germany.*
[b] *EaStCHEM School of Chemistry, University of Edinburgh, West Mains Road, Edinburgh EH9, 3JJ, UK.*
**e-mail: Olaf.WALTER@ec.europa.eu; Polly.Arnold@ed.ac.uk*

Existing research recognizes the critical role played by understanding of metal-ligand covalency in actinide bonding and particularly appealing f-block arene π- and δ-(back)bonding interactions. On the contrary, the interactions of transuranic cations to aromatic π-electron systems remain restricted to the cyclopentadienyl and cyclooctadienyl anions and to our knowledge no transuranic metal-arene interactions have been investigated to date.

Inspired by previous findings of π- and δ-symmetry bonding interactions of the flexible small-cavity macrocycle *trans*-calix[2]benzene[2]pyrrole, H_2L, to uranium and Th^{IV} cations[1], we were interested in the ability of $(L)^{2-}$ to complex the heavier actinides, and report here reactions with neptunium(IV) chloride that result in the spontaneous reduction and formation of mono- and bimetallic Np^{III} complexes, and the structural preference for a bis(arene) type neptunium coordination.

$^{237}NpCl_4$ was treated with the equimolar of dipotassium salt of trans-calix[2]benzene[2]pyrrole (K_2L) in tetrahydrofuran yielded $[(L)^{237}Np(\mu\text{-}Cl)_2{}^{237}NpCl_2(THF)_3]$ (**2**). The similar approach utilizing 1.5 molar equivalent of K_2L afforded the mononuclear complex $[(L)^{237}NpCl]$ (**1**) in 46% isolated yield. Both reactions produced also copious off-white organic residues, potential radical recombination byproducts of the unstable *metalocene*–Np^{IV} bond homolysis step. Suprisingly, this reactivity resulted in the reduction of Np^{IV} to Np^{III} in each case, in the absence of any obvious reducing agent. Complex **2** formally contains an additional equivalent of *in situ* generated $Np^{III}Cl_3$ bound through a chloride bridging rather than participating in ligand bridging.

A concept, syntheses, crystal structures and solution studies by ^1H NMR of the new Np^{III} complexes will be presented and discussed.

References

1. P. L. Arnold, J. H. Farnaby, R. C. White, N. Kaltsoyannis, M. G. Gardiner, J. B. Love, Chem. Sci., **2014**, *5*, 756-765.